UNIVERSITAT
POLITÈCNICA
DE VALÈNCIA

DEPARTAMENTO DE MÁQUINAS Y MOTORES TÉRMICOS

Doctoral Thesis

FEASIBILITY STUDY OF JET-EJECTOR REFRIGERATION SYSTEMS AS A MECHANISM FOR HARNESSING LOW-GRADE THERMAL ENERGY FROM DIFFERENT SOURCES

Presented by:
Mr. Alberto Ponce Mora

Directed by:
Dr. Vicente Dolz Ruiz

in fulfillment of the requisites for the degree of Doctor of Philosophy

Valencia, January 2022

Ph.D. Thesis

Feasibility study of jet-ejector refrigeration systems as a mechanism for harnessing low-grade thermal energy from different sources

AUTHORS

Presented by: MR. ALBERTO PONCE MORA
Supervised by: DR. VICENTE DOLZ RUIZ

Ph.D. ASSESSORS

Member: DR. VINCENT LEMORT
Member: DR. ANTONIO LECUONA NEUMANN
Member: DR. ANGELO ONORATI

Ph.D. COMMITTEE

Chairman: DR. JOSÉ RAMÓN SERRANO CRUZ
Secretary: DR. FRANCISCO VERA GARCÍA
Member: DR. ANGELO ONORATI

Valencia, October 2021

FEASIBILITY STUDY OF JET-EJECTOR REFRIGERATION SYSTEMS AS A MECHANISM FOR HARNESSING LOW-GRADE THERMAL ENERGY FROM DIFFERENT SOURCES

Alberto Ponce Mora

Abstract

Jet-ejector refrigeration systems powered by renewable heat or waste heat sources have the potential to achieve significant primary energy savings when substituting or aiding traditional refrigeration systems. Not surprisingly, the research interest around them has experienced growth in the last few years. Their field of applicability is vast and the present work has been focused on a detailed study of two applications with great potential following a computational approach: (i) air-conditioning generation powered by solar thermal energy and (ii) internal combustion engine intake air refrigeration powered by its exhaust line waste heat.

The research efforts have been directed towards mitigating the negative effect of two of the main weak points of jet-ejector refrigeration systems: their relatively low efficiency and the incapacity of the baseline configuration to operate robustly away from the design conditions. The first issue has been addressed mainly by designing highly optimized jet-ejector geometries using computational fluid dynamics techniques and optimizing the jet-ejector integration in the overall system. The second one has been addressed by carrying out complete characterizations of the refrigeration system response in design and off-design conditions. Advanced strategies to face the refrigeration system performance decay away from design conditions have been proposed, like the utilization of adjustable jet-ejector architectures or the implementation of hot thermal storage tanks.

The system response has been analyzed in off-design conditions with two complementary temporal schemes. The steady-state models have been used to optimize the jet-ejector architectures and the overall system operation for representative operating scenarios, while the transient analysis represents a more realistic approach and accounts for changes in climatic conditions, which have an unpredictable and unstable nature.

The study has been concluded with a thermoeconomic analysis, which has been useful to discern if the highly optimized designs are competitive when compared to existing refrigeration solutions consolidated in the market.

The main findings of the research work prove that the proposed jet-ejector optimization sequence allows maximizing the jet-ejector performance for reference and representative operating conditions. Likewise, the highly optimized adjustable jet-ejector geometry allows for significant improvements when operating in off-design conditions.

The main conclusions of the steady-state analysis for the solar application are that the transformation from thermal power to refrigeration power (COP_{th}) can achieve an efficiency of 37.7%, while the global efficiency achieves 20.1% when highly optimized jet-ejectors are used for an evaporating and condensing conditions of $13°C$ and $40°C$, respectively. In dynamic conditions, the implantation of an adjustable jet-ejector brings improvements in refrigeration system efficiency (COP_{th}) of around 40%, besides improving its capacity to remain in operation. The thermal storage system plays a relevant role in this sense and, for a fixed parabolic trough collector span of 7.1 m, a nominal thermal power consumption of 13.3 kW represents a trade-off between the performance indicators subject to analysis. The thermoeconomic assessment of the most promising system architecture suggests that the operating cost savings are far from compensating for the capital expenditures (16,905 € for a refrigeration capacity of approximately 5.6 kW), evidencing the difficulties of the system to compete against refrigeration solutions currently consolidated in the market and outlining the interest in hybrid solutions.

The main conclusion of the automotive application is that it is feasible to achieve in the engine intake line temperatures below $4°C$, bringing improvements in volumetric engine efficiency of around 11%. Nevertheless, the system shows vulnerabilities when operating in engine operating points different from the design one.

Resumen

Los sistemas de refrigeración por eyección activados por calor de origen renovable o fuentes de calor residual tienen el potencial de alcanzar ahorros energéticos significativos al sustituir o asistir a los sistemas de refrigeración tradicionales. Por tanto, no es de extrañar que el interés científico en torno a ellos haya experimentado un crecimiento en los últimos años. Su campo de aplicabilidad es muy amplio y el presente trabajo se ha centrado en un estudio detallado de dos aplicaciones con gran potencial siguiendo un enfoque computacional: (i) generación de aire acondicionado activado por energía solar térmica y (ii) refrigeración de la admisión de un motor de combustión reutilizando la energía térmica disponible en la línea de escape de este.

Las actividades de investigación han estado dirigidas a mitigar dos de los principales puntos débiles que caracterizan a los ciclos de refrigeración por eyección: su eficiencia relativamente baja y la incapacidad mostrada por la configuración base del ciclo de eyección para operar de forma robusta en condiciones de operación alejadas de las de diseño. La primera cuestión ha sido abordada principalmente diseñando geometrías de eyector altamente optimizadas usando técnicas de mecánica de fluidos computacional y optimizando la integración del eyector en el conjunto del sistema de refrigeración. La segunda cuestión se ha abordado caracterizando el comportamiento del sistema en condiciones de diseño y fuera de diseño. Se han propuesto dos estrategias avanzadas para hacer frente a la caída de prestaciones que sufre el sistema al operar en condiciones fuera de diseño, como son la utilización de eyectores de geometría ajustable o la implementación de tanques de almacenamiento térmico.

La respuesta del sistema se ha analizado en condiciones fuera de diseño con dos aproximaciones temporales complementarias. Los modelos estacionarios se han usado para optimizar las diferentes arquitecturas de eyector y la operación global del sistema en ciertas condiciones de operación representativas, mientras que el análisis transitorio representa un enfoque más realista y tiene en cuenta la naturaleza impredecible e inestable de los cambios en las condiciones climáticas.

El estudio se ha concluido con un análisis termoeconómico, el cual ha sido útil para discernir si los diseños altamente optimizados son competitivos al ser comparados con las soluciones de refrigeración que se encuentran actualmente consolidadas en el mercado.

Los principales hallazgos del trabajo de investigación demuestran que el proceso propuesto de optimización geométrica de eyectores permite maximizar las prestaciones

del eyector para unas condiciones determinadas de referencia. Asimismo, la geometría variable altamente optimizada permite mejoras significativas al operar en condiciones fuera de diseño.

La principal conclusión del análisis en condiciones estáticas para la aplicación termosolar es que la transformación de potencia térmica a potencia de refrigeración puede alcanzar un rendimiento (COP_{th}) del 37.7 %, mientras que el rendimiento global del sistema alcanza el 20.1 % con diseños altamente optimizados de eyector para unas condiciones de evaporación y condensación de $13°C$ y $40°C$, respectivamente. En condiciones dinámicas, la implementación de la geometría variable mejora en torno a un 40% el rendimiento del sistema de refrigeración (COP_{th}), además de incrementar su capacidad de permanecer en funcionamiento. El tanque de almacenamiento térmico juega un papel relevante en este aspecto y, para una envergadura de colector parabólico de 7.1 m, un consumo nominal de 13.3 kW de potencia térmica del tanque ha resultado ser una solución de compromiso para mantener en equilibrio los principales indicadores de prestaciones. El análisis termoeconómico de la arquitectura más prometedora sugiere que el ahorro de coste operativo está lejos de poder compensar la elevada inversión inicial en equipamiento (16.905 € para una capacidad de refrigeración aproximada de 5.6 kW), poniendo de manifiesto la dificultad del sistema para competir con las soluciones de refrigeración actualmente consolidadas en el mercado y resaltando la necesidad de considerar soluciones híbridas.

La principal conclusión de la aplicación en motor de combustión es que la reducción de temperaturas en la línea de admisión por debajo de $4°C$ es factible, produciendo mejoras en el rendimiento volumétrico de en torno al 11%, no obstante, el sistema muestra vulnerabilidades al operar en puntos de motor diferentes al de diseño.

Resum

Els sistemes de refrigeració per ejecció activats per calor d'origen renovable o fonts de calor residual tenen el potencial d'assolir estalvis energètics significatius al substituir o assistir als sistemes de refrigeració tradicionals. Per tant, no és de estranyar que l'interès científic al voltant d'ells haja experimentat un creixement en els últims anys. El seu camp d'aplicabilitat es ampli i el present treball s'ha centrat en un estudi detallat de dos aplicacions amb gran potencial seguint un enfocament computacional: (i) generació d'aire condicionat activat per energia solar tèrmica i (ii) refrigeració de l'admissió d'un motor de combustió reutilitzant l'energia tèrmica disponible en la línia d'escapament d'aquest.

Les activitats d'investigació han estat dirigides a mitigar dos dels principals punts dèbils que caracteritzen als cicles de refrigeració per ejecció: la seua eficiència relativament baixa i la incapacitat mostrada per la configuració base del cicle d'ejecció per a operar de forma robusta en condicions d'operació allunyades de les de disseny. La primera qüestió ha sigut abordada principalment dissenyant geometries d'ejector altament optimitzades usant tècniques de mecànica de fluids computacional i optimitzant la integració de l'ejector en el conjunt del sistema de refrigeració. La segona qüestió s'ha abordat caracteritzant el comportament del sistema en condicions de disseny i fora de disseny. S'han proposat dos estratègies avançades per a fer front a la caiguda de prestacions que pateix el sistema quan opera en condicions fora de disseny, com són la utilització d'ejectors de geometria ajustable o la implementació de tancs de emmagatzemament tèrmic.

La resposta del sistema s'ha analitzat en condicions fora de disseny amb dos aproximacions temporals complementàries. Els models estacionaris s'han usat per a optimitzar les diferents arquitectures d'ejector i l'operació global del sistema en certes condicions d'operació representatives, mentre que l'anàlisi transitori representa un enfocament més realista i té en compte la natura impredictible i inestable dels canvis en les condiciones climàtiques.

L'estudi s'ha conclòs amb un anàlisi termoeconòmic, el qual ha sigut útil per a discernir si els dissenys altament optimitzats són competitius quan es comparen amb les solucions de refrigeració que es troben actualment consolidades al mercat.

Les principals troballes del treball d'investigació demostren que el procés proposat d'optimització geomètrica d'ejectors permet maximitzar les prestacions de l'ejector per a unes condicions determinades de referència. Així mateix, la geometria variable

altament optimitzada permet millores significatives al operar en condicions fora de disseny.

La principal conclusió de l'anàlisi en condicions estàtiques per a l'aplicació termosolar és que la transformació de potència tèrmica a potència de refrigeració pot arribar a un rendiment (COP_{th}) del 37.7 %, mentre que el rendiment global del sistema arriba al 20.1 % amb dissenys altament optimitzats d'ejector per a unes condicions d'evaporació i condensació de $13°C$ i $40°C$, respectivament. En condicions dinàmiques, la implementació de la geometria variable millora al voltant d'un 40 % el rendiment del sistema de refrigeració (COP_{th}), a més d'incrementar la seua capacitat de romandre en funcionament. El tanc d'emmagatzemament tèrmic juga un paper rellevant en aquest aspecte i, per a una llargària de col·lector parabòlic de 7.1 m, un consum nominal de 13.3 kW de potencia tèrmica del tanc ha resultat ser una solució de compromís per a mantenir en equilibri els principals indicadors de prestacions. L'anàlisi termoeconòmic de l'arquitectura més prometedora suggereix que l'estalvi de cost operatiu està lluny de poder compensar l'elevada inversió inicial en equipament (16.905 € per a una capacitat de refrigeració aproximada de 5.6 kW), posant de manifest la dificultat del sistema per a competir amb les solucions de refrigeració actualment consolidades al mercat i ressaltant la necessitat de considerar solucions híbrides.

La principal conclusió de l'aplicació en motor de combustió és que la reducció de temperatures a la línia d'admissió per baix de $4°C$ és factible, produint millores en el rendiment volumètric de al voltant de l'11%, no obstant això, el sistema mostra vulnerabilitats a l'hora d'operar en punts de motor diferents al de disseny.

List of publications

The following papers have been published in international scientific journals and form the basis of this thesis:

- *Numerical optimization of an ejector for waste heat recovery used to cool down the intake air in an IC engine*, by Galindo, Gil, Dolz and Ponce-Mora [1].

- *Thermodynamic analysis and optimization of a jet ejector refrigeration cycle used to cool down the intake air in an IC engine*, by Galindo, Dolz, Tiseira, and Ponce-Mora [2].

- *Numerical evaluation of a solar-assisted jet-ejector refrigeration system: Screening of environmentally friendly refrigerants*, by Galindo, Dolz, García-Cuevas, and Ponce-Mora [3].

- *Numerical assessment of the dynamic behavior of a solar-driven jet-ejector refrigeration system equipped with an adjustable jet-ejector*, by Galindo, Dolz, Tiseira, and Ponce-Mora [4].

- *Optimization of the thermal storage system in a solar-driven refrigeration system equipped with an adjustable jet-ejector*, by Luján, Galindo, Dolz, and Ponce-Mora [5].

Division of work between authors

These publications have been produced in collaboration with other researchers, being the author signatures in order of seniority. The author of this thesis contributed with the development of the computational models, development of resolution strategies and postprocessing of the results presented here. Methodologies and results discussions were conducted in collaboration with my supervisor, Prof. Dolz, as well as with the rest of co-authors.

Other publications

The following list presents another publication in which the author of this thesis was involved during the research activities leading to the present work. Although not directly present in this document, the publication has contributed to understanding the operation of jet-ejector refrigeration systems.

- *Advanced exergy analysis of a jet ejector refrigeration cycle used to cool down the intake air in an internal combustion engine*, by Galindo, Dolz, Pla, and Ponce-Mora [6].

For the lighthouse keepers - past, present and future.

Acknowledgments

First of all, my most sincere acknowledgment to the whole CMT-Motores Térmicos team for giving me the opportunity of being part of it and the grant program *Subvenciones para la contratación de personal investigador predoctoral* for doctoral studies (reference ACIF 2018/124), awarded by *Generalitat Valenciana, Conselleria de Innovación, Universidades, Ciencia y Sociedad Digital* and the European Union for funding this project. All the students, technicians, researchers, professors, and the rest of the staff have contributed in one way or another to the successful completion of my research, and I truly thank them for that.

I am deeply indebted to my fellow grad students, specially, Pau Varela, Nicolás Medina, María Martínez, Lucas González, Fabio Gutiérrez, Juan David Echavarría, Guillermo García, and Miguel Ángel Bernal for their help, empathy, and the fruitful exchange of ideas.

I would like to express my deepest appreciation to my supervisor, Dr. Vicente Dolz Ruiz, for the trust placed in me, his patience, dedication, valuable contributions, and wise guidance in the research field. This is a great leap in my career and my formation and I owe it to him.

I would also like to extend my gratitude to my school friends, Carlos Villegas, and Alejandro Coronado, as well as my university friends, Carlos Llácer, Pau Varela, and Jesús Mario López, for enriching my life with experiences and giving me support, motivation, and understanding.

Finally, I would like to thank my whole family, especially my brother, Alejandro, for supporting, listening, and encouraging me throughout these years, and for giving me good advice during my whole life.

With special affection and love to Beatriz, who came into my life near the end of this chapter and changed everything.

Contents

I   Steady-state evaluation of the refrigeration system   105

4 Steady-state characterization of the fixed-geometry jet-ejector (FJE)107

List of Figures

List of Tables

Nomenclature

Acronyms

AJE : Adjustable Jet-Ejector

AR : Jet-ejector Area Ratio

ARS : Adjustable Refrigeration System

$CAPEX$: Capital Expenditures

CPC : Compound Parabolic Concentrator

DNI : Direct Normal Irradiance [W/m^2]

ETC : Evacuated Tube Collector

EU : European Union

FJE : Fixed-geometry Jet-Ejector

FPC : Flat Plate Collector

FRS : Fixed-geometry Refrigeration System

HTF : Heat Transfer Fluid

IAM : Incidence Angle Modifier [$-$]

ICE : Internal Combustion Engine

$JERS$: Jet-Ejector Refrigeration System (generic reference)

$OPEX$: Operating Expenses

PHE : Plate Heat Exchanger

PTC : Parabolic Trough Collector

SP : Spindle position

$TECS$: Thermal Energy Collecting System

TMY : Typical Meteorological Year

TSS : Thermal Storage System

$VCRS$: Vapor-Compression Refrigeration System

Greek Symbols

α :   Absorptivity $[-]$

β :   Fitting coefficient $[-]$, or Chevron angle of the plate heat exchanger $[°]$

ϵ :   Emissivity $[-]$

η :   Efficiency $[-]$

μ :   Dynamic viscosity $[Pa \cdot s]$

ω :   Jet-ejector entrainment ratio $[-]$

ρ :   Reflectivity $[-]$, or Density $[kg/m^3]$

τ :   Transmissivity $[-]$

θ :   Solar collector indicence angle $[°]$

Roman Symbols

A :   Area $[m^2]$

C :   Monetary cost $[€]$

c :   Specific heat capacity $[J/(kg \cdot K)]$

f :   Thermal storage system volume factor $[m]$

h :   Convective heat transfer coefficient $[W/(m^2 \cdot K)]$, or specific enthalpy $[J/kg]$

R :   Diameter $[m]$

R :   Radius $[m]$

V :   Volume $[m^3]$

x :   Vapor quality $[-]$

Z :   Compressibility factor $[-]$, or Heat Exchanger Zone

Subscripts

abs : Parabolic trough collector absorber

acc : Accumulation term

adv : Advection term

amb : Ambient

aux : Auxiliary system

Nomenclature

co :   Condenser

col :   Solar collector

$comp$:   Compressor

$cond$:   Conduction term

$conv$:   Convection term

e :   Jet-ejector

ev :   Evaporator

ex :   Internal combustion engine exhaust line

ext :   External

g :   Gas

gc :   Parabolic trough collector glasss cover

ge :   Generator

hx :   Heat Exchanger

hyd :   Hydraulic

in :   Inlet

int :   Internal combustion engine intake line, or interior (generic reference)

l :   Liquid

mf :   Jet-ejector mixed flow

mi :   Parabolic trough mirror

opt :   Optimum or Optical

out :   Outlet

pf :   Jet-ejector primary flow

pm :   Pump

rad :   Radiation term

ref :   Reference condition/situation

rf :   Refrigerant

rl :   Refrigeration load

s :   Isentropic process

sat :   Refrigerant saturation condition

sf :   Jet-ejector secondary flow

thr :   Jet-ejector nozzle throat

w :   Dissipation medium (water)

DOCTORAL THESIS

Chapter 1

Introduction

1.1 Background

According to reports of the European Commission, the last five years have been the warmest since records began and the global average temperature has increased by 1.1 °C since the pre-industrial period [9]. Climate change is mainly driven by the greenhouse effect, which occurs naturally on Earth but is being accelerated by the side effects of human activity. Activities like the burning of fossil fuels in industrial processes and transport, deforestation, exploitation of farming livestock, or the release of fluorinated gasses have an enormous contribution to the emission and accumulation of greenhouse gasses. The EU has been making a significant effort to mitigate climate change and to boost the transition towards a climate-neutral and sustainable economy. In fact, in 2019, the emissions were reduced by a 25% when compared to the year 1990 despite the economy has grown up to 62% during these three decades.

According to Eurostat [10], in 2019 only a little fraction of the energy consumed in the EU-27 (19.7 %) came from renewable energy sources. This means that a significant part of the electricity production is still based on non-renewable sources. The use of renewable energy, however, shows an ascending trend. The case of the refrigeration and heating sector is of particular interest due to the high number of units in the market and the foreseeable growing trends. The percentage of the energy generated using renewable sources in these sectors (22.1 %) is comparable to the energy sector general figures. The air-conditioning market represents around 5% of the total energy consumption in European households while it is even greater in the service sector (13 %) [11]. These figures support the fact that the air-conditioning sector is responsible for a significant fraction of the energy budget and, with the current energy scenario, a contributor to global emissions and climate change. This aggravated in summer periods, when the high electricity demand might be supplied by more polluting generation processes, like thermal power stations.

The construction of refrigeration machines, their operation, and maintenance have both a direct and indirect footprint and, as consequence, are subject to increasingly stringent regulations. The direct repercussions are related to leakages of harmful re-

frigerants while the indirect effects are associated with the energy consumption of the systems.

The direct consequences are attributed to incorrect sealing, end-of-life treatment, or decommissioning of the refrigeration units. The increasingly stringent regulations affecting the usage and manipulation of refrigerants and refrigeration units are very helpful to reduce the direct negative impact.

The indirect effects can be abated with the improvement and further innovation in state-of-the-art equipment and also improving insulation or charging new generation refrigerants. The indirect harmful consequences could also be alleviated by substituting or reducing the consumption of electricity, whose generation is currently still far from being completely based on renewable sources. The problem is aggravated especially during peak consumption time slots in summer periods or long-lasting heatwaves due to the high workload of the refrigeration units. The possibility of developing refrigeration machines that make use of greener primary energy sources could be decisive in the seek of net-zero refrigeration equipment.

1.2   Motivation

The harvest of waste heat to produce refrigeration has been highlighted for decades as a promising way to improve the energy efficiency of refrigeration machines and also to combat climate change. The vast majority of research efforts have revolved around sorption systems, relegating to a minor role other thermomechanical technologies. Jet-ejector refrigeration systems offer unique strengths like their mechanical simplicity, their reduced maintenance needs, and their reduced cost. With an adequate design, they might have aptitude to be efficient and price competitive.

In the jet-ejector refrigeration systems the energy efficiency of the overall system lies in the jet-ejector to a large extent and this component is very sensitive to its internal dimensions. The real potential will only be unveiled with ad hoc designs and this is unexplored in the literature due to the elevated computing cost of carrying out extensive optimization campaigns and the high economic and labor cost of manufacturing multiple prototypes and characterize them experimentally. In the present research special care is given to a thorough optimization of the jet-ejectors for their design operating conditions as a mechanism to improve the overall system performance.

The penalty that off-design conditions cause in the jet-ejector efficiency is also a well-known issue that harms its competitiveness. Some advanced strategies have been traditionally contemplated in the literature to mitigate this negative impact. However, the effectiveness of these concepts has not been analyzed and optimized in detail while integrated into the overall refrigeration system working under characteristic steady-state and transient operating conditions.

1.3 Objectives

The main objective of the present investigation is the numerical characterization and optimization of jet-ejector refrigeration systems with a special emphasis on solar refrigeration applications. The purpose is to quantify the refrigeration system performance on the design conditions and different off-design scenarios to provide a realistic estimation of the efficiency that can be expected. More superficially, the feasibility of using jet-ejector refrigeration systems to produce refrigeration harnessing the exhaust energy of an internal combustion engine has also been assessed.

The main goal of the present research can be split into the following secondary objectives:

1. **Refrigeration system assessment in steady-state conditions**

   The definition of steady-state operating conditions representing frequent operating scenarios is a necessary reference framework to optimize designs irrespective of the application. This objective contributes to quantifying the jet-ejector and overall system performance in idealized stable conditions. This approach is focused on both solar refrigeration and automotive applications. The main secondary objectives are listed below:

   - Jet-ejector design: To run validated computational fluid dynamics simulations to optimize the internal geometry of the jet-ejector using real gas models. To study the effect of using new generation benign refrigerants on the jet-ejector performance and to establish a relation between the refrigerant selection, the operating conditions, and the jet-ejector internal geometry.

   - Jet-ejector characterization: To design simple and advanced jet-ejector architectures and to determine the characteristic maps of all the prototypes.

   - Jet-ejector refrigeration system characterization: To generate realistic computational models of the overall system fed with jet-ejector CFD models. To evaluate the system response against different representative boundary conditions.

2. **Refrigeration system assessment in dynamic conditions**

   The response in transient conditions represents a better approximation to the real system behavior. This objective contributes to quantifying realistically the real improvement potential over different scenarios, considering the thermal inertia effects of the cycle elements and the fluctuations in climatic conditions. This approach is exclusively focused on solar refrigeration applications. The main secondary objectives are listed below:

   - Overall system response under variable climatic conditions: To assess the effectiveness of using advanced architectures to maintain an acceptable performance in a wide range of scenarios. To study the instantaneous and real-time response against climatic events of random nature, scarcity of available

5

thermal power, or fluctuations in the ambient temperature.

- Optimum system sizing: To evaluate the effect of different backup system sizing and different strategies of thermal energy consumption and its impact over the main performance indicators.

- Jet-ejector refrigeration system thermoeconomic study and comparison with the mainstream solutions: To compare the financial feasibility of the jet-ejector refrigeration system in the mid-term and long-term when compared to current well-established and dominant technologies.

1.4 Method employed

In Chapter 2 the literature review is presented starting from the general thermomechanical refrigeration solutions to the particular case of the jet-ejector refrigeration systems, highlighting prior research works, main existing barriers as well as research and development opportunities. The methodology of the present research is based on the development of computational models, being explored several approaches to simulate all the elements of the cycle. In Chapter 3 the computational models are described as well as the main assumptions, simplifications, boundary conditions, computational techniques and assembling insights of the models. The refrigeration system assessment is split making the same distinction as in the objectives: the system response is evaluated first in steady-state conditions and then the response under dynamic conditions is assessed. The models are dedicated to present the steady-state and/or the dynamic response of the key components of the refrigeration system.

The aim of the numerical results shown in Chapter 4 is to survey commonly used working fluids with low environmental impact and quantify the maximum performance offered by each refrigerant using highly optimized jet-ejector geometries. The study is applied on fixed jet-ejector geometries and is carried out using a commercial fluid dynamics code. The CFD tools have been essential in this part to determine the jet-ejector response maps. In Chapter 5, an identical characterization procedure is reproduced with an adjustable geometry jet-ejector, however, the calculations are particularized for the most promising refrigerant found in Chapter 4. The adaptation capability offered by the adjustable configuration is also determined with the same computational tools.

In Chapter 6, the jet-ejector maps obtained for the conventional and adjustable geometries are employed to quantify the design and off-design response of the overall refrigeration system considering a solar refrigeration application. Matlab and the optimization utility modeFrontier are the key software utilized in this analysis.

In Chapter 7, the same characterization process is reproduced for the automotive application. The overall refrigeration capacity attainable on the engine intake has been computed with the engine operating under different engine speeds and loads. The boundary conditions coming from the engine have been modeled employing experimental measurements coming from a test bench.

The dynamic analysis starts in Chapter 8 and is focused exclusively on the solar

refrigeration application. Chapter 8 determines the benefits of using a variable geometry jet-ejector over traditional fixed-geometry architectures under realistic climatic conditions. The intention is to discern if the flexibility and enhanced capabilities of the variable-geometry jet-ejector permit a quantitative performance leap. In a complementary way, in Chapter 9 the influence of the thermal backup system capacity and consumption strategy is analyzed in detail to maximize the system performance and reduce undesired periods of inactivity. The dynamic effects are accounted for in the performance of the machines by using transient nodal models.

The analysis is concluded in Chapter 10, where the yearly operating expenditures (OPEX) and the capital expenditures (CAPEX) are determined for the system as well as the amortization period and its financial viability when compared to the consolidated existing solutions (vapor-compression refrigeration systems). The comparison is complemented with estimations of the expected saving assuming a planning horizon of decades and a reasonable evolution of the electricity cost.

Finally, in Chapter 11 the main findings of the research work are summarized and future lines of action are proposed.

Table 1.1 condenses the information of all the tasks carried out.

Modeling approach	Field of application	Objective	Working fluids	Thermal power supplier	Studies
Steady-state analysis	Solar thermal	To produce air-conditioning	R1234yf, R600a and R1234ze	Parabolic trough collector, compound parabolic concentrator and evacuated tube collector	Design and characterization of fixed-geometry jet-ejectors and determination of their impact over the overall cycle
					Design and characterization of adjustable jet-ejectors
					Influence assessment of new generation working fluids
	Automotive	To refrigerate the intake line of an internal combustion engine	R1234yf	Internal combustion engine exhaust line	Design and characterization of fixed-geometry jet-ejectors and determine their impact over the overall cycle
Transient analysis	Solar thermal	To produce air-conditioning	R1234yf	Parabolic trough collector	Influence of variable-geometry jet-ejectors and fixed-geometry jet-ejectors over efficiency indicators
					Influence of thermal storage system sizing
					Thermoeconomic evaluation

Table 1.1: *Summary of the method employed*

Chapter 2

Literature Review

2.1 Available thermomechanical technologies to produce refrigeration by harvesting low-grade thermal energy

Several refrigeration technologies have been postulated in recent decades as promising greener alternatives to consolidated vapor-compression systems. Among them, those that use the residual thermal energy coming from different sources to generate a refrigeration capacity offer great potential because their field of application is vast. There are several well-known options but the technology readiness level and the market penetration of each solution are very heterogeneous. Some of them have reached commercial implantation while others are not developed beyond pilot plants or experimental facilities dedicated to research activities. A critical issue that share all these machines is the relatively poor efficiency transformation from the hot source thermal energy to the refrigeration capacity at the refrigeration medium. Most of the current research around these systems pursue an efficiency improvement to facilitate competitiveness against the traditional refrigeration solutions.

2.1.1 Jet-ejector refrigeration systems

In the jet-ejector refrigeration systems the refrigerant is divided into two loops (see Figure 2.1): In the so-called *power loop*, a pump rises the refrigerant pressure in a liquid state, and then it is evaporated with the thermal energy transferred by the hot stream flowing in the other side of the heat exchanger (generator). The pressure and temperature of the heat exchange process are limited by the thermal level of the incoming hot source. After leaving the generator, the superheated or vapor-saturated refrigerant penetrates in the jet-ejector and expands as it passes through a converging or a converging-diverging nozzle, selected depending on the application. The primary flow expansion permits the entrainment and mixing of the secondary flow, which travels in the so-called *refrigeration loop*. After the mixing process inside the jet-ejector occurs, the mixed stream is compressed in the diffuser section leaving the jet-ejector at an

intermediate pressure. Downstream, the mixed flow condenses rejecting heat to a medium with an intermediate temperature level. The condensing pressure depends on the temperature of the heat dissipation medium.

Downstream, the refrigerant leaves the condenser in a liquid state; one part is recirculated towards the pump while the remaining part is expanded in the expansion valve to the evaporating pressure. The refrigerant at low temperature evaporates in the evaporator absorbing heat from the medium to be refrigerated. The evaporating pressure depends on the refrigeration needs of the medium.
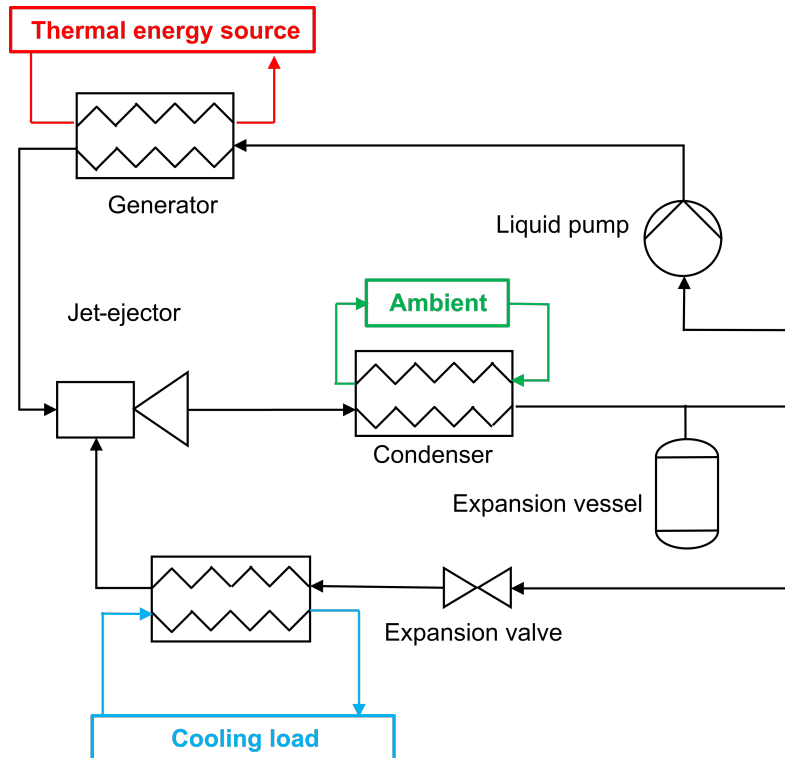
Figure 2.1: *Schematic illustration of a baseline jet-ejector refrigeration system.*

The application scope of jet-ejector refrigeration systems is broad. The use of waste-heat driven jet-ejector refrigeration systems have been proposed, among others, in automotive applications to cool down the passenger cabin or to cool down the engine intake line [2, 12], as an auxiliary mechanism in a gas turbine for performance enhancement [13] or as a solar activated air-conditioning system [14, 15]. The implementation of jet-ejector refrigeration systems is also very attractive in the food processing industry [16].

There also exists a multitude of examples of hybridizations [17, 18] and advanced configurations [19, 20]. These combinations are intended to address the two main weak points of the baseline configuration of the jet-ejector refrigeration systems: their relatively low efficiency transformation from thermal energy to refrigeration capacity and the difficulties of the baseline configuration to maintain a robust performance when the operating conditions differ from the design conditions. Despite its relatively low operational flexibility this technology shows potential strengths like low cost, low

mechanical complexity, reduced maintenance needs, and reliability.

2.1.2 Rankine-based and Stirling-based thermomechanical refrigeration systems

In some thermomechanical systems, the heat energy coming from the heat source is converted into mechanical work to assist a vapor-compression refrigeration system or another heat driven refrigeration machine with secondary mechanical power needs (jet-ejector refrigerator, sorption refrigerator...) [21]. The heat engine converting heat power to mechanical power can be, for example, a Rankine cycle [22, 23].

In Figure 2.2 a conventional vapor-compression refrigeration system powered by a Rankine cycle is depicted. The thermal energy in the heat engine is transformed to mechanical work rejecting heat to the environment. In the vapor-compression refrigeration system, heat is removed from the refrigeration load dissipating heat to a medium at an intermediate temperature. These cycles are attractive for investigation because they allow for electricity production when there are no refrigeration needs [24]. This permits maintaining high performance at off-design conditions and adequate exploitation in a wide range of temperatures in the hot source. They are also flexible in design since the utilization of diverse refrigerants including those with low environmental impact and those which are suitable to produce refrigeration below $0°C$ [24] is admissible. The main drawback of these systems is their relatively low efficiency; they require higher temperatures in the generator to improve the energy efficiency conversion from thermal energy to mechanical energy. Their field of application is diverse and extends from solar-powered refrigeration systems [22, 23], refrigeration systems activated by geothermal energy [25, 26] and implementations in the food processing industry [27], where both refrigeration needs and waste heat sources are usually present.

Using Stirling cycles to produce refrigeration is another alternative that has attracted research efforts [28]. Although they can work at high temperatures that are unreachable for Rankine-based systems and their design is relatively simple, increasing its capacity implies decreasing its surface-to-volume ratio, which negatively affects its efficiency.

2.1.3 Sorption refrigeration

In sorption machines the refrigeration effect is produced thanks to the physical or chemical attraction between two substances forming the working pair, the sorbent and the sorbate (refrigerant). Figure 2.3 depicts a schematic illustration of a closed absorption system.

The sorption process occurs in the absorber, where the sorbent absorbs the refrigerant in the gas phase coming from the evaporator and rejects heat to the environment. Then, the mixture is pumped to the generator to rise its pressure with an intermediate stage that is frequently implemented to absorb heat from the rich sorbent mixture coming from the generator back to the absorber. When the mixture arrives at the generator it is evaporated at high pressure. The heat power required to regenerate the
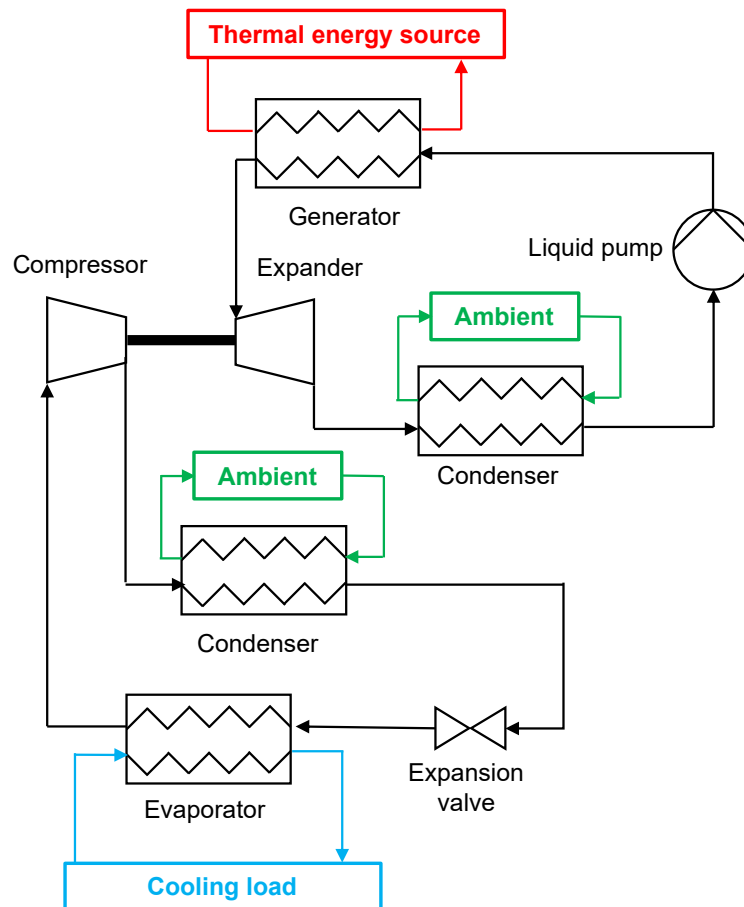
Figure 2.2: *Schematic depiction of a Rankine-based thermomechanical refrigeration system. Layout with separated power and refrigeration cycles in which the refrigerator corresponds with a vapor-compression refrigeration system.*
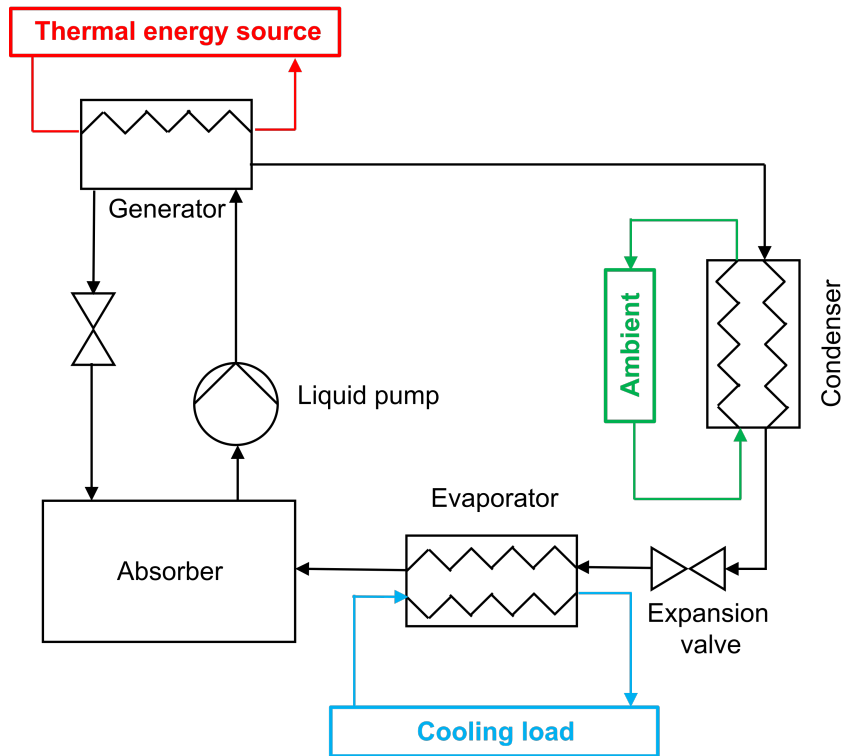
Figure 2.3: *Schematic illustration of a baseline absorption refrigeration system*

sorbent and separating the refrigerant comes from the external thermal energy source. It is frequent in real equipment to include gas-fired backup systems to guarantee a correct operation with an energy deficit in the driving source [29]. The refrigerant evaporates first and leaves the generator in gas state. In practice, absorption machines are equipped with one or more rectification stages downstream of the generator to purify the refrigerant mixture. The refrigerant at high pressure and temperature is then condensed at the condenser dissipating heat to the environment (medium at an intermediate temperature). The resulting condensed flow expands in an expansion valve and produces the desired refrigeration effect as it absorbs heat in the evaporator from the hotter incoming stream (refrigeration medium). The cycle is closed when the refrigerant in gas state enters again into the absorber.

Absorption systems traditionally have concentrated most part of the research efforts in the field of thermomechanical systems due to their higher efficiencies when compared to other thermomechanical refrigeration techniques, that is, they consume less thermal power from the hot source for a given refrigeration capacity and refrigeration temperature. Besides, they show increasing reliability [30, 31], durability [32], and flexibility in terms of applications. Indeed, they can operate efficiently with low-grade heat sources of different thermal levels, so the technical solution is compatible with a multitude of applications. There are abundant examples in the literature of solar-assisted absorption machines dedicated to solar air-conditioning [33, 34, 35], or installations devoted to harvesting low-grade energy coming from the exhaust line of automotive engines [36, 37] and marine engines [38].

Despite their relatively high efficiency within the thermomechanical systems, they require high investment cost, extensive maintenance and present specific technical hurdles like [39]: (i) mechanical complexity, (ii) difficulties on heat rejection at elevated ambient temperatures, (iii) crystallization problems in LiBr/Water systems, (iv) needs of external water supply and bacteria treatment in evaporative cooling towers, (v) excessive volume of the heat exchangers resulting in packaging problems in buildings, or (vi) high specific cost in the small-scale market because of scalability problems in the state-of-the-art heat exchangers. Yet, the technological readiness level of absorption machines is more advanced than the other thermomechanical alternatives; there are firms specialized in the construction and distribution of functional equipment.

Adsorption machines work with a similar operating principle: the vapor-compression refrigeration system is replaced by the so-called thermal compressor and an adsorbent. The liquid substance (refrigerant or adsorbate) is caught on the surface of the solid porous substance (adsorbent) by means of physical or chemical mechanisms. When heat is applied, the process can be reversed and the refrigerant is separated from the solid substance in a process called desorption or regeneration [40, 21]. Most of the research efforts are focused on physical adsorption because the chemical process is not completely reversible and produces a chemical alteration in the composition of the adsorbate and the adsorbent.

Multiple adsorbent beds are required to maintain a continuous operation after the adsorbent saturation and this is a remarkable technical barrier. The adsorption machines have comparable efficiency to absorption ones but are heavier and bulkier, and they require large heat transfer surfaces [16]. Also, high-efficiency systems require regeneration processes to partly recover the supplied thermal power to regenerate the adsorbent. This causes complex heat transfer loops and control difficulties [16]. These issues are currently detrimental to achieve a widespread use. However, these solutions might be competitive in large-scale applications; in this sector, their low refrigeration power densities are not so decisive and the tight price margins of the small-scale market are not present.

The field of application of adsorption machines is also vast and it is not hard to find pilot systems in solar refrigeration applications [41, 42], exploitation of low-grade heat in the exhaust line of internal combustion engines [43] or food preservation [44].

2.2 Fundamentals of jet-ejector refrigeration systems

2.2.1 Overall system operating principle

As anticipated before, the overall jet-ejector refrigeration system performance strongly depends on the conditions at which the heat exchange processes occur, namely the conditions in the generator (hot driving flow), evaporator (medium with refrigeration needs), and condenser (reference medium to dissipate heat).

The heat exchange process occurring in the generator depends primarily on the ther-

mal level of the hot source. In case there is sufficient thermal level to drive the system, the designer has some flexibility to decide the most convenient operating pressure/temperature in the generator depending upon the cycle characteristics. Depending on the thermodynamic properties of the refrigerant, the heat exchange process might occur in subcritical or supercritical conditions, as can be observed in the T-s diagrams of Figures 2.4 and 2.5.

As shown in Figures 2.4 and 2.5 the conditions in the condenser are regulated by the temperature of the heat dissipation medium. Higher ambient temperatures force higher condensing temperatures or, analogously, higher condensing pressures. The expansion vessel situated downstream of the condenser would be used in a real experimental facility to control the condensing pressure. Similarly, the targeted evaporating temperature determines the minimum temperature achievable in the refrigerated medium. Lower evaporating temperatures imply lower operating pressures in the evaporator.

As can be deduced from the description of the heat exchange processes in the generator, condenser, and evaporator, the jet-ejector operation is determined by its surrounding elements. It acts as a passive compressor that uses the energy of the primary flow to induce a pressure rise in the flow coming from the evaporator. The pressure rise induced in the jet-ejector and its entrainment capacity are two competing operational parameters and a trade-off exists [45]. Ideally, one would desire to maximize both parameters simultaneously, however, in practice, enhancing one of them through a thorough geometrical design of the jet-ejector is detrimental to the other one.

2.2.2 Jet-ejector operating principle

The jet-ejector is a passive device with no moving parts whose mission is to compress the low-pressure flow coming from the evaporator (low pressure secondary flow) to the mid-pressure conditions required for the refrigerant condensation. The high-pressure stream coming from the generator (primary flow) transfers energy and momentum to the secondary flow to achieve an effective mixing. Figure 2.6 depicts the main sections of a typical jet-ejector and shows qualitatively the evolution of the velocity and pressure profiles along the jet-ejector axis.
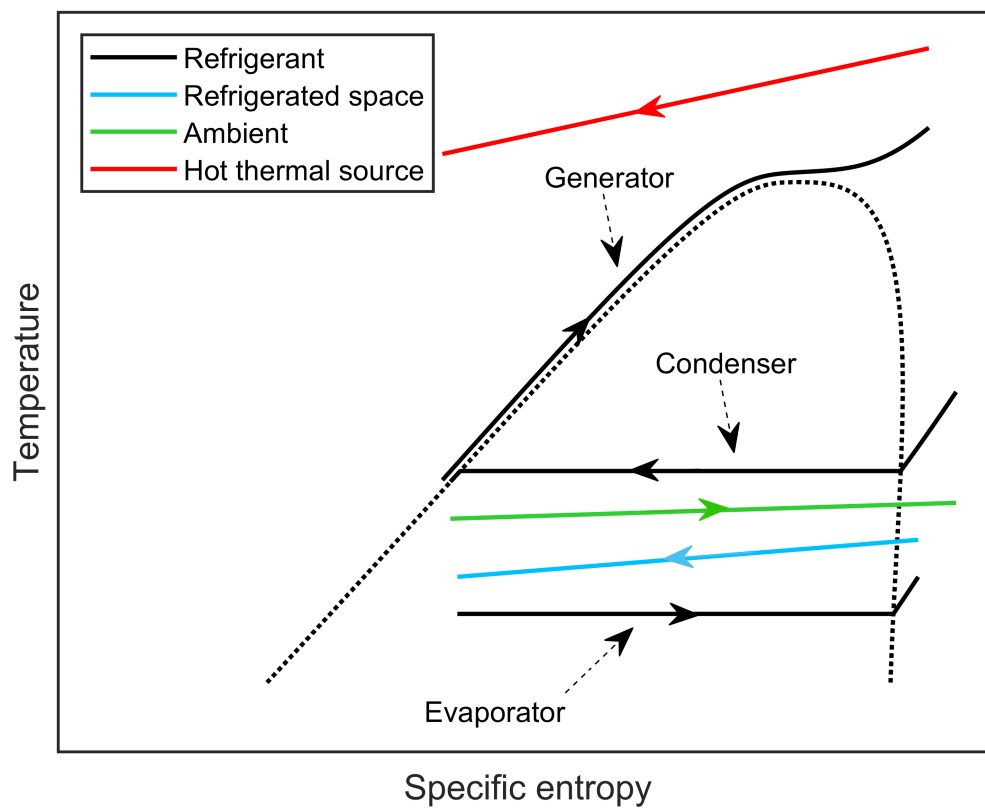
Figure 2.4: *Schematic view of the heat exchange processes occurring in the heat exchangers assuming that the refrigerant leaves the generator at supercritical conditions*
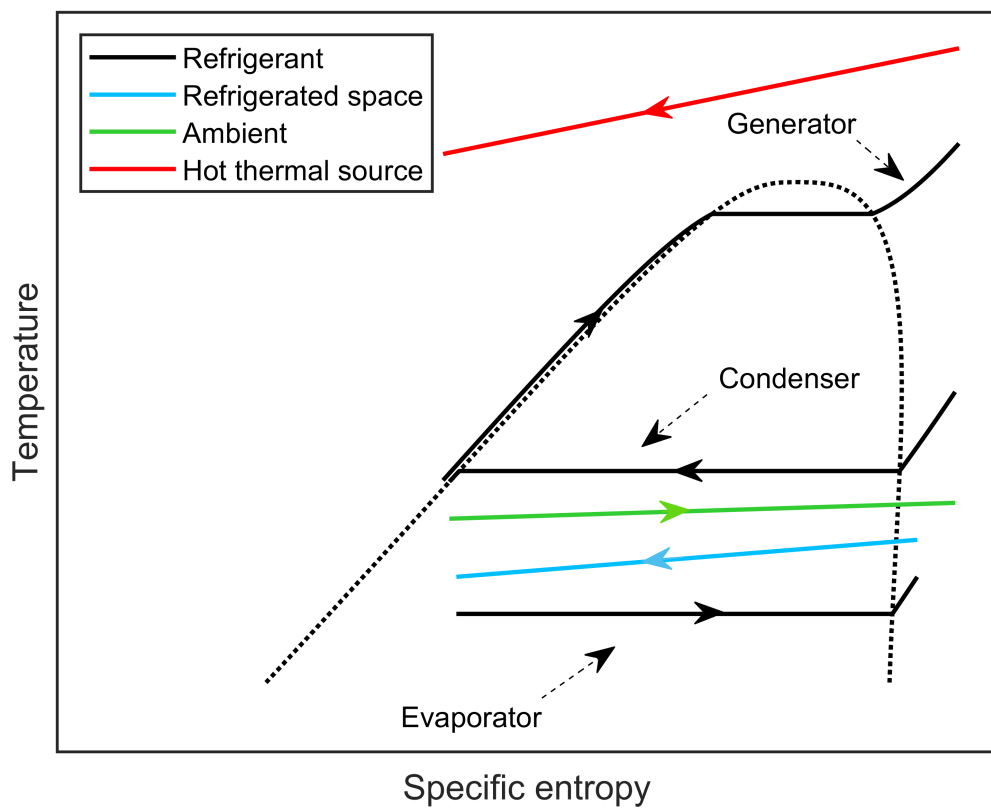
Figure 2.5: *Schematic view of the heat exchange processes occurring in the heat exchangers assuming that the refrigerant leaves the generator at subcritical conditions*
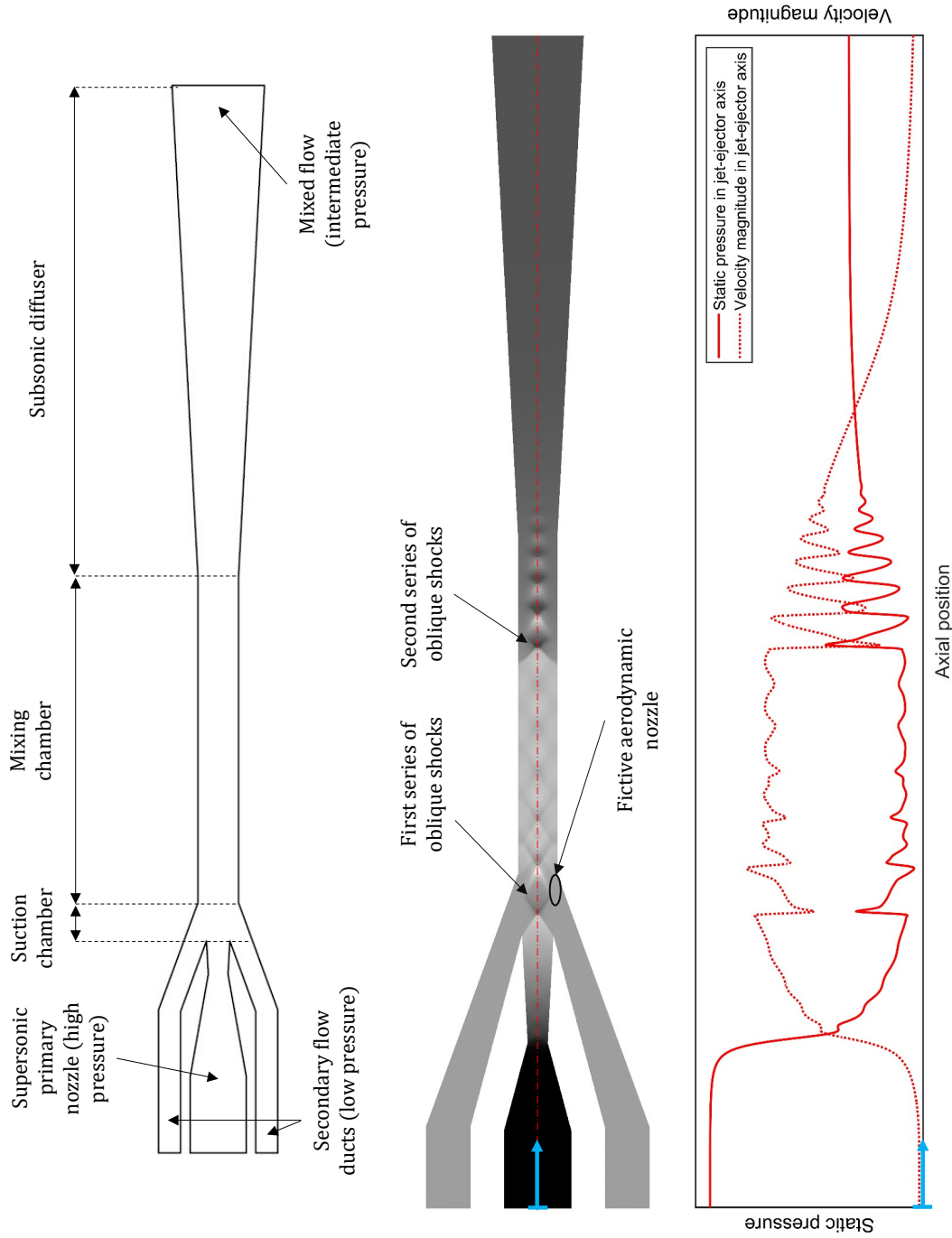
Figure 2.6: *Schematic illustration of the jet-ejector constructive parts*

Inside the jet-ejector, the primary flow expands in the converging or converging-diverging nozzle converting its internal energy into kinetic energy. The converging-diverging profile is very common in jet-ejectors designed for refrigeration applications because the jet-ejector operates under a relatively high pressure difference.

The primary flow passing through the converging-diverging nozzle converges down to the throat and is further expanded in supersonic conditions in the diverging section. If the nozzle is operating at the choking condition the mass flow rate would be maximum. As the flow expands, its pressure is reduced and it is accelerated. If the nozzle is well-designed for the jet-ejector operating conditions, at the nozzle outlet surroundings the primary flow would be at sufficiently low pressure to promote the secondary flow suction.

The shockwave pattern and the flow adaptation generated downstream the primary nozzle would depend on the primary flow inlet pressure, the nozzle area ratio, and also on the pressure at the primary nozzle discharge zone. If the expansion throughout the nozzle leads to a nozzle exit pressure lower than the surroundings, the nozzle would be operating in the overexpanded regime. In this case, the primary flow would be adapted to the surrounding area by a series of oblique shocks that compress the flow. Oppositely, in the under-expanded flow regime, the primary nozzle exit flow is adapted to the surroundings abruptly by expansion waves. The expansion waves cause that the flow reaches a higher supersonic level [46]. The latter case occurs when the primary nozzle expands the flow to a pressure level higher than those reigning at the suction chamber. The flow pattern generated immediately downstream of the primary nozzle has been termed by some authors as the first series of oblique shocks [46] (see Figure 2.6).

The primary nozzle outlet flow pattern interacts with the incoming secondary flow in the suction chamber. Throughout the entrainment process, the secondary flow expands as it is accelerated in an apparent or "fictive" aerodynamic nozzle [47] formed between the jet-ejector wall and primary flow jet core (see Figure 2.6). The apparent nozzle is located downstream the primary nozzle but its position depends on the operating conditions. The suction of the secondary flow is favored by the depression generated by the primary flow expansion. This mechanism partly explains the entrainment phenomena of the secondary flow, however, the momentum transfer of the primary flow through shear effect due to the high velocity difference plays a major role [48]. At the apparent nozzle, the secondary flow may reach sonic conditions, and downstream this point the greatest fraction of the secondary flow starts the mixing process. The flow conditions in the mixing chamber determine the secondary flow behavior and the associated jet-ejector operating modes. The flow phenomena and the physics occurring inside the jet-ejector are quite complex (shockwave propagation and reflection in the wall and the jet core, turbulent mixing, momentum transfer...) and deep comprehension of the underlying phenomena is still a challenge [49].

In the mixing chamber, the primary and secondary flows are mixed completely. Downstream, the recompression of the mixed flow through a series of strong shockwaves that return the flow to subsonic conditions occurs. These shocks are usually termed in

the literature as "second series of oblique shocks" [46] (see Figure 2.6). The position of this flow structure depends on the momentum of the mixed flow and the backpressure. The last part of the recompression takes place in the diverging section of the subsonic diffuser, facilitating the pressure rise until reaching the condensing pressure.

The listed below jet-ejector operating modes can be distinguished depending on the condensing and the evaporating pressure/temperature. The transition between operating modes can be easily identified if the entrainment ratio (ω), that is, the ratio between the secondary and primary flows, is represented against the evaporating pressure or temperature (P_{ev}, T_{ev}) and the condensing pressure or temperature (P_{co}, T_{co}), as depicted in Figure 2.7.
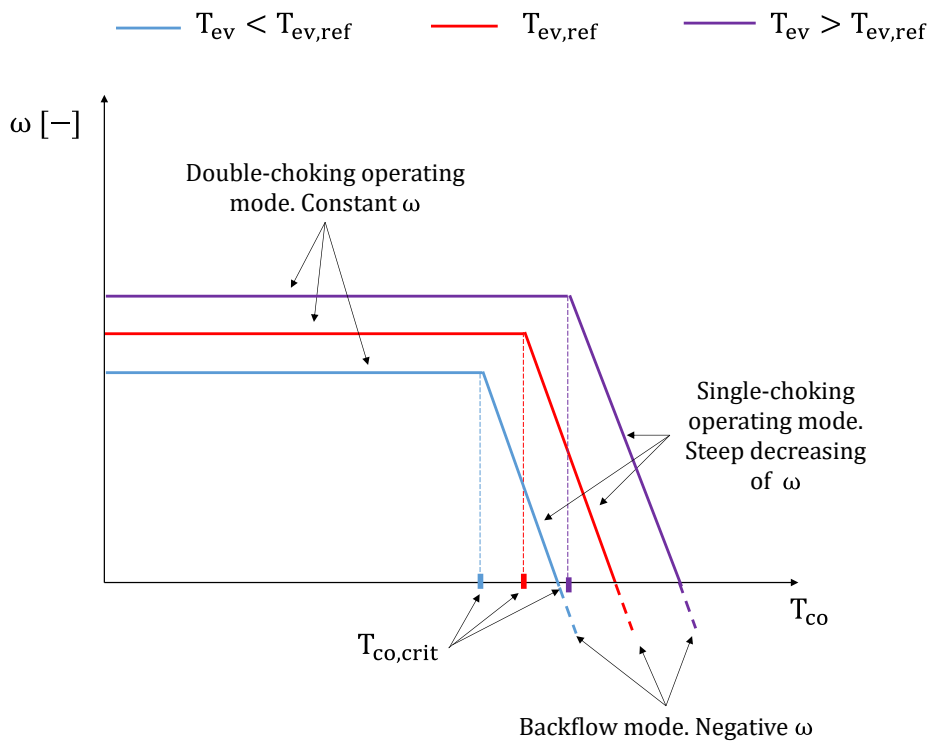
Figure 2.7: *Schematic illustration of the three jet-ejector operating modes*

- In the double-choking operating mode (design mode) both the secondary and the primary flows reach choking conditions and the secondary mass flow rate does not change with jet-ejector backpressure until a certain critical value called critical condensing temperature/pressure ($T_{co,crit}$). As the backpressure approximates to the critical point, the second series of oblique shocks move upstream without affecting the jet-ejector entrainment ratio.

  Increasing the evaporating temperature/pressure above the reference value ($T_{ev} > T_{ev,ref}$) increases the entrainment ratio and also permits extending the range of the double-choking operating mode thanks to the higher momentum induced to the mixed flow. A reduction in the evaporating temperature ($T_{ev} < T_{ev,ref}$) has the opposite effect.

- In the single-choking operating mode (off-design mode) only the primary flow is at the choked condition. The relatively high backpressure displaces the second series of oblique shocks upstream disturbing the entrainment of secondary flow and the secondary flow is no longer choked in the fictive nozzle. At this operating regime, the entrainment ratio is very sensitive to the backpressure and small pressure differences generate abrupt changes in the drawn mass flow rate.

- In the backflow mode (malfunctioning mode) the adverse pressure gradient avoids the secondary flow to penetrate inside the jet-ejector. The flow at the mixing chamber leaves the jet-ejector through the secondary duct so the component is not fulfilling its function at all.

The jet-ejector is the key element of the refrigeration system and its response determines the overall system efficiency. It requires a careful geometric design to the so-called reference or design operating conditions. These design conditions must be representative of the standard or most frequent operation to guarantee a stable performance. If the conditions are highly changeable the designer should consider advanced strategies like variable geometry jet-ejectors or multiejector racks.

With a movable spindle, the jet-ejector maps can be transformed as shown in Figure 2.8. In each spindle position, the jet-ejector behaves as a conventional jet-ejector and the double-choking and single-choking operating modes can be clearly identified. The entrainment ratio at the critical condition for different spindle positions defines the optimum operating envelope of the adjustable jet-ejector and the optimum spindle displacement law (marked in black in Figure 2.8).

The adjustable configuration permits substantial improvements in all the operating range when compared to a conventional jet-ejector: Beyond the critical condensing temperature the entrainment ratio gets worse than in the jet-ejector design conditions but it does not suffer a drastic performance drop as occurs with the fixed-geometry jet-ejector. Below the critical condensing temperature the entrainment ratio can be improved with an adequate spindle displacement.

The variation of the effective nozzle area as the spindle is displaced axially is qualitatively depicted in Figure 2.9. The spindle margin regulation is limited and the effective area can be varied between two extreme positions: null effective area and throat area defined by a jet-ejector without a spindle.

2.2.3   Definition of performance indicators

The following expressions define mathematically local and global performance indicators. These definitions are widely adopted in the literature and are constantly referenced in the present research.

The entrainment ratio (ω) is one of the most important performance indicators and is decisive to achieve an efficient refrigeration system (Equation 2.1). High entrainment ratio values imply that the stream that produces the refrigeration effect (secondary flow) is high per unit of motive stream mass flow rate (primary flow).
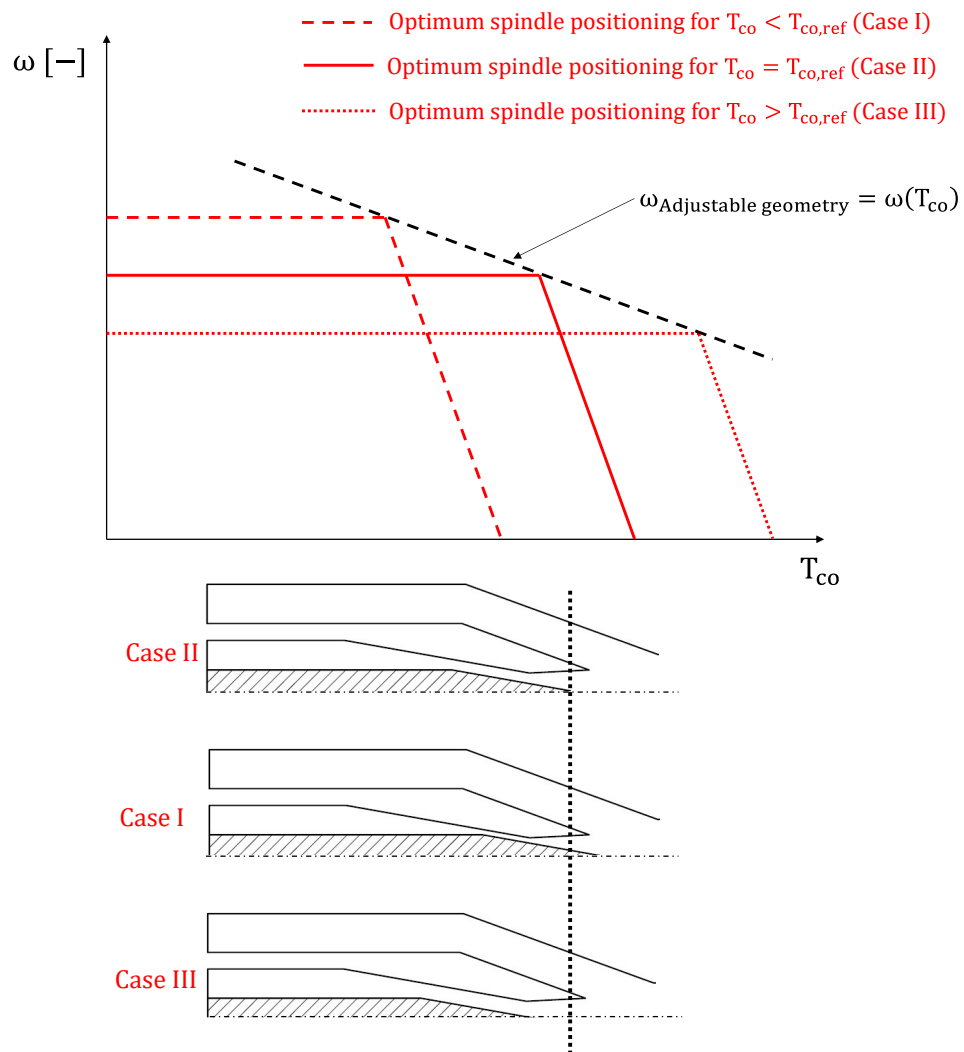
Figure 2.8: *Operating envelope of an adjustable jet-ejector*
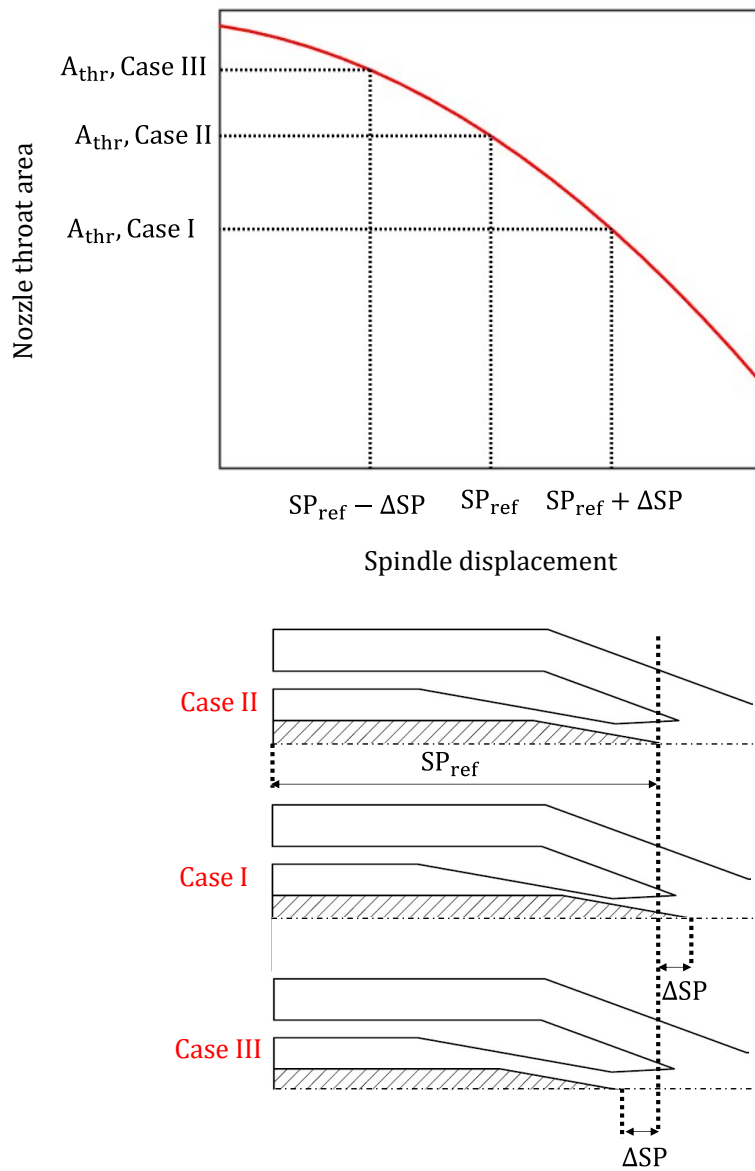
Figure 2.9: *Variation of the effective nozzle throat area with the spindle movement*

$$\omega = \frac{\dot{m}_{sf}}{\dot{m}_{pf}} \tag{2.1}$$

The jet-ejector compression ratio (π) is the ratio between the condensing pressure and evaporating pressure (Equation 2.2). High compression ratios are detrimental to obtain high entrainment ratios, however, allow the system to enlarge the temperature difference between the reference medium and the refrigerated medium.

$$\pi = \frac{P_{mf}}{P_{sf}} \tag{2.2}$$

The refrigeration capacity is defined as the thermal power extracted from the enclosed space with refrigeration needs $\left(\dot{Q}_{ev} \right)$ (Equation 2.3):

$$\dot{Q}_{ev} = \dot{m}_{sf} \cdot (h_{out,ev} - h_{in,ev}) \tag{2.3}$$

The thermal energy consumed in the generator is the thermal energy consumed by the driving flow to energize the secondary flow and produce the refrigeration effect $\left(\dot{Q}_{ge} \right)$ (Equation 2.4):

$$\dot{Q}_{ge} = \dot{m}_{pf} \cdot (h_{out,ge} - h_{in,ge}) \tag{2.4}$$

The thermal coefficient of performance (COP_{th}) (Equation 2.5) is an efficiency indicator that is nothing but the thermal power required in the driving hot source per unit of refrigeration capacity. To improve the energy efficiency of the refrigeration system and to reduce the operating costs the COP_{th} must be maximized.

$$COP_{th} = \eta_{th,ref} = \frac{\dot{Q}_{ev}}{\dot{Q}_{ge}} = \frac{\dot{m}_{sf} \cdot (h_{out,ev} - h_{in,ev})}{\dot{m}_{pf} \cdot (h_{out,ge} - h_{in,ge})} = \omega \cdot \left(\frac{h_{out,ev} - h_{in,ev}}{h_{out,ge} - h_{in,ge}} \right) \tag{2.5}$$

The hydraulic coefficient of performance (COP_{hyd}) corresponds with the traditional COP definition in vapor-compression refrigeration systems. This expression neglects the contribution of the thermal power delivered by the hot driving source and it is useful to compare with non-thermally assisted refrigeration systems. The pump power consumption represents the only external power supply, together with the power consumed by auxiliary equipment.

$$COP_{hyd} = \frac{\dot{Q}_{ev}}{\dot{W}_{pm} + \dot{W}_{aux}} \tag{2.6}$$

In the solar refrigeration context, the capacity to transform from solar irradiance to thermal energy is governed by the efficiency parameter $\eta_{sol,th}$ (Equation 2.7):

$$\eta_{sol,th} = \frac{\dot{Q}_{ge}}{A_{col} \cdot G} \qquad (2.7)$$

The overall efficiency of the conversion process (η_{ov}), which accounts for the efficiency transformation from solar power to thermal power and from thermal power to refrigeration capacity is shown in Equation 2.8.

$$\eta_{ov} = \eta_{sol,th} \cdot \eta_{th,ref} \qquad (2.8)$$

2.2.4 Review of the baseline configuration of jet-ejector refrigeration systems

The jet-ejector refrigeration systems are in the spotlight of the present research and have concentrated an extraordinary amount of research interest and efforts in the last years. A good example of this is the number of recent publications. According to Scopus, in the last ten years (the period between 2011 and 2021) 1103 documents have been published tagged with the keywords "ejector refrigeration" having a remarkable ascending trend since 2015. Even so, this technology has not convinced the designers of pilot refrigeration installations, who have given prominence to sorption systems. Jet-ejector refrigeration systems show relatively low efficiency, however, they present some compelling virtues like mechanical simplicity, reliability, simple construction, low cost of the refrigeration system equipment with an adequate economy of scale, and lower maintenance costs since they have few moving parts being the jet-ejector a passive device [8, 50, 51]. In comparison with other thermomechanical technologies, jet-ejector refrigeration systems excel in some of these respects and gain attractiveness when multiple criteria are on the table rather than an exclusively-based efficiency judgment [52]. They also stand out for their flexibility; the field of applicability is vast and a multitude of configurations, hybridizations, and integration possibilities exist [53].

Some of the following research works are not centered in solar refrigeration or automotive applications but are conceived for generic applications in which these domains have a place. Hence, the conclusions would be applicable.

Research papers about the overall system operation with an experimental and/or numerical approach.

The thermodynamic properties of the refrigerants are a key factor at the time of designing and optimizing an efficient refrigeration machine. There are also other criteria intervening in the decision-making, like the environmental impact of the refrigerants, their flammability properties, toxicity, cost, usage limitations, availability in the market... The working fluid sensitivity studies have mainly a computational character because the complexity of testing different refrigerants in the same installation is out-of-reach of most research groups.

Chen et al. [54] surveyed the convenience of using different working fluids classified in wet fluids, dry fluids, and isentropic fluids using a simple numerical model. The pro-

cesses occurring inside the jet-ejector and the whole refrigeration system were described on the basis of energy, momentum, and mass conservation principles. The comparison shed light on the refrigerants that maximized the COP_{th}. The R600 was selected as the best candidate due to its higher COP_{th} and its reduced ecological impact. The influence of the minimum superheating degree of the flow leaving the generator to avoid the appearance of droplets as the flow expands inside the jet-ejector was evaluated for each refrigerant.

Smierciew et al. [55] presented a numerical study of a jet-ejector refrigeration system intended to operate with low-grade energy sources and different refrigerants (isobutane, R1234ze(E), R1234ze(Z), R1234yf, R123, and R134a). They found that the refrigerant R1234ze might be an alternative for isobutane for safety reasons. The processes occurring in the refrigeration system were modeled with simple mathematical expressions (conservation principles).

Kasperski and Gil [56] used a theoretical model developed by Huang et al. [57] to assess the performance of nine hydrocarbons in a jet-ejector refrigeration system. They assumed an evaporating temperature of $10°C$ and a condensing temperature of 40 $°C$ for all the calculations. Isobutane (R600a) offered the peak overall system efficiency ($COP_{th} = 0.32$, $\omega = 0.45$) but they found that none of the refrigerants behave robustly away from its optimum generator temperature. They also highlighted that heptane and octane were not favorable when it comes to efficiency.

Gil and Kasperski [58] also used the theoretical model of Huang et al. [57] to evaluate the suitability of common solvents and synthetic refrigerants as working fluids for jet-ejector refrigeration systems powered by high-temperature energy sources. Also in this work, they assumed an evaporating temperature of $10°C$ and a condensing temperature of 40 $°C$ for all the calculations. R236fa was the working fluid that maximized the COP_{th} (0.23) and entrainment ratio among the non-flammable synthetic refrigerants. The solvents were indicated for high temperature applications and the peak COP_{th} values were found for cyclopentane (>0.35).

As can be deduced from the cited scientific researches, the selection of adequate refrigerants has awakened the interest of the scientific community studying jet-ejector refrigeration systems. These studies serve, at the same time, to characterize the system behavior in steady-state conditions.

Another point of interest is the system response under dynamic conditions. The transient response of the system has special relevance, for example, in solar air-conditioning applications due to the unstable and random nature of solar irradiance. Also, the evolution of the ambient temperature, which strongly affects the refrigeration system response, may fluctuate significantly along a single day.

Allouche et al. [59] presented a numerical model to predict the transient behavior of a jet-ejector air-conditioning system in Tunis. The simulation was performed in TRNSYS software integrating a phase change material as a storage medium. The refrigeration system was sized for providing refrigeration in an indoor space of $140m^3$. They found that the storage system was essential to maintain comfort demands in the

refrigerated space and a 1000 l storage volume maximized the COP_{th} guaranteeing adequate refrigeration needs 95% of the time. Larger volumes increased the thermal inertia with no benefit over performance.

Tashtoush et al. [60] simulated using TRNSYS the dynamic response of a solar jet-ejector refrigeration system operating with R134a as the working fluid. The refrigeration system was rated for a refrigeration capacity of 7 kW. The sensitivity of different solar collector typologies, collector tilting, receiver areas, and the size of the thermal storage system was subject to analysis and optimization. They pointed out that the rated refrigeration capacity was met using a surface of 60-70 m^2 of evacuated tube collectors and they also highlighted the importance of integrating a storage tank of 2 m^3 for thermal stability. They found that the overall system efficiency, which accounts for the solar collector efficiency and the refrigeration system efficiency, ranged between 0.32 and 0.47.

Pollerberg et al. [15] tested a pilot solar-powered installation of a jet-ejector refrigeration system fitted with parabolic trough collectors. One of the main novelties of their investigation was the fact that water acted as working fluid. They also performed quasi-dynamic simulations to quantify the expected annual mean efficiency of the solar collector, the annual COP_{th}, and the refrigeration system efficiency. A specific price of 0.62 €/kWh and 0.15 €/kWh for refrigeration capacity production was obtained for a German and Egyptian location, respectively.

Research works dealing with the jet-ejector itself

Again, there are studies from a numerical perspective or installations dedicated to performing empirical characterizations of this single element.

Numerical works based on simplified jet-ejector models (set of algebraic equations) have attracted research efforts. Generally, these models are based on a 0D model description of the phenomena occurring inside the jet-ejector and have the aim of predicting the jet-ejector response under different operating conditions with low computational cost; such approaches have several advantages like the reduced calculation time but they do not consider some of the key jet-ejector internal dimensions that critically affect its operation.

Huang et al. [57] developed a 0D model to predict the jet-ejector behavior in the double-choking operating mode. Their model adopted the constant-pressure mixing hypothesis and used expressions of compressible isentropic flow assuming ideal gas. Their analytical results were verified and fed with experimental data of jet-ejector prototypes using R141b as a working fluid. Their research work has been a valuable reference for most of the research works dealing with jet-ejector models published later.

Chen et al. [61] proposed an enhanced approach that used simplified 0D models to predict the jet-ejector response in both double-choking and single-choking operating modes. Their model was also founded on isentropic compressible flow equations. Also, in this case, the constant-pressure mixing hypothesis was adopted. Their comparison with experimental results demonstrated that their model accurately predicts the

jet-ejector performance over all ranges of operation for R141b, air, and propane. Maximum errors of 20 % in entrainment ratio were found when estimating the jet-ejector performance in the single-choking operating mode while the double-choking operating mode showed maximum discrepancies of 18% for the jet-ejector operating with air.

García del Valle et al. [62] proposed a more complex 1D modelization technique that includes real gas effects and consisted of linearization of axisymmetric supersonic flow. The model was developed in three different zones of the jet-ejector (primary nozzle region, secondary flow region and mixing region) and it was devoted to predicting the jet-ejector entrainment ratio in the double-choking operating mode. The model response was evaluated against experimental data and the discrepancies were in the order of 7%. They found that for the refrigerants and geometries modeled, the ideal gas assumption was also adequate and the precision of the results was not negatively affected.

In the numerical field, there are a lot of research works dealing with Computational Fluid Dynamics (CFD) simulations. These models allow for a more realistic prediction of internal flow phenomena that cannot be captured with experimental techniques or simplified models.

Ruangtrakoon et al. [46] carried out a CFD sensitivity analysis to investigate the effect of different primary nozzle geometries on a jet-ejector prototype that used water as refrigerant. They assessed the effect of the condensing pressure, the primary flow pressure, the effect of the nozzle throat diameter with fixed critical mass flow rate, fixed upstream conditions, and the primary nozzle expansion level. Special attention was paid to the visualization of internal flow and the mixing process occurring inside as the operating conditions change. All of these design parameters affected decisively the jet-ejector performance and explained the flow structures generated inside.

Zhu and Jiang [63] compared the flow pattern observed with a schlieren technique in a transparent jet-ejector with the predictions made by a CFD code with a 3D geometry. The flow visualization was focused on the mixing chamber area. They were able to identify different flow patterns in the double-choking and single-choking operating modes. They also reported that the shockwaves with shorter lengths facilitated the mixing of primary and secondary flows and improved the jet-ejector efficiency. In the CFD analysis, the effect of four turbulence models was surveyed. The RNG k-ϵ was the most accurate to predict mass flow rates and the shockwave structure.

There are a lot of examples in the literature of testing facilities dedicated to characterizing jet-ejectors in different operating conditions.

Yan et al. [64] tested experimentally a jet-ejector operating with R134a under different primary flow and outlet flow conditions. They outlined the importance of the jet-ejector backpressure on its operation demonstrating empirically the inflection point over the entrainment ratio when caused when the critical backpressure is exceeded. They also found that an increase in the primary flow pressure leads to an increase in the critical backpressure and a decrease in entrainment ratio for a fixed secondary flow pressure. The existence of an optimum primary flow pressure that maximizes the

entrainment ratio was also pointed out.

García del Valle et al. [65] tested experimentally several jet-ejector prototypes operating with R134a as working fluid. Among all the prototypes analyzed were different suction chamber designs, mixing chamber arrangements, and diffuser profiles. Their influence over the critical conditions was determined and some of the proposed designs appeared to be more effective to achieve higher critical conditions.

Scott et al. [66] presented an experimental characterization of a jet-ejector operating with R245fa. The purpose of their study was to have a reliable reference for validating computational models. The critical condensing temperature was obtained for different conditions in the evaporator and the generator. The jet-ejector performance curve was completely determined for a variable condensing temperature, a temperature in the generator of $90°C$, and an evaporating temperature of $5°C$. They found that the CFD model overpredicts the critical condensing temperature with a 16%.

2.2.5 Review of advanced strategies to enhance the performance of the baseline configuration

The limited market penetration of jet-ejector refrigeration technologies is partly due to the inability of a particular jet-ejector design to show a robust performance when either the design refrigeration load, the outdoor conditions, or the heat source thermal level are altered [67]. The reference operating conditions for which the jet-ejector is designed exercise a decisive influence on its performance and a jet-ejector with a fixed geometry suffers a severe performance degradation away from its design region. To compensate for the drastic efficiency deterioration away from design conditions, several technical solutions have been proposed.

Use of variable-geometry jet-ejectors.

The rationale of using variable geometry jet-ejectors is to tune one or more jet-ejector internal dimensions to compensate the negative effect over efficiency caused by a change in the operating conditions (generator pressure/temperature, condensing pressure/temperature, or evaporating pressure/temperature). This concept would allow the system to operate with a reasonable efficiency even if the operating conditions change. The main drawbacks are the mechanical complexity and the difficulties of creating robust control laws.

Owing to manufacturing limitations in real systems the vast majority of adjustable jet-ejector arrangements consist of a needle moving axially dedicated to opening or closing the jet-ejector primary nozzle throat. In this manner, the jet-ejector area ratio (AR), that is, the ratio between the mixing chamber area and the primary nozzle throat area), can be varied. Fundamentally, the needle or spindle movement is useful to compensate for variations in the ambient temperature and the thermal level of the hot driving energy source, which is a relevant aspect in multitude of applications. This mechanism has been used in both heat driven based refrigeration systems and compressor-based hybridizations. The following literature review is only centered on

heat driven based systems.

Chen et al. [68] created a two-dimensional theoretical model based on the method of characteristics to describe the evolution of the primary flow in the mixing section and the velocity profile of the secondary flow in the effective or fictive nozzle. They found that the model provided accurate results for multiple nozzle configurations and flow regimes. In another research work, Chen et al. [69] tested experimentally variable geometry supersonic and subsonic jet-ejectors intended for solar refrigeration applications in multiple operating conditions. Their experimental results were complemented with computational simulations. The research work revealed that the variable geometry design was an effective way for extending the capacity regulation of the refrigeration system since the variable geometry allowed for an ideally expanded flow in diverse operating conditions.

Ma et al. [70] studied experimentally a novel variable geometry steam jet-ejector suitable for solar refrigeration. The primary flow passing through the nozzle was tuned using a movable spindle. They found that the spindle movement affects the jet-ejector critical backpressure and for given operating conditions the optimum COP_{th} and entrainment ratio are closely linked to the optimum jet-ejector area ratio.

Pereira et al. [71] tested experimentally a variable geometry jet-ejector prototype rated for 1.6 kW of refrigeration capacity using the environmentally benign refrigerant R600a (isobutane). The prototype had the capacity to both alter the primary nozzle throat area as well as the nozzle exit position and was designed to operate under variable condensing temperatures. For a generating temperature of 83°C and an evaporating temperature of 9°C, the COP_{th} ranged between 0.45 and 0.88. The potential gain when compared to a traditional jet-ejector refrigeration system was also highlighted: the COP_{th} improvement was as high as 85%. The existence of an optimum area ratio was also demonstrated using experimental data.

Yen et al. [72] studied the response of a variable throat jet-ejector using computational techniques (CFD). They established curve-fitting relationships between the optimum spindle positioning and the operating temperatures, in particular, the generator, condenser, and evaporator operating temperatures. A simple and precise mathematical expression in the form $AR_{opt} = AR_{opt}(T_{ge}, T_{co}, T_{ev})$ was proposed to reflect the optimum jet-ejector area ratio or, equivalently, the optimal spindle positioning for a wide range of operating conditions. This permitted to achieve optimal performance with varying solar heat supply and full characterization of the jet-ejector.

Varga et al. [73] evaluated with CFD a variable geometry jet-ejector operating with two low-ecological impact refrigerants: R600a and R152a. According to the authors, the spindle positioning constituted a good technical solution to extend/improve the range of a jet-ejector with a fixed configuration. An adequate spindle movement resulted in remarkable performance enhancement with low condensing temperatures (increase up to 177% in entrainment ratio).

Varga et al. [74] tested experimentally the dynamic response of a small-scale jet-ejector refrigeration system intended for air-conditioning applications. The refrigera-

tion system was rated for a refrigeration capacity of 1.5 kW and was equipped with a variable-geometry jet-ejector operating with R600a. Furthermore, a small storage tank (50 l) was proposed to be a useful mechanism to extend the system utilization for about 20 min in absence of solar irradiance. They reported that the delivered refrigeration capacity ranged between 1 kW to 2 kW depending on the operating conditions. The thermal COP_{th} ranged between 0.15 and 0.4 and the average electrical COP corresponded to 4.3. The greater flexibility offered by the variable geometry jet-ejector was also highlighted.

Other philosophies consider different mechanical degrees of freedom to alter the jet-ejector internal geometry. Normally, these are more challenging due to the difficulties to perform adequate assembling and fine-tuning.

Use of thermal storage systems

The idea behind using thermal storage systems is to decouple the refrigeration system operation from the immediate availability of thermal power in the hot driving source. Hence, the rationale of using thermal storage systems is to prolong the delivery of refrigeration power with a lack or scarcity thermal energy. This is of special importance in solar refrigeration applications.

The most convenient thermal storage system design is strongly influenced by the application and the operational requirements, and is not a clear consensus in the literature about the most appropriate design strategies. For example, Sparber et al. [75] analyzed pilot solar cooling installations and pointed out the necessity of standardization rules in the storage system sizing. A high variability while selecting the most adequate storage system size in relation to the solar collector surface was observed. Some authors have preferred hot storage systems dedicated to feeding the generator while others have considered more attractive to integrate a thermal storage medium directly coupled to the evaporator. The latter concept is usually called cold thermal storage.

Dennis and Garzoli [76] examined theoretically a jet-ejector refrigeration system equipped with a cold storage tank and a variable geometry jet-ejector using the software TRNSYS. The solar fraction underwent an increase of 46%-50% if a 60 MJ cold storage is incorporated when compared with the baseline system with no storage medium. If the system is further enhanced including a variable geometry jet-ejector refrigeration system the solar fraction increases up to 63%. With such configuration, the system could operate with a solar collector area of only 12.8 m^2.

Diaconu et al [14] presented a numerical analysis of a jet-ejector refrigeration system powered by solar energy and equipped with a cold thermal storage tank. The simulation was fed with climatic data of a hot location (Bechar, Algeria). It was found that the cold storage system was advantageous to maintain comfort needs. An optimum cold storage medium mass was identified to minimize the periods in which the indoor space temperature exceeds the comfort temperature threshold.

Chen et al. [77] tested experimentally a jet-ejector refrigeration system with a

cylindrical cold thermal storage tank that used a phase-change material as a storage medium. The system was powered by a 120 $°C$ thermal source and it was designed to work with an evaporating temperature of 3 $°C$ -5 $°C$. The storage tank was connected to the evaporator of the refrigeration system. The cold storage system was demonstrated to be useful when the heat input was not enough.

Tashtoush et al. [7] found that a thermal storage tank of 2 m^3 facilitated thermal stability and steady operation considering an evacuated tube collector area of 60 m^2 and a targeted refrigeration capacity of 7 kW.

More recently, Van Nguyen et al. [78] studied the dynamic response of a variable-geometry solar-driven jet-ejector refrigeration system with a rated refrigeration capacity of 1.5 kW, a thermal storage tank of 50 l, and four evacuated tube collectors with a total absorber area of 13 m^2. Their research work revealed that the storage tank was an effective way to extend about 20 minutes the system operation with the absence or insufficient solar irradiance.

Use of hybridized configurations

There is a multitude of hybridizations postulated in the theoretical plane, however, few have been tested experimentally. Priority has been given in the present introduction to those that make a simplified integration to the well-established vapor-compression refrigeration technology. These are: (i) Compressor-boosted jet-ejector refrigeration systems in which a compressor is dedicated to increasing the secondary flow pressure (see Figure 2.10) and (ii) Vapor-compression refrigeration systems integrated into a cascade disposition with a jet-ejector refrigeration system.

The compressor-boosted system has the capability of improving the jet-ejector entrainment ratio and also increasing its critical condensing temperature. This solution is particularly interesting because it avoids duplicated elements if the traditional vapor-compression refrigeration is thought to act as a backup.

Cheng et al. [79] evaluated numerically the performance of several compressor-boosted jet-ejector refrigeration systems for solar refrigeration applications working with R1234ze(E). In their research work, the baseline configuration equipped with a booster was contrasted with several advanced architectures. Paying attention to their configuration labeled as BERC1, in which the booster is located between evaporator and jet-ejector, they found that with an outlet temperature in the generator of 90 $°C$ and an evaporating temperature of 5 $°C$, the entrainment decreases from 0.738 to 0.438 when the condensing temperature increases from 30 $°C$ to 40 $°C$.

Dorantes et al. [80] presented a mathematical simulation of the thermal behavior of a solar ejector-compression refrigeration system able to produce 100 kg of ice each day (2 kW of rated refrigeration capacity). The refrigeration system was designed to work with the R142b refrigerant, a generating temperature of 105 $°C$, a condenser temperature of 30 $°C$, and an evaporating temperature of $-10°C$. They obtained a $COP_{th} = 0.34$ in nominal conditions. The annual average COP was 0.21 and the overall system efficiency (combination of refrigeration system and solar collector) was 0.11.
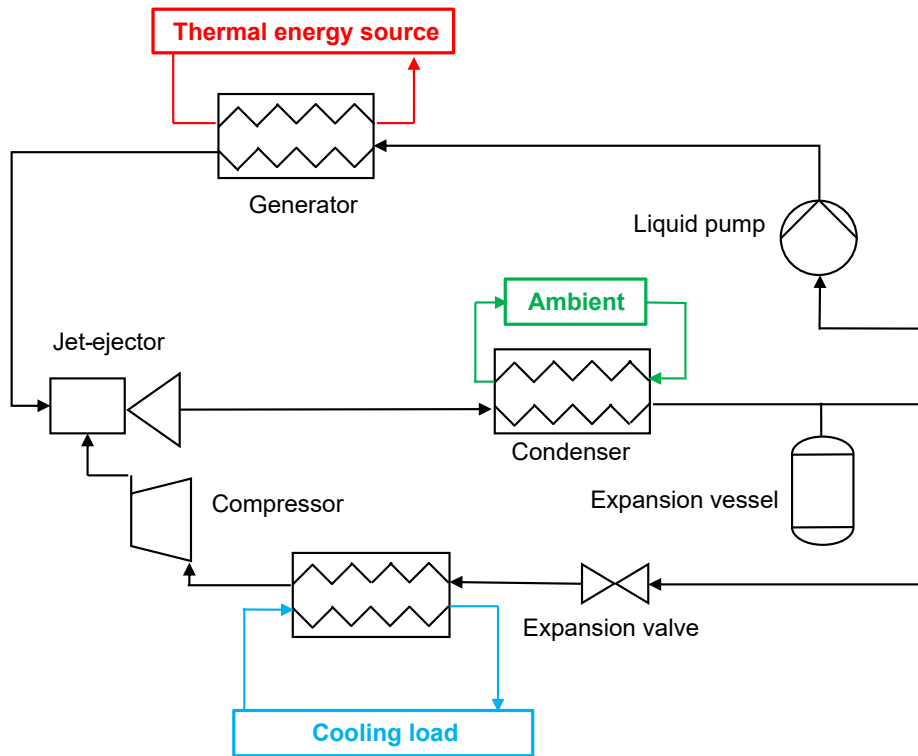
Figure 2.10: *Schematic representation of a compressor-boosted jet-ejector refrigeration system*

In the second assembling (ii) the jet-ejector is dedicated to producing a refrigeration capacity in an evaporative condenser (see Figure 2.11). The condensing pressure of the vapor-compression refrigeration system, which is in standard conditions determined by the ambient temperature is reduced thanks to the refrigeration effect, thus diminishing the compressor workload.

Hernández et al. [17] surveyed a hybrid compressor and ejector refrigeration system working with R142b and R134a for a solar refrigeration application. The concept was evaluated with a rated refrigeration capacity of 1 kW at -10 °C. The system reached a $COP_{th} = 0.48$ and worked under moderate temperatures at the generator (85 °C) and the condenser (30 °C). The importance of an adequate refrigerant selection was also highlighted.

Vidal and Colle [18] simulated using TRNSYS a combined ejector-vapor-compression cycle for solar refrigeration applications using realistic climatic data. The compression machine worked with R134a as working fluid whilst the jet-ejector refrigeration system worked with R141b. A flat plate collector and an auxiliary burner (natural gas-fired) acted as thermal energy suppliers. Their study aimed to perform a thermoeconomical optimization varying what they call the intercooler temperature and the solar collector area. The intercooler corresponds with an evaporative condenser shared between both cycles. On the jet-ejector refrigeration side, it acts as the evaporator while it operates as a condenser in the vapor-compression refrigeration system. The conditions under which the system would be competitive compared to a conventional refrigeration
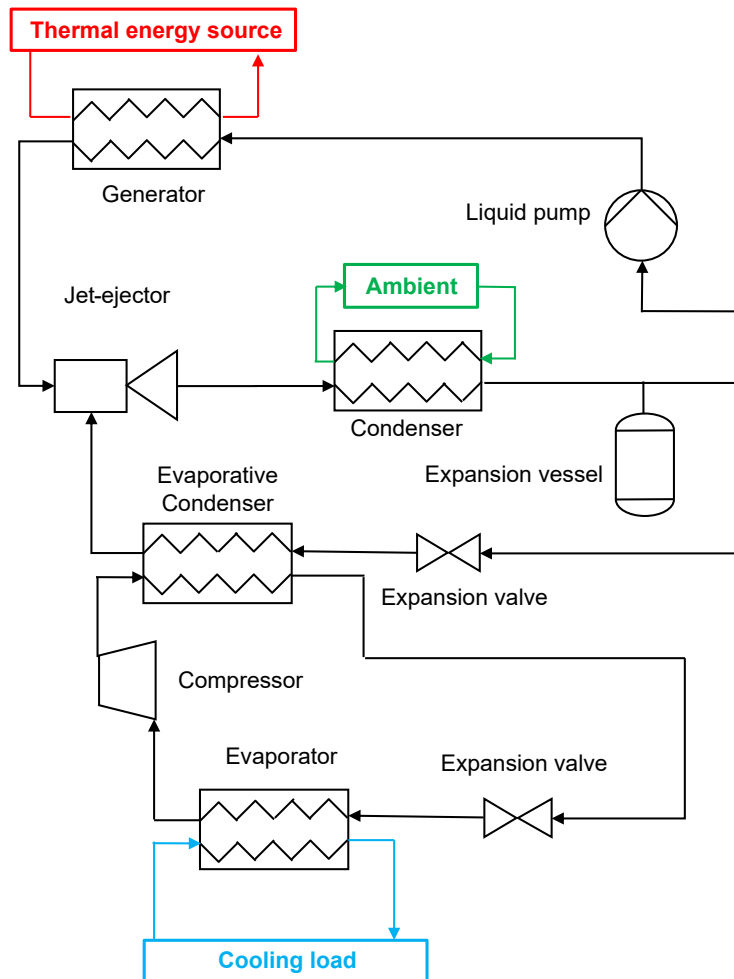
Figure 2.11: *Schematic representation of a jet-ejector refrigeration system and a conventional vapor-compression refrigeration system in a cascade disposition*

system were specified and the COP_{th} of the combined system reached 0.89.

Utilization of multiejector racks

The implementation of a jet-ejector rack has the prospective of improving the off-design performance in terms of both scalability and capacity to withstand off-design ambient and/or thermal source temperatures. One or more jet-ejectors with different internal designs and/or sizes could be switched depending on the heat power available in the hot source or the refrigeration power demands. In a fixed-geometry jet-ejector, the mass flow rate passing through it is not a degree of freedom as the primary nozzle is normally at the choked regime, so the thermal level of the hot source dictates the generator operating pressure. In the same manner, the secondary mass flow rate is given by the boundary conditions and the geometric dimensions.

The use of multiejector racks has been adopted commercially in the CO_2 refrigeration industry as a pressure recovery mechanism [81, 82]. Each jet-ejector is rated for a different capacity so the controller varies how many and which jet-ejectors are being utilized to provide the optimal performance. In the thermomechanical refrigeration field, multiejector systems also have a great potential but its application is far less explored [83].

Aligolzadeh and Hakkaki-Fard [84] proposed a jet-ejector refrigeration system fitted with an array of parallel jet-ejectors to operate near its maximum efficiency. Each jet-ejector was dedicated to operating in a range of condensing temperatures and was geometrically optimized according to this range. The maximum expected refrigeration capacity was 2 kW and the maximum ambient temperature was 40 °C. They reported that this enhanced configuration improved the seasonal COP_{th} up to 85% when compared with the baseline layout with a single jet-ejector. Also, they highlighted that the COP_{th} could be enhanced up to 47.2 % in comparison with the baseline configuration merely considering two jet-ejectors.

Sokolov and Hershgal [85] proposed a parallel array of jet-ejectors to expand the operating range of the refrigeration machine. For their approach, the jet-ejectors were activated according to the operating backpressure to avoid the sharp performance degradation occurring with a single fixed-geometry jet-ejector. This approach demonstrated to be an effective mechanism to enlarge the system operating capabilities.

2.3 Applicability of thermally activated refrigeration technologies to produce solar air-conditioning

2.3.1 Air-conditioning market and penetration of solar-driven refrigeration technologies

The International Energy Agency (IEA) estimates that the energy required for space cooling is going to grow three-fold over the next 30 years worldwide with the present regulations and projections [39]. The reason for this is mainly due to the population

growth in warm areas and the increasing living and comfort standards.

There is a clear consensus in the literature about the fact that the market of air conditioning systems has been growing intensely worldwide in the last few decades with special emphasis on refrigeration systems adapted to residential and commercial buildings. Balaras et al. [86] studied the particular case of European countries and found that in the period between 1987 and 2007 the number of refrigeration units with a refrigeration capacity of over 12 kW has increased by a factor of five [86]. Pezzutto et al. [11] surveyed the actual space refrigeration market in Europe for the residential and multiple other areas (education and health facilities, offices, hotels, and bars...). They also outlined the growth potential of the space cooling market, especially in households (small-scale refrigeration) due to the increasing comfort standards. One key point to understand the growth of refrigeration units in the domestic sector is that the whole refrigerated floor area (4%) lags behind the service sector (30%). Other factors explaining the potential growth are the slowly changing climate conditions (gradual increment of the annual average temperature) caused by global warming and the new architecture trends (larger glazing areas in buildings).

Contrasting the well-established market of the traditional vapor-compression refrigeration machines, the number of thermomechanical refrigeration units is still scarce and does not constitute a mature market. Up until now, thermomechanical systems have not been commercially settled in the area of solar refrigeration despite the maturity of some of these technologies. The absorption machines, which are deemed as the most promising refrigeration technology activated by a heat source, have been commercially available for years but are frequently sized for a rated refrigeration demands above 40 kW and the market for low refrigeration capacities is virtually non-existent.

The lack of practical experience among designers, architects, technicians, and builders makes the implantation of solar refrigeration systems less attractive than those solutions already consolidated [86]. However, in the last years, several initiatives with public funding have emerged to boost the development and implantation of solar-driven refrigeration technologies.

Above all, the main barrier is their high initial investment cost [21], generally attributed to the elevated cost of the solar collector. Most existing machines can be classified in prototypes for research purposes or pilot installations with no widespread use.

The below-listed factors are other issues that explain the low market penetration [39]. These can be considered as the "weak points" common to all solar-driven thermomechanical refrigeration systems.

- **Relatively low energy conversion efficiency**, that is, the solar energy is not converted efficiently in refrigeration energy. The poor efficiency is translated in an oversizing of the solar collector field to reach the targeted refrigeration capacity with the associated cost increase.

- **Operational limitations and control complexity**, such as the difficulties to operate satisfactorily in multiple situations (variable refrigeration needs, inter-

ruption of the solar irradiance supply, variable ambient temperature...). Indeed, solar refrigeration technologies are heavily dependent on climatic conditions.

- **Incapacity of the baseline configurations to behave robustly** in a wide range of scenarios making it necessary to implement advanced strategies to enhance performance. This increases significantly the cost, the control difficulties, and the mechanical complexity of the system. Frequently, these upgrades are not completely effective to provide a long-lasting thermal energy supply. This is the case of the thermal storage systems, for instance, which have a relatively short autonomy.

- **Necessity of coupling backup systems.** Frequently, traditional refrigeration systems or gas-fired boilers must act as a backup to guarantee a continuous operation. By themselves, these systems are not autonomous devices in all the operation scenarios. The backup systems tend to be inefficient and require elaborated control strategies, being necessary a dynamic response based on the climatic conditions and the short-term weather forecast. The hybridization of solar-driven and traditional technologies in which the solar loop is intended to assist or improve the efficiency of an already existing electricity-dependent machine represents a promising alternative.

- **Redundancy of equipment.** These technologies must coexist with conventional refrigeration machines to provide a continuous operation if there are neither backup systems nor hybridized architectures.

- **Parasitic energy consumption of the auxiliary systems**, as might be, fans, pumps for water recirculation systems, or electronics for control systems.

- **Not well-established distribution channels for not being a settled commercial product.**

- **Lack of publicity campaigns disseminating successful pilot projects.** Currently, these systems are not seen as trustworthy options among designers and customers due to the lack of references and signs of success. The diffusion of satisfactory results in pilot plants has been frequently limited to academia.

2.3.2 Initiatives to promote the use of solar refrigeration systems

The incipient market opportunities offered by these technologies have not gone unnoticed for public institutions and some initiatives have proliferated in Europe with public funding to promote and publicize solar-assisted refrigeration.

SACE (Solar Air Conditioning in Europe) 2002-2004

SACE was an initiative of the EU to promote the adoption of refrigeration technologies driven by solar thermal power. The project was aimed for assessing and gathering the state-of-the-art solar refrigeration technologies, future needs, weak points, lines of innovation or improvement and measures to promote an effective market penetration [86].

The researchers in charge surveyed 54 pilot solar refrigeration plants operating around different European locations. The standardized analysis was focused on points for improvement, economic analysis, potential economic and energy savings, and limitations when compared to traditional refrigeration systems. They found that the vast majority of the sample (80%) was composed of sorption refrigeration machines, which traditionally has been the preferred solution due to its superior efficiency. The operating cost of the plants was found to range between 1286 to 8420 €/kW (refrigeration production) excluding the cost associated with some auxiliary equipment. It was pointed out as the main conclusion that solar air-conditioning systems have great potential and could bring significant primary energy savings (in the range of 40%-50%) when compared to established technical solutions, however, more research efforts are still required to obtain cost-competitive units.

SOLAIR (SOLar AIR Conditioning in Europe) 2007-2009

The project involved 13 partners from different European research institutions and had the objective of promoting the market implementation of small and medium-sized (up to 105 kW capacity) thermally driven air conditioning systems [87]. It was focused on the residential and commercial sector paying special attention to the integration with existing solar heating systems. The main results of the study revealed some overriding points to focus future lines of action [87]:

- To reduce equipment costs.

- To improve the technical and financial support.

- To acquire practical experience and develop tailored training for all the actors involved (technicians, designers, builders, investors, companies...).

- To standardize and disseminate the information, recommendations, and guidelines derived from the research efforts and the practical experience.

- To publicize success cases and the strengths offered by these technologies.

2.3.3 Potential advantages of solar-driven refrigeration systems

The application of solar-assisted thermomechanical technologies has great potential in the current context. The effects of climate change urge the development of greener technologies with lower environmental impact. The air-conditioning and refrigeration units are responsible for a remarkable fraction of the energy budget worldwide.

The use of solar energy as an energy source has the potential to partially or completely alleviate the burden caused by traditional refrigeration systems by substituting the electricity grid power with solar thermal energy, which is a renewable, unlimited, and worldwide available energy source. The use of solar thermal energy is of special interest in the field of refrigeration and air conditioning due to some strategic issues [87, 39, 16, 88, 32]:

- Reduction of CO_2 emissions and primary energy consumption of the refrigeration units.

- Diminution of the public electricity grid load in terms of both peak consumption and standard energy consumption patterns.

- Integration capabilities, which allow for a versatile coupling with existing solar heating systems.

- Noise and vibration mitigation when compared with conventional systems.

- Capacity to provide the maximum refrigeration supply in time slots with the greatest needs thanks to an almost synchronization between the availability of solar irradiance and daily maximum temperatures.

- High durability as well as cheaper and simpler maintenance.

2.3.4 Solar collector available technologies

The solar collectors are heat exchangers that transform the radiation energy to the internal energy of the transport medium. In the field of solar thermal engineering four collector categories dominate the market.

- **Parabolic Trough Collectors (PTC):**

  In PTCs, the Sun beams are reflected in the mirror and are directed towards the focus of the parabola. As a result, the incident Sun rays are concentrated in the receiver, which is placed in the focal line. The receiver tube is formed by an absorber tube through which the thermal fluid circulates and it is encapsulated in a glass cover, which is intended to protect the absorber tube from oxidation and avoid thermal losses [89]. The cavity formed between the receiver tube and the absorber is vacuum-sealed also for that purpose. Figure 2.12 presents a schematic illustration of a PTC. The implementation of Sun-tracking systems is frequent to obtain high-performance collectors. Hence, the entire module can be adequately oriented.

  This kind of solar collector has been traditionally used in solar power plants for electricity generation or process heat applications since they can deliver a wide range of temperatures 50-400$°C$ [90], however, they have been also postulated for solar refrigeration applications [7].

  The selection of a PTC instead of the other available technologies is not frequent beyond industrial applications, nevertheless, it does not necessarily entail a higher economic cost [91, 7] and could be adequate for the residential sector.

- **Flat Plate Collectors (FPC):** In flat plate collectors the Sun beams pass through a transparent glazing and impinges in an absorber surface composed of a material with high absorptivity, retaining a portion of the energy. From this layer, the heat is transferred to the tubes through which the heat transfer fluid circulates. These types of collectors are popular for low and medium tempera-

ture applications, like domestic water heating or room heating [92]. The use of FPCs has been disregarded in the present investigation because their maximum achievable temperature is normally limited to around 80-90°C [93, 90]. As will be seen later, a low temperature/pressure in the generator may limit the jet-ejector refrigeration system performance.

A major requisite for this type of collector is to be cheap and durable.

- **Compound Parabolic Concentrator (CPC):** CPCs are highly efficient solar collector technologies and come from the development and optimization of cone concentrators intended to have elevated concentrating ratios [94].

  CPCs can reflect all the incident solar radiation to the absorber element but the incident radiation must be within a specific range of incidence angles [90]. To maximize the reception of solar radiation an adequate orientation and Sun-tracking systems are usually implemented. In this sense, two parabolic profiles are usually faced to mitigate the accommodation needs. To reduce costs, the parabola is usually truncated with little variation of the collector performance.

  According to the literature [90], the CPCs can deliver hot fluid in temperature ranges between 60 °C and 240 °C, and their field of application is vast. There are successful implementations of CPCs in solar water heating systems, solar refrigeration systems, space cooling and heating applications, solar desalination, or generation of industrial process heat.

- **Evacuated Tube Collector (ETC):** This non-concentrating collector typology is also indicated for the low/medium temperature range and is more versatile than the FPCs [95]. Indeed, they usually show the highest efficiency among the non-concentrating technologies [96].

  The ETC is formed by several evacuated tubes, which are cylindrical tubes containing a heat pipe inside. To enhance the heat transfer properties, ETCs use liquid-gas phase change materials. The Sun irradiance is captured by an absorbing selective coated surface with low emissivity placed inside the tube. The material with good absorbance properties is surrounded by a sealed vacuum layer to minimize conduction and convection losses. The heat accumulated by the selective coating material is transmitted to the fluid confined in the heat pipe facilitating its transition to the gas phase. The heat is then transferred to the working fluid circulating through the collector at the condenser heat pipe.

  There exist a high variability in design between commercial models but the ETCs can operate in the temperature range of 50 °C - 200 °C [90] with acceptable efficiency. Therefore, this typology is also popular for water heating and domestic applications.

2.3.5 Thermal storage system available technologies

Depending on the heat storage principle the thermal storage system can be classified as:
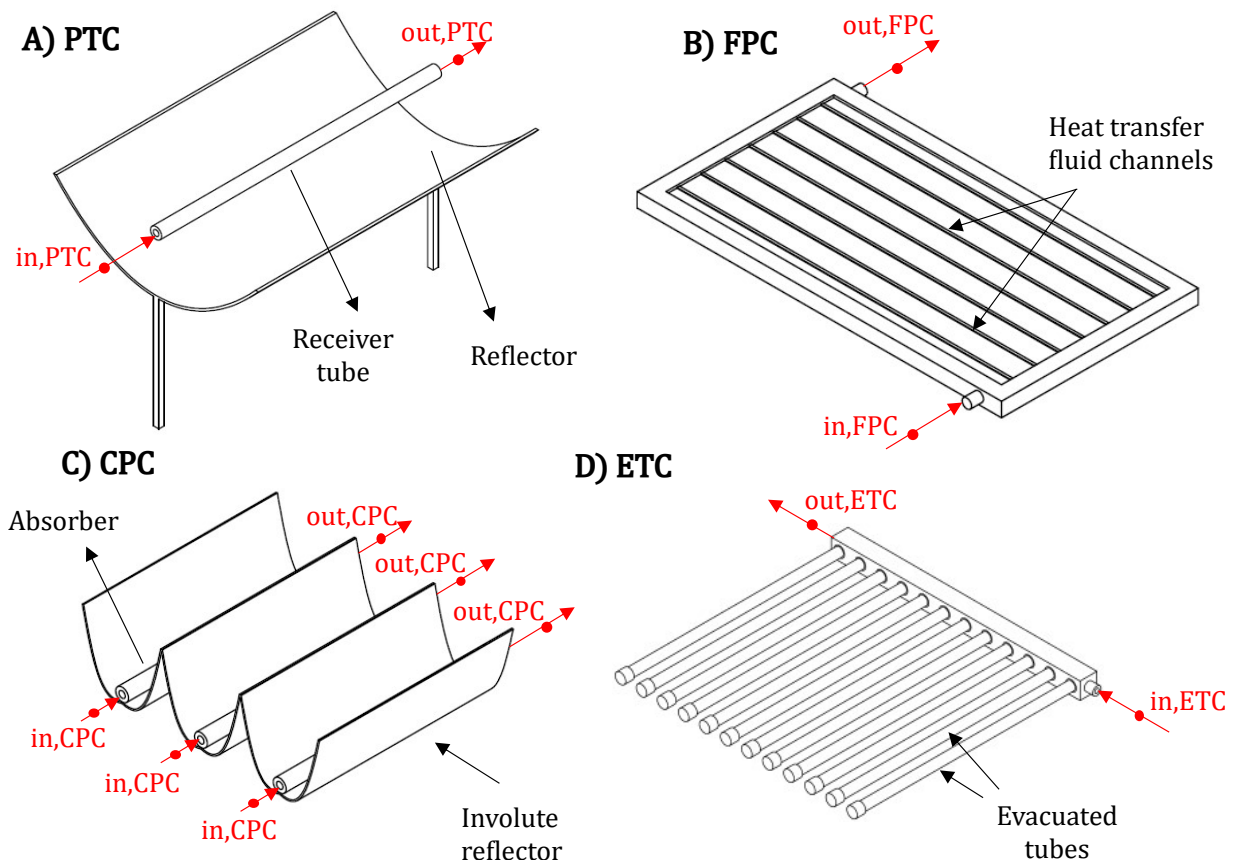
Figure 2.12: *Most commonly used solar collector typologies*

- **Sensible heat storage systems**, in which the thermal power coming from the collecting device is used to raise the temperature of a liquid or solid substance (water, thermal oil, molten salt, rock, sands...). This technology is frequently implemented due to its lower cost and the use of materials with low toxicity [97].

- **Latent heat storage systems**, in which phase transition in storage material occurs. The main advantage of using phase change materials is their high-energy storage density at a nearly constant temperature [98].

- **Thermochemical storage systems**, which are based on reversible exothermic/endothermic chemical reactions. Despite their higher complexity and cost, are characterized by their compactness, high storage density, low heat losses, and long availability [99].

Based on the temperature gradient in the storage medium, the thermal storage systems can be also divided into thermally stratified and thermally mixed. The stratification is usually preferred due to its positive effect on solar collector efficiency [99].

2.4 Applicability of thermally activated refrigeration technologies to produce refrigeration in ICEs

In an automotive internal combustion engine (ICE), the thermal power available even downstream of the aftertreatment system is abundant. Unlike other applications implementing thermally activated refrigeration systems, here, the efficiency transformation from thermal power to refrigeration capacity would not be a critical issue since the hot driving hot flow exists, has abundant thermal energy (it represents approximately one-third of the energy contained in the fuel) and is currently wasted. The concept of using the vehicle's exhaust waste heat to produce refrigeration has been postulated in the literature and most of the research works consider sorption machines. A widely extended concept in these research works is the production of air-conditioning inside the cabin.

Manzela et al. [100] tested experimentally an ammonia-water absorption refrigeration system driven by an ICE exhaust energy. The thermally powered unit was thought to be used for vehicle air-conditioning. They reported that temperatures ranging between 4 $°C$ and 13 $°C$ could be achieved in the refrigerator depending on the engine load and they highlighted that even better results could be attained with a dedicated machine. The feasibility of the refrigeration concept was confirmed without inducing severe pressure losses in the exhaust line.

Du et al. [101] characterized empirically a water-ammonia absorption refrigeration system powered by a Diesel engine exhaust line. The refrigeration unit was intended for freezing the cargo and reached a refrigeration capacity of 33.8 kW with a $COP_{th} = 0.53$ at an evaporating temperature ranging between -21.7 $°C$ and -15.5 $°C$. They demonstrated that the system is reliable even in different engine operating points, as well as compact and efficient.

2.4. APPLICABILITY OF THERMALLY ACTIVATED REFRIGERATION TECHNOLOGIES TO PRODUCE REFRIGERATION IN ICES

Koehler et al. [37] tested experimentally an absorption refrigeration system that recovered waste heat from a truck exhaust line and generated a refrigeration capacity to preserve the perishable goods. The refrigeration system was rated for a refrigeration capacity of 5 kW and showed a $COP_{th} = 0.27$, with some room for improvement with an optimized design. The concept feasibility was tested under different driving scenarios (mountain driving, plain road driving, and testing in urban areas with traffic). They found that a little fraction of the time the system is unable to operate due to scarcity of energy in the exhaust line (the need for a backup system is pointed out) while in other situations only a fraction of the total energy available is used.

In state-of-the-art ICEs, supercharging is an extended practice. It allows increasing the pressure of the air coming into the cylinder. This subsystem aims to increase the pressure in the intake manifold so that it is possible to burn more fuel or to burn the same fuel in better conditions. As a result, the engine power or its efficiency can be increased and the pollutant emissions can be reduced in Diesel engines. Since the compression process is not isothermal, the air temperature in the intake line increases after passing through the turbocharger compressor. To counteract this effect, it is frequent to add a heat exchanger downstream the compressor to reduce the air temperature and increase its density before entering into the engine. This cooling effect is beneficial to the engine and positively affects its performance, reducing peak temperatures during combustion. The temperature reduction achieved using this cooling mechanism is limited by the ambient temperature, the engine operating point, or the radiator position but it is possible to cool down the intake air to a temperature ranging between 40 °C and 70 °C [102].

A similar line of action would be to induce an extra temperature diminution downstream of the turbocharger compressor by using a refrigeration machine (artificial means). The refrigeration machine would have a remarkable engine power consumption if it would be mechanically coupled to the engine or it would be electrically driven using an alternator. Another promising implementation would be to produce the refrigeration effect using a thermally powered refrigeration machine. Thermomechanical refrigeration systems also present mechanical or electrical power consumption, in this case, associated with the pressure pump operation, but it is much lower than the compressor power consumption in a conventional vapor-compression refrigeration system.

To the author's knowledge, the benefits achieved with this implementation over the engine performance have only been corroborated in few research works, among which the investigation of Cipollone et al. [102] stands out due to its empirical nature. In their experimental setup, a vapor-compression refrigeration machine was simply inserted in a Diesel engine intake line downstream the compressor turbocharger without manipulating the default engine settings. As they mentioned, the vapor-compression refrigeration system could be the on-board air-conditioning system when it is not used to avoid additional onboard components. They reported that with an artificial reduction of the temperature ranging between 10.7 °C and 20 °C they achieved several benefits in a Diesel engine. That temperature reduction permitted an increase in mass flow rate in the cylinders of 5% at high load and high speed while for lower loads and speeds the increase is in the range of 2%-3.5%. They also found that the average re-

duction in fuel consumption corresponded to 2% reaching peak values of 6%. In terms of pollutant emissions the average reduction in CO_2, CO, NO_x and soot reached 5.8%, 8%, 14% and 9%, respectively. The NO_x reduction was associated with the reduction in the peak combustion temperature (the exhaust manifold temperature was reduced in the range of 15 °C - 40 °C). The HC emissions, notwithstanding, underwent an increase in the range of 2%-23%.

The potential benefits of this implementation could be split into direct and indirect. The former can be estimated with general engine performance indicators. The latter would be a result of the complex chemical and physical phenomena occurring during combustion. The real improvement potential of the indirect benefits is uncertain and would only be unveiled with a smart and ad-hoc tuning of the default engine settings as well as thorough experimental campaigns.

Direct benefits:

- Improvement of cylinder filling.

- Increase of the air and fuel mass flow rates maintaining the air-fuel ratio. According to Equation 2.9 the increase of the air density allows to improve the air mass flow rate ($\dot{m}_{air}$) for a given engine displacement (V_{engine}) and volumetric efficiency (η_{vol}) [103].

$$\dot{m}_{air} = \eta_{vol} \cdot V_{engine} \cdot \rho_{air} \cdot \frac{n}{2} \qquad (2.9)$$

Where n corresponds with the engine speed. If it is assumed that the ICE efficiency (η_{engine}) is not altered the ICE power would grow linearly with the air mass flow rate as expressed in Equation 2.10 [103].

$$\dot{W}_{engine} = LHV \cdot \eta_{engine} \cdot F \cdot \dot{m}_{air} \qquad (2.10)$$

Where LHV is the lower heating value of the fuel and F is the air-fuel ratio.

Indirect benefits:

- Reduction of pollutant emissions associated with the reduction in the peak combustion temperatures. The reduction might be especially promising for NO_x.

- Fuel consumption saving.

- Reduction of thermal loads.

The coupling of all the phenomena involved evidence the importance of a global pros and cons evaluation. For example, the lower combustion temperature would, at the same time, cause a reduction in the temperature of the exhaust line or generate some backpressure attributed to the refrigeration system heat exchangers. Unlike the air-conditioning thermomechanical concepts, here the thermal power availability is coupled with the refrigeration needs (the mass flow rate passing through the intake and exhaust

lines is almost the same). Hence, the driving behavior, that is, the engine operating point influences the thermal power availability and the refrigeration needs.

Besides, this technical solution would not be exempt from constructive penalties in the vehicle like the extra weight, the packaging problems, or safety issues due to refrigerant leakages. There would be also operational challenges like designing a robust control system over the entire driving cycle. The refrigeration needs demanded are expected to change notoriously and be unsteady in different engine operating points as the engine trapped mass flow rate does. The control system also should implement strategies to face the intermittent operation due to insufficient thermal level or thermal inertia effects, like heating-up periods, or response against sudden changes in the driving behavior.

As mentioned before, there are examples in the open literature of absorption refrigeration machines dedicated to recovering waste heat from the exhaust line and transform it to a refrigeration capacity dedicated to reducing the ICE intake air temperature. The implementation of jet-ejector refrigeration systems as a waste heat recovery mechanism for the same purpose is also promising because are simpler, more lightweight, and compact than sorption systems. Furthermore, their lower efficiency is not a critical aspect in this application since the obtention of the hot driving flow has no direct cost.

Novella et al. [36] studied numerically the impact of an absorption refrigeration system coupled to a 1.6 l Diesel engine. The aim was to produce a refrigeration capacity in the engine intake line by recovering waste heat from the exhaust line. They showed that a temperature around 5 $°C$ could be attainable and their theoretical analysis demonstrated that an enhancement of around 4% in the engine indicated efficiency could be expected, which is associated with a reduction in the heat rejection through the combustion chamber walls. Additionally, they appreciated an improvement in volumetric efficiency, a reduction in the peak pressure and temperature reached during the combustion process, as well as a reduction in the thermomechanical loads and NO_x emissions. On the contrary, the CO underwent an increase. They pointed out the interest of recalibrating the engine to maintain peak pressure while the intake temperature changes.

Zegenhagen and Ziegler studied theoretically the feasibility of using a jet-ejector refrigeration system in a gasoline engine for intake air refrigeration, however, their evaluation was based on data coming from an experimental campaign carried out to characterize the refrigeration system separately. In their analysis, they demonstrated that the energy available in the exhaust line is sufficient to produce a refrigeration effect ranging between 2.3 kW and 5.3 kW and reduce the intake line temperature ranging from -2.3 $°C$ to 11.6 $°C$. They also outlined that the penalty induced over the engine fuel consumption due to the weight of the system (around 40 kg) is low and the backpressure generated in the ICE could be mitigated with a smart integration of the elements.

2.5 Innovation of the present research

The present investigation deals with a detailed modelization and optimization of jet-ejector refrigeration systems for two different applications. One of the main novelties is that the jet-ejector, which is the core element of the refrigeration system is always modeled following a CFD-based design approach. This is an uncommon aspect in the available literature; it makes a more elaborated modelization of the flow phenomena occurring inside and captures better the influence of each geometric configuration than the simple mathematical models commonly used. The adoption of this approach presents some advantages but is frequently difficult due to the intensive requirements of computational resources.

The thorough design of the jet-ejector internal shape and an adequate working fluid selection is one of the key actions to get a cost-competitive system and impacts directly in another weak point of these systems: their relatively poor performance in comparison with absorption refrigeration. The possibility of studying the system's potential with a highly optimized jet-ejector for specific refrigerants is an extra original facet.

Taking the CFD-based jet-ejector design as the cornerstone, the refrigeration system has been evaluated in both steady-state and transient conditions. Special emphasis has been put on the performance decay caused by the off-design operation, which is one of the main vulnerabilities of jet-ejector refrigeration systems. This is another remarkable innovative aspect.

The transient evaluation includes an in-depth examination of two of the preferred advanced strategies to improve the jet-ejector off-design performance: the utilization of variable geometry jet-ejectors and the use of hot thermal storage systems. The potential gain offered by optimized and adjustable jet-ejector geometries in dynamic conditions when compared to a fixed jet-ejector configuration has been evaluated in depth and is practically unpublished until now.

The characterization of the system corresponds with a multifaceted analysis that includes detailed equipment sizing and monetary cost estimation. The overall cost has been split into variable costs (operating expenditures) and fixed costs (capital expenditures).

2.6 Summary

This chapter presents the foundations of thermomechanical refrigeration systems in general and jet-ejector refrigeration systems in particular, with special emphasis on the jet-ejector, which is the key element of the cycle. Firstly, these refrigeration concepts are described for generic applications and then are particularized for solar refrigeration utilization and waste heat recovery in internal combustion engines. The most promising attributes of this emerging technology are discussed and current existing barriers are identified.

Centered in the field of jet-ejector refrigeration systems, state-of-the-art devel-

opment in both experimental facilities and modeling techniques has been presented. The exploratory literature review has prioritized the current development of advanced strategies to face the well-known off-design performance degradation, like adjustable jet-ejectors, multiejector racks, hybridized configurations, or the implementation of thermal storage systems.

Finally, the main scientific contributions of the present research are highlighted.

Chapter 3

Description of the computational models

3.1 Introduction

This chapter is dedicated to presenting the models of each key element composing the jet-ejector refrigeration system. Such systems are depicted in the detailed system architectures of Figure 3.1 for the solar refrigeration application and in Figure 3.2 for an automotive application. As can be observed, both applications share most of the components. The elements pertain to the refrigeration system itself (generator, condenser, evaporator, jet-ejector, pressure pump, and expansion valve) or the thermal energy supply system in the solar application (solar collector and thermal storage system). Additionally, for all the models it is specified how the system elements interact with each other and with the surrounding environment. The T-s diagram of a jet-ejector refrigeration system for a generic application is depicted in Figure 3.3.

The modeling technique has been specified for each relevant element of the system to improve the clarity and readability. The nature of the model (transient or steady-state response), as well as the main governing equations or software setup have been detailed. Table 3.1 roughly summarizes the main features of each model. The Internal Combustion Engine (ICE) application is not accounted as a model since it is coupled to the refrigeration system exchanging information in the form of boundary conditions.

In the following, the Thermal Energy Collecting System (TECS) corresponds to a general term that encompasses the solar collector (CPC, ETC, or PTC) and the Thermal Storage System (TSS). The term JERS (Jet-Ejector Refrigeration System) designates the refrigeration system generically while the concepts FRS (Fixed-geometry Refrigeration System), and ARS (Adjustable Refrigeration System) are particularized depending on the jet-ejector architecture.
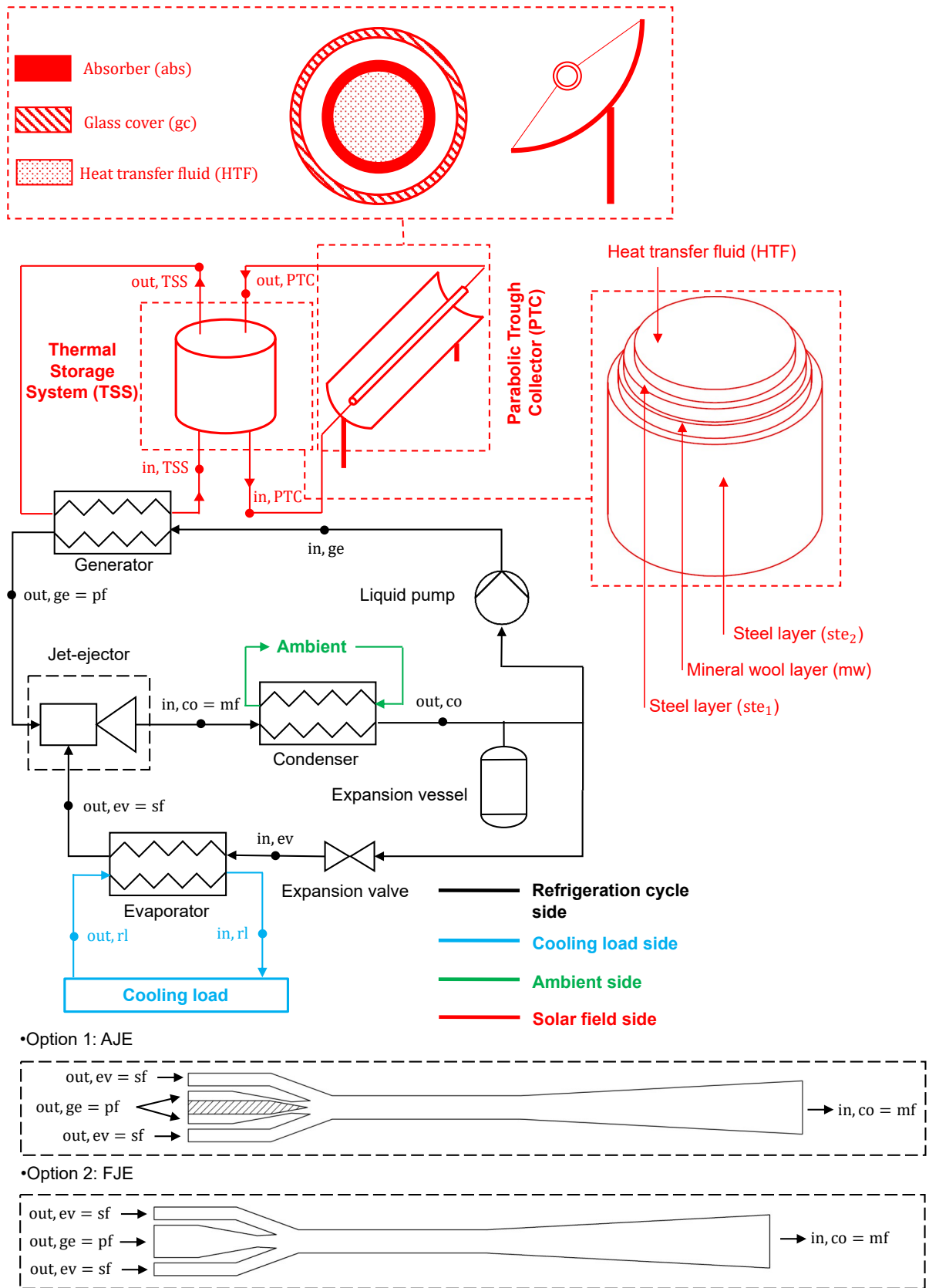
Figure 3.1: *General representation of the solar driven refrigeration system with all the subsystems attached*
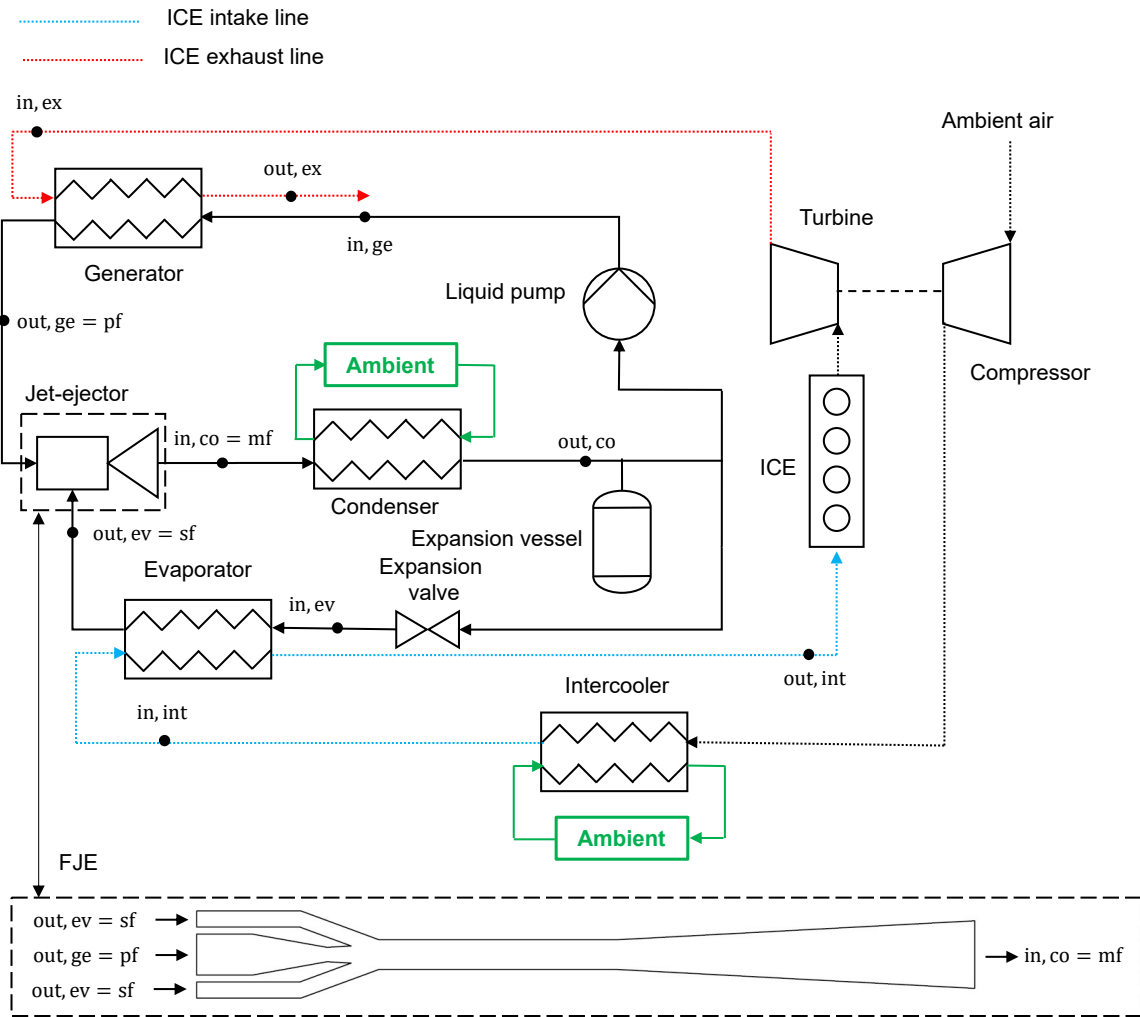
Figure 3.2: *Jet-ejector refrigeration system driven by the waste heat of an ICE exhaust line*
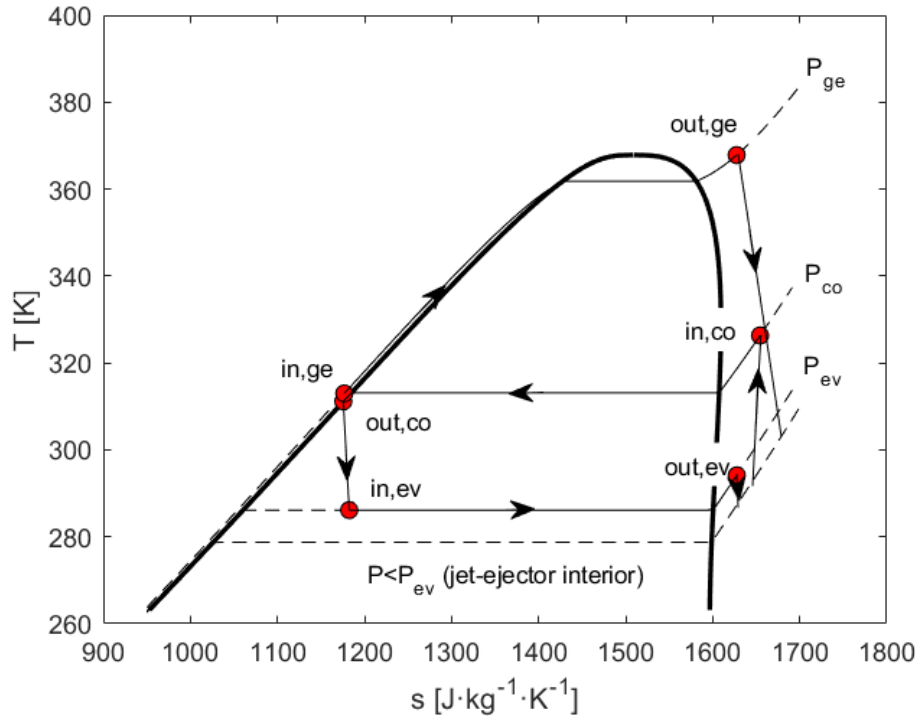
Figure 3.3: *T-s diagram of the jet-ejector refrigeration system*

Main system	Model	Nature of the model	Model characteristics
TECS	Solar collector	Transient/Steady	Nodal model/Efficiency curve
TECS	Thermal storage system	Transient	Nodal model
JERS	Generator	Steady	Model based on energy and mass conservation
JERS	Condenser	Steady	Model based on energy and mass conservation
JERS	Evaporator	Steady	Model based on energy and mass conservation
JERS	Jet-ejector	Steady	CFD
JERS	Pressure pump	Steady	Model based on energy and mass conservation
JERS	Expansion valve	Steady	Model based on energy and mass conservation

Table 3.1: *Summary of the computational models and the modeling technique*

3.2 Solar thermal collector

3.2.1 Description of the steady model

To determine the most versatile solar collector typology different architectures of thermal collectors have been evaluated under different solar irradiance scenarios. The efficiency in the solar collector field side, that is, the capability of the solar collector to transform solar irradiance into thermal power ($\eta_{sol,th}$), can be determined for different types of collecting devices by using the Hottel-Whillier-Bliss performance curves in a quadratic form (Equation 3.1) [7, 104, 88]:

$$\eta_{sol,th} = \eta_0 \cdot \left(K_{\theta b}\left(\theta\right) \cdot \frac{G_b}{G} + K_{\theta d} \cdot \frac{G_d}{G} \right) - a_1 \cdot \left(\frac{T_{avg,col} - T_{amb}}{G} \right) - a_2 \cdot G \cdot \left(\frac{T_{avg,col} - T_{amb}}{G} \right)^2 \tag{3.1}$$

Where the solar irradiance data coming from satellite observations are used to compute the ratio between direct and global solar irradiance (G_b/G) as well as the ratio between the diffuse and global solar irradiance (G_d/G). Additionally, η_0 is the zero-loss collector efficiency, a_1 is the heat loss coefficient, a_2 is the temperature dependence of the heat loss coefficient, $K_{\theta d}$ is the diffuse incidence angle modifier and $K_{\theta b}$ is the direct incidence angle modifier (null angle of incidence assumed $\theta = 0$). The aforementioned fitting coefficients must be adjusted for each particular collector technology and model. Figure 3.4 represents the dependence between the solar collector efficiency and the operating temperatures for each model presented in Table 3.2. As a general trend, the PTC models offer a more robust behavior and show less efficiency degradation when its operating temperature increases.

Collector model	$\eta_0[-]$	$a_1 \left[W/\left(m^2 \cdot K \right) \right]$	$a_1 \left[W/\left(m^2 \cdot K^2 \right) \right]$	$K_{\theta d}$
$ETC_{Model-1}$	0.745	2.007	0.005	0.85
$CPC_{Model-1}$	0.644	0.749	0.005	0.54
$PTC_{Model-1}$	0.693	0.476	0.003128	0.07
$PTC_{Model-2}$	0.59	0.932	0	0.048
$PTC_{Model-3}$	0.68	0.4	0.0015	0.073

Table 3.2: *Fitting coefficients of performance curves for different collector models. Source: [7]*

3.2.2 Description of the transient nodal model

The transient model is centered on the PTC architecture due to its high versatility and the possibility of designing a low-cost module. A thermal model has been created to predict the dynamic response of the PTC line receiver under variable ambient conditions.
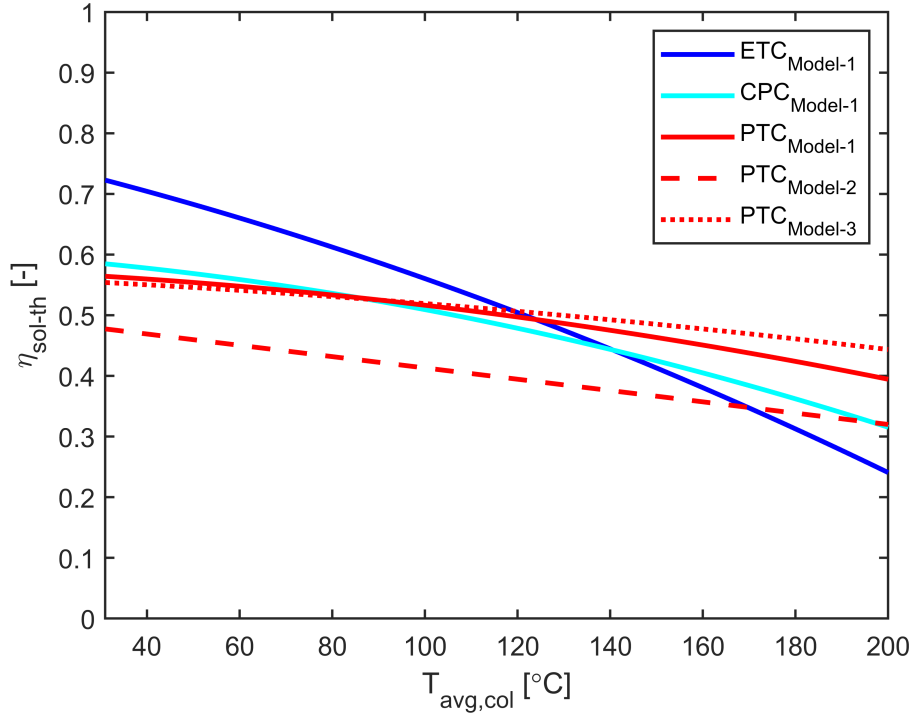
Figure 3.4: *Solar collector efficiency curves for $G = 1000\,W/m^2$ and $T_{amb} = 31°C$*

Description of PTC constructive characteristics

A PTC with a span of 7.08 m, an aperture area of 5.76 m, and a total collecting area of 40.78 m^2 has been chosen for the analysis. The collecting device is equipped with a tube receiver almost identical to a Schott PTR70 unit. It is composed of an external glass cover, a vacuum film and a metal layer (absorber) containing the heat transfer fluid. The Syltherm 800, a highly stable, long-lasting silicone polymer designed for high-temperature applications, has been considered as the heat transfer fluid.

The solar collector model considered in the present research work is identical to the model EuroTrough but has a lower span. This is a high-performance thermal collector that has been widely adopted in concentrated solar power applications. Furthermore, its capacity to provide the heat transfer fluid at temperatures above 150 °C makes it more beneficial to be coupled with a thermal storage tank.

The main technical features of the PTC line and the reflector are specified in Table 3.3. Figure 3.5 serves as a descriptive sketch of the PTC architecture and anticipates at a first glance the heat transfer phenomena involved.

Description of the nodal model

The nodal model described in the present investigation is based on the model developed by Fasquelle et al. [105]. The most relevant heat transfer phenomena occurring between the heat transfer fluid, the absorber, the glass cover, and the source term of the incident solar irradiance have been considered.

Parameter	Value	Units
L	7.08	m
PTC parabola aperture	5.76	m
A_{col}	40.78	m^2
$R_{abs,ext}$	0.035	m
$R_{abs,int}$	0.033	m
ρ_{abs}	8000	kg/m^3
k_{abs}	54	$W/(m \cdot K)$
$c_{p,abs}$	500	$J/(kg \cdot K)$
ϵ_{abs}	0.12	-
α_{abs}	0.7919	-
$R_{gc,ext}$	0.06	m
$R_{gc,int}$	0.0575	m
ρ_{gc}	2400	kg/m^3
k_{gc}	1.05	$W/(m \cdot K)$
$c_{p,gc}$	753	$J/(kg \cdot K)$
ϵ_{gc}	0.86	-
α_{gc}	0.02	-
τ_{gc}	0.92	-

Table 3.3: *Main constructive properties of the PTC layers*
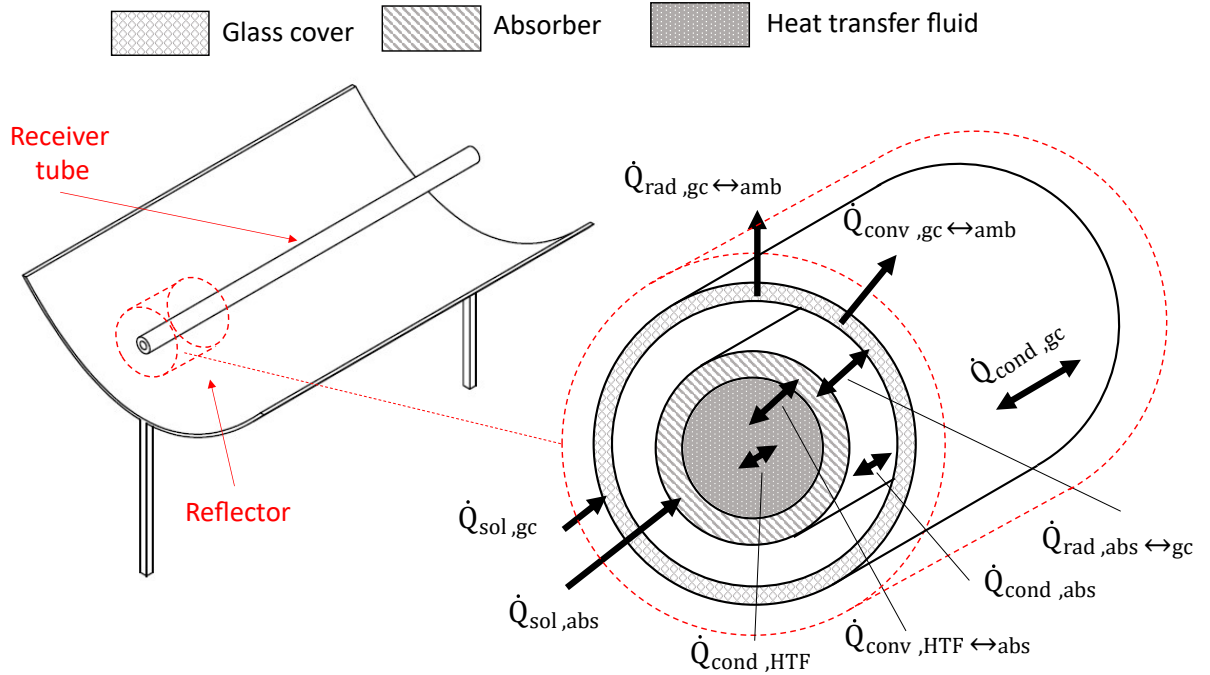
Figure 3.5: *Schematic view of the PTC internal structure*
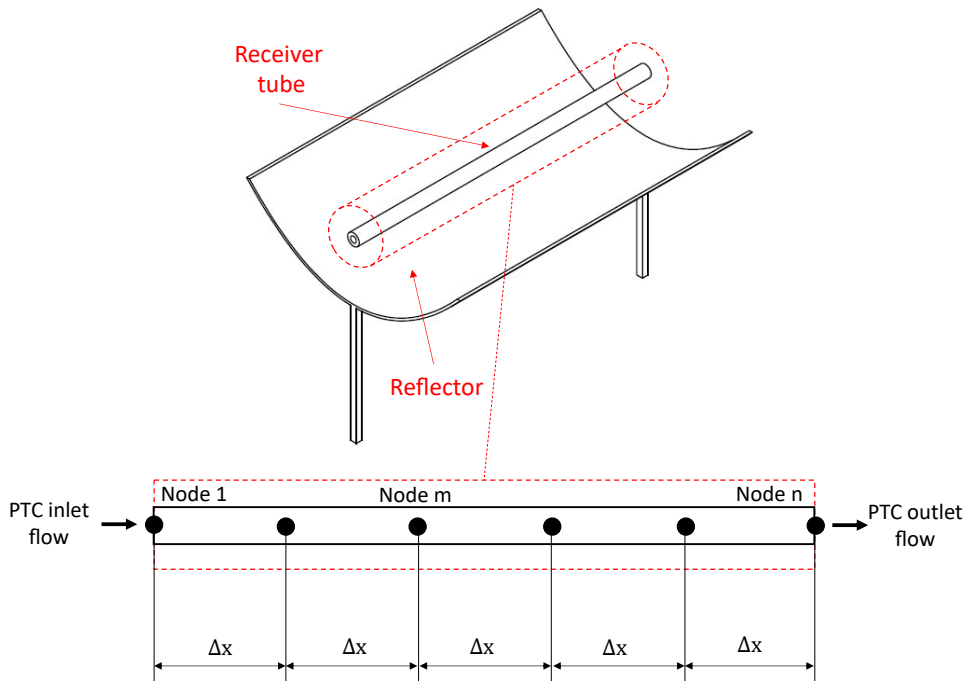
Figure 3.6: *PTC discretization in spatial nodes*

The main hypothesis and simplifications of the computational model are listed below:

- The heat transfer by conduction from the PTC line towards the structural support of the module has been neglected.

- A two-axis tracking system, which is assumed to be actively controlled, guarantees an optimum Sun tracking and orientation of the module.

- The incident solar irradiance is assumed to be uniform along the glass cover and the absorber span, that is, all the discretized portions receive the same solar flux.

- The glass cover and the absorber are separated by a vacuum chamber.

- The glass cover loses heat by radiation to the sky temperature which is assumed to be 8 °C below the ambient temperature [105].

- The velocity distribution of the HTF is assumed to be uniform in all the transversal sections along the PTC line span.

- Pressure losses associated with the HTF circulation inside the pipes are neglected.

- Thermal expansion effects associated with the heating of the pipes are neglected.

The heat transfer mechanisms occurring in all the material layers of the PTC line are depicted in Figure 3.5. The nodal discretization over the PTC span is illustrated in Figure 3.6.

Equation 3.2 represents a heat power balance in a general form for the PTC line

absorber:

$$\boxed{\dot{Q}_{acc,abs} = \dot{Q}_{sol,abs} + \dot{Q}_{cond,abs} + \dot{Q}_{conv,HTF\leftrightarrow abs} + \dot{Q}_{rad,abs\leftrightarrow gc}} \quad (3.2)$$

Splitting all the equation terms:

- **Absorber accumulative term** $\left(\dot{Q}_{acc,abs}\right)$:

  General expression:

$$\dot{Q}_{acc,abs} = \rho_{abs} \cdot c_{p,abs} \cdot V_{abs} \cdot \frac{\partial T_{abs}}{\partial t} \quad (3.3)$$

Discretizing Equation 3.3 for the first node '1', a generic node 'm', and the last node 'n':

$$\begin{cases} \dot{Q}^i_{acc,abs,1} = \rho_{abs} \cdot c_{p,abs} \cdot A_I \cdot \frac{\Delta x}{2} \cdot \frac{T^{i+1}_{abs,1} - T^i_{abs,1}}{\Delta t} \\ \dot{Q}^i_{acc,abs,m} = \rho_{abs} \cdot c_{p,abs} \cdot A_I \cdot \Delta x \cdot \frac{T^{i+1}_{abs,m} - T^i_{abs,m}}{\Delta t} \\ \dot{Q}^i_{acc,abs,n} = \rho_{abs} \cdot c_{p,abs} \cdot A_I \cdot \frac{\Delta x}{2} \cdot \frac{T^{i+1}_{abs,n} - T^i_{abs,n}}{\Delta t} \end{cases} \quad (3.4)$$

- **Absorber source term** $\left(\dot{Q}_{sol,abs}\right)$:

  General expression:

$$\dot{Q}_{sol,abs} = P_{abs} = DNI \cdot A_{col} \cdot \eta_{opt,abs} \quad (3.5)$$

$$\eta_{opt,abs} = \eta_{opt} \cdot \alpha_{abs} \cdot \tau_{gc} \quad (3.6)$$

$$\eta_{opt} = \epsilon_1 \cdot \epsilon_2 \cdot \epsilon_3 \cdot \epsilon_4 \cdot \epsilon_5 \cdot \epsilon_6 \cdot IAM(\theta) \cdot \rho_{mi} \quad (3.7)$$

Where the technical specifications for the EuroTrough collector are pro-

vided in the PTC dynamic simulation tool developed by PSA-CIEMAT [106]:

$$\begin{cases} IAM(\theta) = 1 \rightarrow \text{Attainable with a two-axis tracking system and a real-time control.} \\ \epsilon_1 = 1 \rightarrow \text{Shadowing parameter.} \\ \epsilon_2 = 1 \rightarrow \text{Tracking error.} \\ \epsilon_3 = 1 \rightarrow \text{Geometry error.} \\ \epsilon_4 = 1 \rightarrow \text{Dirt on mirrors.} \\ \epsilon_5 = 1 \rightarrow \text{Dirt on the heat collecting element.} \\ \epsilon_6 = 0.943 \rightarrow \text{Unaccounted effects.} \\ \rho_{mi} = 0.939 \rightarrow \text{Mirror reflectivity.} \end{cases}$$

(3.8)

Discretizing Equation 3.5 for the first node '1', a generic node 'm' and the last node 'n':

$$\begin{cases} \dot{Q}^i_{sol,abs,1} = P^i_{abs} \cdot \frac{\Delta x}{2 \cdot L} = DNI^i \cdot A_{col} \cdot \eta_{opt,abs} \cdot \frac{\Delta x}{2 \cdot L} \\ \dot{Q}^i_{sol,abs,m} = P^i_{abs} \cdot \frac{\Delta x}{L} = DNI^i \cdot A_{col} \cdot \eta_{opt,abs} \cdot \frac{\Delta x}{L} \\ \dot{Q}^i_{sol,abs,n} = P^i_{abs} \cdot \frac{\Delta x}{2 \cdot L} = DNI^i \cdot A_{col} \cdot \eta_{opt,abs} \cdot \frac{\Delta x}{2 \cdot L} \end{cases}$$

(3.9)

Where L corresponds with the total PTC span.

- **Absorber axial conduction term $\left(\dot{Q}_{cond,abs} \right)$:**

General expression:

$$\dot{Q}_{cond,abs} = k_{abs} \cdot V_{abs} \cdot \frac{\partial^2 T_{abs}}{\partial x^2}$$

(3.10)

Discretizing Equation 3.10 for the first node '1', a generic node 'm', and the last node 'n':

$$\begin{cases} \dot{Q}_{cond,abs,1} = k_{abs} \cdot A_I \cdot \Delta x \cdot \frac{T^i_{abs,2} - T^i_{abs,1}}{\Delta x^2} \\ \dot{Q}_{cond,abs,m} = k_{abs} \cdot A_I \cdot \Delta x \cdot \frac{T^i_{abs,m+1} - 2 \cdot T^i_{abs,m} + T^i_{abs,m-1}}{\Delta x^2} \\ \dot{Q}_{cond,abs,n} = k_{abs} \cdot A_I \cdot \Delta x \cdot \frac{T^i_{abs,n-1} - T^i_{abs,n}}{\Delta x^2} \end{cases}$$

(3.11)

- **Convection between the absorber and the HTF $\left(\dot{Q}_{conv,HTF \leftrightarrow abs} \right)$:**

General expression:

$$\dot{Q}_{conv,HTF \leftrightarrow abs} = h_{HTF \leftrightarrow abs} \cdot A_{HTF \leftrightarrow abs} \cdot (T_{HTF} - T_{abs})$$

(3.12)

Discretizing Equation 3.12 for the first node '1', a generic node 'm', and the last node 'n':

$$
\begin{cases}
\dot{Q}^i_{conv,HTF\leftrightarrow abs,1} = h_{HTF\leftrightarrow abs} \cdot \frac{A_{III}}{2} \cdot \left(T^i_{HTF,1} - T^i_{abs,1}\right) \\
\dot{Q}^i_{conv,HTF\leftrightarrow abs,m} = h_{HTF\leftrightarrow abs} \cdot A_{III} \cdot \left(T^i_{HTF,m} - T^i_{abs,m}\right) \\
\dot{Q}^i_{conv,HTF\leftrightarrow abs,n} = h_{HTF\leftrightarrow abs} \cdot \frac{A_{III}}{2} \cdot \left(T^i_{HTF,n} - T^i_{abs,n}\right)
\end{cases}
\tag{3.13}
$$

- **Radiation between the absorber and the glass cover** $\left(\dot{Q}_{rad,abs\leftrightarrow gc}\right)$:

The radiation modelization between these material layers considers the heat transfer between two semi-infinite and concentric tubes. Expressed in a mathematical general form:

$$
\dot{Q}_{rad,abs\leftrightarrow gc} = A_{abs\leftrightarrow gc} \cdot \frac{\sigma \cdot \left(T^4_{gc} - T^4_{abs}\right)}{\frac{1}{\epsilon_{abs}} + \frac{1-\epsilon_c}{\epsilon_c} \cdot \frac{D_{abs,ext}}{D_{abs,int}}}
\tag{3.14}
$$

Discretizing Equation 3.14 for the first node '1', a generic node 'm', and the last node 'n':

$$
\begin{cases}
\dot{Q}^i_{rad,abs\leftrightarrow gc,1} = \frac{A_{II}}{2} \cdot \frac{\sigma \cdot \left(\left(T^i_{gc,1}\right)^4 - \left(T^i_{abs,1}\right)^4\right)}{\frac{1}{\epsilon_{abs}} + \frac{1-\epsilon_c}{\epsilon_c} \cdot \frac{D_{abs,ext}}{D_{abs,int}}} \\
\dot{Q}^i_{rad,abs\leftrightarrow gc,m} = A_{II} \cdot \frac{\sigma \cdot \left(\left(T^i_{gc,m}\right)^4 - \left(T^i_{abs,m}\right)^4\right)}{\frac{1}{\epsilon_{abs}} + \frac{1-\epsilon_c}{\epsilon_c} \cdot \frac{D_{abs,ext}}{D_{abs,int}}} \\
\dot{Q}^i_{rad,abs\leftrightarrow gc,n} = \frac{A_{II}}{2} \cdot \frac{\sigma \cdot \left(\left(T^i_{gc,n}\right)^4 - \left(T^i_{abs,n}\right)^4\right)}{\frac{1}{\epsilon_{abs}} + \frac{1-\epsilon_c}{\epsilon_c} \cdot \frac{D_{abs,ext}}{D_{abs,int}}}
\end{cases}
\tag{3.15}
$$

Equation 3.16 represents a heat power balance in a general form for the PTC line HTF:

$$
\boxed{\dot{Q}_{acc,HTF} = \dot{Q}_{cond,HTF} + \dot{Q}_{conv,HTF\leftrightarrow abs} + \dot{Q}_{adv,HTF}}
\tag{3.16}
$$

Splitting all the equation terms:

- **HTF accumulative term** $\left(\dot{Q}_{acc,HTF}\right)$:

General expression:

$$
\dot{Q}_{acc,HTF} = \rho_{HTF} \cdot c_{p,HTF} \cdot V_{HTF} \cdot \frac{\partial T_{HTF}}{\partial t}
\tag{3.17}
$$

Discretizing Equation 3.17 for the first node '1', a generic node 'm', and the last node 'n':

$$
\begin{cases}
\dot{Q}^i_{acc,HTF,1} = \rho_{HTF} \cdot c_{p,HTF} \cdot A_{IV} \cdot \frac{\Delta x}{2} \cdot \frac{T^{i+1}_{HTF,1} - T^i_{HTF,1}}{\Delta t} \\
\dot{Q}^i_{acc,HTF,n} = \rho_{HTF} \cdot c_{p,HTF} \cdot A_{IV} \cdot \Delta x \cdot \frac{T^{i+1}_{HTF,m} - T^i_{HTF,m}}{\Delta t} \\
\dot{Q}^i_{acc,HTF,m} = \rho_{HTF} \cdot c_{p,HTF} \cdot A_{IV} \cdot \frac{\Delta x}{2} \cdot \frac{T^{i+1}_{HTF,n} - T^i_{HTF,n}}{\Delta t}
\end{cases}
\tag{3.18}
$$

- **HTF axial conduction term $\left(\dot{Q}_{cond,HTF} \right)$:**

General expression:

$$
\dot{Q}_{cond,HTF} = k_{HTF} \cdot V_{HTF} \cdot \frac{\partial^2 T_{HTF}}{\partial x^2}
\tag{3.19}
$$

Discretizing Equation 3.19 for the first node '1', a generic node 'm', and the last node 'n':

$$
\begin{cases}
\dot{Q}^i_{cond,HTF,1} = k_{HTF} \cdot A_{IV} \cdot \Delta x \cdot \frac{T^i_{HTF,2} - T^i_{HTF,1}}{\Delta x^2} \\
\dot{Q}^i_{cond,HTF,m} = k_{HTF} \cdot A_{IV} \cdot \Delta x \cdot \frac{T^i_{HTF,m+1} - 2 \cdot T^i_{HTF,m} + T^i_{HTF,m-1}}{\Delta x^2} \\
\dot{Q}^i_{cond,HTF,n} = k_{HTF} \cdot A_{IV} \cdot \Delta x \cdot \frac{T^i_{HTF,n-1} - T^i_{HTF,n}}{\Delta x^2}
\end{cases}
\tag{3.20}
$$

- **Convection between the absorber and the HTF $\left(\dot{Q}_{conv,HTF \leftrightarrow abs} \right)$:**

General expression:

$$
\dot{Q}_{conv,HTF \leftrightarrow abs} = h_{HTF \leftrightarrow abs} \cdot A_{HTF \leftrightarrow abs} \cdot (T_{abs} - T_{HTF})
\tag{3.21}
$$

Discretizing Equation 3.21 for the first node '1', a generic node 'm', and the last node 'n':

$$
\begin{cases}
\dot{Q}^i_{conv,HTF \leftrightarrow abs,1} = h_{HTF \leftrightarrow abs} \cdot \frac{A_{III}}{2} \cdot \left(T^i_{abs,1} - T^i_{HTF,1} \right) \\
\dot{Q}^i_{conv,HTF \leftrightarrow abs,m} = h_{HTF \leftrightarrow abs} \cdot A_{III} \cdot \left(T^i_{abs,m} - T^i_{HTF,m} \right) \\
\dot{Q}^i_{conv,HTF \leftrightarrow abs,n} = h_{HTF \leftrightarrow abs} \cdot \frac{A_{III}}{2} \cdot \left(T^i_{abs,n} - T^i_{HTF,n} \right)
\end{cases}
\tag{3.22}
$$

- **Advection term associated to the HTF circulation $\left(\dot{Q}_{conv,HTF \leftrightarrow abs} \right)$:**

General expression:

$$
\dot{Q}_{adv,HTF} = -\rho_{HTF} \cdot c_{p,HTF} \cdot u_{HTF} \cdot V_{HTF} \cdot \frac{\partial T_{HTF}}{\partial x}
\tag{3.23}
$$

The advection term is null in the first node (PTC inlet) since the temperature upstream is assumed to be uniform and equal to the first node temperature. Discretizing Equation 3.23 for a generic node 'm' and the last node 'n':

$$
\begin{cases}
\dot{Q}^i_{adv,HTF,m} = \rho_{HTF} \cdot c_{p,HTF} \cdot u_{HTF} \cdot A_{IV} \cdot \Delta x \cdot \frac{T^i_{HTF,m-1} - T^i_{HTF,m}}{\Delta x} \\
\dot{Q}^i_{adv,HTF,n} = \rho_{HTF} \cdot c_{p,HTF} \cdot u_{HTF} \cdot A_{IV} \cdot \Delta x \cdot \frac{T^i_{HTF,n-1} - T^i_{HTF,n}}{\Delta x}
\end{cases}
\tag{3.24}
$$

Equation 3.25 represents a heat power balance in a general form for the PTC line glass cover:

$$
\boxed{\dot{Q}_{acc,gc} = \dot{Q}_{sol,gc} + \dot{Q}_{cond,gc} + \dot{Q}_{conv,gc\leftrightarrow amb} + \dot{Q}_{rad,abs\leftrightarrow gc} + \dot{Q}_{rad,gc\leftrightarrow amb}}
\tag{3.25}
$$

- **Glass cover accumulative term $\left(\dot{Q}_{acc,gc}\right)$:**

General expression:

$$
\dot{Q}_{acc,gc} = \rho_{gc} \cdot c_{p,gc} \cdot V_{gc} \cdot \frac{\partial T_{gc}}{\partial t}
\tag{3.26}
$$

Discretizing Equation 3.26 for the first node '1', a generic node 'm', and the last node 'n':

$$
\begin{cases}
\dot{Q}^i_{acc,gc,1} = \rho_{gc} \cdot c_{p,gc} \cdot A_V \cdot \frac{\Delta x}{2} \cdot \frac{T^{i+1}_{gc,1} - T^i_{gc,1}}{\Delta t} \\
\dot{Q}^i_{acc,gc,m} = \rho_{gc} \cdot c_{p,gc} \cdot A_V \cdot \Delta x \cdot \frac{T^{i+1}_{gc,m} - T^i_{gc,m}}{\Delta t} \\
\dot{Q}^i_{acc,gc,n} = \rho_{gc} \cdot c_{p,gc} \cdot A_V \cdot \frac{\Delta x}{2} \cdot \frac{T^{i+1}_{gc,n} - T^i_{gc,n}}{\Delta t}
\end{cases}
\tag{3.27}
$$

- **Glass cover source term $\left(\dot{Q}_{sol,abs}\right)$:**

General expression:

$$
\dot{Q}_{sol,gc} = P_{gc} = DNI \cdot A_{col} \cdot \eta_{opt,gc}
\tag{3.28}
$$

$$
\eta_{opt,gc} = \eta_{opt} \cdot \alpha_{gc}
\tag{3.29}
$$

The optical efficiency η_{opt} has been already defined in Equation 3.7.

Discretizing Equation 3.28 for the first node '1', a generic node 'm', and the last node 'n':

$$\begin{cases} \dot{Q}^i_{sol,gc,1} = P^i_{gc} \cdot \frac{\Delta x}{2 \cdot L} = DNI^i \cdot A_{col} \cdot \eta_{opt,gc} \cdot \frac{\Delta x}{2 \cdot L} \\ \dot{Q}^i_{sol,gc,m} = P^i_{gc} \cdot \frac{\Delta x}{L} = DNI^i \cdot A_{col} \cdot \eta_{opt,gc} \cdot \frac{\Delta x}{L} \\ \dot{Q}^i_{sol,gc,n} = P^i_{gc} \cdot \frac{\Delta x}{2 \cdot L} = DNI^i \cdot A_{col} \cdot \eta_{opt,gc} \cdot \frac{\Delta x}{2 \cdot L} \end{cases} \quad (3.30)$$

- **Glass cover axial conduction term $\left(\dot{Q}_{cond,gc} \right)$:**

General expression:

$$\dot{Q}_{cond,gc} = k_{gc} \cdot V_{gc} \cdot \frac{\partial^2 T_{gc}}{\partial x^2} \quad (3.31)$$

Discretizing Equation 3.31 for the first node '1', a generic node 'm', and the last node 'n':

$$\begin{cases} \dot{Q}^i_{cond,gc,1} = k_{gc} \cdot A_V \cdot \Delta x \cdot \frac{T^i_{gc,2} - T^i_{gc,1}}{\Delta x^2} \\ \dot{Q}^i_{cond,gc,m} = k_{gc} \cdot A_V \cdot \Delta x \cdot \frac{T^i_{gc,m+1} - 2 \cdot T^i_{gc,m} + T^i_{gc,m-1}}{\Delta x^2} \\ \dot{Q}^i_{cond,gc,n} = k_{gc} \cdot A_V \cdot \Delta x \cdot \frac{T^i_{gc,n-1} - T^i_{gc,n}}{\Delta x^2} \end{cases} \quad (3.32)$$

- **Convection between the glass cover and the ambient $\left(\dot{Q}_{conv,gc \leftrightarrow amb} \right)$:**

General expression:

$$\dot{Q}_{conv,gc \leftrightarrow amb} = h_{conv,gc \leftrightarrow amb} \cdot A_{conv,gc \leftrightarrow amb} \cdot (T_{amb} - T_{gc}) \quad (3.33)$$

Discretizing Equation 3.33 for the first node '1', a generic node 'm', and the last node 'n':

$$\begin{cases} \dot{Q}^i_{conv,gc \leftrightarrow amb,1} = h_{conv,gc \leftrightarrow amb} \cdot \frac{A_{VI}}{2} \cdot \left(T^i_{amb} - T^i_{gc,1} \right) \\ \dot{Q}^i_{conv,gc \leftrightarrow amb,m} = h_{conv,gc \leftrightarrow amb} \cdot A_{VI} \cdot \left(T^i_{amb} - T^i_{gc,m} \right) \\ \dot{Q}^i_{conv,gc \leftrightarrow amb,n} = h_{conv,gc \leftrightarrow amb} \cdot \frac{A_{VI}}{2} \cdot \left(T^i_{amb} - T^i_{gc,n} \right) \end{cases} \quad (3.34)$$

- **Radiation between the absorber and the glass cover $\left(\dot{Q}_{rad,abs \leftrightarrow gc} \right)$:**

General expression:

$$\dot{Q}_{rad,abs \leftrightarrow gc} = A_{abs \leftrightarrow gc} \cdot \frac{\sigma \cdot \left(T^4_{abs} - T^4_{gc} \right)}{\frac{1}{\epsilon_{abs}} + \frac{1 - \epsilon_c}{\epsilon_c} \cdot \frac{D_{abs,ext}}{D_{abs,int}}} \quad (3.35)$$

Discretizing Equation 3.35 for the first node '1', a generic node 'm', and the last node 'n':

$$
\begin{cases}
\dot{Q}^i_{rad,abs\leftrightarrow gc,1} = \dfrac{A_{II}}{2} \cdot \dfrac{\sigma \cdot \left(\left(T^i_{abs,1}\right)^4 - \left(T^i_{gc,1}\right)^4\right)}{\frac{1}{\epsilon_{abs}} + \frac{1-\epsilon_c}{\epsilon_c} \cdot \frac{D_{abs,ext}}{D_{abs,int}}} \\[4mm]
\dot{Q}^i_{rad,abs\leftrightarrow gc,m} = A_{II} \cdot \dfrac{\sigma \cdot \left(\left(T^i_{abs,m}\right)^4 - \left(T^i_{gc,m}\right)^4\right)}{\frac{1}{\epsilon_{abs}} + \frac{1-\epsilon_c}{\epsilon_c} \cdot \frac{D_{abs,ext}}{D_{abs,int}}} \\[4mm]
\dot{Q}^i_{rad,abs\leftrightarrow gc,n} = \dfrac{A_{II}}{2} \cdot \dfrac{\sigma \cdot \left(\left(T^i_{abs,n}\right)^4 - \left(T^i_{gc,n}\right)^4\right)}{\frac{1}{\epsilon_{abs}} + \frac{1-\epsilon_c}{\epsilon_c} \cdot \frac{D_{abs,ext}}{D_{abs,int}}}
\end{cases}
\tag{3.36}
$$

- **Radiation between the glass cover and the sky** $\left(\dot{Q}_{rad,gc\leftrightarrow sky}\right)$:

General expression:

$$
\dot{Q}_{rad,gc\leftrightarrow sky} = A_{gc\leftrightarrow sky} \cdot \sigma \cdot \epsilon_{gc} \cdot \left(T^4_{sky} - T^4_{gc}\right) \tag{3.37}
$$

Discretizing Equation 3.37 for the first node '1', a generic node 'm', and the last node 'n':

$$
\begin{cases}
\dot{Q}^i_{rad,gc\leftrightarrow sky,1} = \dfrac{A_{VI}}{2} \cdot \sigma \cdot \epsilon_{gc} \cdot \left(\left(T^i_{sky}\right)^4 - \left(T^i_{gc,1}\right)^4\right) \\[3mm]
\dot{Q}^i_{rad,gc\leftrightarrow sky,m} = A_{VI} \cdot \sigma \cdot \epsilon_{gc} \cdot \left(\left(T^i_{sky}\right)^4 - \left(T^i_{gc,m}\right)^4\right) \\[3mm]
\dot{Q}^i_{rad,gc\leftrightarrow sky,n} = \dfrac{A_{VI}}{2} \cdot \sigma \cdot \epsilon_{gc} \cdot \left(\left(T^i_{sky}\right)^4 - \left(T^i_{gc,n}\right)^4\right)
\end{cases}
\tag{3.38}
$$

Where the spatial spacing depends on the PTC span (L) and the total number of computational nodes (n):

$$
\Delta x = \frac{L}{n-1} \tag{3.39}
$$

$$
A_I = \pi \cdot \left(R^2_{abs,ext} - R^2_{abs,int}\right) \tag{3.40}
$$

$$
A_{II} = 2 \cdot \pi \cdot R_{abs,ext} \cdot \Delta x \tag{3.41}
$$

$$
A_{III} = 2 \cdot \pi \cdot R_{abs,int} \cdot \Delta x \tag{3.42}
$$

$$
A_{IV} = \pi \cdot R^2_{abs,int} \tag{3.43}
$$

$$
A_V = \pi \cdot \left(R^2_{gc,ext} - R^2_{gc,int}\right) \tag{3.44}
$$

$$
A_{VI} = 2 \cdot \pi \cdot R_{gc,ext} \cdot \Delta x \tag{3.45}
$$

Experimental validation

The nodal model of the PTC has been validated by using experimental data coming from a test campaign carried out at PSA-CIEMAT (Plataforma Solar de Almería) [106]. It must be outlined that the PTC used to adjust the nodal model has the same architecture and technical specifications as the prototype used in the present investigation being the only difference in the PTC total span. To assess the reliability of the nodal model transient response it has been fed with the same record of instantaneous climatic parameters (solar irradiance, ambient temperature, and incidence angle), and operational inputs (HTF mass flow rate, PTC inlet temperature, and focusing-defocusing patterns) registered during the experimental campaign. As can be observed in Figures 3.7 and 3.8 the nodal approximation of the PTC predicts with good agreement the evolution of the PTC outlet temperature. The precision of the computational results is also guaranteed under highly changeable operating conditions like the sharp changes in the focusing pattern.

Tests from the experimental campaign carried out at PSA-CIEMAT have been used to validate the collector response against changes in direct solar irradiance. The objective is to study the response with the independence of the input parameters. Specifically, the evolution of the outlet PTC temperature given by the model has been contrasted with experimental data with a sudden decrease in the solar irradiance (change in the focusing pattern from 100% to 0%). As can be observed in the Figure 3.9, the further reduction of the temperature predicted by the model indicates its lower thermal inertia. However, some degree of uncertainty exists. The sampling interval of the acquisition system in the experimental facility ($\Delta t = 75s$) produces uncertainty about the exact focusing/defocusing law and the onset of the defocusing. This uncertainty would be removed with a lower time resolution in the acquisition system.

The validation process is considered satisfactory in the absence of data with more time resolution. The slight discrepancies found in the model have very little influence on the model precision.

3.3 Thermal Storage System

The thermal storage system operates as a heat reservoir with the capacity of providing hot thermal oil provisionally if the solar irradiance supply is interrupted. In the end, the TSS is intended to facilitate a continuous operation decoupling the thermal energy supply from the immediate availability of solar irradiance. The decision to include a hot sensible thermal storage system is sustained on its low cost and the use of materials with low toxicity [97]. Furthermore, a hot storage medium would facilitate a heating supply during winter periods and potential energy savings, contributing to the system's financial sustainability.

The implementation of a cold thermal storage system could be very helpful to dampen the fluctuations in refrigeration capacity and also to provide a refrigeration capacity exceeding the rated refrigeration capacity for which the jet-ejector refrigeration
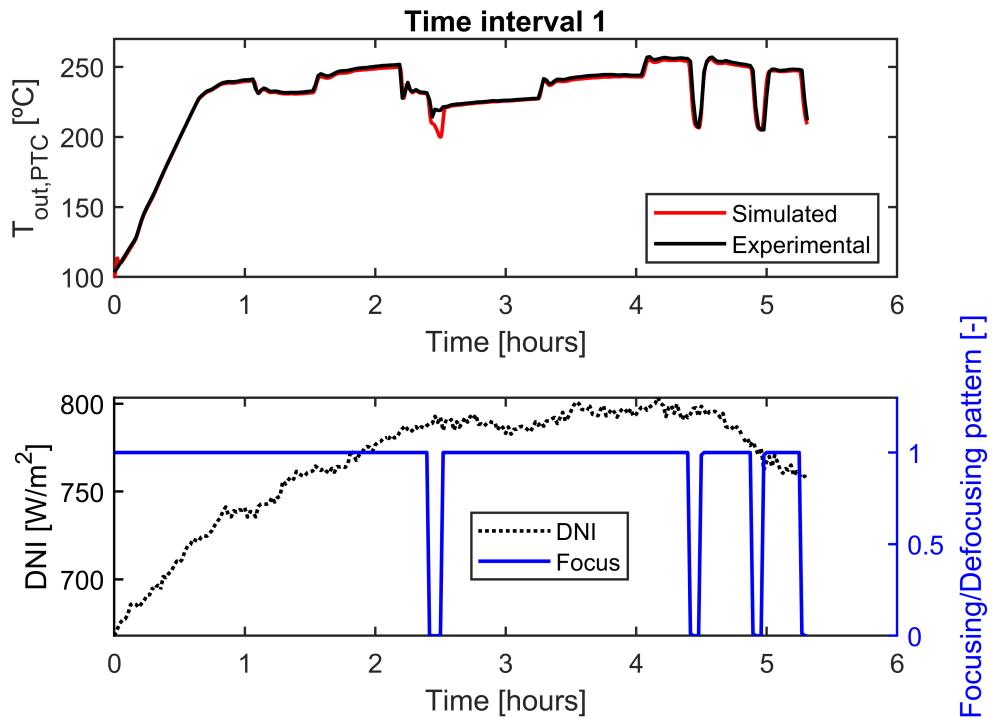
Figure 3.7: *Temporal evolution of the PTC outlet temperature (simulated vs experimental): Time slot 1*
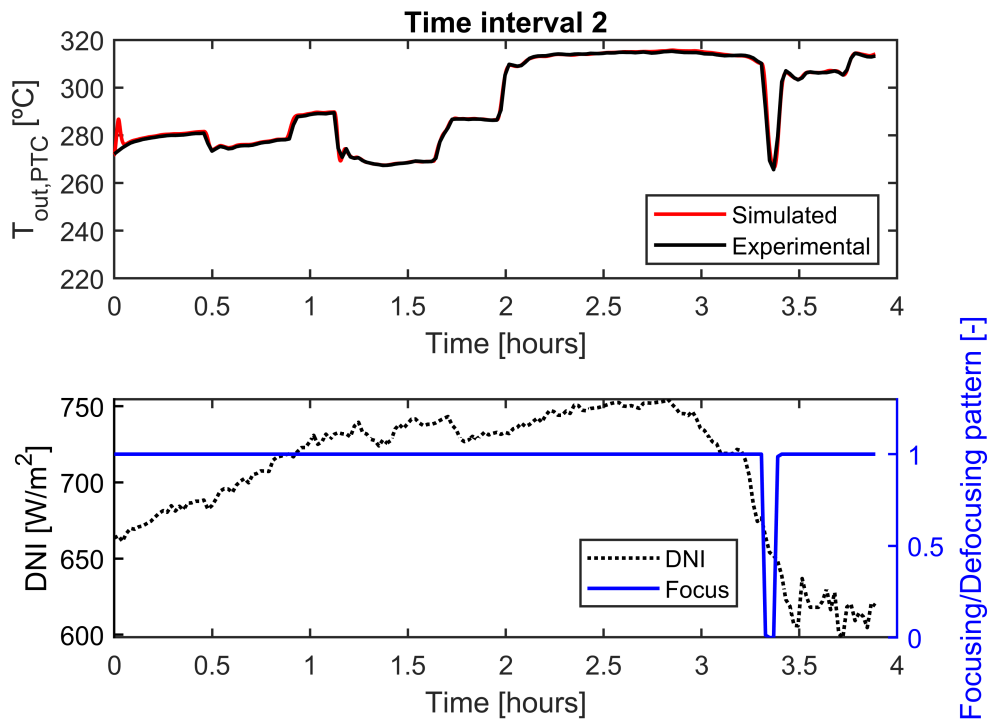
Figure 3.8: *Temporal evolution of the PTC outlet temperature (simulated vs experimental): Time slot 2*
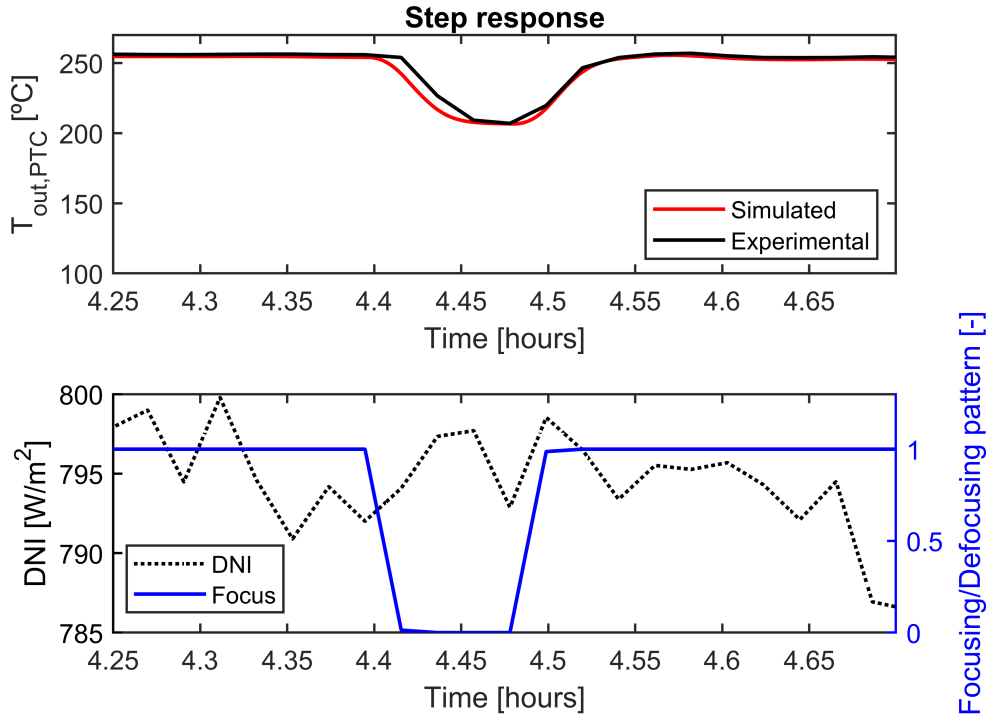
Figure 3.9: *System response against a sudden change in DNI*

system is sized. Regarding the cold TSS, there are two relevant aspects to consider: (i) having both systems (hot and cold TSS) would increase the capital expenditures, (ii) having only the cold TSS would make it difficult to store the solar heat during the winter season.

The thermal oil Syltherm 800, whose thermal properties (density, specific heat capacity, thermal conductivity and viscosity) are modeled as as a function of the temperature in Equations 3.46, 3.47, 3.48 and 3.49 has been used as the heat transport and storage medium [105].

$$\rho_{HTF}\left(T_{HTF}\right) = 1269 - 1.5206 \cdot T_{HTF} + 1.7901 \cdot 10^{-3} \cdot T_{HTF}^2 - 1.6706 \cdot 10^{-6} \cdot T_{HTF}^3 \quad (3.46)$$

$$c_{p,HTF}\left(T_{HTF}\right) = 1107.9 + 1.7073 \cdot T_{HTF} \quad (3.47)$$

$$k_{HTF}\left(T_{HTF}\right) = 0.1901 - 18.807 \cdot 10^{-5} \cdot T_{HTF} \quad (3.48)$$

$$\mu_{HTF}\left(T_{HTF}\right) = e^{0.59405 \cdot \left[[ln(T_{HTF})]^2 - 11.164 \cdot ln(T_{HTF}) + 49.041\right]} \cdot 10^{-3} \quad (3.49)$$

3.3.1 Description of constructive characteristics

The decision of selecting a sensible heat storage system is mainly sustained on its reduced cost when compared to latent heat tanks [97] and also on its simplicity [107]. According to Sarbu and Sebarcievici [97], the cost of a complete sensible heat storage system ranges between 0.1 and 10 €/kWh while in the case of a latent heat storage system the cost oscillates between 10 and 50 €/kWh. Sensible heat storage systems would be the best option if priority is given to a low-cost implementation.

A latent heat storage system would be the most adequate option from the operational point of view; the jet-ejector refrigeration system suffers performance degradation away from the design operating conditions and a phase-change storage medium would guarantee a nearly constant temperature in the hot driving flow, which is beneficial to maximize the system efficiency.

Inside the tank, it is assumed that a perfect and complete mixing occurs with the flow coming from the PTC and the flow recirculated from the generator. If the incoming flow is hotter than the heat transfer fluid contained in TSS, the stored HTF undergoes a temperature rise. In the same manner, if the JERS is activated the pumping system recirculates thermal oil towards the generator. There, the heat power is transferred from the HTF to the refrigerant and the temperature inside the TSS diminishes.

The TSS is assumed to be cylindrical with an aspect ratio between radius and height that minimizes its external area for a given volume. As depicted in Figure 3.10, the TSS external jacket is formed by two structural steel layers that house a thick layer of mineral wool thought to isolate the hot HTF and reduce thermal losses. The thermal properties of the cylinder layer materials are specified in Table 3.4.
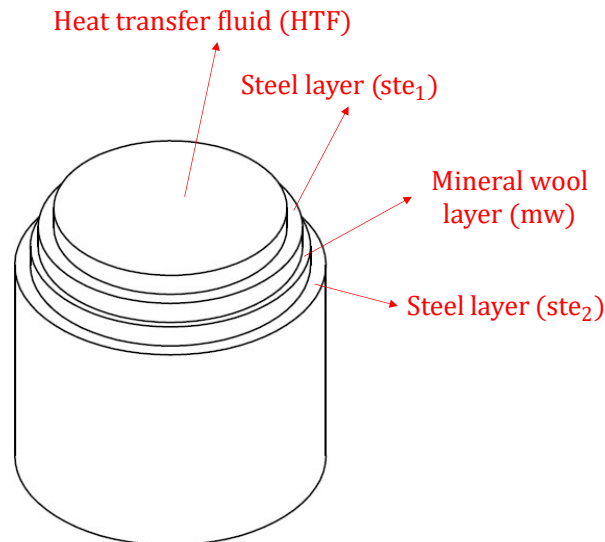
Figure 3.10: *Internal layout of the TSS*

The size of the tank has a strong influence on the overall system performance because it is responsible for maintaining an adequate thermal level to drive the JERS continuously. An oversized tank would have a great capacity to prolong much time

Layer	Material	Thickness [cm]	k $[W/(m \cdot K)]$
Internal (ste_1)	304 stainless steel	1	21
Intermediate (mw)	Mineral wool	3	0.04
External (ste_2)	304 stainless steel	1	21

Table 3.4: *Thermal properties of each layer of the TSS jacket*

the system's operation in the absence of solar irradiance but, at the same time, would have more thermal inertia and would restore the minimum thermal level to operate more slowly. Conversely, a relatively small tank would exhibit a rapid response under changing climatic events but it only would be able to maintain an adequate thermal level during short time slots. These opposite trends evidence the need for an optimum sizing adapted to specific design criteria of each particular application.

The TSSs are usually sized in relation to the surface collecting area. The Spanish regulation provides some useful prompts in this regard for solar thermal water heating systems [108, 109] as presented in Equation 3.50:

$$0.05 \ m < \frac{V_{TSS}}{A_{col}} < 0.18 \ m \tag{3.50}$$

3.3.2 Description of the transient nodal model

The nodal model approach is identical to the one presented for the PTC dynamic modeling. Figure 3.11 points out the heat transfer phenomena assumed. The selection of heat transfer mechanisms involved is supported by the research work of Zaversky et al. [110].

The general power balance inside the HTF housed in the TSS is presented in Equation 3.51:

$$\boxed{\dot{Q}_{acc,TSS} = \dot{Q}_{conv,TSS \leftrightarrow ste_1} + \dot{Q}_{ge} + \dot{Q}_{HTF} + \dot{Q}_{rad,TSS \leftrightarrow ste_1}} \tag{3.51}$$

Splitting all the equation terms:

- **Accumulative term of the heat transfer fluid contained in the TSS node** $\left(\dot{Q}_{acc,TSS}\right)$**:**

General expression:

$$\dot{Q}_{acc,TSS} = \rho_{TSS} \cdot c_{p,TSS} \cdot V_{TSS} \cdot \frac{\partial T_{TSS}}{\partial t} \tag{3.52}$$

Discretizing for a time interval 'i':

$$\dot{Q}^i_{acc,TSS} = \rho_{TSS} \cdot c_{p,TSS} \cdot V_{TSS} \cdot \frac{T^{i+1}_{TSS} - T^i_{TSS}}{\Delta t} \tag{3.53}$$
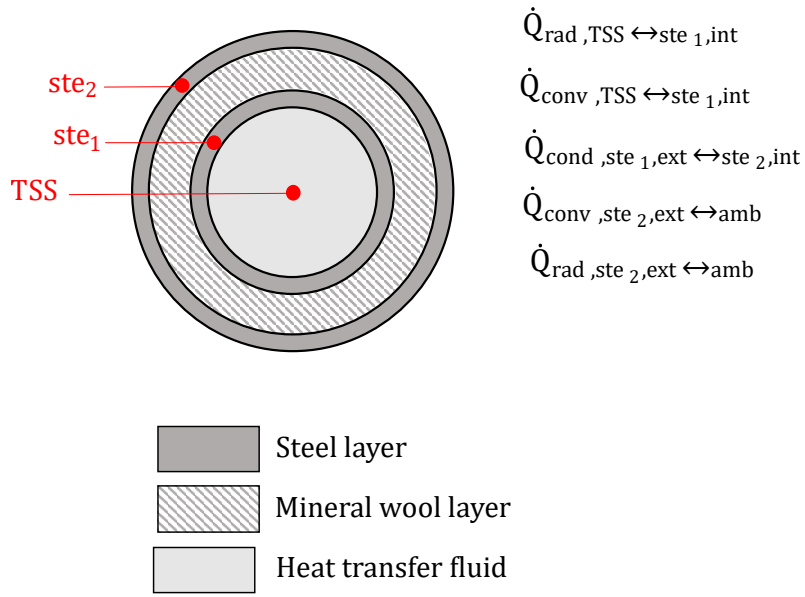
Figure 3.11: *Heat transfer phenomena ocurring between the HTF, the TSS jacket and the ambient*

- **Convection term between the heat transfer fluid contained in the TSS and the internal steel layer (ste_1) $\dot{Q}_{conv,TSS\leftrightarrow ste_1}$:**

  General expression:

  $$\dot{Q}_{conv,TSS\leftrightarrow ste_1} = h_{TSS\leftrightarrow ste_1} \cdot A_{ste_1} \cdot (T_{ste_1} - T_{TSS}) \tag{3.54}$$

  Discretizing for a time interval 'i':

  $$\dot{Q}^i_{conv,TSS\leftrightarrow ste_1} = h_{TSS\leftrightarrow ste_1} \cdot A_{ste_1} \cdot \left(T^i_{ste_1} - T^i_{TSS}\right) \tag{3.55}$$

  It must be outlined that the natural convection heat transfer coefficient $h_{TSS\leftrightarrow ste_1}$ has been estimated using a Nusselt correlation dependent of the Grashof and Prandtl dimensionless numbers $Nu = Nu\,(Pr, Gr)$.

- **Thermal power consumed by the JERS $\left(\dot{Q}_{ge}\right)$:**

  General expression:

  $$\dot{Q}_{ge} = \dot{m}_{ge} \cdot c_{p,ge} \cdot (T_{in,TSS} - T_{TSS}) \tag{3.56}$$

  Discretizing for a time interval 'i':

  $$\dot{Q}^i_{ge} = \dot{m}_{ge} \cdot c_{p,ge} \cdot \left(T^i_{in,TSS} - T^i_{TSS}\right) \tag{3.57}$$

69

It must be noted that when the TSS temperature is below the threshold value (minimum temperature to guarantee an adequate functioning) the JERS is deactivated and $\dot{Q}_{ge} = 0$.

- **Radiation term between the heat transfer fluid contained in the TSS and the internal steel layer $\left(\dot{Q}_{rad,TSS\leftrightarrow ste_1} \right)$:**

General expression:

$$\dot{Q}_{rad,TSS\leftrightarrow ste_1} = \epsilon_{TSS} \cdot \sigma \cdot A_{ste_1} \cdot \left(T_{ste_1}^4 - T_{TSS}^4 \right) \tag{3.58}$$

Discretizing for a time interval 'i':

$$\dot{Q}_{rad,TSS\leftrightarrow ste_1}^i = \epsilon_{TSS} \cdot \sigma \cdot A_{ste_1} \cdot \left(\left(T_{ste_1}^i \right)^4 - \left(T_{TSS}^i \right)^4 \right) \tag{3.59}$$

The general power balance in the internal steel layer (ste_1) is presented in Equation 3.51:

$$\boxed{\dot{Q}_{acc,ste_1} = \dot{Q}_{conv,TSS\leftrightarrow ste_1} + \dot{Q}_{cond,ste_1\leftrightarrow ste_2} + \dot{Q}_{rad,TSS\leftrightarrow ste_1}} \tag{3.60}$$

Splitting all the equation terms:

- **Accumulative term of the internal steel layer node $\left(\dot{Q}_{acc,ste_1} \right)$:**

General expression:

$$\dot{Q}_{acc,ste_1} = \rho_{ste_1} \cdot c_{p,ste_1} \cdot V_{ste_1} \cdot \frac{\partial T_{ste_1}}{\partial t} \tag{3.61}$$

Discretizing for a time interval 'i':

$$\dot{Q}_{acc,ste_1}^i = \rho_{ste_1} \cdot c_{p,ste_1} \cdot V_{ste_1} \cdot \frac{T_{ste_1}^{i+1} - T_{ste_1}^i}{\Delta t} \tag{3.62}$$

- **Convection term between the heat transfer fluid contained in the TSS and the internal steel layer node $\left(\dot{Q}_{conv,TSS\leftrightarrow ste_1} \right)$:**

General expression:

$$\dot{Q}_{conv,TSS\leftrightarrow ste_1} = h_{TSS\leftrightarrow ste_1} \cdot A_{ste_1} \cdot \left(T_{TSS} - T_{ste_1} \right) \tag{3.63}$$

Discretizing for a time interval 'i':

$$\dot{Q}_{conv,TSS\leftrightarrow ste_1}^i = h_{TSS\leftrightarrow ste_1} \cdot A_{ste_1} \cdot \left(T_{TSS}^i - T_{ste_1}^i \right) \tag{3.64}$$

70

- **Radiation term between the heat transfer fluid contained in the TSS and the internal steel layer** $\dot{Q}_{rad,TSS \leftrightarrow ste_1}$:

General expression:

$$\dot{Q}_{rad,TSS \leftrightarrow ste_1} = \epsilon_{TSS} \cdot \sigma \cdot A_{ste_1} \cdot \left(T_{TSS}^4 - T_{ste_1}^4\right) \tag{3.65}$$

Discretizing for a time interval 'i':

$$\dot{Q}_{rad,TSS \leftrightarrow ste_1}^i = \epsilon_{TSS} \cdot \sigma \cdot A_{ste_1} \cdot \left(\left(T_{TSS}^i\right)^4 - \left(T_{ste_1}^i\right)^4\right) \tag{3.66}$$

- **Conduction term modeling the heat transfer mechanism between the internal steel layer and the external steel layer** $\dot{Q}_{cond,ste_1 \leftrightarrow ste_2}$:

$$\dot{Q}_{cond,ste_1 \leftrightarrow ste_2} = \frac{T_{ste_2} - T_{ste_1}}{\frac{ln\left(\frac{R_{ext,mw}}{R_{int,mw}}\right)}{2 \cdot \pi \cdot L \cdot k_{mw}}} \tag{3.67}$$

Discretizing for a time interval 'i':

$$\dot{Q}_{cond,ste_1 \leftrightarrow ste_2}^i = \frac{T_{ste_2}^i - T_{ste_1}^i}{\frac{ln\left(\frac{R_{ext,mw}}{R_{int,mw}}\right)}{2 \cdot \pi \cdot L \cdot k_{mw}}} \tag{3.68}$$

The conduction heat transfer mechanism has been neglected in the internal steel layer assuming that this structural sheet does not have insulating properties (null thermal resistance). Thus, the temperature through this layer is uniform:

$$T_{ste_1,int} = T_{ste_1,ext} \tag{3.69}$$

The general power balance for the external steel layer is presented in Equation 3.70:

$$\boxed{\dot{Q}_{acc,ste_2} = \dot{Q}_{cond,ste_1 \leftrightarrow ste_2} + \dot{Q}_{conv,ste_2 \leftrightarrow amb} + \dot{Q}_{rad,ste_2 \leftrightarrow amb}} \tag{3.70}$$

Splitting all the equation terms:

- **Accumulative term in the external steel layer node** $\left(\dot{Q}_{acc,ste_2}\right)$:

General expression:

$$\dot{Q}_{acc,ste_2} = \rho_{ste_2} \cdot c_{p,ste_2} \cdot V_{ste_2} \cdot \frac{\partial T_{ste_2}}{\partial t} \tag{3.71}$$

Discretizing for a time interval 'i':

$$\dot{Q}^i_{acc,ste_2} = \rho_{ste_2} \cdot c_{p,ste_2} \cdot V_{ste_2} \cdot \frac{T^{i+1}_{ste_2} - T^i_{ste_2}}{\Delta t} \tag{3.72}$$

- **Conduction term modeling the heat transfer mechanism between the internal steel layer and the external steel layer $\dot{Q}_{cond,ste_1 \leftrightarrow ste_2}$:**

$$\dot{Q}_{cond,ste_1 \leftrightarrow ste_2} = \frac{T_{ste_1} - T_{ste_2}}{\frac{ln\left(\frac{R_{ext,mw}}{R_{int,mw}}\right)}{2 \cdot \pi \cdot L \cdot k_{mw}}} \tag{3.73}$$

Discretizing for a time interval 'i':

$$\dot{Q}^i_{cond,ste_1 \leftrightarrow ste_2} = \frac{T^i_{ste_1} - T^i_{ste_2}}{\frac{ln\left(\frac{R_{ext,mw}}{R_{int,mw}}\right)}{2 \cdot \pi \cdot L \cdot k_{mw}}} \tag{3.74}$$

The conduction heat transfer mechanism has been neglected in the external steel layer assuming that this structural sheet does not have insulating properties (null thermal resistance). Thus, the temperature through this layer is uniform:

$$T_{ste_2,int} = T_{ste_2,ext} \tag{3.75}$$

- **Convection heat transfer between external steel layer and the ambient $\dot{Q}_{conv,ste_2 \leftrightarrow amb}$:**

General expression:

$$\dot{Q}_{conv,ste_2 \leftrightarrow amb} = h_{ste_2 \leftrightarrow amb} \cdot A_{ste_2} \cdot (T_{amb} - T_{ste_2}) \tag{3.76}$$

Discretizing for a time interval 'i':

$$\dot{Q}^i_{conv,ste_2 \leftrightarrow amb} = h_{ste_2 \leftrightarrow amb} \cdot A_{ste_2} \cdot \left(T^i_{amb} - T^i_{ste_2}\right) \tag{3.77}$$

- **Radiation heat transfer between the external steel layer and the ambient $\dot{Q}_{rad,ste_2 \leftrightarrow amb}$:**

General expression:

$$\dot{Q}_{rad,ste_2 \leftrightarrow amb} = \epsilon_{ste_2} \cdot \sigma \cdot A_{ste_2} \cdot \left(T^4_{sky} - T^4_{ste_2}\right) \tag{3.78}$$

Discretizing for a time interval 'i':

$$\dot{Q}^i_{rad,ste_2 \leftrightarrow amb} = \epsilon_{ste_2} \cdot \sigma \cdot A_{ste_2} \cdot \left(\left(T^i_{sky}\right)^4 - \left(T^i_{ste_2}\right)^4\right) \tag{3.79}$$

3.4 Jet-ejector refrigeration system

3.4.1 Working fluid selection

The system performance has been evaluated considering environmentally friendly working fluids to meet the increasingly stringent regulations, specifically, R1234yf, R1234ze, and R600a. The Ozone Depletion Potential (ODP) of all the refrigerants under consideration is zero while their Global Warming Potential (GWP) is very low (R1234yf, GWP = 4; R1234ze, GWP = 6; R600a, GWP=3). All of them have been considered before in solar refrigeration applications or automotive equipment [71, 111, 112]. For the operating temperatures of a thermally driven refrigeration system working in a warm Mediterranean climate, the listed refrigerants present reasonable operating pressures during the phase change processes occurring at the generator, condenser, and evaporator. This key issue is essential to lower the costs because the required equipment could be easily found in the commercial offer of the supplier firms.

3.4.2 Generator

Definition of reference operating conditions

In the generator, the refrigerant evaporates at high pressure and temperature. The refrigerant heats up and evaporates as it passes through this element while the hot driving source is cooled down as it dissipates thermal power to incoming flow in the refrigerant side. To improve the efficiency of the heat exchange process a counterflow arrangement has been assumed.

The most convenient operating conditions in the generator depend on the thermal level of the hot driving flow and also depend on the system condensing temperature and the evaporating temperature. The jet-ejector non-dimensional maps couple the conditions of the generator to the operating conditions in the other branches of the cycle. The optimum generating conditions are a priori unknown, provided that the pinch point in the heat exchanger is satisfied. Different operating conditions in the generator for the reference condensing and evaporating conditions have been subject to study to determine those that maximize the JERS COP_{th}.

In both the steady-state and the transient analysis a temperature threshold of 120 $^\circ C$ has been considered below which it is assumed that the driving flow is not hot enough to activate the JERS. This design criteria represents a conservative value and allows the system more flexibility while selecting the operating conditions in the generator. The JERS, however, could operate below this threshold but might suffer severe performance degradation. The magnitude of this performance drop has been quantified in the following chapters for different JERS architectures.

Equation 3.80 represents the heat power balance in both sides of the heat exchanger for the solar application, which is assumed to occur at constant pressure ($P_{in,ge} = P_{out,ge}$). Hence, the pressure losses inside the heat exchanger are neglected.

$$\dot{Q}_{ge} = \dot{m}_{pf} \cdot (h_{out,ge} - h_{in,ge}) = \dot{m}_{TSS} \cdot (h_{out,TSS} - h_{in,TSS}) \qquad (3.80)$$

In the same manner, Equation 3.81 describes the power balance with the generator coupled to the exhaust line in the automotive application.

$$\dot{Q}_{ge} = \dot{m}_{pf} \cdot (h_{out,ge} - h_{in,ge}) = \dot{m}_{ex} \cdot (h_{in,ex} - h_{out,ex}) \qquad (3.81)$$

Heat exchange process in the generator

Figure 3.12 shows schematically the heat exchange process occurring in the generator splitting into two zones.

- Z_1: Single-phase thermal oil (liquid phase) and refrigerant heating (liquid phase).

- Z_2: Single-phase thermal oil (liquid phase) and supercritical heating of the refrigerant.

As will be discussed later, in the reference case taken to perform the thermoeconomic study, the refrigerant reaches supercritical conditions during the heating process. The total area required in the generator has been estimated by splitting the overall heat exchange process into the aforementioned zones:

$$A_{ge} = A_{ge,Z_1} + A_{ge,Z_2} \qquad (3.82)$$
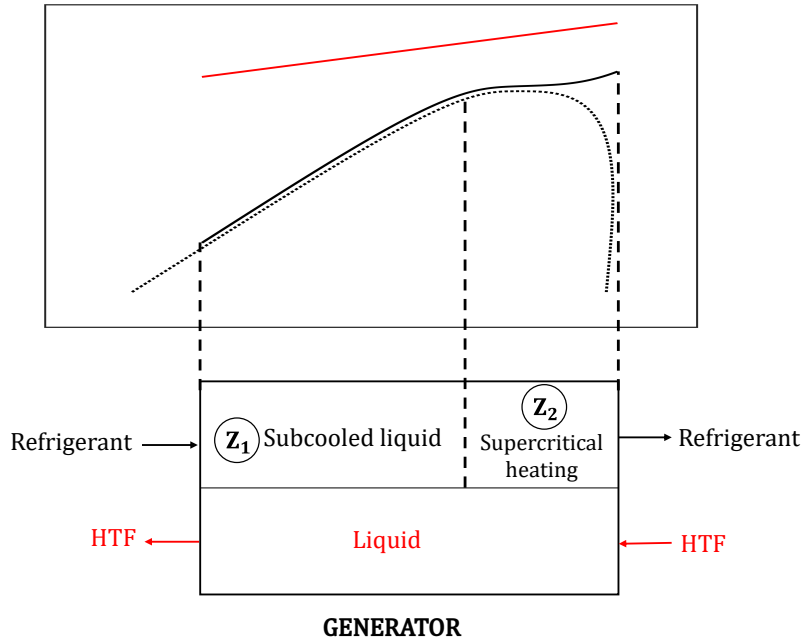
Figure 3.12: *Partitioning of the heat exchange process in the generator in different subzones*

3.4.3 Condenser

Definition of reference operating conditions

In the condenser, the refrigerant condenses at an intermediate pressure and temperature as it dissipates heat to the reference medium. The cooling water flows on the other side of the heat exchanger and undergoes a slight temperature increase. To improve the efficiency of the heat exchange process a counterflow arrangement has been assumed.

The condensing temperature of the heat exchanger is established by the ambient temperature. To determine the condensing temperature as a function of the ambient temperature a pinch point of $7°C$ has been assumed in the heat exchanger as well as $2°C$ of liquid subcooling. Such security margin is thought to prevent the refrigerant from entering into the expansion valve and the pump in saturated liquid conditions or two-phase flow near saturated conditions. The pinch point assumption is also coherent when compared to research works dealing with refrigeration systems [113, 114].

The heat exchange process occurring in the condenser is depicted in Figures 2.5 and 2.4.

- In the steady model the condensing temperature corresponds to $T_{co} = 40°C$, which is calculated with the pinch point considerations and a reference ambient temperature of $T_{amb,ref} = 31°C$. This value is a good estimation of the average daily maximum ambient temperature in a warm Mediterranean location during July and comes from the climate data records of Valencia (Spain). The selection of such a high reference ambient temperature means that a fixed-geometry jet-ejector thoroughly designed for this reference ambient temperature would have a wide operative range in terms of condensing temperatures at the cost of a lower achievable entrainment ratio.

- In the transient model the condensing temperature changes constantly depending on the instantaneous ambient temperature. The pinch point considerations exposed above are also applicable in the transient approach. Thermal inertia effects have been neglected in this heat exchanger.

Equation 3.83 balances the heat power exchange in the condenser in both the dissipation medium and the refrigerant sides and is valid for both the solar and the automotive application. The heat exchange process is assumed to occur at constant pressure $(P_{in,co} = P_{out,co})$. Hence, the pressure losses inside the heat exchanger are neglected.

$$\dot{Q}_{co} = (\dot{m}_{sf} + \dot{m}_{pf}) \cdot (h_{in,co} - h_{out,co}) = \dot{m}_w \cdot c_{p,w} \cdot (T_{out,w} - T_{in,w}) \tag{3.83}$$

Heat exchange process in the condenser

Figure 3.13 depicts the heat exchange process occurring in the condenser splitting the diagram into three zones according to the refrigerant state.

- Z_1: Single-phase water (liquid phase) and subcooled refrigerant cooling (liquid phase).

- Z_2: Single-phase water (liquid phase) and refrigerant condensation (phase change).

- Z_3: Single-phase water (liquid phase) and superheated refrigerant cooling (gas phase).

The area required in the condenser has been estimated by splitting the heat exchange process into the aforementioned zones:

$$A_{co} = A_{co,Z_1} + A_{co,Z_2} + A_{co,Z_3} \tag{3.84}$$
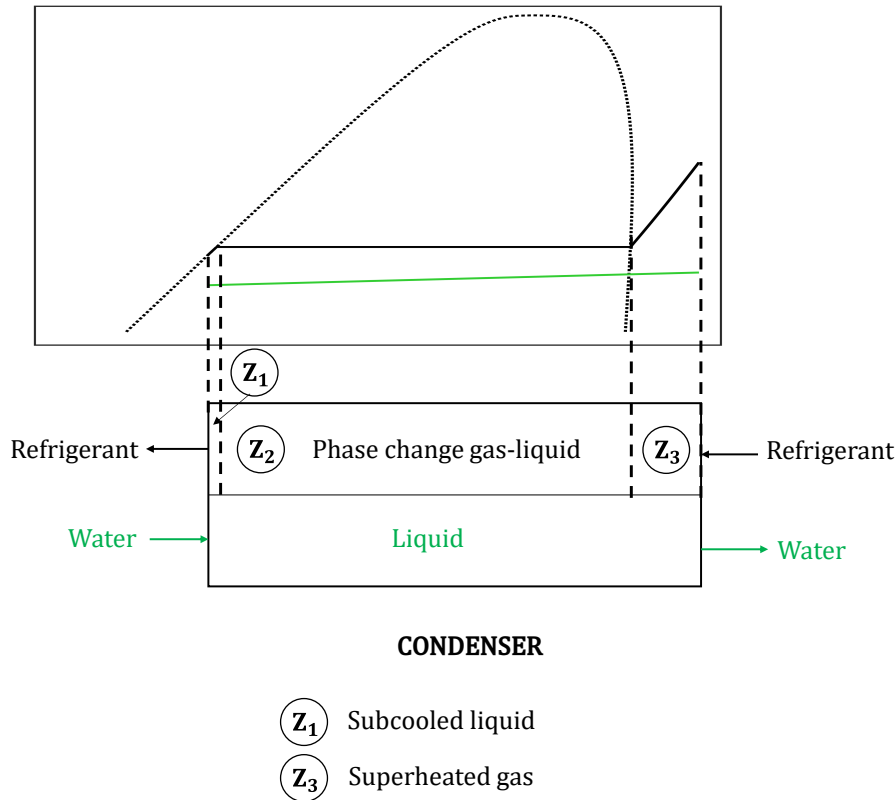
Figure 3.13: *Partitioning of the heat exchange process in the condenser in different subzones*

3.4.4   Evaporator

Definition of reference operating conditions

The solar-powered refrigeration system is intended to work with an evaporating temperature appropriate for air-conditioning applications, specifically, an evaporating temperature of $13°C$ [73, 58]. Assuming a pinch point in the heat exchanger of $7°C$, a temperature of $20°C$ would be attainable in the indoor refrigerated space. The pinch

point assumption is also coherent when compared to research works dealing with refrigeration systems [113, 114]. The target evaporating temperature is conserved in both the steady and transient analysis. Therefore, the refrigeration demand is constant irrespective of the modeling approach. It is considered in the transient analysis, notwithstanding, that there are no refrigeration needs when the ambient temperature is below 25 °C.

Equation 3.85 determines the refrigeration capacity balancing the heat power exchange between the refrigerant passing through the evaporator and the refrigerated medium. The heat exchange process is illustrated in Figures 2.5 and 2.4 and it is assumed to occur at constant pressure ($P_{in,ev} = P_{out,ev}$). Hence, the pressure losses inside the heat exchanger are neglected.

$$\dot{Q}_{ev} = \dot{m}_{sf} \cdot (h_{out,ev} - h_{in,ev}) = \dot{m}_{rl} \cdot c_{p,rl} \cdot (T_{in,rl} - T_{out,rl}) \tag{3.85}$$

In the automotive application, the same pinch point constraints are applicable, however, in this case, the aim is to reduce the intake temperature as much as possible so the evaporating temperature is a priori unknown. Indeed, the temperature reduction induced in the ICE intake line is considered as the main performance indicator. Equation 3.86 expresses the thermal power balance in the intake line.

$$\dot{Q}_{ev} = \dot{m}_{sf} \cdot (h_{out,ev} - h_{in,ev}) = \dot{m}_{int} \cdot (h_{in,int} - h_{out,int}) \tag{3.86}$$

Heat exchange process in the evaporator

Figure 3.14 depicts the heat exchange process occurring in the evaporator splitting the diagram into two segments according to the refrigerant state.

- Z_1: Refrigerated medium (gas phase) and refrigerant evaporation (phase change).

- Z_2: Refrigerated medium (gas phase) and superheated refrigerant heating (gas phase).

The area required in the evaporator has been estimated by splitting the heat exchange process into the aforementioned zones:

$$A_{ev} = A_{ev,Z_1} + A_{ev,Z_2} \tag{3.87}$$

3.4.5 Pressure pump and expansion valve

The liquid pump has been modeled considering an isentropic efficiency ($\eta_{pm} = 85\%$), as expressed in Equation 3.88. It has been assumed to have a response without delays.

$$\eta_{pm} = \frac{h_{out,pm,s} - h_{in,pm}}{h_{out,pm} - h_{in,pm}} \tag{3.88}$$
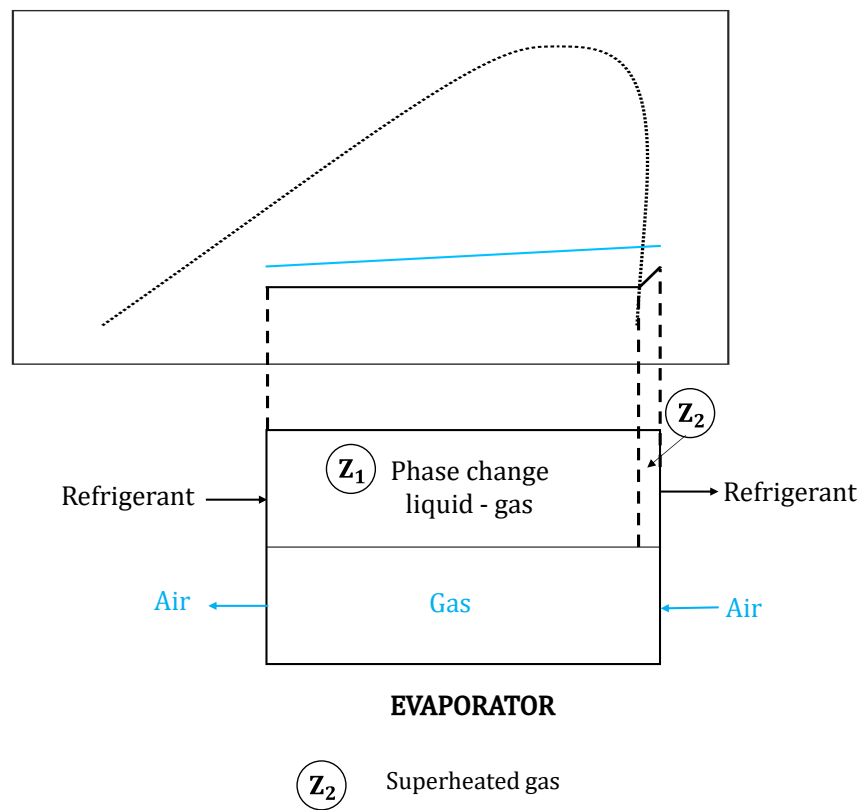
Figure 3.14: *Partitioning of the heat exchange process in the evaporator in different subzones*

where $h_{in,pm} = h_{out,co}$, and $h_{out,pm} = h_{in,ge}$. The expansion valve has been assumed to the isenthalpic so $h_{out,co} = h_{in,ev}$.

3.5 Jet-ejector

3.5.1 Geometry description

Figure 3.15 depicts the axisymmetric view of the fixed jet-ejector configuration (FJE) and Table 3.5 describes its most influential dimensions. These geometric parameters strongly affect the jet-ejector performance (maximum achievable entrainment ratio ω) and must be accurately predicted for a reference operating conditions. The nozzle exit position ($L_{e,1}$), the nozzle exit diameter ($D_{e,1}$), the nozzle throat diameter ($D_{e,3}$) and mixing section diameter ($D_{e,2}$) are considered as the four crucial geometric parameters [115, 116].

The FJE has been modeled using commercial and open-source CFD codes. All of the dimensions have been edited manually in the CFD code with the exception of the nozzle throat diameter, which is scaled for the rated thermal power consumption $\left(\dot{Q}_{ge}\right)$ or the targeted refrigeration load $\left(\dot{Q}_{ev}\right)$. The rest of the dimensions must be scaled accordingly and this simplifies the optimization process. The most convenient strategy to achieve an efficient FRS is to carry out a detailed geometry optimization for steady-state operating conditions that are assumed to be the most typical in a standard operation. The reference conditions established to do so are the already presented: $T_{co} = 40°C$, $T_{ev} = 13°C$ and a temperature of the hot thermal source of $120°C$ or above. The above conditions are coherent for both automotive and solar applications.

Figure 3.16 represents the axisymmetric view of the adjustable jet-ejector configuration (AJE). In the AJE, the primary nozzle effective area can be changed by displacing axially a spindle with a sharp tip. The spindle is intended to be automatically displaced as the ambient temperature changes to modify the jet-ejector area ratio, which is defined in Equation 3.89.

$$AR = \left(\frac{D_{e,2}}{D_{e,3}}\right)^2 \tag{3.89}$$

The spindle tuning permits the jet-ejector to operate near its design condition and confers the jet-ejector great versatility. The aim is to prevent the jet-ejector from:

1. Suffering a severe performance degradation associated with the single-choking operating mode when the critical condensing temperature is exceeded. This is accomplished by moving the spindle backwards and, hence, reducing the jet-ejector AR, as shown in Figure 2.8.

2. Reaching a constant efficiency when the condensing temperature is below the critical condensing temperature and the operating conditions are, indeed, more

favorable to obtain an enhanced efficiency rather than being deadlocked. This is achieved by moving the spindle forwards to increase the jet-ejector AR, as shown in Figure 2.8.

3. Enlarging the operative range with a lack of temperature in the generator caused by a temperature reduction in the hot driving source. However, as will be discussed later, using the spindle for this compensation is less versatile and its behavior is coupled with the condensing temperature.

The most adequate algorithm to design an efficient adjustable jet-ejector is to optimize its internal geometry for a fixed spindle position and reference operating conditions. The reference conditions for the AJE design are the same specified for the FJE. The reference spindle position must be selected so that the designer must let room for displacement in the spindle, since the mechanism must move the piece backwards when the critical condensing temperature is exceeded and move it forwards otherwise. It must be noted that the FJE with a static spindle position is equivalent to a jet-ejector with fixed geometry.

Parameter	Description	Units
$L_{e,1}$	Nozzle exit position (NXP)	mm
$L_{e,2}$	Mixing chamber length	mm
$L_{e,3}$	Diffuser length	mm
$L_{e,4}$	Primary nozzle inlet length	mm
$D_{e,1}$	Nozzle exit diameter	mm
$D_{e,2}$	Mixing chamber diameter	mm
$D_{e,3}$	Nozzle throat diameter	mm
$D_{e,4}$	Nozzle inlet diameter	mm
SP	Spindle position	mm
$\alpha_{e,1}$	Diverging angle of the diffuser	°
$\alpha_{e,2}$	Converging angle of the suction chamber	°
$\alpha_{e,3}$	Diverging angle of the nozzle	°
$\alpha_{e,4}$	Converging angle of the nozzle	°

Table 3.5: *Description of the key geometric dimensions of the jet-ejector*
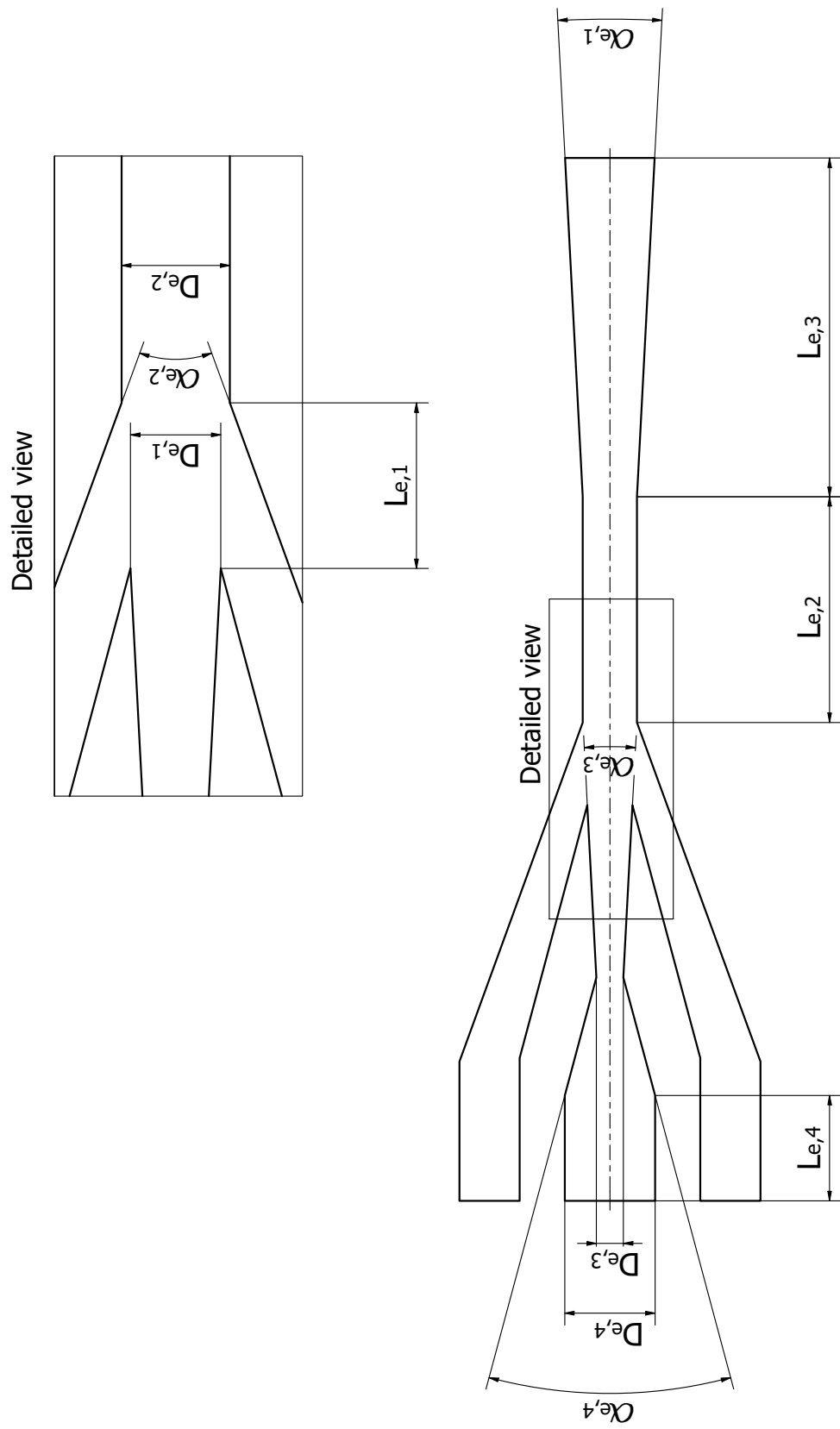
Figure 3.15: *General and detailed view of the FJE*
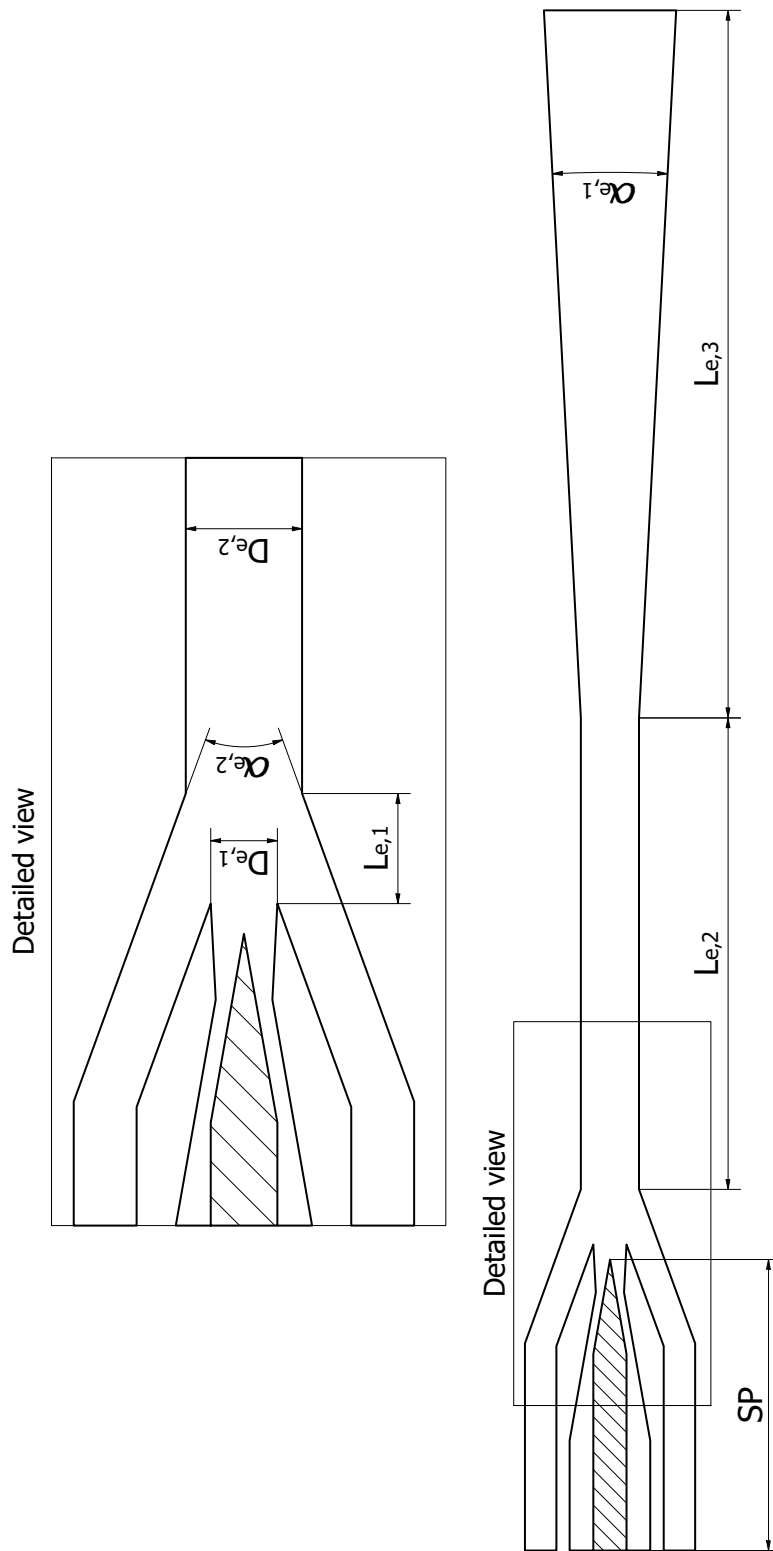
Figure 3.16: General and detailed view of the AJE

3.5.2 Computational model to determine the primary nozzle mass flow rate ($\dot{m}_{pf}$)

The mass flow rate passing through the jet-ejector has been predicted with the one-dimensional theoretical model of Zegenhagen and Ziegler [117]. Their model (Equation 3.90) estimates the complex processes occurring inside a jet-ejector assuming steady-state isentropic flow with reals gas effects. Essentially, the set of equations accounts for the variations of the compressibility factor (Z) due to deviations from the ideal gas law. These effects cannot be neglected when the refrigerant operates at high pressure and temperature and have a remarkable impact on the mass flow rate predicted by the nozzle equation at the choked condition.

Equation 3.90 determines the mass flow rate at the choking condition introducing real gas effects.

$$\dot{m}_{pf} = \left(\frac{A_{thr,effective}}{A_{thr}} \right) \cdot A_{thr} \cdot \sqrt{\frac{\tilde{\kappa}_{pf}}{K_{pf} \cdot Z_{ref} \cdot R \cdot T_{pf}}} \cdot P_{pf} \cdot \left(\frac{2}{\tilde{\kappa}_{pf} + 1} \right)^{\left(\frac{\tilde{\kappa}_{pf}+1}{2 \cdot \left(\tilde{\kappa}_{pf}-1 \right)} \right)} \quad (3.90)$$

Where:

$$\tilde{\kappa} = \frac{c_{p,pf}/c_{v,pf}}{1 - K_p} \quad (3.91)$$

$$K_p = \left(\frac{\partial K}{\partial P} \cdot \frac{P}{K} \right)_T \quad (3.92)$$

$$Z_{ref} = Z \left(T = 298.15 \ K, P = 1 \ kPa \right) \quad (3.93)$$

Where, Z_{ref} is the compressibility factor at the reference thermodynamic conditions ($T = 298 \ K$) and ($P = 1 \ kPa$). The ideal gas law deviation coefficient (K_{pf}) is calculated assuming the thermodynamic conditions at the primary nozzle inlet. The thermodynamic properties of the gas have been obtained using the CoolProp database. The coefficient K_p has been calculated by solving the partial derivative numerically using Coolprop. For more details about the model, the reader should refer to the work of Zegenhagen and Ziegler [117]. The Equation 3.94 is extremely useful to size the jet-ejector with flexibility by manipulating the scaling factor λ (Equation 3.94).

$$\dot{m}_{pf} = \left(\frac{A_{thr,effective}}{A_{thr}} \right) \cdot \pi \cdot (R_{thr} \cdot \lambda)^2 \cdot \sqrt{\frac{\tilde{\kappa}_{pf}}{K_{pf} \cdot Z_{ref} \cdot R \cdot T_{pf}}} \cdot P_{pf} \cdot \left(\frac{2}{\tilde{\kappa}_{pf} + 1} \right)^{\left(\frac{\tilde{\kappa}_{pf}+1}{2 \cdot \left(\tilde{\kappa}_{pf}-1 \right)} \right)}$$

$$(3.94)$$

Table 3.6 validates the computational model comparing the values of mass flow rate predicted by the model with an experimental test campaign carried out by the same

authors. As can be observed, the model is an effective tool to predict the mass flow rate passing through the jet-ejector nozzle considering a refrigerant at high pressure and temperature. Lower and upper bounds are defined in the experimental data since there are several measurements for each operating point and some dispersion was reported. Experimental errors derived from the experimental campaign are not accounted for in the definition of the lower and upper bounds.

P_{pf} [bar]	ΔT [$^\circ C$] (superheating temperature)	Experimental $\dot{m}_{pf}$, lower bound [g/s]	Experimental $\dot{m}_{pf}$, upper bound [g/s]	Predicted $\dot{m}_{pf}$ with the model [g/s]
30	3.1	88.5	92.4	93.3
30	7.3	87.1	91.0	91.1
30	12.2	84.7	88.1	89.2
32	2.4	100.2	102.9	101.1
32	6.7	96.5	98.7	98.3
32	11.0	94.8	97.6	96.1
34	3.2	104.3	107.7	108.1
34	7.4	100.3	104.5	104.9
34	12.1	97.6	100.5	102.2

Table 3.6: *Mass flow rate passing through the jet-ejector primary nozzle using R134a as refrigerant (experimental vs predicted with the computational model). The experimental data comes from the research work of Zegenhagen and Ziegler [8]*

3.5.3 CFD model to determine the entrainment ratio (ω) implemented in a commercial code

Description of the computational mesh and mesh independence study

A quadrilateral structured mesh with wall refinement (see Figure 3.18) has been selected due to the prevalence of axial flow. Global skewness, orthogonal quality, and aspect ratio have been checked as quality indicators and fulfill comfortably with general recommendations. The number of cells of the computational domain is around 55,000 in all simulations with slight variations due to the different dimensions of each geometry in the parametric study. The influence of the number of elements is evaluated by comparing the Mach number along the jet-ejector axis and the entrainment ratio of three cases with different mesh refinement degrees (see Figure 3.17). There are small discrepancies in the position and magnitude of strong shockwaves, however, differences in entrainment ratio are lower than 1% with respect to the case with the highest number of cells.

The discrepancies found in Mach number distribution in some axial positions can be attributed to the strong gradients occurring due to the shockwave pattern. It is common in the literature to carry out a detailed mesh refinement in these particular zones to capture the shockwave structure. Such strategy has been avoided, giving priority to the computational economy due to the high number of simulations that
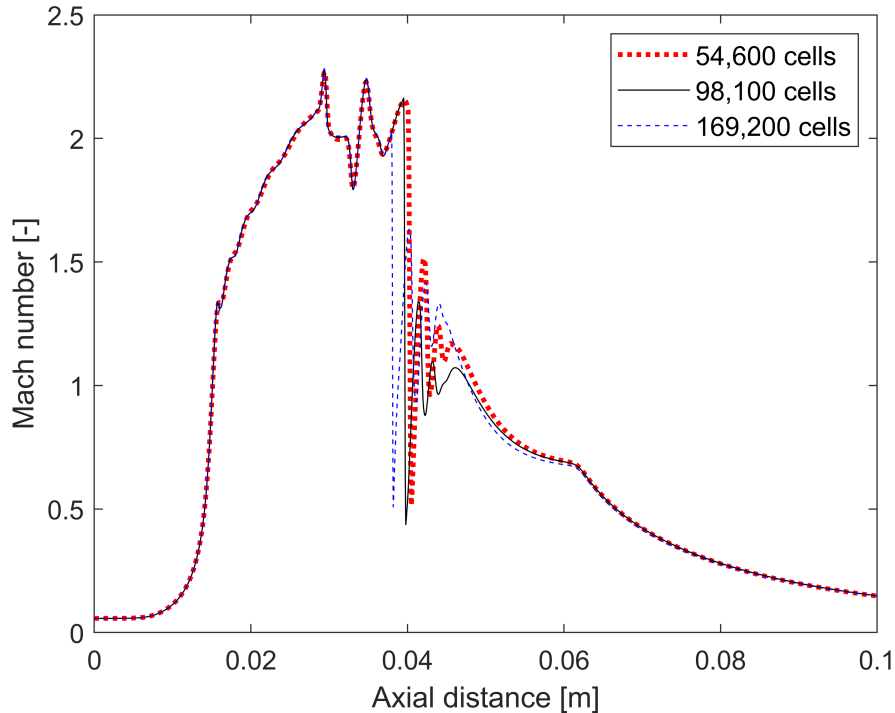
Figure 3.17: *Mach number distribution along the jet-ejector's axis of symmetry*

have been required to perform an exhaustive optimization of the jet-ejector internal geometry. These minor differences are considered admissible so the mesh with the lower number of elements (54,600) is selected according to the following criteria:

- The local flow phenomena occurring inside the jet-ejector (flow pattern) is described only from a qualitative point of view. Therefore, the main trends described on the flow pattern when the jet-ejector internal geometry is modified would remain valid, regardless of the slight discrepancies in the position and magnitude of strong shockwaves.

- The global performance of the jet-ejector is computed from a quantitative point of view by using the jet-ejector entrainment ratio. The validation process, as well as the low discrepancies between the three meshes under consideration (less than 1%), guarantee that this global parameter is estimated with precision.

CFD setup

The CFD setup covers the configuration of the computational models dedicated to solving the conservation equations in the computational domain. The main areas of the setup are summarized and presented in the following bullet points:

- **Working fluid model**

  The thermodynamic properties of R1234yf, R1234ze, and R600a stored at the CFD code, and based on the formulations of Richter et al. [118], McLinden et al.

[119] and Bücker et al. [120]. Real gas models have been considered instead of an ideal gas assumption since the absolute pressure inside the jet-ejector is assumed to be relatively high and, in this situation, the behavior of both models might not be similar [117]. The NIST libraries containing thermodynamic properties of the refrigerants are dynamically loaded into the solver when real gas models are activated. The fluid thermodynamic variables can be determined accurately in a pressure and temperature bounded range.

- **Numerical schemes**

The steady-state time-marching scheme implemented in the commercial code has been used in all the simulations. First-order upwind spatial discretization schemes for turbulence and conservation equations are used in the first instance and then switched to second-order schemes when stability is attained.

At the early stages of calculation, the SIMPLE pressure-velocity coupling scheme is considered and then switched to a Coupled scheme after reaching final boundary conditions and stabilization. Least Square Cell-Based is selected as gradient scheme and diffusion terms are discretized following a second-order central difference form. The pressure-based coupling model has been employed because current implementations of this approach have been reformulated in to work successfully with high Mach number compressible flow. Furthermore, satisfactory results implementing this approach when simulating the jet-ejector internal flow have been reported in the literature [121]. Density-based formulations have been also tested but offered poor performance in terms of stability.

- **Turbulence model**

The Reynolds Averaged Navier Stokes (RANS) approach has been employed in all simulations, and both the standard $k - \epsilon$ and SST $k - \omega$ have been utilized as the turbulence model. The SST $k - \omega$ turbulence model, which is very popular in literature when modeling supersonic flow inside jet-ejectors, has been used in most of the CFD studies [121, 122, 123]. It combines the strengths of the $k - \epsilon$ model while modeling free streams and the virtues of $k - \omega$ to approach wall-bounded problems. Despite the $k - \epsilon$ it is not the most recommended turbulence model while simulating supersonic flow in jet-ejectors, it has proved to do an accurate description of phenomena occurring inside the jet-ejector as well as accurate predictions of global flow parameters like entrainment ratio [124, 121, 125, 126]. The $k - \epsilon$ model has been used only to explore the sensitivity of the calculations to other turbulence models.

As will be discussed later in the validation subsection, the predictions of entrainment ratio have a similar degree of precision irrespective of the turbulence model used (Besagni et al., 2015; Croquer et al., 2016; Gagan et al., 2014; Hakkaki-Fard et al., 2015). The internal configuration of the turbulence model and the fitting parameters are the default provided by the code. No modifications have been made since the coefficients provide results adjusted to experimental data of other authors.

- **Monitors**

  Several calculation monitors have been created to register the evolution of default or predefined parameters as the simulation progresses. For each iteration, the monitors are printed in the record file together with the calculation residuals. The monitors play a key role while deciding if the case is converged or not. Besides the default residuals, the following monitors have been added:

  - Static pressure monitors in primary and secondary inlets as well as static pressure in the jet-ejector outlet.

  - Primary, secondary, and outlet mass flow rate monitors. Also, the net sum of the mass flow rates is calculated and registered.

- **Boundary conditions**

  Primary and secondary inlets are set to static pressure boundary conditions and the outlet zone of the jet-ejector is set to total pressure (see Figure 3.18). Total and static values in both inlets are supposed to be essentially the same because the inlet velocity is neglected as a common approximation [121]. Hence, the mass flow rates passing through the jet-ejector are a result of the pressure and temperature boundary conditions in the inlets and the outlet as well as its internal shape.

  Total temperature is also imposed on both inlets and it is equal to static temperature following the previous criteria. Some degree of gas superheating is specified in the temperature boundary condition to avoid the appearance of two-phase flow as the stream expands. To reduce the calculation time and to account for the 3D geometry domain, the axisymmetric condition is assigned at the jet-ejector mid-line. According to some authors [51], 3D effects in the flow can be neglected.

  The walls are defined as adiabatic, impermeable, and smooth surfaces in which the no-slip condition is satisfied. A schematic representation of the jet-ejector domain is represented in Figure 3.18. To sum up, the following boundary conditions are assigned in the CFD cases to solve the governing equations:

  - Domain with axisymmetry.

  - Two pressure inlet assignments (primary flow and secondary flow). Static pressure and static temperature are imposed in these pressure inlets.

  - One pressure outlet assignment (mixed flow).

  - Wall to bound fluid and solid regions.
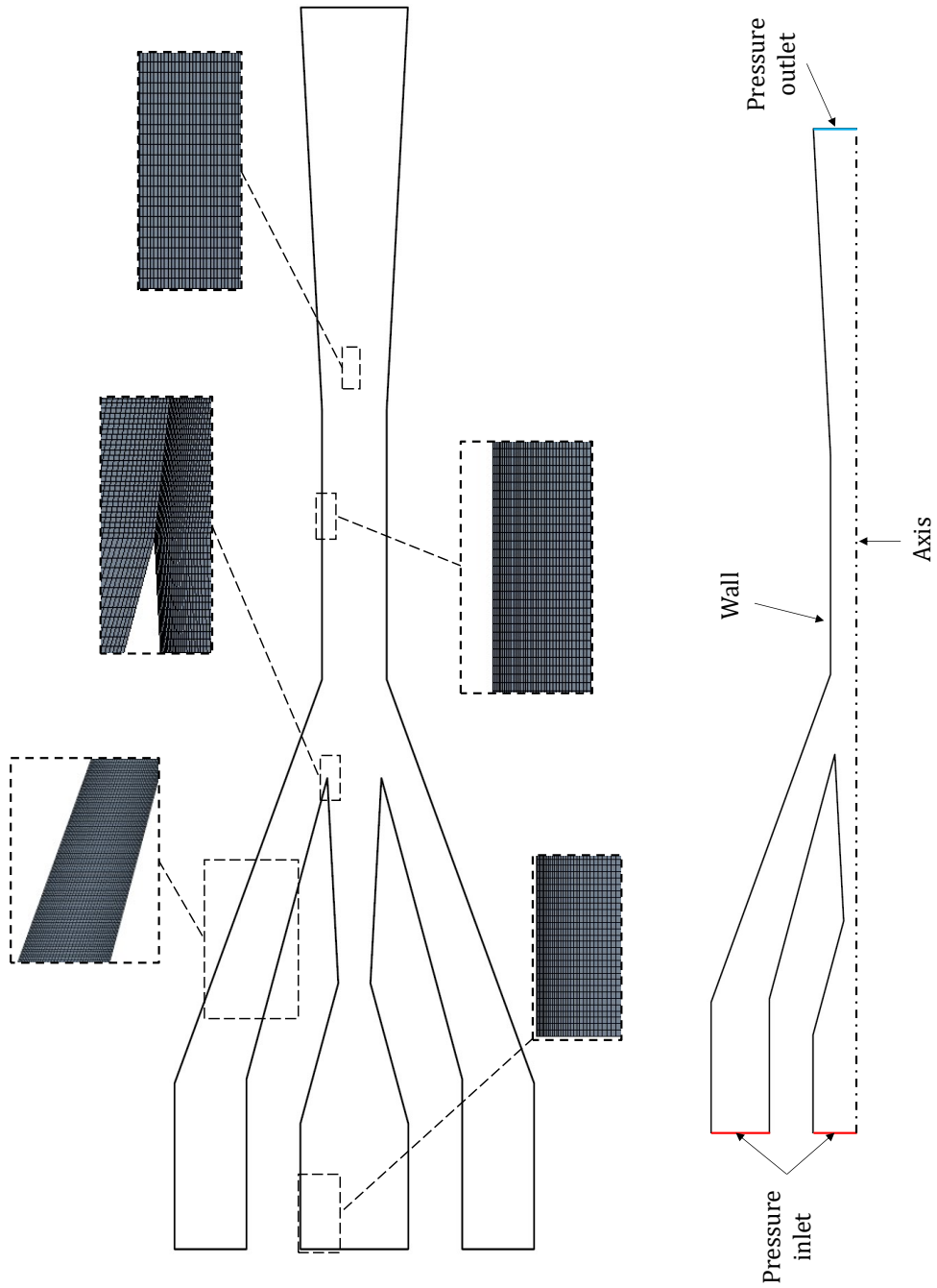
Figure 3.18: *Detailed view of the computational mesh and boundary condition categories*

Resolution and convergence criteria

Due to the NIST real gas model approach, the solution converges at a slower rate than those with ideal gas assumptions. The converging process of the calculation is also more unstable. The solution diverges if the flow properties exceed the bounded ranges even though the states are physically coherent. To avoid an aggressive convergence strategy, the boundary conditions are changed dynamically and the relaxation factors are manipulated as the calculation advances. Different transitions have been performed to progressively achieve the desired pressure boundary conditions in both inlets and the outlet. Gradual pressure increments in the primary inlet are the best strategy, especially in the early stages of calculation since the solution oscillates. Four criteria are examined to consider each case as converged:

- Inlet and outlet mass flow rates do not vary with iterations, i.e., values are constant.

- The balance between the inlet and outlet mass flow rates is at least three orders of magnitude lower than the minimum inlet mass flow.

- Calculation residuals are stable.

- Prescribed pressure and temperature boundary conditions do not vary with iterations.

The execution time to consider each computational simulation as converged is highly dependent on the flow regime inside the jet-ejector and, therefore, on the case boundary conditions. The number of iterations required to fulfill the above-listed requisites is around 20,000 in the double-choking operating mode but it is found to be higher in those cases operating in the single-choking operating mode due to the high sensitivity of entrainment ratio on the critical condensing temperature/pressure. The mass flow rate balance and the secondary mass flow rate stabilization are always the most limiting factors. As a general strategy, when there exists uncertainty about the jet-ejector operating mode in a particular simulation, more iterations than the hypothetically required for convergence are specified. As the time consumed per simulation is not excessive using a computing cluster, this conservative approach is feasible.

The computational simulations have been resolved in the computing cluster Rigel owned by Universitat Politècnica de València which has the CFD code installed and offers to the university research staff access to more than 72 high-performance computing nodes. The capacity of the cluster to launch simultaneously multiple CFD simulations if there are available computing nodes has been a fundamental aspect to resolve the high amount of simulations covered in this dissertation. The following list enumerates the steps required to generate and resolve a computational case from the case initialization to the simulation finally converged.

1. The case is first initialized in a local computer, setting up the turbulence model, the numerical schemes, the monitors, and the initial boundary conditions. Only a few iterations are executed to realize that there are no initial errors and the initialization is performed without incidences. Successively, the files .cas and

.dat, which collect all the information of the case (geometry, mesh, setup, and preliminary results), are generated.

2. The files .cas and .dat are uploaded to the computing cluster using the SSH file transfer protocol together with the journal files (.jou) and the script file (.sh). The journal file contains all the sequence of instructions that must be applied on the .dat and .cas files. The journal files are extremely useful as they permit the execution of multiple predefined operations automatically and sequentially, saving a lot of time for the user. Besides, it permits gradual changes in boundary conditions. Before each change, sufficient iterations for stabilization are performed, especially in the initial stages of calculation. This special treatment is fundamental to deal with convergence difficulties associated with the calculation with real gas libraries.

   The script file contains the request of computational resources (number of nodes demanded, maximum hours to perform the calculation...) and also the instructions to execute the CFD code and the case in the platform.

3. The simulation concludes following the prompts given in the .sh and .jou files and, as a result, output .cas and .dat files are generated. The entrainment ratio is calculated from the monitors of mass flow rate on each inlet.

4. The resulting files are downloaded to work with them locally. The residuals and monitor files contain the most relevant information about the course of the calculation (evolution of residuals and monitors) while the .cas and .dat files store the final results (calculated values and user-defined parameters on each cell of the computational domain).

Postprocessing and generation of FRS and ARS performance envelopes

The CFD postprocessing software capabilities have been used in a local computer to obtain Mach contours and the entrainment ratio. The entrainment ratio, which has been the main jet-ejector performance indicator, has been computed by dividing the mass flow rate monitors set in the secondary and primary inlets.

The CFD calculations are mainly dedicated to optimize the jet-ejector key internal dimensions and to characterize the jet-ejector response in off-design operating conditions. At the end of the optimization and characterization process, all the information has been collected on simple mathematical expressions (Equation 3.95 and 3.96) fitted to the maps presented in Figures 2.7, and 2.8.

$$\begin{cases} \omega_{FRS}\left(T_{co}\right) = \beta_{1,FRS} + \beta_{2,FRS} \cdot T_{co} + \beta_{3,FRS} \cdot T_{ev}, & \text{if } T_{co} \leq T_{co,crit} \\ \omega_{FRS}\left(T_{co}\right) = \beta_{4,FRS} + \beta_{5,FRS} \cdot T_{co} + \beta_{6,FRS} \cdot T_{ev}, & \text{if } T_{co} > T_{co,crit} \end{cases} \tag{3.95}$$

$$\omega_{ARS}\left(T_{co}\right) = \beta_{1,ARS} + \beta_{2,ARS} \cdot T_{co} \tag{3.96}$$

3.5.4 Experimental validation of the CFD setup

Double-choking operating mode

The CFD approach used in this study has been compared to experimental data available in the literature to guarantee that the present CFD model is predicting accurately the jet-ejector entrainment ratio, which is the key parameter in this investigation to model the jet-ejector performance. The experimental results under consideration are those reported by Hakkaki-Fard et al. [127, 125] and García del Valle et al. [65] (geometry "A") and their study comprises entrainment ratio determination for different jet-ejector geometries and operating conditions using R134a as working fluid.

In the former experimental study the generating pressure (P_{pf}) ranges between 29 bar ($T_{sat} = 84.6°C$) and 19.3 bar ($T_{sat} = 65.9°C$), the evaporating pressure (P_{sf}) ranges between 2.65 bar ($T_{sat} = -2.7°C$) and 4.15 bar ($T_{sat} = 10°C$) and the condensing pressure (P_{mf}) varies between 4.2 bar ($T_{sat} = 10.4°C$) and 8.4 bar ($T_{sat} = 33°C$). In the present validation process only the operating points in which the jet-ejector operates in the double-choking mode have been reproduced. In the latter experimental work the generating pressure (P_{pf}) ranges between 25.98 bar ($T_{sat} = 79.4°C$) and 31.9 bar ($T_{sat} = 89.1°C$), the evaporating pressure (P_{sf}) varies between 3.49 bar ($T_{sat} = 5°C$) and 4.15 bar ($T_{sat} = 10°C$), and the condensing pressure (P_{mf}) changes between 7.47 bar ($T_{sat} = 28.9°C$) and 8.97 bar ($T_{sat} = 35.4°C$). The evaporating and condensing temperatures of the refrigerants in both the experimental results (R134a) and the numerical approach of the present study (R1234yf, R1234ze, and R600a) lead to relatively high operating pressures. Therefore, the real gas effects considered in the CFD setup have special significance [117].

The maximum relative error in the entrainment ratio between the computational and the experimental results is not exceeding 9.3% considering the experimental data of Hakkaki-Fard et al., and 9.5% when compared with the results of García del Valle et al. (see Figure 3.19), if the SST $k - \omega$ turbulence model is used. The quality of the prediction is very similar when the $k - \epsilon$ turbulence model is used. Hence, the CFD method is providing reliable estimations of the jet-ejector entrainment ratio in the double-choking operating mode. The discrepancies between the computational simulations and the experimental results are in the range of deviation commonly reported in other research works [128, 121, 47].

Single-choking operating mode

Typically, the CFD models simulating the transition between the jet-ejector double-choking and single-choking operating modes tend to overestimate the critical condensing pressure/temperature. The discrepancies between the computational calculations and the experimental data are normally attributed to the surface roughness of the jet-ejector inner walls [123] and this parameter depends to a large extent on the manufacturing process and technique. The experimental results reported by Shestopalov et al. [129] have been considered to quantify the overestimation induced when the current smooth-surface approach is adopted. The results collected in Table 3.7 demonstrate that the error committed is notoriously diminished when a surface roughness
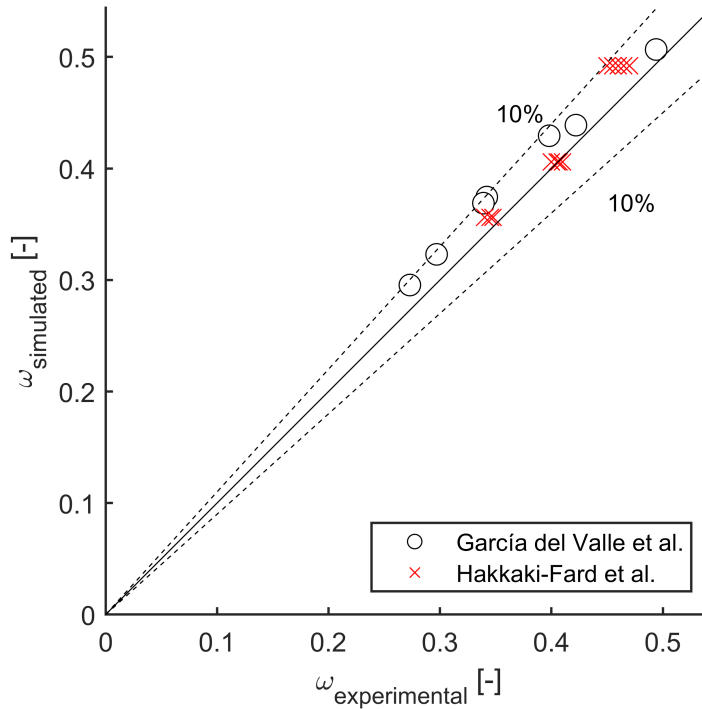
Figure 3.19: *Experimental values of entrainment ratio (ω) vs entrainment ratio predicted with the present CFD approach for the model SST $k - \omega$*

$\epsilon = 10\,\mu m$ is considered in the CFD models. It must be outlined that the difference between the simulated and the computational results is approximately zero in Table 3.7 when $\epsilon = 10\,\mu m$.

Hence, the smooth-surface approach represents a reliable approximation and the discrepancies can be explained by introducing a relatively small artificial surface roughness. The negative effect of the surface finishing could be mitigated by improving the manufacturing process but the CFD code represents a good approximation to reflect the FJE and the AJE performance in the single-choking operating mode. In the end, the CFD results with perfect surface finishing hypothesis and the experimental results would tend to overlap as the manufacturing technique is improved.

Table 3.7 also proves that the aforementioned conclusions are not altered when the computational mesh is further refined.

3.5.5 CFD model to determine the entrainment ratio (ω) implemented in OpenFoam

The jet-ejector CFD simulations necessary to determine the jet-ejector entrainment ratio have also been successfully implemented using the open-source code OpenFoam. The implementation and simulation of the cases in OpenFoam have a strategic interest for a multitude of research centers and organizations because it is free and has an extensive range of customization features.

T_{ev} [°C]	Number of elements in the computational mesh	$\Delta T_{co,crit}$ ($\epsilon = 10\mu m$)	$\Delta T_{co,crit}$ ($\epsilon = 0\mu m$)
8	62,500 (reference mesh)	0	0.64
	110,300 (refined mesh)	0	0.64
12	62,500 (reference mesh)	0	0.55
	110,300 (refined mesh)	0	0.55
16	62,500 (reference mesh)	0	0.5
	110,300 (refined mesh)	0	0.5

Table 3.7: *Discrepancies in critical condensing temperature using R245fa as working fluid. $\Delta T_{co,crit}$ refers to the difference between the corresponding case with surface roughness and the experimental results, which have an unknown surface finishing*

The validity of the simulation has been checked reproducing the jet-ejector simulated and tested experimentally by Hakkaki-Fard et al. [127, 125] working with R134a. The "Ejector I" of their experimental campaign operating with $P_{ge} = 29$ bar, $P_{co} = 2.65$ bar and $P_{ev} = 2.65$ bar is the one reproduced using OpenFoam. The setup listed below captures accurately the jet-ejector physics since the entrainment ratio of the simulated jet-ejector ($\omega = 0.42$) is very close to the one reported from experimental tests ($\omega = 0.41$). The jet-ejector contour and its boundaries (zones) have been defined directly with blockMeshDict utility and the mesh has been generated with blockMesh tool. The following list summarizes some key aspects of the simulation:

- An axisymmetric domain has been considered.

- The turbulent transient solver rhoPimpleFoam has been employed. According to the OpenFoam user guide, it is indicated for heat, ventilation, and air-conditioning applications with compressible flow.

- First order upwind discretization schemes to gain stability have been set during preliminary stages of calculation and then are switched to second-order schemes to improve the precision of the results once the preliminary solution is converged.

- The mesh has been created without taking care of wall refinement so wall functions have been used to model near-wall region.

- The simulation time step is limited by the Courant-Friedrichs-Levy (CFL) number. Due to the high velocity of the flow, working with a fixed time step might soar the CFL number. The CFL has been maintained below 10 during the first stage of the convergence process and then switched to 5.

- The mass flow rates in both inlets and the outlet have been the main convergence indicators.

- The calculations have been launched in parallel in a local computer calling the decomposeParDict utility, which contributes to saving significant computing costs.

Since this suite does not have libraries or databases containing the real thermodynamic conditions of the refrigerants, the Peng-Robinson equation of state particularized for the thermodynamic properties of the refrigerant under investigation for the validation process (R134a) has been selected instead. This real gas approximation is also common in the literature and has demonstrated to provide reliable results [123].

3.6 Heat exchange correlations

3.6.1 Justification

This section presents heat exchange correlations that will be used to size the heat exchangers of the refrigeration system. Subsequently, the size of the elements will be translated to monetary cost. This is an essential part of the methodology followed to determine the CAPEX (Capital Expenditures) and the OPEX (Operating Expenses).

The OPEX and CAPEX estimation methodology will be applied for (i) the solar driven system proposed in the present research and (ii) the technical solution that is currently consolidated in the market, that is, a conventional vapor-compression refrigeration system. The CAPEX frequently accounts for the investment in equipment, manufacturing costs, and installation costs, while the OPEX accounts for costs associated with the system operation like the electricity costs. The study goes through three fundamental stages or actions:

1. **To determine the reference operating conditions.** The definition of reference conditions will serve to fix the reference power consumed by the pump, the heat power transferred in the heat exchangers, the mass flow rate passing through the two loops of the refrigeration system, or the PTC collecting area. These conditions are susceptible to change during a standard operation, however, the definition of reference representative operating conditions is a good basis.

2. **To correlate the system operating conditions with equipment sizing.** In the case of heat exchangers, the definition of reference operating conditions would allow estimating an internal heat exchange area, which in the end is a better indicator of cost and size. The same rationale has been applied to estimate the sizing of the other components: their operating conditions and the refrigerating needs have been correlated with experimentally-based or theoretically-based correlations to predict the scale of the components. Before estimating the monetary cost, this analysis is essential. This correlations used in this analysis are introduced in subsection 3.6.2.

3. **To translate the equipment selection and sizing to monetary cost.** This can be done by selecting commercial equipment which cost is representative and known or by using generalized correlations. The former approach has only been considered acceptable when the diversity and commercial availability of the equip-

ment is reduced. This is the case, for instance, of the PTC collector owing to the reduced number of manufacturers and open data. For the rest of the elements, priority has been given to the use of general scope models. This analysis is introduced in Section 3.7.

3.6.2 Definition of mathematical expressions

The heat power exchanged in the generator, the condenser, or the evaporator can be estimated as expressed in Equation 3.97.

$$\dot{Q} = A \cdot U \cdot \Delta T_{LMTD} \tag{3.97}$$

Where ΔT_{LMTD} is the logarithmic mean temperature difference.

The area of each heat exchanger subzone (A_{Z_i}) defined in Section 3.4 could be estimated by discretizing Equation 3.97 in different subzones, as expressed in Equation 3.98. Then, the total area of the heat exchanger would be calculated as the summation of all the subzones ($A = \sum A_{Z_i}$)

$$\dot{Q}_{Z_i} = A_{Z_i} \cdot U_{Z_i} \cdot \Delta T_{LMTD,Z_i} \tag{3.98}$$

The overall heat transfer coefficient (U) for the constructive characteristics of a Plate Heat Exchanger (PHE) is defined as expressed in Equation 3.99.

$$U = \frac{1}{\frac{1}{h_{HTF/w/rl}} + \frac{1}{h_{rf}} + \frac{\epsilon}{k_{PHE}}} \tag{3.99}$$

Figure 3.20 represents schematically the internal layout of the PHE layers. In the Layer 1 the convective heat transfer is the dominating phenomenon. The convective heat transfer coefficient $\left(h_{HTF/w/rl}\right)$ will be defined later as a function of the refrigerant heat exchange process (evaporation, condensation, single-phase heating or cooling, or supercritical heating). In Layer 2 the heat is transferred by conduction. In Layer 3, heat is transferred by convection and the heat transfer coefficient is calculated as a function of the fluid nature (thermal oil, water, or air) using a single-phase correlation.

The convective heat transfer coefficient can be calculated as:

$$h = h\left(Nu, k, D\right) \tag{3.100}$$

Where,

$$Nu = Nu\left(Re, Pr\right) \tag{3.101}$$

Layer 1→Refrigerant h_{rf}

Layer 2→ Metal sheet k_{PHE}

Layer 3→Thermal oil (HTF), $h_{HTF/w/rl}$
heat dissipation medium
(water), or indoor air with
refrigeration needs (rl)

PHE Control Volume
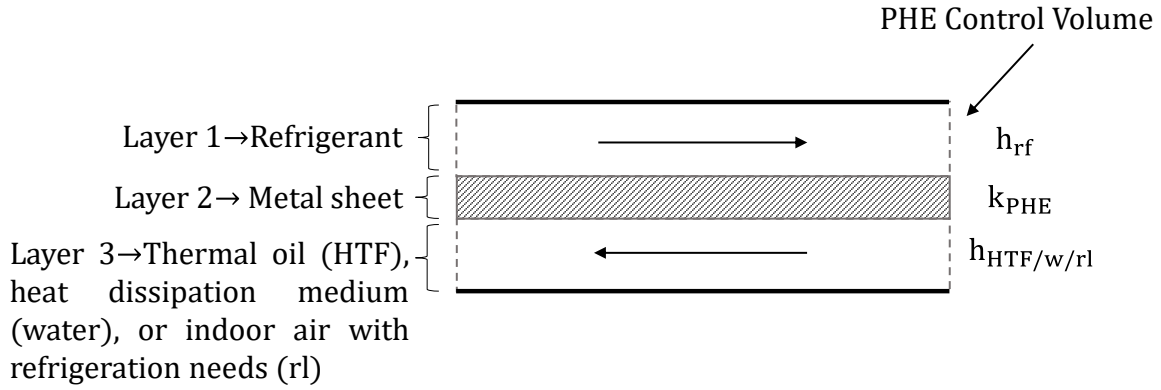
Figure 3.20: *Internal cavity of a counterflow PHE*

$$Re = \frac{G \cdot D_h}{\mu} \to G = \frac{\dot{m}}{n_{ch} \cdot W_{PHE} \cdot b} \tag{3.102}$$

$$Pr = \frac{c_p \cdot \mu}{k} \tag{3.103}$$

$$D_h = 2 \cdot b \tag{3.104}$$

In the previous expressions, n_{ch} is the number of channels of the PHE and b is the width of the corrugation in the PHE sheets. The thermal properties of the the refrigerant have been obtained using CoolProp database, the thermal properties of the thermal oil come from the correlations collected by Fasquelle et al. [105] and are calculated as a function of the temperature and pressure: $\mu = \mu(P,T)$, $k = k(P,T)$ and $c_p = c_p(P,T)$. The terms Re and Nu are the Reynolds and Nusselt numbers, respectively.

1. For single phase heat exchange process the correlation of Chisholm and Wanniarachchi has been used [130]:

$$Nu = 0.724 \cdot \left(\frac{6 \cdot \beta}{\pi}\right) \cdot Re^{0.583} \cdot Pr^{1/3} \tag{3.105}$$

Where $\beta = \pi/3$ is the chevron angle of the PHE.

2. The convective heat transfer coefficient for condensation has been predicted using the correlation proposed by Yan et al. [131, 132]. According to their study, it has validity for R1234yf, among other refrigerants:

$$h_{co} = 4.118 \cdot \frac{k_l}{D_h} \cdot Re_{eq}^{0.4} \cdot Pr_l^{1/3} \tag{3.106}$$

Where,

$$Re_{eq} = \frac{G_{eq} \cdot D_h}{\mu_l} \rightarrow G_{eq} = G \cdot \left[(1 - x_m) + x_m \cdot \left(\frac{\rho_l}{\rho_g} \right)^{1/2} \right] \tag{3.107}$$

$$Pr_l = \frac{c_{p,l} \cdot \mu_l}{k_l} \tag{3.108}$$

Where x_m corresponds with the mean vapor quality during the condensation process, and the subindices "l" and "g" denote the liquid and gas properties, respectively.

3. The convective heat transfer coefficient for evaporation in subcritical conditions has been estimated using the correlation proposed by Kim et al. [133, 132]. It has been used in the literature for different refrigerants including R1234yf:

$$h_{ev} = 5.323 \cdot \frac{k_l}{D_h} \cdot Re_{eq}^{0.42} \cdot Pr^{1/3} \tag{3.109}$$

4. The convective heat transfer coefficient for a heating process in supercritical conditions has been calculated using the correlation proposed by Forooghi and Hooman [134].

$$Nu = 0.187 \cdot Re^{0.71} \cdot Pr^{0.35} \cdot \left(\frac{\tilde{c}_p}{c_{p,bulk}} \right)^{0.5} \cdot \left(\frac{\rho_{wall}}{\rho_{bulk}} \right)^{0.3} \tag{3.110}$$

$$\tilde{c}_p = \frac{\int_{T_{wall}}^{T_{bulk}} c_p \cdot dT}{T_{bulk} - T_{wall}} \tag{3.111}$$

3.7 Monetary cost correlations

3.7.1 Jet-ejector refrigeration system

Equation 3.112 links the cost of the generator, condenser and evaporator with their internal heat exchange area [135, 136]:

$$C_{hx} \, [\text{\texteuro}] = 190 + 310 \cdot A_{hx} \tag{3.112}$$

Where, the area of the heat exchanger (A_{hx}) is expressed in $[m^2]$. The correlation cost of the heat exchangers shows good agreement with the expressions reported in other bibliographical sources [137].

Equation 3.113 links the cost of the pressure pump with its mechanical power consumption [135], where the pump power consumption $\left(\dot{W}_{pm} \right)$ is expressed in $[W]$:

$$C_{pm} \, [\text{\euro}] = 500 \cdot \left(\frac{\dot{W}_{pm}}{300} \right)^{0.25} \tag{3.113}$$

As mentioned in the literature, the cost of the expansion valve is usually neglected in thermoeconomic analysis because it is far lower in comparison with the rest of the elements [138].

There is more uncertainty about the cost of the jet-ejector because this is a component frequently designed ad hoc for the characteristic operating conditions of each application and the jet-ejectors commercially available do not fit with the present application. Despite these difficulties to find precise estimations, some authors propose indicative correlations [139, 140, 141]. The proposed correlations have been used to estimate the jet-ejector cost. The CEPCI cost index correction is included to update the component cost according to the present inflation.

$$C_e \, [\text{\euro}] = 15962 \cdot \dot{m}_{pf} \cdot \left(\frac{T_{pf}}{\frac{P_{pf}}{10^6}} \right)^{0.05} \cdot \left(\frac{P_{mf}}{10^6} \right)^{-0.75} \cdot \frac{558.3}{585.7} \cdot \frac{0.83\text{\euro}}{1\$} \tag{3.114}$$

To simplify the analysis and reduce the uncertainty degree, the cost of the control system and the labor cost do not participate in the comparison between refrigeration systems. Also, it is worth mentioning that the jet-ejector refrigeration system is likely to have an even higher CAPEX because the two loops of the system would require more piping length and, therefore, more refrigerant charge. A reliable estimation would require a complete definition of the installation. Anyway, the monetary cost associated to the piping and refrigerant charge would be very low when compared to the most expensive elements (solar collector and thermal storage system). The inclusion of this cost would not change the main conclusions of the thermoeconomic study.

3.7.2 Solar collector

Price disparities in the solar collector module have been found in the open scientific literature due to the scarce amount of devices commercially available. Cabrera et al. [7] collected cost, performance, and constructive characteristics of different thermal collector technologies including PTCs. They found that an investment costs of $310 \, \text{\euro}/m^2$, $190 \, \text{\euro}/m^2$, and $440 \, \text{\euro}/m^2$ for three different products. More recently, the National Renewable Energy Laboratory (NREL) updated the baseline cost of a PTC according to recent technological developments [142]. The aim was to provide a guide for designers of solar concentrating power technologies. They found that the SkyTrough model has an estimated installed cost of $170 \, \$/m^2$ while the Ultimate Trough model shows an estimated installed cost of $178 \, \$/m^2$. Though, they pointed out that the material costs are very sensitive to the fluctuations in the commodities market.

Supposing an optimistic scenario, Equation 3.115 would be a good predictor of the current cost of a PTC module:

$$C_{col}\,[\text{€}] = 170 \cdot A_{col} \cdot \frac{0.83\text{€}}{1\$} = 141 \cdot A_{col} \tag{3.115}$$

3.7.3 Thermal storage system

The cost prediction of the hot thermal storage tank has a degree of uncertainty considerable. Sarbu and Sebarchievici [97] pointed out that a cost ranging between $0.1 - 10\,\text{€}/kWh$ can be expected for sensible heat storage systems. Rodríguez-Hidalgo et al. [108] surveyed different sensible thermal storage units dedicated to indoor space heating using domestic solar collectors. According to their study, the tank volume and the material from which the tank structure is made determines its price. If priority is given to the most economic solution, a vitrified steel tank should be selected. Equation 3.116 correlates the cost of this constructive solution with its internal volume:

$$C_{TSS}\,[\text{€}] = 1000 \cdot 3.4586 \cdot V_{TSS}^{0.6589} \tag{3.116}$$

3.7.4 Vapor-compression refrigeration system

The cost of a conventional vapor-compression refrigeration system has been considered to establish a cost comparison between this consolidated solution and the novel solar driven alternative. The cost correlations of the heat exchangers of the conventional vapor-compression refrigeration system are those presented for the JERS. However, it might be differences in the size of the elements and it might affect its final pricing. The cost of the compressor has been estimated with a widely used literature correlation [140, 139, 143] (Equation 3.117). The CEPCI cost index correction is included to update the component cost.

$$C_{comp}\,[\text{€}] = \frac{573 \cdot \dot{m}_{rf}}{0.9 - \frac{\eta_{comp,s}}{100}} \cdot \left(\frac{P_{co}}{P_{ev}}\right) \cdot ln\left(\frac{P_{co}}{P_{ev}}\right) \cdot \frac{558.3}{585.7} \cdot \frac{0.83\text{€}}{1\$} \tag{3.117}$$

3.8 Integration of the numerical models for the steady-state approach

The JERS governing equations are fed with the jet-ejector entrainment ratio maps coming from CFD simulations and are subsequently solved to maximize the power efficiency transformation from thermal energy to refrigeration capacity (COP_{th}). The equations modeling the operation of each element are sequentially solved as depicted in the flowchart of Figure 3.21. The model of the JERS is based on the conservation of mass and energy in each element. The main assumptions, constraints, and objectives are listed below:

- The primary and secondary flow expansion processes have been modeled assuming a constant isentropic efficiency, which is a frequent approximation in the
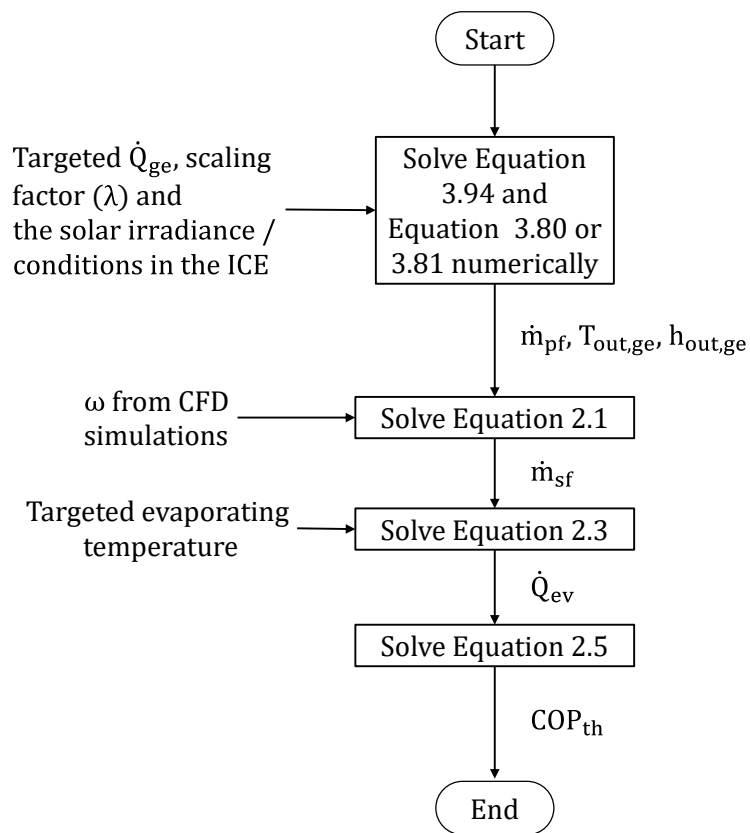
Figure 3.21: *Resolution sequence of the JERS equations*

literature [144]. The rough calculation of the primary and secondary flow expansions is helpful to estimate if a two-phase flow appears.

- A single-phase hypothesis has been adopted. This means that saturated vapor and superheated gas are considered as the only valid states in the jet-ejector inlets while saturated liquid or subcooled liquid are the only admissible states at the condenser outlet. Two-phase flow is physically valid but the jet-ejector models do not tolerate such circumstances and any prediction would not be rigorous.

- The jet-ejector is considered as adiabatic and its outlet temperature is calculated with the energy conservation expression (Equation 3.118).

$$h_{out,ge} \cdot \dot{m}_{pf} + h_{out,ev} \cdot \dot{m}_{sf} = (\dot{m}_{sf} + \dot{m}_{pf}) \cdot h_{in,co} \tag{3.118}$$

The jet-ejector model, the solar collector steady model, and the refrigeration system model are assembled as shown in Figure 3.22.
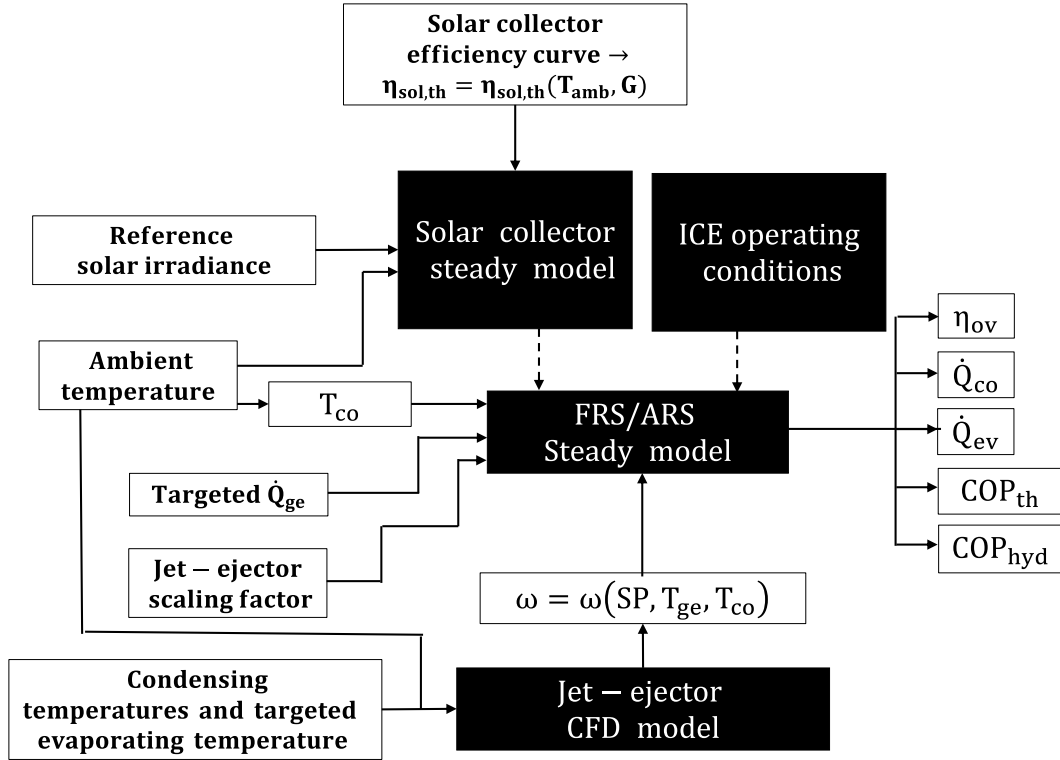
Figure 3.22: *Interaction between all the models devoted to characterizing the refrigeration system steady-state response*

3.9 Integration of the numerical models for the transient approach

The numerical models for the dynamic approach only affect the solar application. The models are linked together and interact as depicted in Figure 3.23. On the solar field

side, the PTC is constantly recirculating thermal oil from the storage tank depending on the instantaneous solar irradiance. The mass flow rate circulating through the PTC corresponds to its nominal value ($\dot{m} = 3\,kg/s$) if the solar irradiance is greater than zero. In the absence of solar irradiance, the mass flow rate passing through the PTC is 50% of its nominal value if the hour under consideration is within the time-span 05:00-20:00 (this criterion assumes a temporary presence of clouds) and 10% of the nominal value otherwise (night period).

A simple control algorithm has been implemented to activate/deactivate the FRS/ARS depending on several variables being monitored instantaneously. Fundamentally, the refrigeration system is intended to be active every day in the period comprising 08:00 to 19:00 if the ambient temperature is above 25 °C. This threshold temperature represents a simplification in the model; in a real indoor space there might exist refrigeration needs even if ambient temperature is below 25 °C owing to the solar gains. If the PTC receives solar irradiance out of this time span, as normally happens in the morning early hours, the resulting thermal power is dedicated to heating the TSS. Based on a pinch point analysis in the generator, the refrigeration system is switched on only if the temperature inside the TSS is above 120 °C. If the temperature of the TSS drops below the prescribed threshold during operation, the refrigeration system switches off automatically to restore the minimum thermal level. On the contrary, if the TSS temperature exceeds 300 °C the PTC is automatically defocused to avoid thermal degradation of the HTF.

The resulting set of partial differential equations is discretized in nodes and resolved following an explicit scheme for the time discretization, a second-order central differencing scheme for the second-order derivative terms, and a backwards differencing scheme for the first-order derivative terms. The time step has been reduced to $\Delta t = 1s$ to guarantee numerical stability. It is assumed that the start-up of the thermally driven refrigeration system occurs on the first day of each month at 00:00 and the initial temperature of all the components corresponds to the ambient temperature. Starting from this initial condition, the temperature evolution in each node of the PTC and the TSS is sequentially solved. The unknown nodal temperatures for the new time step are computed exclusively based on the nodal temperatures resolved in the preceding time step. The computational model that predicts the dynamic behavior of the refrigeration system has been programmed using Matlab®software.

3.10   Summary

The present chapter describes the computational models dedicated to predicting the refrigeration system performance.

The explanation starts elaborating on the steady-state and the transient models of the solar collector and the transient model of the thermal energy storage system. The key insights are provided about the solar collector model validation with experimental data.

Thereafter, the efforts are focused on describing the whole refrigeration system
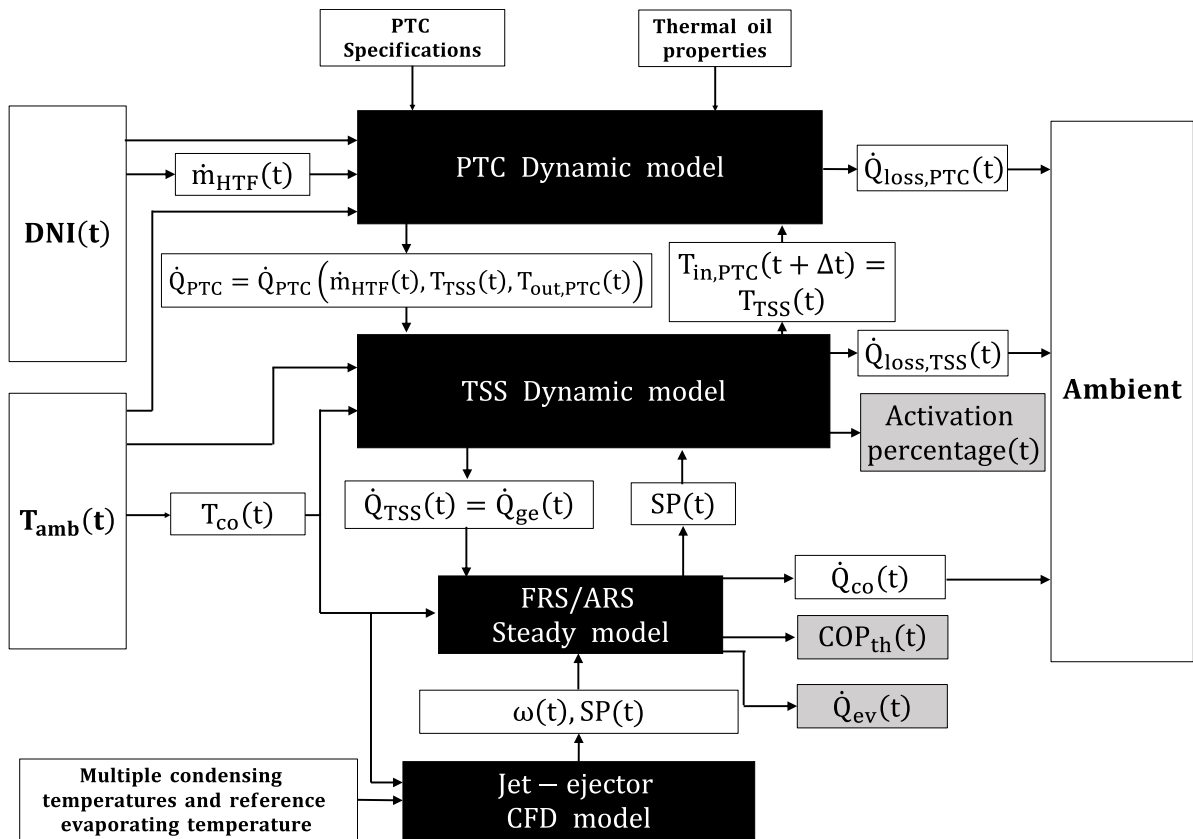
Figure 3.23: *Interaction between all the models devoted to characterizing the refrigeration system dynamic response*

excluding the jet-ejector. These are based on general and simple principles of energy and mass conservation. Subsequently, the jet ejector modeling approach and validation are presented. The jet-ejector is the key element of the system and its CFD calculation requires special dedication due to the complexity of the setup, the resolution strategy, and the convergence process of the solution.

Then, two sections are dedicated to explaining how the steady-state and transient models interact, exchange information, and are solved sequentially.

Finally, heat transfer correlations, which are the basis to size the system for a given refrigeration capacity or rated thermal energy consumption, are enumerated. The heat transfer correlations have been directly linked with the size of the elements and economic cost correlations. The aim is to estimate the budget of a jet-ejector refrigeration system and the budget of a vapor-compression refrigeration system, that is, the refrigeration solution widely adopted nowadays.

Part I

Steady-state evaluation of the refrigeration system

Chapter 4

Steady-state characterization of the fixed-geometry jet-ejector (FJE)

4.1 Introduction

The present chapter is devoted to showing the results of the Fixed-Geometry Jet-Ejector (FJE) internal shape optimization for different ecological and new generation refrigerants. In combination with geometrical parameters, the jet ejector primary flow pressure, which depends on the thermal level of the hot energy source, has been also optimized with an entrainment ratio maximization criteria. As long as the pinch point in the heat exchanger is satisfied the designer has room for selecting the generating pressure/temperature.

The sensitivity study of key jet-ejector dimensions and entrainment ratio maximization has been helpful to select the most appropriate working fluid option and internal shape from the perspective of the jet-ejector itself.

It must be highlighted that the jet-ejector optimization process and working fluid selection yield conclusions and optimized models that could be transferred to both the automotive and solar applications since the operating conditions considered to do the optimization process are compatible.

4.2 Working fluid selection and optimum design for the FJE

4.2.1 Definition of the study

The jet-ejector area ratio has proven to be one of the most sensitive parameters on jet-ejector performance and its influence over the mixing process has been widely studied in the literature [145, 115]. For this reason, it has been treated as a design variable. Additionally, the nozzle exit area determines the expansion level of the primary flow, i.e., the thermodynamic conditions of the primary flow leaving the nozzle. The in-

fluence of this design parameter over the jet-ejector internal phenomena has proven
to be decisive [46] so it has been considered as the second geometric variable under
investigation. The nozzle exit position, designated as $L_{e,1}$ in Figure 3.15, or NXP in
the literature, is also crucial in the jet-ejector operation [146] and it must be opti-
mized together with the primary nozzle exit diameter and mixing chamber diameter to
maximize the jet-ejector performance. It must be noted that for a fixed nozzle throat
diameter, the mixing chamber diameter, the primary nozzle exit diameter, and the
nozzle exit position govern primary flow expansion as well as the suction and mixing
processes of the secondary flow.

In Table 4.1 the geometric variables subject to optimization are labeled as "Vari-
able" while the dimensions labeled as "Constant" are not altered during the optimiza-
tion process. The same geometric dimensions can be identified visually in Figure 3.15.
In regard to the geometric parameters labeled as "Constant", the diverging angle in the
supersonic primary nozzle ($\alpha_{e,3}$) and the diverging angle in the diffuser section ($\alpha_{e,1}$)
are reduced to avoid flow detachment. Moreover, the mixing chamber length ($L_{e,2}$)
and the diffuser length ($L_{e,3}$) guarantee uniform flow fields across the radial direction.
These values are coherent when compared to other research works [129, 65, 69].

Dimension		Value	Dimension		Value
$D_{e,1}[mm]$	Variable	-	$L_{e,3}[mm]$	Constant	45
$D_{e,2}[mm]$	Variable	-	$L_{e,4}[mm]$	Constant	7
$D_{e,3}[mm]$	Variable	1.8 (reference)	$\alpha_{e,1}\,[°]$	Constant	6
$D_{e,4}[mm]$	Constant	6	$\alpha_{e,2}\,[°]$	Constant	40
$L_{e,1}[mm]$	Variable	-	$\alpha_{e,3}\,[°]$	Constant	6
$L_{e,2}[mm]$	Constant	30	$\alpha_{e,4}\,[°]$	Constant	30

Table 4.1: *Main jet-ejector internal dimensions*

The following list describes in detail how each geometric dimension is optimized.

- $D_{e,1}$: Optimized in a factorial study together with $D_{e,2}$.

- $D_{e,2}$: Optimized in a factorial study together with $D_{e,1}$.

- $L_{e,1}$: Optimized after the factorial study involving $D_{e,1}$ and $D_{e,2}$ is concluded.
  The findings of this optimization process are assumed to remain the same in-
  dependently of the primary flow pressure in the jet-ejector. The rationale of
  this decision is that the $L_{e,1}$ is less decisive in jet-ejector performance than $D_{e,1}$
  and $D_{e,2}$. Furthermore, reducing the number of simulations is essential for an
  affordable computing cost.

- $D_{e,3}$: The jet-ejector nozzle throat diameter does not form part of the CFD opti-
  mization study but it is adjusted and optimized conveniently by using the already
  introduced scaling factor (λ). Indeed, the scaling factor also scales proportionally
  the rest of the jet-ejector dimensions.

Besides, the primary flow pressure (P_{pf}) is also introduced in the study. When the hot source is at a sufficient thermal level and the pinch point is not a limiting factor, the JERS can operate with multiple primary flow pressures. The most convenient selection for the reference primary flow pressure is a priori unknown. For this reason, it has also been introduced in the optimization process. The flowchart of Figure 4.1 shows the optimization algorithm sequentially solved. The condensing temperature and the evaporating temperature have been set equal to the reference values, that is, $40°C$ and $13°C$, respectively.

More than 330 simulations including changes in geometry and primary flow pressure have been conducted to complete the analysis.

4.2.2   Results

Figure 4.2 illustrates the optimum entrainment ratio ω_{ope} found in a cross parametric study involving the primary nozzle exit diameter ($D_{e,1}$), the mixing area diameter ($D_{e,2}$) and the primary flow pressure P_{pf}. The optimum entrainment ratio values for R1234yf, R1234ze and R600a are found for a primary pressure of 35.14 bar, 33.35 bar and 31.29 bar, respectively. Table 4.2 shows the optimum value of the key dimension for each refrigerant at its optimum primary pressure.

R1234yf	
Dimension	**Optimum value**
$D_{e,1}[mm]$	2.6
$D_{e,2}[mm]$	4.4
$D_{e,3}[mm]$	1.8 (reference)
$L_{e,1}[mm]$	3.5
R1234ze	
Dimension	**Optimum value**
$D_{e,1}[mm]$	3
$D_{e,2}[mm]$	4.9
$D_{e,3}[mm]$	1.8 (reference)
$L_{e,1}[mm]$	3.5
R600a	
Dimension	**Optimum value**
$D_{e,1}[mm]$	3.4
$D_{e,2}[mm]$	5.7
$D_{e,3}[mm]$	1.8 (reference)
$L_{e,1}[mm]$	3.5

Table 4.2: *Optimum values of the jet-ejector key dimensions*
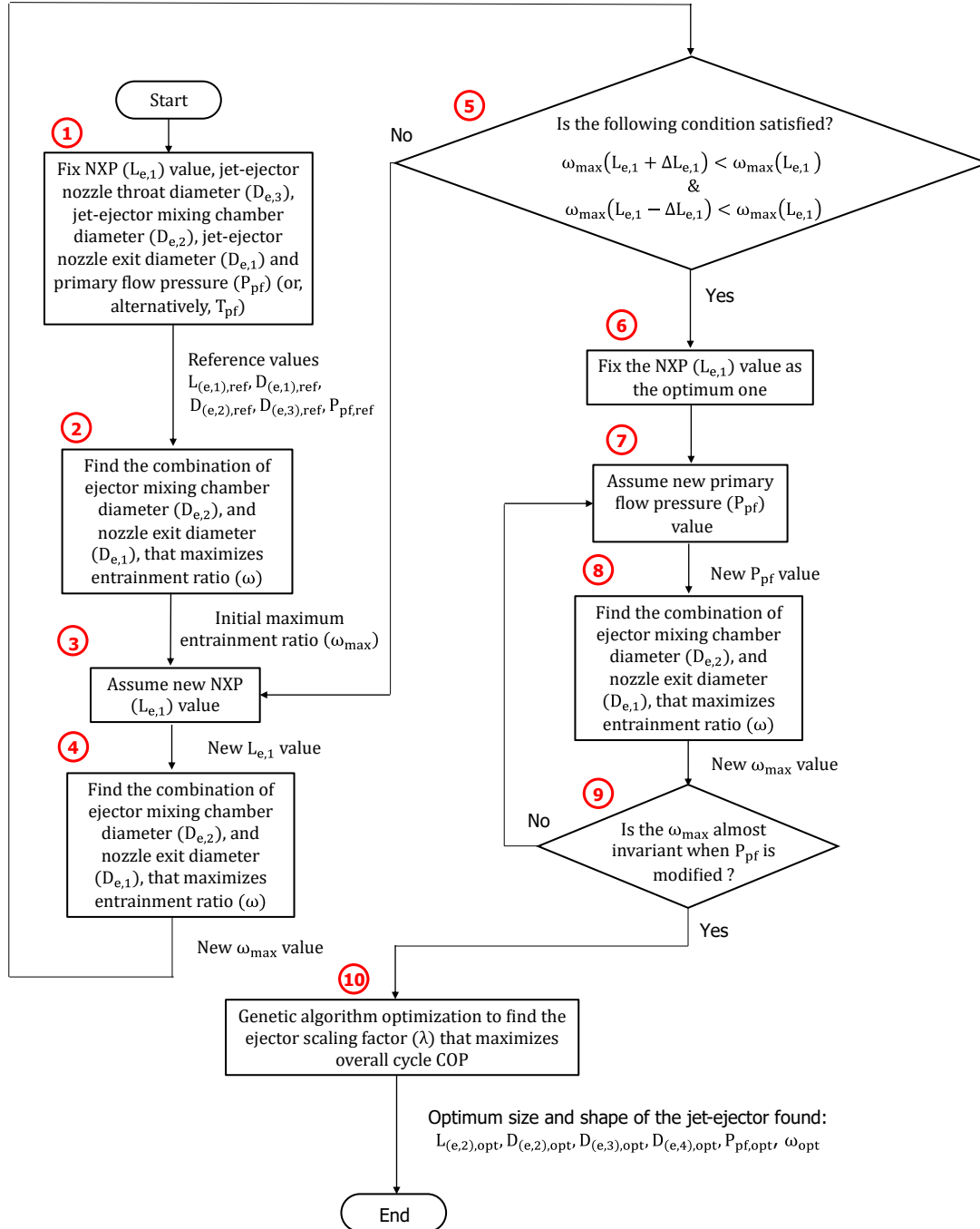
Figure 4.1: *Flow diagram followed to optimize the jet-ejector internal dimensions*

In Figure 4.2 only the nearest values to the optimum are shown. As can be observed, the entrainment ratio is highly sensitive on its key dimensions, an aspect that evidences the importance of a precise manufacturing process and a fine surface finishing. Another important fact is that optimum jet-ejector entrainment ratio for the three refrigerants under evaluation is very close (0.405, 0.417, and 0.464). This suggests that the working fluid selection is not so influential if the jet-ejector internal geometry is thoroughly designed.
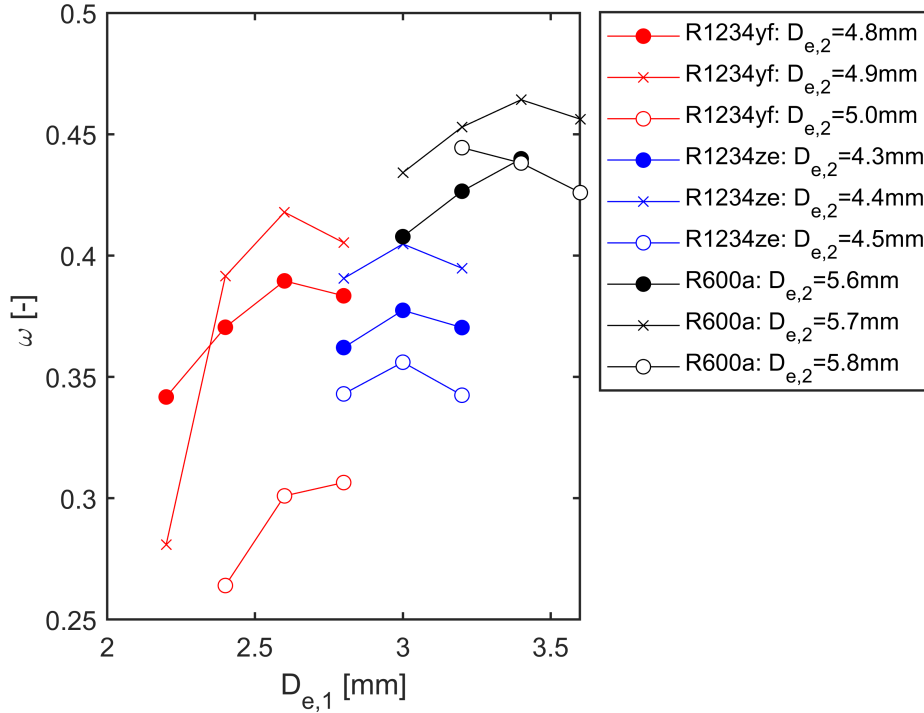
Figure 4.2: *Sensitivity analysis of key dimensions for the three refrigerants under evaluation (R1234yf, R1234ze and R600a). $D_{e,3} = 1.8\,mm$ and $L_{e,1} = 3.5\,mm$.*

Figure 4.3 represents the influence of the NXP ($L_{e,1}$) over the entrainment ratio. The aim of the optimization process is not to find global optimum NXP but to find an optimum NXP in certain operating conditions that would be at least acceptable when the jet-ejector primary pressure changes. Such simplification is intended to reduce significantly the number of geometries involved in the optimization process and to reduce the computational cost. Figure 4.3 demonstrates that the NXP has a lower level of influence and slight modifications in this geometric dimension do not affect dramatically the entrainment ratio. Nevertheless, the existence of an optimum is clear and an adequate design of this parameter is also essential.

To graphically illustrate the jet-ejector entrainment ratio improvement resulting from the optimization process when all the dimensions are optimized combinedly, Figure 4.4 is provided. The lack of smoothness in some entrainment ratio curves can be attributed to the discretization interval of the geometric dimensions (usually 0.1 mm in the most sensitive geometric parameters) when searching for the optimum geometry. Marginal improvements in entrainment ratio could be achieved if the discretization
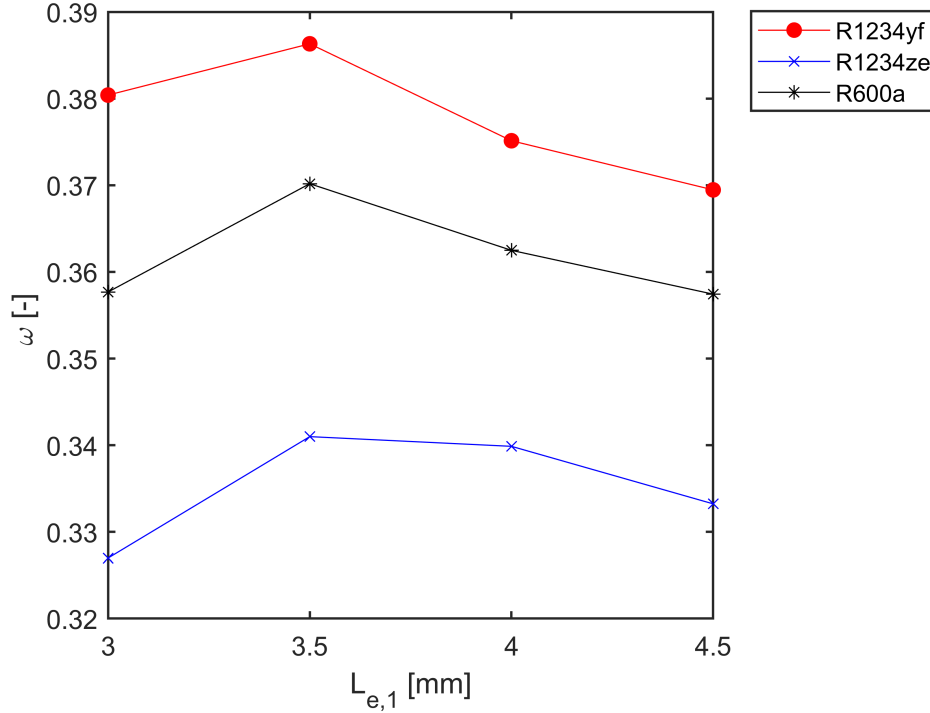
Figure 4.3: *Determination of the NXP influence over the optimum geometries for* $P_{pf} = 29.1\,bar$.

interval in the optimization process is reduced at the expense of increasing notoriously the number of simulations required to characterize each refrigerant. Hence, this strategy would be not attractive from the computational economy perspective and it does not change the conclusions of the study.

Figure 4.4 shows that the generating pressure does not have a decisive influence over the entrainment ratio if the jet-ejector internal geometry is carefully designed. A diminution over the maximum achievable entrainment ratio is found if the generating pressure decreases for a fixed condensing pressure. This trend is maintained regardless of the fluid under consideration. It is also observed that both the primary nozzle area ratio and the jet-ejector AR tend to increase to counteract the increase of the generating pressure in the optimum geometries. If the optimum geometries for each refrigerant are analyzed under uniform conditions at the jet-ejector inlet it is observed that the working fluid with the highest specific volume (R600a) presents the smallest jet-ejector throat diameter ($D_{e,3}$) and, consequently, the smallest jet-ejector size, followed by R1234ze and R1234yf.

The refrigerant R600a shows the maximum entrainment ratio ($\omega_{opt} = 0.464$) for $P_{pf} = 31.29$ bar, followed by R1234yf ($\omega_{opt} = 0.417$) for $P_{pf} = 35.14$ and R1234ze ($\omega_{opt} = 0.405$) for $P_{pf} = 33.35$. A priori, it is not possible to discern which working fluid is the most convenient in terms of COP_{th} maximization. For that purpose, the whole refrigeration system must be evaluated.
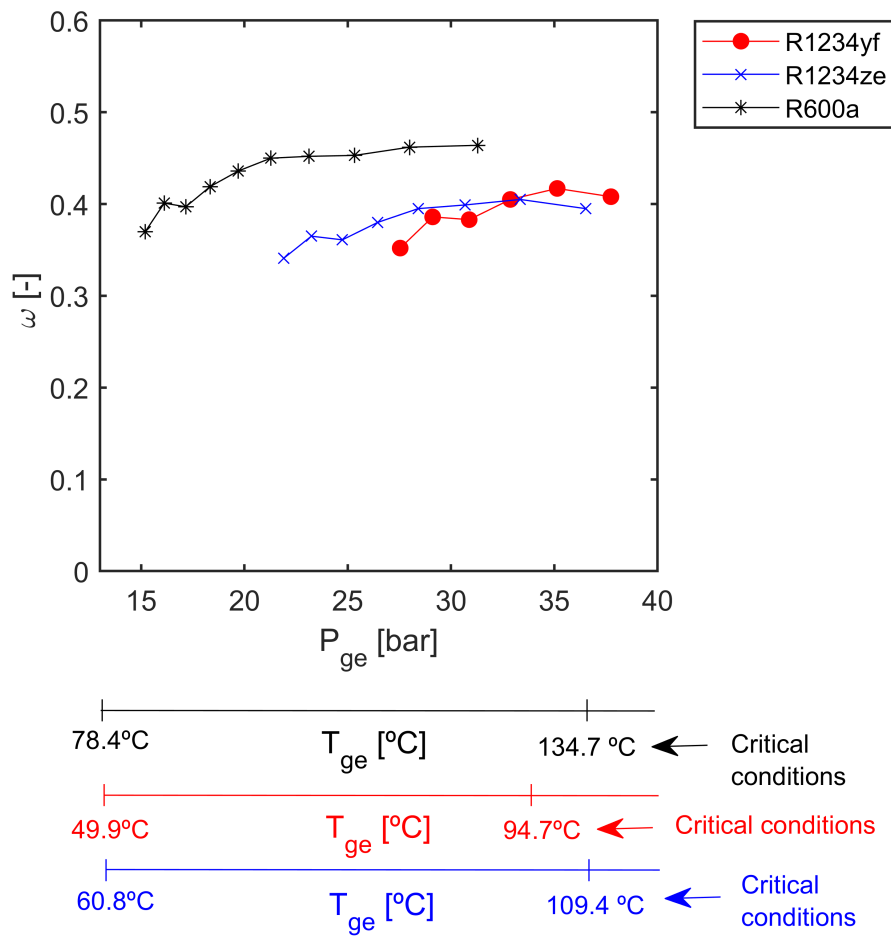
Figure 4.4: *Optimum jet-ejector entrainment ratio for each primary flow operating pressure. For each point, the geometry has been optimized in detail.*

4.3 Evaluation of the FJE response in off-design ambient conditions and off-design thermal source conditions

As shown before, the jet-ejector operating with R600a offers the most proficient performance, however, as will be reasoned later, the R1234yf should be selected when the overall system performance is analyzed. Hence, the off-design performance exploration of the jet-ejector is focused on this particular refrigerant. The optimum design for R1234yf has been subject to off-design operating conditions, different from the optimum ones, to assess its response. Specifically, the response of the jet-ejector geometry designated as the optimum has been tested against different generating, condensing, and evaporating conditions to explore its versatility. Anyway, the conclusions could be extended to the rest of the refrigerants under evaluation.

4.3.1 Definition of the study

To evaluate the adaptation capabilities of the FJE two complementary studies have been conducted.

- **Assesment of the FJE operation in off-design ambient conditions and off-design refrigeration requirements:** A variation in the condensing temperature is equivalent to a variation in the ambient conditions. The increase of the condensing temperature has particular interest because it leads to an inflection point in entrainment ratio with the associated sharp degradation in performance. The condensing temperature has been varied in the analysis between $35.6°C$ and $43.0°C$ or equivalently, the condensing pressure has been varied between 9.1 bar and 11 bar. It is, indeed, a narrow margin but is sufficient to see the catastrophic effect on jet-ejector performance that has the fact of working beyond the critical condensing temperature.

  A change in the evaporating temperature of the machine is translated into a variation in the refrigeration level. Thus, if the evaporating temperature increases the jet-ejector works in more favorable conditions but the attainable temperature is higher. A situation like this may occur when the machine works under variable refrigerating needs. The evaporating temperature has been varied in the present analysis between $5.6°C$ and $16.3°C$ or equivalently, the evaporating pressure has been changed between 3.8 bar and 5.3 bar.

- **Assesment of the FJE capability to withstand a diminution of the temperature in the hot driving source:** A decrease in the generating pressure, which means that the hot thermal source reduces its temperature, corresponds to a usual operation scenario. The hot flow coming from the thermal source could be interrupted for some reason or its temperature could be reduced. The reference case, optimized geometrically for a $P_{ge} = 35.14$ bar, has been simulated against generating pressures ranging from 25 to 33 bar, that is, generating temperatures ranging from 77.6 $°C$ and 91.4 $°C$.

The decision only contemplates a reduction and not an increase in the thermal source temperature because this complicates the proper operation. An increase in the thermal level is, indeed, favorable for a proper functioning of the system.

4.3.2 Results

- **Assesment of the FJE operation in off-design ambient conditions and off-design refrigeration requirements:** Figure 4.5 shows the steady response of the FJE as the condensing temperature increases. As can be observed, the transition between the double-choking and the single choking operating mode is distinguished: the entrainment ratio is not perturbed when the condensing temperature increases until a certain critical value above which the entrainment ratio drops.

It should be outlined that as the evaporating temperature increases, the evaporating pressure increases as well, and this helps the jet-ejector to improve its performance. The entrainment ratio in the double-choking operating mode rises and the critical condensing temperature is delayed. This means that the jet-ejector can operate satisfactorily under higher ambient temperatures. This enhancement is quantified in approximately $\Delta T_{co,crit} = +1.2°C$ with a relative variation of the evaporating temperature of $\Delta T_{ev} = +3.6°C$ when the curves with $T_{ev} = 9.4°C$ and $T_{ev} = 13°C$ of Figure 4.5 are considered. The enhancement of the operative range of the jet-ejector can be attributed to the increase in momentum of the jet core and the capacity to counteract the effect of the backpressure.
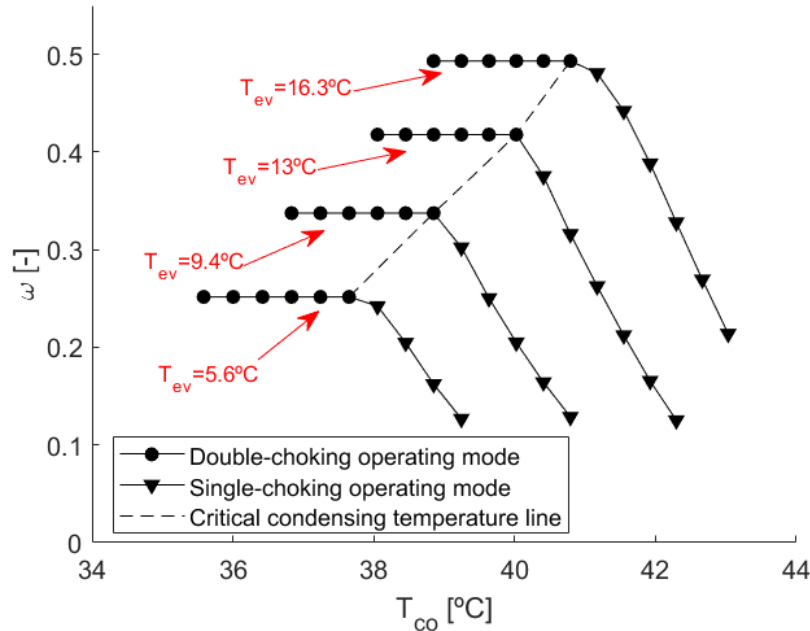
Figure 4.5: *Evolution of the jet-ejector entrainment ratio (ω) as the condensing temperature increases for different evaporating temperatures. The generating pressure remains fixed (35.14 bar)*

Table 4.3 demonstrates that the scattered data can be approximated to two planar surfaces with an acceptable error. Equation 3.95 presents the fitting coefficients of both planar surfaces. The lower precision of the single-choking model (higher RMSE) can be attributed to the fluctuating nature of the CFD numerical solution and the high sensitivity of the flow structure to slight variations in the operating conditions.

Equation 4.1 represents the double-choking performance map of the optimized FRS.

$$
\begin{aligned}
\omega_{FJE}\left(T_{co}, T_{ev}\right) = -6.03 - 9.638 \cdot 10^{-5} \cdot \left(T_{co} + 273.15\right) \\
+ 0.02264 \cdot \left(T_{ev} + 273.15\right), \text{if } T_{co} \leq T_{co,crit}
\end{aligned} \tag{4.1}
$$

Equation 4.2 represents the single-choking performance map of the optimized FRS.

$$
\begin{aligned}
\omega_{FJE}\left(T_{co}, T_{ev}\right) = 25 - 0.1323 \cdot \left(T_{co} + 273.15\right) \\
+ 0.05891 \cdot \left(T_{ev} + 273.15\right), \text{if } T_{co} > T_{co,crit}
\end{aligned} \tag{4.2}
$$

	$R^2[-]$	$RMSE[-]$
Double-choking operating mode	0.9999	8.39E-04
Single-choking operating mode	0.9795	0.0156

Table 4.3: *Goodness of fit of the FJE operating modes. RSME: Root Mean Square Error, R^2: Coefficient of determination*

To gain more insights, Figure 4.6 shows the second series of oblique shocks moving upstream as the condensing pressure increases. In Figure 4.6, case I., the jet-ejector is working in the double-choking operating mode. The entrainment ratio in the double choking operating mode is $\omega = 0.233$. It must be outlined that the contours shown in Figure 4.6 do not correspond to the operating points depicted in Figure 4.5. Other geometry participating in the optimization process has been selected to visualize more clearly the characteristic evolution of the second series of oblique shocks.

As the condensing pressure increases, the second series of oblique shocks move upstream with no remarkable effect in the entrainment ratio (Case II.) and, therefore, without affecting its ability to suction secondary flow. When the critical condensing temperature is exceeded (case III. of Figure 4.6), the second series of oblique shocks displace towards the suction chamber disrupting the entrainment and mixing of the secondary flow. The degradation caused is still modest in this case and the entrainment ratio drops slightly $\omega = 0.189$.

- **Assesment of the FJE capability to withstand a diminution of the thermal level in the hot driving source:** Figure 4.7 shows the effect of a

I. $P_{co} = 10.79$ bar, $(T_{co} = 42.3°C)$, $P_{ev} = 4.80$ bar $(T_{ev} = 13\,°C)$, $\omega = 0.233$
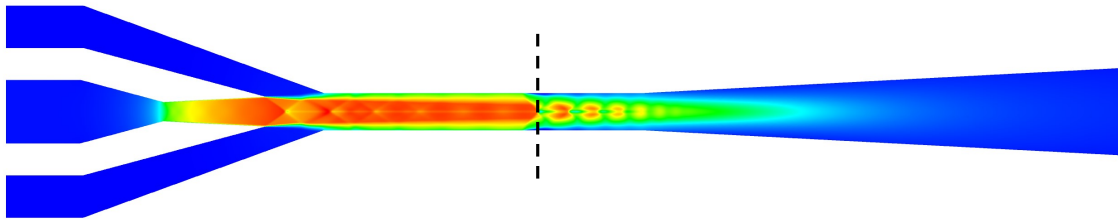
II. $P_{co} = 11.39$ bar $(T_{co} = 44.5°C)$, $P_{ev} = 4.80$ bar $(T_{ev} = 13\,°C)$, $\omega = 0.233$
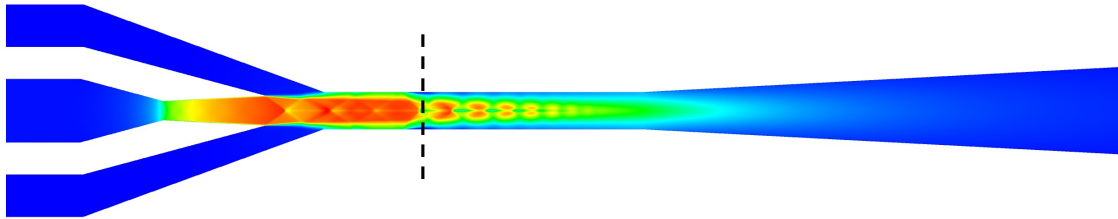
III. $P_{co} = 11.59$ bar $(T_{co} = 45.1°C)$, $P_{ev} = 4.80$ bar $(T_{ev} = 13\,°C)$, $\omega = 0.189$
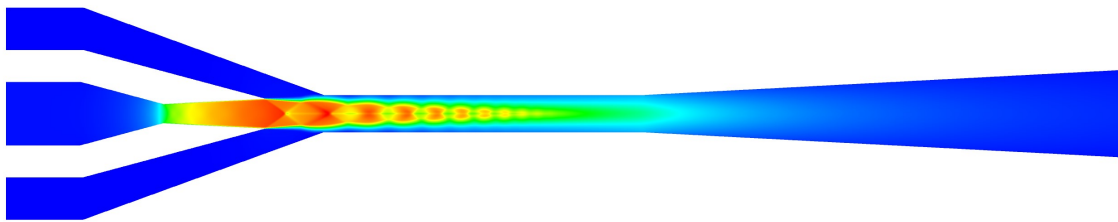
Figure 4.6: *Evolution of the jet-ejector internal shockwave pattern as the condensing pressure increases. The position of the second series of oblique shocks is marked in dashed lines.*

diminution in the generating pressure for the optimized geometry. As can be seen, the jet-ejector entrainment ratio y severely degraded revealing once again the low adaptation capability of the FJE. The reason for this performance deterioration can be found in the FJE double-choking and single choking maps. The optimized geometry taken as reference for this study is very close to its critical condensing temperature and also very close to its critical backpressure ratio $(\pi_{co,ge} = P_{co}/P_{ge})_{crit}$. Maintaining the condensing conditions, a diminution in the generating pressure entails an increase in the pressure ratio $\pi_{co,ge} = P_{co}/P_{ge}$. What happens is that the jet-ejector ceases to operate in the double-choking operating mode and moves into the single-choking operating mode. Below a generating pressure of 30.87 bar, a complete malfunctioning situation is found due to backflow and the FJE is not entraining secondary flow.
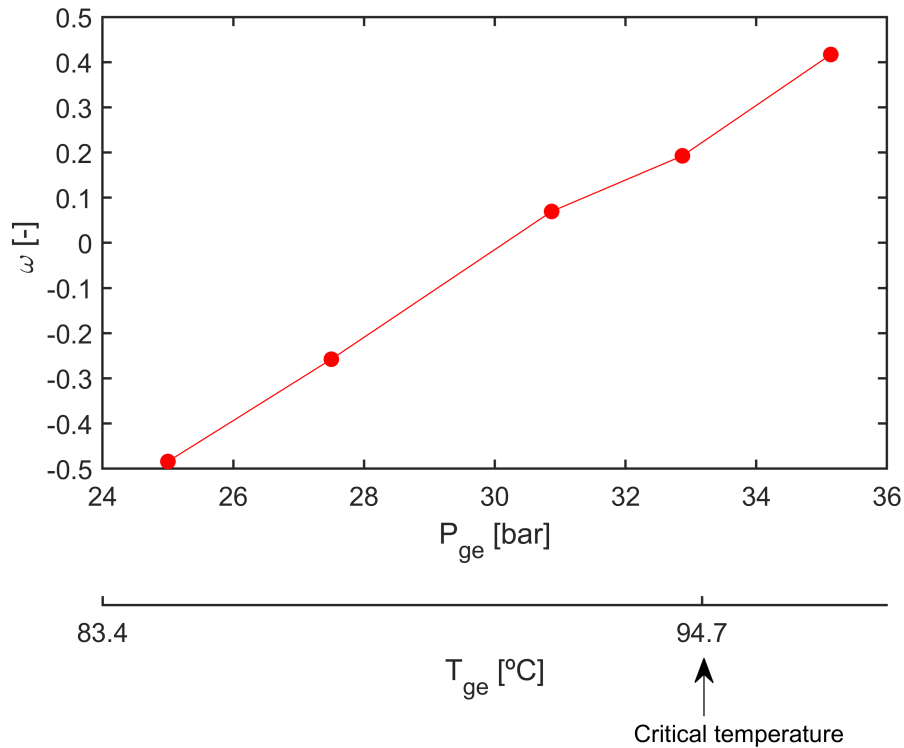
Figure 4.7: *Effect of reducing the primary flow pressure (P_{ge}) on the entrainment ratio for the FJE.*

4.4 Summary

In this chapter, a thorough optimization of the jet-ejector geometry for different working fluids and operating conditions has been conducted. The capability of the FJE to withstand changing conditions has been assessed. Specifically, the repercussion of

variable refrigerating demands, variable ambient temperatures, and a diminution in the thermal level of the hot driving source over the FJE entrainment ratio have been analyzed.

Simple mathematical expressions that collect information about the off-design response of a particular geometry have been obtained $\omega = \omega\left(T_{ev}, T_{co}\right)$. These expressions have been very helpful in the subsequent analysis to evaluate the response of the overall system in steady-state and dynamic conditions. The jet-ejector optimized geometry and its response maps are versatile and they will be used to evaluate both the solar and the automotive application.

Chapter 5

Steady-state characterization of the adjustable jet-ejector (AJE)

5.1 Introduction

This chapter is dedicated to exploring the geometrical optimization and off-design characterization of the Adjustable Jet-Ejector (AJE). Firstly, the working fluid is chosen based on the conclusions obtained for the FJE (Fixed-Geometry Jet-Ejector) analysis. Then, a reference AJE position is defined and its geometry is again thoroughly optimized for the reference boundary conditions and the reference static spindle position. The optimization process of this "frozen" geometry is identical at the methodological level to the one applied for the FJE and seeks to maximize the jet-ejector entrainment ratio. Finally, the reference optimized geometry is altered by displacing the spindle. The aim is to elucidate which spindle position is the most convenient to enhance the jet-ejector entrainment ratio for some representative condensing temperatures of warm periods in the Mediterranean climates and off-design conditions in the hot driving source.

5.2 Working fluid selection and optimum design for the AJE

5.2.1 Definition of the study

Also for the AJE, the environmentally friendly refrigerant R1234yf has been chosen for the simulations and jet-ejector performance quantification. On this occasion, the working fluid sensitivity study has been left aside, thus adopting the hypothesis that the refrigerant influence can be mitigated with an adequate jet-ejector design. Selecting the same working fluid is also helpful to fairly compare between the FJE and the AJE and avoid biased results. As will be discussed later, the response of the overall refrigeration system has been assessed contrasting the flexibility offered by the AJE with the mechanical simplicity of the FJE.

This time, the optimization process of the internal jet-ejector geometry has been simplified taking into account the level of influence of each geometric dimension based on what has been learned from the FJE optimization. However, it does not stop being a comprehensive optimization. Figure 5.1 represents sequentially the steps followed to maximize the entrainment ratio. The knowledge gained in the FJE optimization has been a good starting point for the trial-and-error process. A reference spindle position (SP=13 mm) and reference primary flow pressure $P_{pf} = 35.14$ bar have been maintained throughout the optimization process. The reference spindle position (SP=13 mm) has a wide margin to change the jet-ejector AR by displacing the spindle downwards and upwards. The evaporating and condensing temperatures are set in the geometrical optimization process equal to those selected for the FJE assessment, that is, $T_{co} = 40°C$ and $T_{ev} = 13°C$.
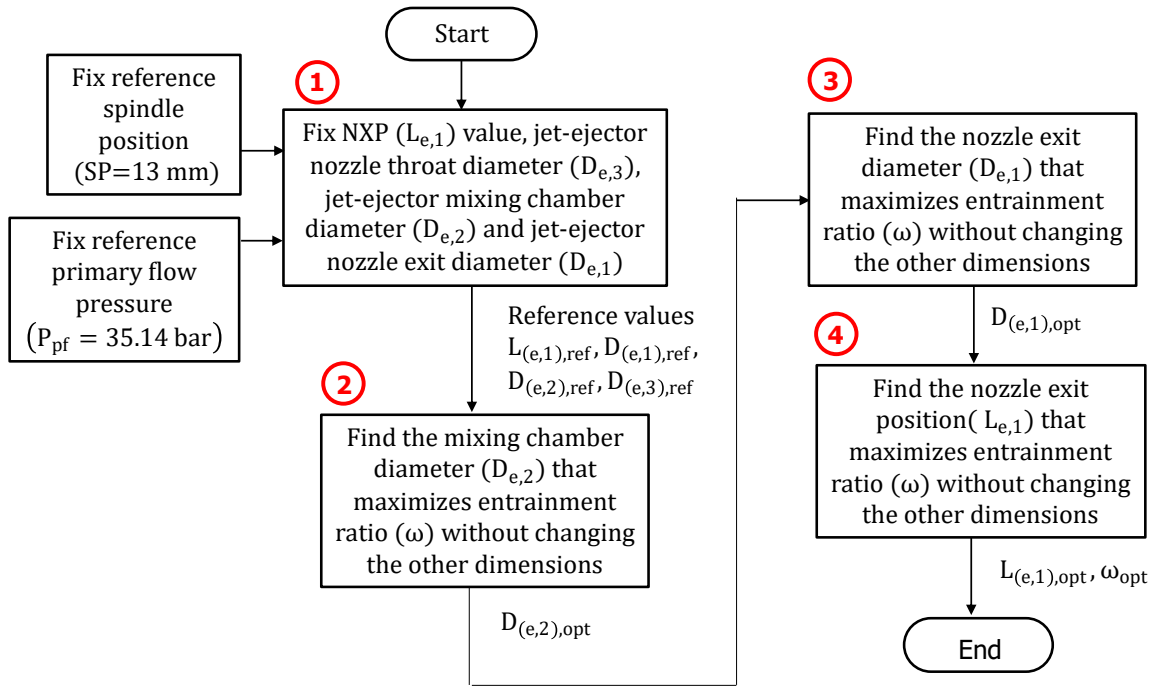
Figure 5.1: *Flow diagram for the AJE optimization*

5.2.2 Results

The maximum entrainment ratio found when the AJE reference geometry is optimized is not exactly the one obtained for the FJE, however, it is very close (0.402 for the AJE vs 0.417 for the FJE). The subtle differences are attributed to the spindle, which slightly modifies the expansion and entrainment processes. Nonetheless, the optimization process has proven to be equally effective.

Figure 5.2 represents graphically the influence of the mixing chamber diameter ($D_{e,2}$), the primary nozzle exit diameter ($D_{e,1}$) and the NXP ($L_{e,1}$) on the prototype performance. The mixing chamber diameter stands as the most influential geometric dimension. Small changes in this parameter lead to high variability in entrainment ratio.
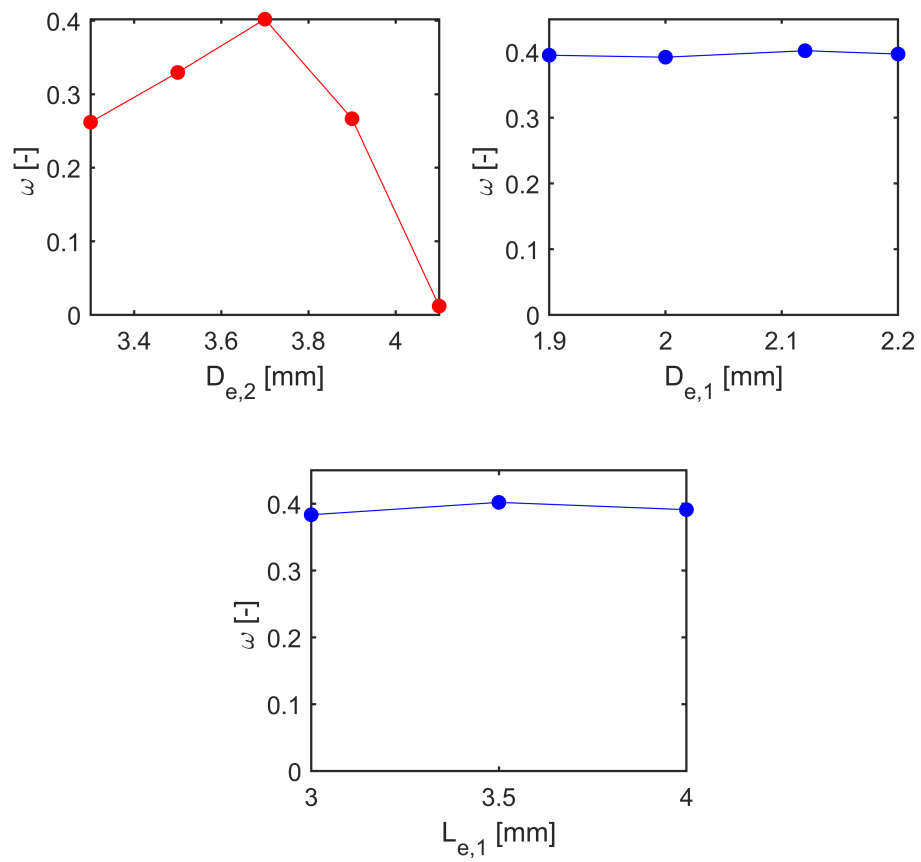
Figure 5.2: *Influence of the key geometric dimensions of the AJE over the entrainment ratio.*

5.3   Evaluation of the AJE in off-design ambient conditions and variable conditions in the hot thermal source

5.3.1   Definition of the study

To evaluate the adaptation capabilities of the AJE two complementary studies have been conducted:

- **Assessment of the AJE operation in off-design ambient conditions:** The condensing conditions in the refrigeration machine are constantly varying along the day and a change in the condensing pressure (backpressure) affects the jet-ejector itself and the overall system to a great extent. The system malfunctioning associated with variations in the condensing temperature has the greatest potential to be improved by using a mechanically driven spindle. For this reason, this study has been addressed in a high level of detail and full characterization of the operating envelope has been performed.

  The starting point to conduct the analysis is the case with the reference spindle position (SP=13 mm). The reference arrangement has a sufficient margin for increasing and reducing the effective section in the primary nozzle covering a wide range of condensing temperature scenarios. The condensing temperature has ranged in the study between 35.1 $°C$ and 45.1 $°C$ (8.99 bar - 11.59 bar). The spindle portion inside the jet-ejector has ranged between SP=12.20 mm and SP=13.89 mm, this is, an AR varying between 4.82 and 7.92.

- **Assessment of the AJE operation in off-design ambient conditions in combination with a reduction of the thermal level in the hot driving source:** This study evaluates the effect of different spindle positioning when the condensing and the generating temperature differ from the design conditions. Also, the optimum spindle positioning is provided for different operating scenarios. The generating temperature and, consequently, the generating pressure must be reduced inevitably to face a diminution in the hot source temperature. The temperature of the heat exchange process in the generator has been varied between a generating temperature of 77$°C$ and a supercritical process at 35.14 bar in which a temperature of approximately 99$°C$ is reached.

5.3.2   Results

- **Assessment of the AJE operation in off-design ambient conditions:**

  Having found the AJE optimum reference geometry, CFD simulations have been carried out to determine the jet-ejector critical condensing temperature for multiple spindle positions. These simulations are intended to characterize the performance envelope of different AJE families of geometries and the AJE with the reference spindle position. The entrainment ratio results are depicted in Figure 5.3 for the AJE envelope and three different geometries showing a fixed spindle

position among which the reference AJE is included. The reference AJE has an
AR=5.70 (Figure 5.3) and in its double-choking operating mode, the entrainment
ratio equals 0.402. Conversely, when it operates at its single-choking operating
mode its performance is severely degraded.
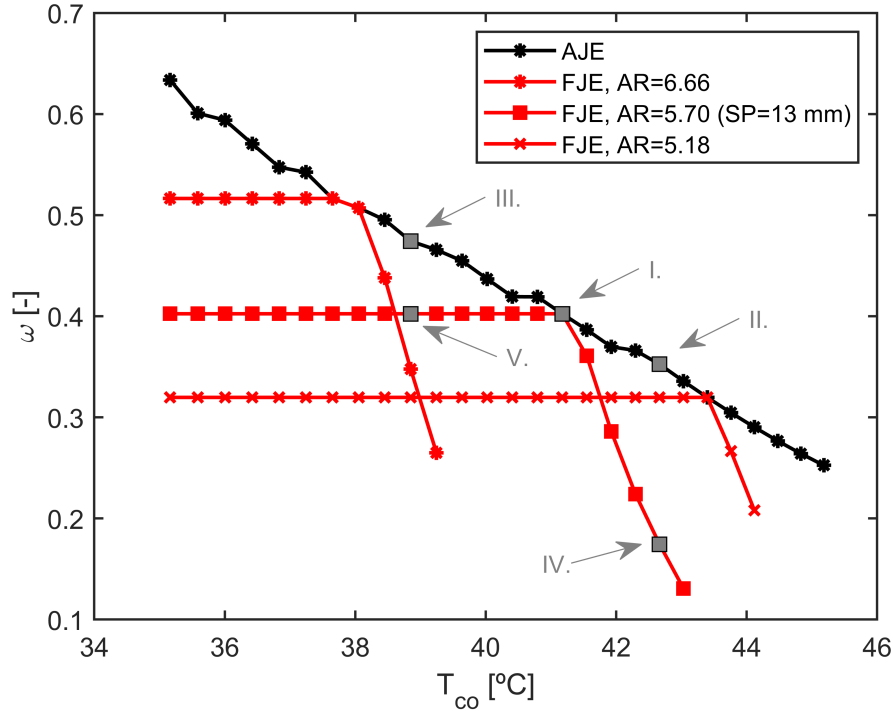
Figure 5.3: *Response of the AJE and three fixed spindle positions as the condensing temperature varies. The conditions in the generator and evaporator remain fixed* $(P_{ge} = 35.14\,bar)$ *and* $(T_{ev} = 13°C)$.

Each point marked in black in the AJE envelope corresponds to a geometrical configuration in which the spindle movement changes the jet-ejector AR. The number of simulations required to generate each point of the envelope is considerable because the critical condensing temperature for each AR must be iteratively searched for. It should be outlined that the operating envelope of the ARS follows a linear trend and it has been fitted to a linear expression with precision. A linear fitting gives a coefficient of determination $R^2 = 0.9971$ and a $RSME = 0.00587$. The coefficients of the fitting are presented in Equation 5.1.

$$\omega_{AJE}\left(T_{co}\right) = -0.0362838 \cdot \left(T_{co} + 273.15\right) + 11.804 \qquad (5.1)$$

The axial displacement of the spindle induces changes in expansion, entrainment, and mixing processes of the secondary and primary flows and therefore alters the position and magnitude of the shockwaves produced downstream. A profound understanding of this complex phenomenon would require an in-depth analysis that would exceed the scope of the present dissertation.

As can be observed in Figure 5.3, moving the jet-ejector spindle upwards to increase the primary nozzle throat area is beneficial to increase the jet-ejector critical condensing temperature. Nevertheless, it reduces the jet-ejector entrainment ratio. Additionally, the increment in the nozzle throat effective area entails an increment of primary mass flow rate passing through it as depicted in Figure 5.4. Indeed, the primary mass flow rate passing through the jet-ejector primary nozzle is proportional to the nozzle throat effective area if the nozzle is at the choking condition.

The spindle displacement downwards causes the opposite effect; it reduces the critical condensing temperature positively affecting the jet-ejector entrainment ratio and diminishing the mass flow rate passing through the nozzle.

These performance maps are used in the dynamic computational model that compares the ARS and FRS and quantifies the potential improvement offered by the ARS. The entrainment ratio evolution with spindle position demonstrates that an optimum area ratio exists for each condensing temperature and reveals a high sensitivity in jet-ejector performance to changes in ambient conditions. A continuous fine-tuning of the jet-ejector spindle is essential to guarantee that the refrigeration system operates at its optimum condition. Moving the spindle position to compensate for variations in the ambient temperature is an effective way to avoid performance degradation.

Five characteristic cases have been marked in Figure 5.3. In Point I, the reference AJE geometry operates at the critical condensing temperature. It pertains to the AJE operating envelope and represents the maximum condensing temperature that the system can withstand if the spindle is not moved without incurring in severe performance degradation. The points III-V and II-IV can be paired and, for a certain condensing temperature, represent the maximum entrainment ratio achievable with the spindle fixed at the reference position and a spindle optimally displaced, respectively.

Figure 5.5 shows the Mach contours of several characteristic cases computed with CFD simulations. Each case can also be identified in the maps of Figure 5.3 and represent different condensing temperatures with active control of the spindle. Indeed, the spindle is positioned optimally for the condensing temperature under evaluation since all the points belong to the AJE operating envelope. The spindle implementation is a useful backpressure compensation mechanism since it delays the progression of the second series of oblique shocks upstream impeding the perturbation of the secondary flow entrainment in the suction chamber.

Figures 5.6 and 5.7 compare the shockwave pattern of two cases: one of them has the reference spindle position while in the other one the spindle is optimally positioned. As can be observed, a slight spindle movement has a tangible impact on the internal shock train structure and entrainment ratio.

Figure 5.8 includes in the analysis the optimum spindle positioning when the variations in ambient temperature are combined with a diminution in the thermal
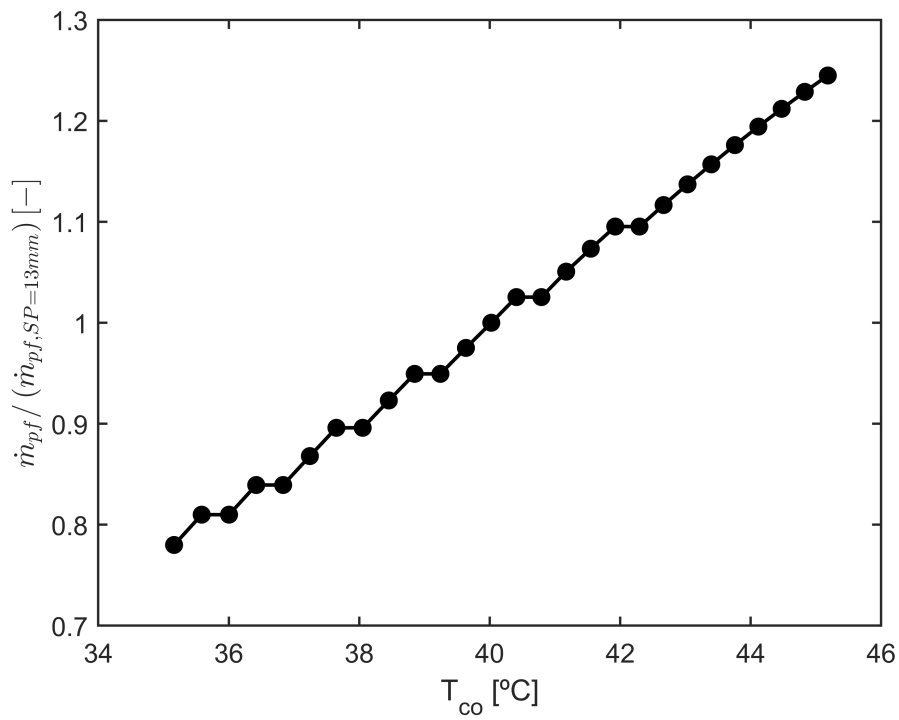
Figure 5.4: *Primary mass flow rate versus condensing temperature for the AJE envelope. The results are non-dimensionalized with the primary mass flow rate of the AJE reference geometry (SP=13 mm).*

III. P_{co} = 9.89 bar (T_{co} = 38.8 °C), ω = 0.472, SP = Reference + 0.33 mm
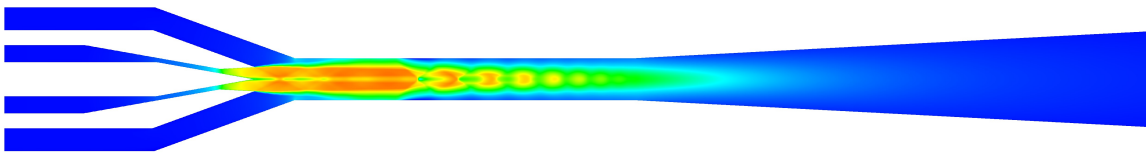
I. P_{co} = 10.49 bar, (T_{co} = 41.2 °C), ω = 0.402, SP = Reference = 13 mm
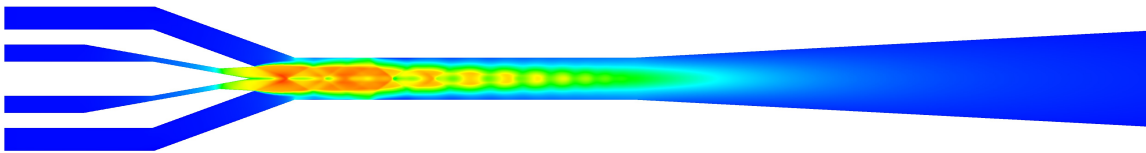
II. P_{co} = 10.89 bar (T_{co} = 42.7 °C), ω = 0.352, SP = Reference − 0.24 mm
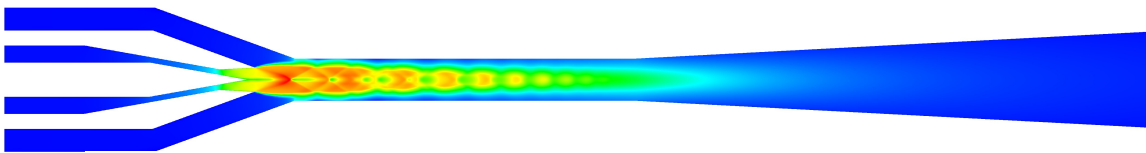
Figure 5.5: *Mach number contour plots of different points pertaining to the AJE
operating envelope. The cases are depicted in Figure 5.3.*
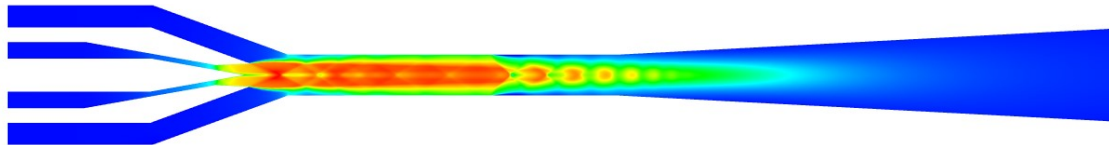
V. P_{co} = 9.89 bar (T_{co} = 38.8 °C), ω = 0.402, SP = Reference

III. P_{co} = 9.89 bar (T_{co} = 38.8 °C), ω = 0.472, SP = Reference + 0.33 mm
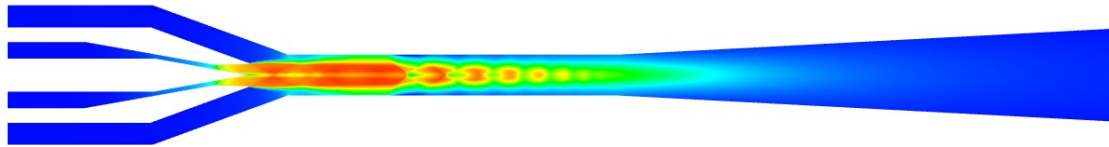
Figure 5.6: *Flow pattern (contours of Mach number) of the jet-ejector (Mach number) comparing the action of the spindle displacement. V. Non-optimized spindle position for P_{co} = 9.89 bar, III. Optimized spindle position for P_{co} = 9.89 bar. The cases are depicted in Figure 5.3.*

IV. P_{co} = 10.89 bar (T_{co} = 42.7 °C), ω = 0.174, SP = Reference
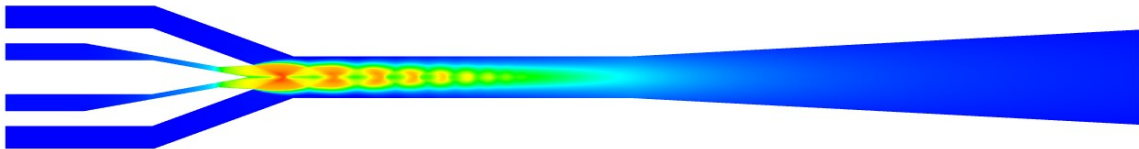
II. P_{co} = 10.89 bar (T_{co} = 42.7 °C), ω = 0.352, SP = Reference − 0.24 mm
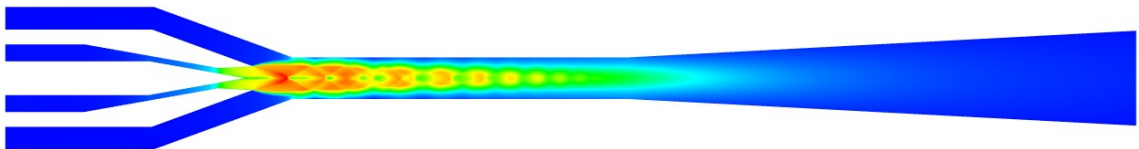
Figure 5.7: *Flow pattern (Mach number contours) of the jet-ejector (Mach number) comparing the action of the spindle displacement. IV. Non-optimized spindle position for P_{co} = 10.89 bar, III. Optimized spindle position for P_{co} = 10.89 bar. The cases are depicted in Figure 5.3*

level of the hot driving source, that is, the temperature of the hot driving source. This might occur, for example, when the solar collector is not receiving sufficient irradiation and the TSS starts cooling down due to the action of the ARS thermal power consumption and/or heat losses to the ambient.

Red dashed lines represent operating points with the same spindle position and, consequently, the same jet-ejector AR. The AR=4.22 represents the regulation limit offered by the spindle. In the red dashed line of AR=4.22, the spindle is completely retired from the primary nozzle throat so it has no effect and the nozzle throat area corresponds to its maximum. If the condensing temperature is further increased when there is no regulation margin, that is, when AR=4.22, the entrainment ratio would drop as happens with the FJE.

Using the spindle to compensate for variations in the hot source thermal level does not appear to be so flexible. The "thermal amplitude" of the hot driving source is much wider than the amplitude found in the typical condensing conditions in the condenser. For example, for the solar application, time slots with sufficient temperature to drive the system can be followed by periods with a complete scarcity of available energy.

The utilization of a spindle against varying conditions in the generator is, notwithstanding, beneficial when the AJE results are compared with those obtained for the FJE (Figure 4.7). The AJE achieves acceptable entrainment ratios in operating conditions in which de FJE shows complete malfunctioning due to backflow.

As the thermal level of the hot driving source decreases, the ability to withstand a higher condensing pressure is reduced. For example, in the nominal conditions, that is, when the generator operates at $P_{ge} = 35.14$ bar, the spindle is effective to manage condensing temperatures near to 48 $^{\circ}C$. In contrast, when the generating pressure decreases to 25 bar, the spindle can hardly withstand a condensing pressure of 38 $^{\circ}C$. This suggests that a low thermal level in the generator and a high ambient temperature represent the most challenging conditions for the FRS and the ARS to operate satisfactorily.

5.4 Summary

In this chapter, a thorough geometric design has been carried out for the AJE as well as a comprehensive performance characterization in several off-design conditions.

As demonstrated with the FJE design, the geometrical optimization process for the reference operating conditions is a key design step for the AJE to get a jet-ejector with good performance. Unlike in the FJE design process, here the designer has to select an adequate reference spindle position because the regulation margin of the spindle is crucial to compensate for the well-known off-design performance decay shown by the conventional designs.

The AJE has proven to be an effective technical solution to gain flexibility against changes in the ambient temperature or a temperature reduction in the hot driving
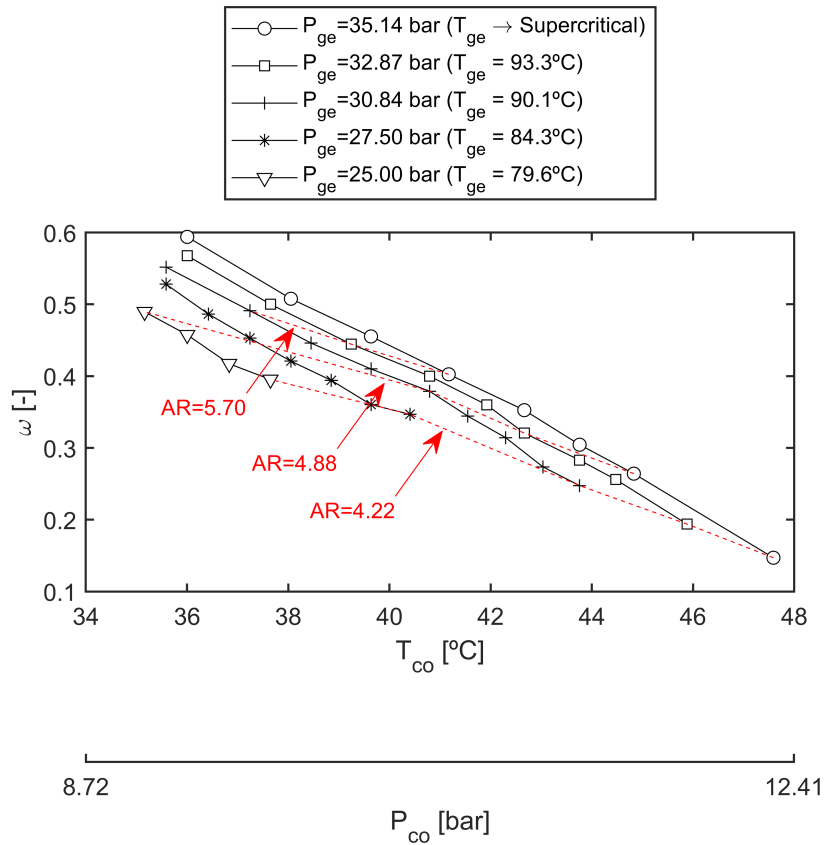
Figure 5.8: *Optimum spindle movement to compensate changes in the generator conditions (reduction of temperature in the hot driving flow) and the condenser (variable ambient temperature).*

source. Given the unstable nature of climatic conditions, the AJE would be helpful for
improving the performance of the baseline configuration practically in all the operation
envelope.

The main drawback lies in its higher mechanical complexity and the necessity of
carrying out a fine spindle tuning, as well as implementing governing laws based on
the real-time evolution of climatic conditions. In the following chapters, these superior
capabilities have been translated to overall system efficiency improvement to check the
real improvement potential.

Chapter 6

Steady-state performance characterization of the ARS and the FRS for a solar application

6.1 Introduction

The purpose of this chapter is to analyze the refrigeration system in steady-state conditions from a global perspective, coupling the jet-ejector to the rest of the elements of the refrigeration system and the solar field. The key point is to translate the jet-ejector characterization in design and off-design operating conditions to the overall system performance for both the Fixed-geometry Refrigeration System (FRS) and the Adjustable Refrigeration System (ARS). The design analysis has been conducted for different solar irradiance scenarios and different solar collector typologies. In the off-design exploration, the FRS and ARS response have been compared with ambient conditions away from the ones established to design the jet-ejector. Besides, the response of both architectures is assessed under changing conditions in the hot driving source. The off-design studies intend to confirm the superior versatility of the adjustable refrigeration system already anticipated in Chapters 4 and 5.

6.2 Definition of the climatic conditions

The steady-state model of the refrigeration system has been fed with solar irradiance values and ambient temperatures that are representative of warm periods in Mediterranean latitudes. The data comes from the EUMETSAT CMF SAF web user interface [147] and PVGIS (Photovoltaic Geographical Information System) platform developed by the EU [148]. As described in the project website, "The focus of PVGIS is research in solar resource assessment, photovoltaic (PV) performance studies, and the dissemination of knowledge and data about solar radiation and PV performance". The database contains historical climatic data (ambient temperature, solar irradiance, relative humidity, air pressure, wind speed/ wind direction...) along the Typical Meteorological

Year (TMY) in wide geographical areas including Europe. The data has been managed following two complementary approaches: the JERS steady model has been fed with discrete values of solar irradiance and ambient temperature while the dynamic model has been fed with hourly or instantaneous data records of the TMY.

Figure 6.1 shows the hourly distribution of global solar radiation and ambient temperature over the same area for every day in July of the TMY. As can be observed in Figure 6.1, some days the sky is partially cloudy, however, the hourly evolution of global solar irradiance follows a similar pattern. The collected dataset of daily surface irradiance parameters comes from hourly measurements of geostationary Meteosat satellites. The solar radiation products are defined for a particular geographical area (Valencia, Spain), nevertheless, the irradiance pattern would be comparable in other Mediterranean latitudes. The selected data set is representative and is helpful to visualize trends or maximum expected values.

Figure 6.2 shows the solar hourly global and diffuse solar irradiance evolution over three illustrative sample days with a clear sky. This reduced sample is useful to fix reference irradiance values for multiple idealized conditions. Table 6.1 collects good approximations of global and diffuse solar irradiance in time slots with usual refrigeration needs. These discrete and time-independent measures are used later to elucidate the achievable efficiency in the overall system in steady-state conditions.
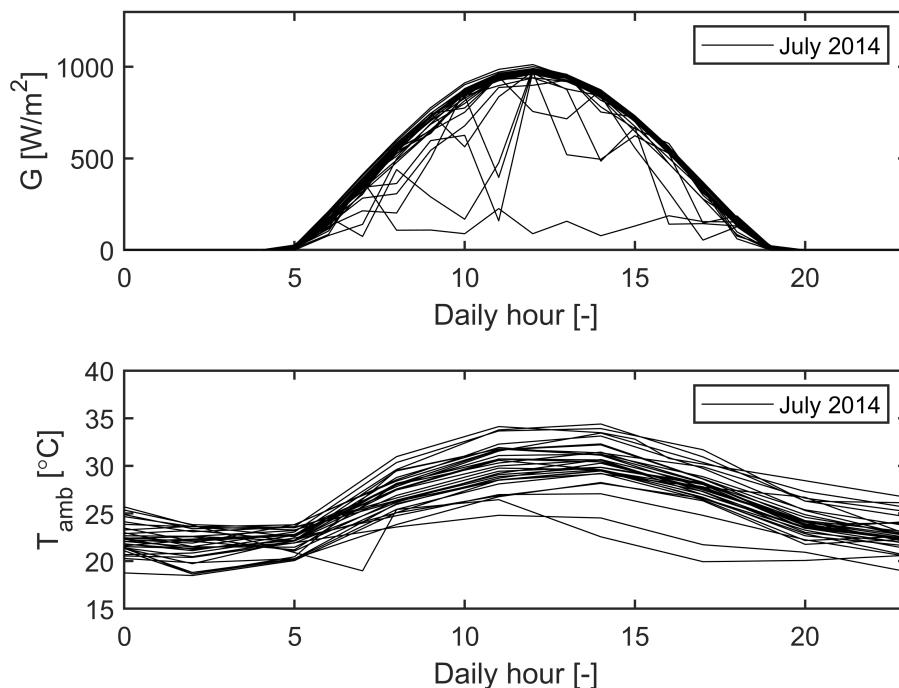
Figure 6.1: *Superposition of instantaneous daily global solar irradiance in Valencia Airport (July in the TMY) and daily evolution of the ambient temperature.*
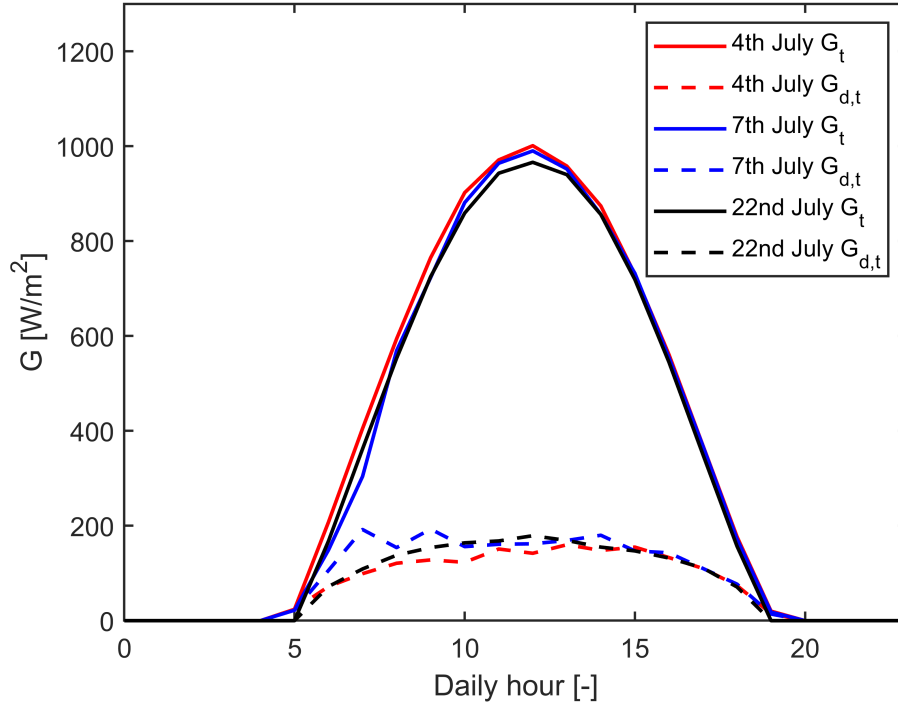
Figure 6.2: *Global and diffuse solar irradiance on three sample days with a clear sky scenario (July in the TMY)*

Case	Daily hour	$G\,[W/m^2]$	$G_d/G\,[-]$
C1	11:30-12:30	1000	0.18
C2	10:00-11:00 & 14:00-15:00	850	0.19
C3	09:00-10:00 & 15:00-16:00	700	0.21
C4	08:00 & 17:00 or Partially cloudy sky	450	0.25

Table 6.1: *Four characteristic cases considered in the JERS steady model*

6.3 Definition of the study

Three studies have been performed in this chapter. The first and second studies contemplate the cycle characterization in design conditions while the third study represents an exploration of the off-design response of the FRS and the ARS. Here the methodology followed in each study is described.

"Design" characterization:

1. The objective of the first design study is to determine the response of the refrigeration system and the overall system operating with three working fluids (R1234yf, R1234ze, and R600a) with the optimized jet-ejector geometries presented in the preceding chapters. In the design analysis, only the FRS intervenes since the operating conditions are assumed to be static and the system can be conveniently designed. In other words, in design conditions, the FRS offers the same potential as the ARS.

   A sensitivity analysis has been also included to assess the influence of different thermal collector technologies and solar irradiance scenarios.

2. The second study aims to demonstrate how the jet-ejector scaling affects the rated thermal power of the system. The intention is to outline the importance of a careful design also from the perspective of the system sizing.

"Off-design" characterization:

3. The aim of this analysis is to determine the response of the FRS and the ARS under representative steady scenarios of (i) off-design ambient temperature, (ii) off-design conditions in the hot driving source.

6.3.1 Hypothesis, constraints, and resolution strategy

The determination of the cycle performance consists of an optimization process in which the jet-ejector size must be matched with rated thermal power consumption. The optimization process has been carried out using modeFrontier, a multidisciplinary design optimization platform. The program is directly linked with Matlab and manipulates predefined input parameters to maximize a user-defined objective (COP_{th} maximization), trying to satisfy several constraints applied to the thermodynamic conditions of each cycle point. The fulfillment of such restrictions categorizes the resulting operating points as feasible or unfeasible and modifies the search criteria in real-time.

The following constraints are set in modeFrontier and must be satisfied irrespective of the study:

- Minimum pinch points in the heat exchangers of 7 $^\circ C$.

- Single-phase flow hypothesis. Only saturated vapor, saturated liquid, subcooled liquid, or superheated gas are considered valid states.

- The thermodynamic states at the jet-ejector entries must guarantee that the flow

remains as superheated gas after an expansion process that is assumed isentropic.

The resolution strategy has been changed depending on the study:

"Design" characterization:

1. In this study a rated thermal power consumption of $\dot{Q}_{ge} = 10$ kW has been set. For each refrigerant, the optimum jet-ejector scale has been selected to achieve such thermal power consumption. The influence over the refrigeration system performance of using different working fluids, solar collector technologies, and solar irradiance scenarios has been assessed.

2. In this study the optimum jet-ejector scale for different targeted thermal power capacities has been determined. For each capacity in the generator, the algorithm has selected the optimum jet-ejector scale (λ).

"Off-design" characterization:

3. This analysis aims to determine the response of the FRS and the ARS under representative steady scenarios of (i) variable ambient temperature, (ii) variable conditions in the hot driving source. In the first study (i), the jet-ejector scale (λ) is fixed and a reference $\dot{Q}_{ge} = 10$ kW is set as the reference condition. In the second study (ii), the jet-ejector scale is also fixed and the rated thermal power $\left(\dot{Q}_{ge}\right)$ is not fixed a priori because the change of primary flow conditions might induce variations in the thermal power consumed.

In both cases, the system response is determined according to the procedure shown in Figure 3.21.

6.4 Refrigeration system characterization in design conditions

6.4.1 Influence of different working fluids

The aim of this study is to deepen the sensitivity analysis of working fluids already performed in the previous chapters. In this section, the analysis is carried out from the perspective of the whole refrigeration system so the conclusions are of a general nature. Again, the working fluids are R1234yf, R1234ze, and R600a, being the model fed with the entrainment ratio results already presented. The intention is to estimate the $COP_{th} = \eta_{th,ref}$, taking as the basis the jet-ejector entrainment ratio (ω) characterized with CFD.

For the steady-state screening of working fluids, one of the parabolic trough collectors, specifically the $PTC_{Model-3}$, has been selected as the reference collector due to its superior operational behavior in a wider range of collector temperatures and solar irradiance conditions when compared to other collector technologies. The sensitivity study of working fluids has been carried out for a fixed irradiance level (1000 W/m^2) and an ambient temperature of 31 $°C$. Hence, the solar collector efficiency is almost

invariant except for the slight differences in collector inlet temperature ($T_{in,col}$) when
the generating pressure varies. The maximum solar irradiance intensity ($1000 \ W/m^2$),
expected in the most favorable conditions, has been selected to maximize the solar
collector performance. The aim is to evaluate the refrigeration system in the best-case
scenario.

Figure 6.3 depicts the FRS efficiency ($\eta_{th,ref}$), the solar collector efficiency ($\eta_{sol,th}$)
and the overall system efficiency (η_{ov}) against the generating pressure for each re-
frigerant. As specified in the optimization algorithm, a detailed jet-ejector geometric
optimization has been conducted for each operating pressure and each refrigerant.

As the generating pressure increases, the FRS efficiency does not exhibit a de-
creasing trend but it is almost constant. Therefore, this demonstrates that the FRS
performance could be marginally enhanced at the expense of a more robust generator
capable to withstand higher pressure. It might not be attractive from a cost-benefit
criteria because the equipment cost would increase and the efficiency improvement
($\eta_{th,ref}$) is insignificant. The maximum FRS efficiency corresponds to $\eta_{th,ref} = 0.377$,
$\eta_{th,ref} = 0.355$, and $\eta_{th,ref} = 0.352$ for R1234yf, R600a and R1234ze, respectively. It is
noteworthy that the refrigerant with the highest jet-ejector entrainment ratio (R600a)
is not the refrigerant with the highest $\eta_{th,ref}$. This is because more thermal power
per unit of refrigeration capacity demand is required to get superheated gas at the
corresponding generating pressure.

The power consumption of the liquid pump is far less when compared to the input
thermal power of the generator; however, this would be another factor of relevance
when evaluating the generating pressure. The power consumption of the liquid pump
has been determined for the rated thermal power in the generator (10 kW) and depends
on the thermodynamic properties of each working fluid (i.e. the specific volume of each
refrigerant, enthalpy variation across the pump...) and the liquid pump pressure ratio.
R1234yf shows the greatest power consumption varying between 134 W for the lowest
operating pressure ($P_{pf} = 27.54$ bar) and 209 W for the highest ($P_{pf} = 37.74$ bar),
followed by R1234ze (85W for $P_{pf} = 21.91$ bar and 174W for $P_{pf} = 36.52$ bar), and
R600a (59W for $P_{pf} = 15.20$ bar and 146W for $P_{pf} = 31.29$ bar).

All the refrigerants under consideration offer similar efficiencies when the over-
all system is assessed. R1234yf maximizes the solar irradiance conversion to refrig-
eration power ($\eta_{ov} = 0.201$), closely followed by R1234ze ($\eta_{ov} = 0.187$) and R600a
($\eta_{ov} = 0.184$). This suggests that other criteria should prevail when selecting one of
the previous refrigerants for this application (refrigerant or equipment cost, availability,
flammability...) rather than the system efficiency.

The present results have been compared with data available in the literature. The
aim is to quantify the effectiveness of the optimization procedure introduced in this
research as a way to improve the FRS performance. A rigorous comparison is quite
hard because the evaporating and condensing temperatures considered in the present
paper, 13 °C and 40 °C, respectively, are not exactly reproduced in the available
literature. Nevertheless the COP_{th} results have been compared with some external
data of jet-ejector refrigeration systems working at similar operating conditions. Bellos
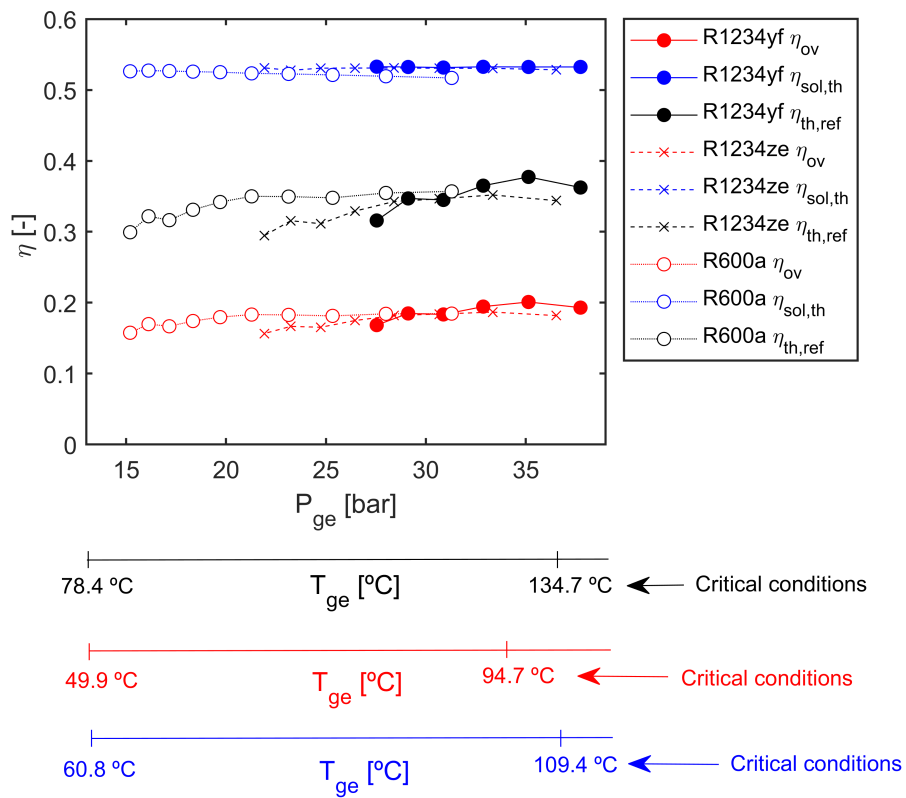
Figure 6.3: *Optimum FRS efficiencies for different primary flow operating pressures
and different working fluids* ($T_{co} = 40°C, T_{ev} = 13°C, G = 1000W/m^2$).

and Tzivanidis [104] reported a maximum $COP_{th} = 0.299$ using R141b as working fluid for a condensing temperature of 40 °C and an evaporating temperature of 10 °C. Also for the same operating temperatures, Kasperski and Gil [56] reported a maximum $COP_{th} = 0.32$ for R600a. More recently, the same authors calculated a maximum $COP_{th} = 0.23$ [58], keeping the same condensing and evaporating temperatures and considering only non-flammable synthetic refrigerants operating low-grade heat sources (below 140 °C). Chen et al. [54] obtained a maximum $COP_{th} = 0.38$ and $COP_{th} = 0.25$ for an evaporating temperature of 10 °C, and a condensing temperature of 35 °C and 40 °C, respectively, when R245fa and R600 are used as refrigerants.

From the previous literature search is not possible to discern whether the superior operational behavior reported in the study can be attributed to the higher evaporating temperature or, alternatively, the optimization process and working fluid have an appreciable influence. To elucidate the effect of the optimization process, the operational behavior of the FRS has been compared with literature data of a FRS working under a higher or equal evaporating temperature and a lower condensing temperature which are, indeed, more beneficial conditions.

Chen et al. [54] performed a screening of working fluids and obtained a COP_{th} ranging between 0.21 and 0.46 for a condensing temperature of 35°C and an evaporating temperature of 13°C. Nehdi et al. [149] reported a COP_{th} ranging between 0.3 and 0.41 (depending on the working fluid under examination) for an evaporating temperature of 15°C and a condensing temperature of 35°C. These values are comparable with the ones indicated in the present study so this would suggest that the thorough optimization of the jet-ejector internal geometry would have a remarkable positive effect on the FRS performance.

6.4.2 Influence of different solar collector technologies and solar irradiance scenarios

Figure 6.4 shows for the refrigerant R1234yf the overall efficiency, the efficiency transformation from solar irradiance to thermal power ($\eta_{sol,th}$) and the efficiency conversion from thermal power to refrigeration capacity ($\eta_{th,ref} = COP_{th}$) for the peak solar irradiance (1000 W/m^2) and different solar collector models. The $ETC_{Model-1}$ shows the peak efficiency ($\eta_{sol,th} = 0.565, \eta_{ov} = 0.213$) in the most favorable conditions (1000 W/m^2). On the contrary, the $PTC_{Model-2}$ shows the poorest efficiency in the same climatic conditions ($\eta_{sol,th} = 0.425, \eta_{ov} = 0.161$).

Figure 6.5 shows the influence of different static solar irradiance scenarios over the overall system efficiency. The solar irradiance characteristic cases are the same already presented in Table 6.1. As can be observed, a reduction in solar irradiance reduces the overall system efficiency. The efficiency diminution is attributed to the solar collector efficiency drop ($\eta_{sol,th}$). As can be observed, the PTCs show the most robust response showing a lower performance degradation as the solar irradiance diminishes. Among them, the $PTC_{Model-3}$ proves to be the best option. The $ETC_{Model-1}$, oppositely, suffers a steeper efficiency deterioration.
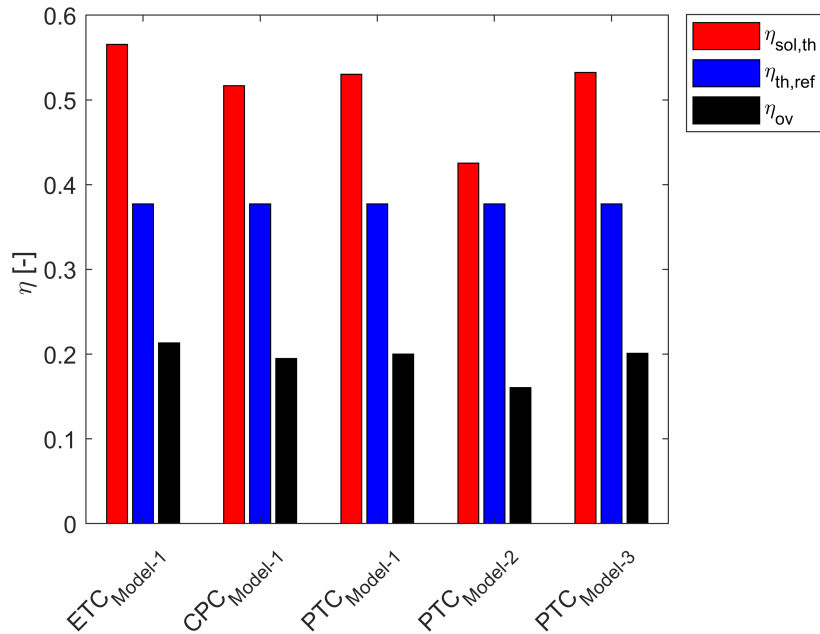
Figure 6.4: *System efficiencies for the peak solar irradiance* $1000\,W/m^2$.

This trend aligns with the efficiency characterization presented in Figure 3.4 coming from the literature.

6.5 Definition of an adequate jet-ejector scale

If the operating temperatures/pressures are defined, the jet-ejector scale determines the mass flow rates passing through each loop of the refrigeration system. An adequate selection is a key issue in the ARS and the FRS to achieve the desired rated thermal power consumption $\left(\dot{Q}_{ge}\right)$ and refrigeration power generation $\left(\dot{Q}_{ev}\right)$. Figure 6.6 shows the optimum scaling factor that would be required to achieve different rated refrigeration capacities for the FRS. The scaling factor (λ) depicted in Figure 6.6 must be applied on the reference dimensions shown in Tables 4.1 and 4.2.

It must be outlined that the case showing $\lambda = 1.255$ and $\dot{Q}_{ev} = 3.77$ kW is targeted for thermal power consumption of 10 kW and has been considered as the reference case throughout this chapter.

This design procedure would be equivalent in the ARS and the expected trend would be identical, that is, the jet-ejector sizing would be directly related to the rated thermal power consumption or, alternatively, to the refrigeration capacity.
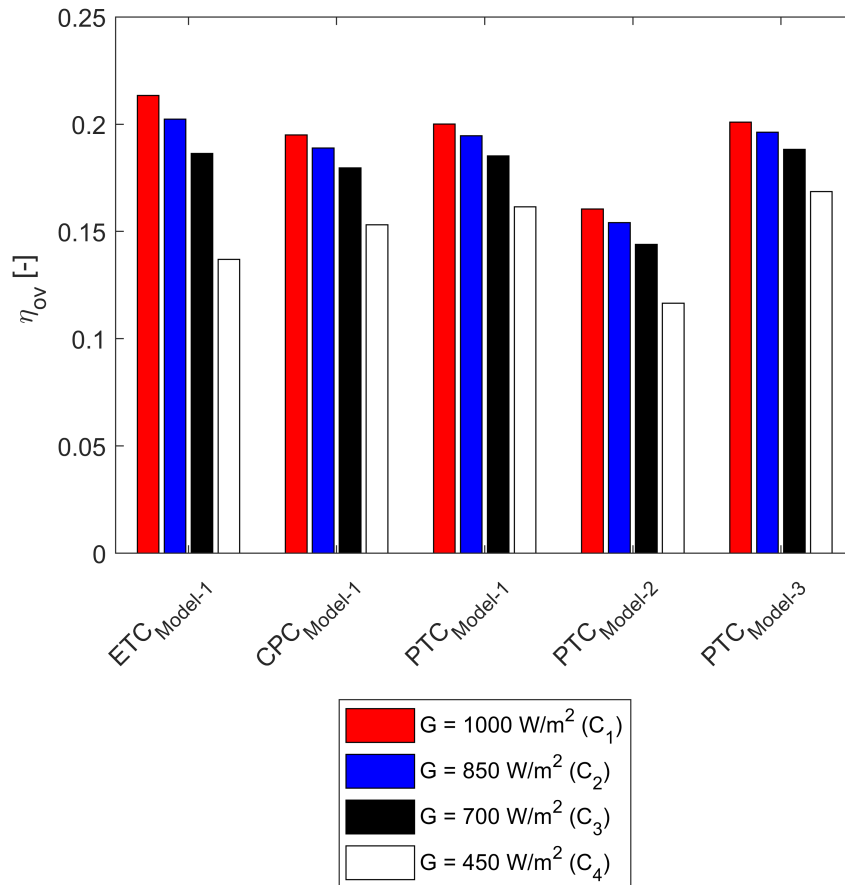
Figure 6.5: *Influence of solar irradiance on the overall system efficiency for different solar collector models.*
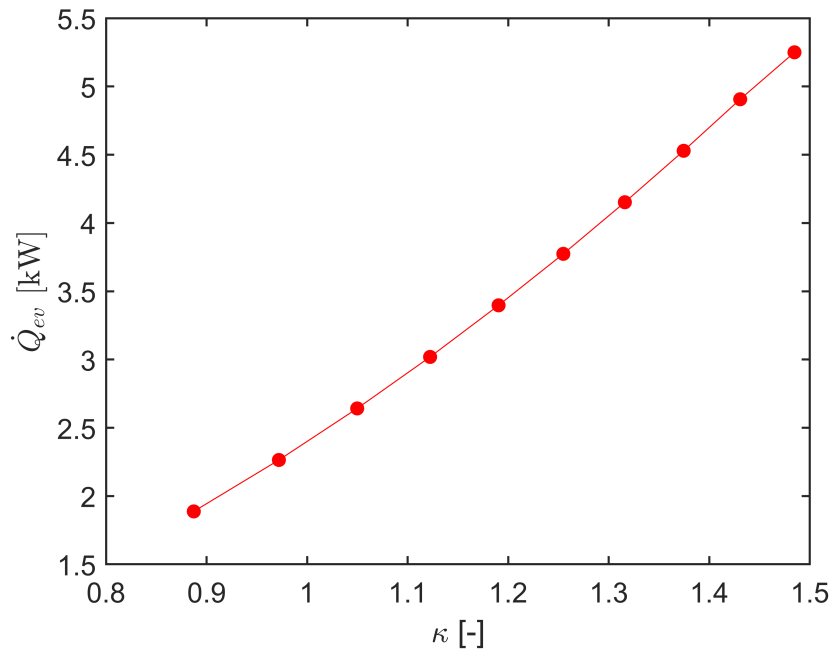
Figure 6.6: *Optimum scaling factor for different rated refrigeration capacities*

6.6 Refrigeration system characterization in off-design conditions: ARS versus FRS

6.6.1 Off-design ambient temperature

Figure 6.7 compares the efficiency of two refrigeration system architectures and their response against changing condensing conditions. As anticipated in the previous chapter the ARS offers a more flexible response, especially in the zone where the FRS operates in the subcritical mode. Here the performance gap is more pronounced. The benefits of the ARS layout are evident in all the operating envelope, being the FRS and ARS performance only comparable in the design point.

6.6.2 Off-design conditions in the hot driving source

Temperature diminution in the hot driving stream

As anticipated in the FJE characterization, the FRS suffers a severe performance degradation when the operating pressure/temperature in the generator is reduced due to a diminution in the thermal level of the driving source. Figure 6.8 informs about the magnitude of the performance drop. As a combined effect, the refrigeration capacity $\left(\dot{Q}_{ev} \right)$ and the thermal power consumed in the generator $\left(\dot{Q}_{ge} \right)$ are declined due to a reduction of the primary flow pressure. With the advanced configuration (ARS) the spindle would be helpful to avoid the drastic performance drop observed in the FRS. It has an acceptable regulation margin when compared to the FRS, however, its operating range is limited. The capacity to withstand a reduction in the temperature of

143
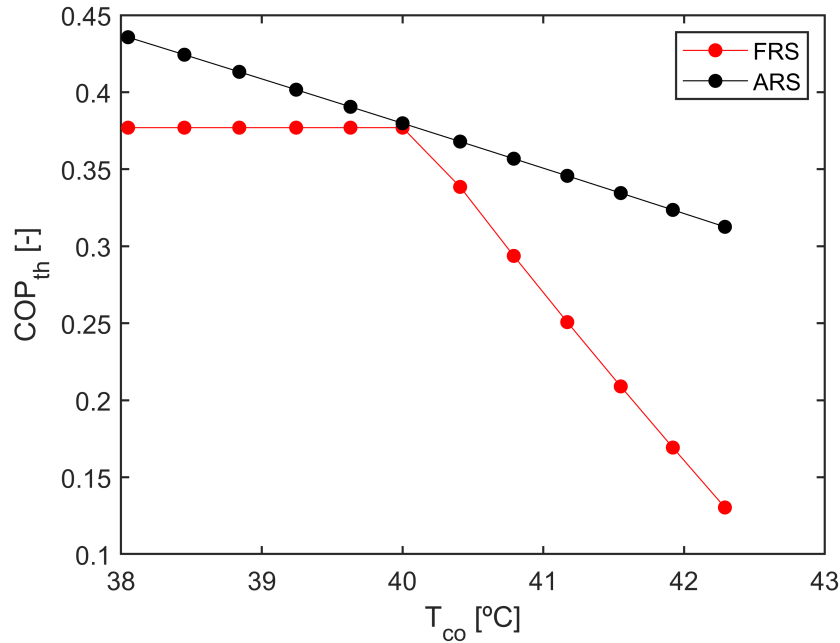
Figure 6.7: *Influence of the condensing temperature over COP_{th} for the FRS and the ARS. Both the ARS and the FRS work with $P_{ge} = 35.14\,bar$.*

the hot driving source is coupled with the ambient temperature as seen in Figure 5.8. For example, in the case depicted in Figure 6.8 it is expected that below 27.50 bar the system would suffer a severe degradation since the spindle has reached its maximum regulation capability because AR=4.22 (the spindle is completely out of the nozzle, as explained in Chapter 4).

Mass flow rate variation in the hot driving stream

A priori, a variation of the mass flow rate in the hot driving source could be the desired strategy depending on the hot driving source's thermal level. A reduction of the mass flow rate could be interesting as a conservative strategy to maintain operation against adverse climatic events, for example, in case of foreseen scarcity of solar irradiance to preserve the heat reservoir temperature. On the contrary, an increase in the mass flow rate of thermal oil could be interesting in case of sufficient thermal level to generate more refrigeration capacity or when high solar irradiance availability is foreseen in the coming hours.

With a sufficient temperature in the hot driving source, one could presume that increasing the hot thermal oil mass flow rate through the generator would be used to produce an additional refrigeration capacity. What is happening is that the flow passing through the primary nozzle throat is at choking condition and the mass flow rate cannot be modified without changing the primary flow pressure. The extra thermal power could be used to superheating the primary flow, which does not bring any benefit in terms of efficiency and is indicative of solar collector oversizing.
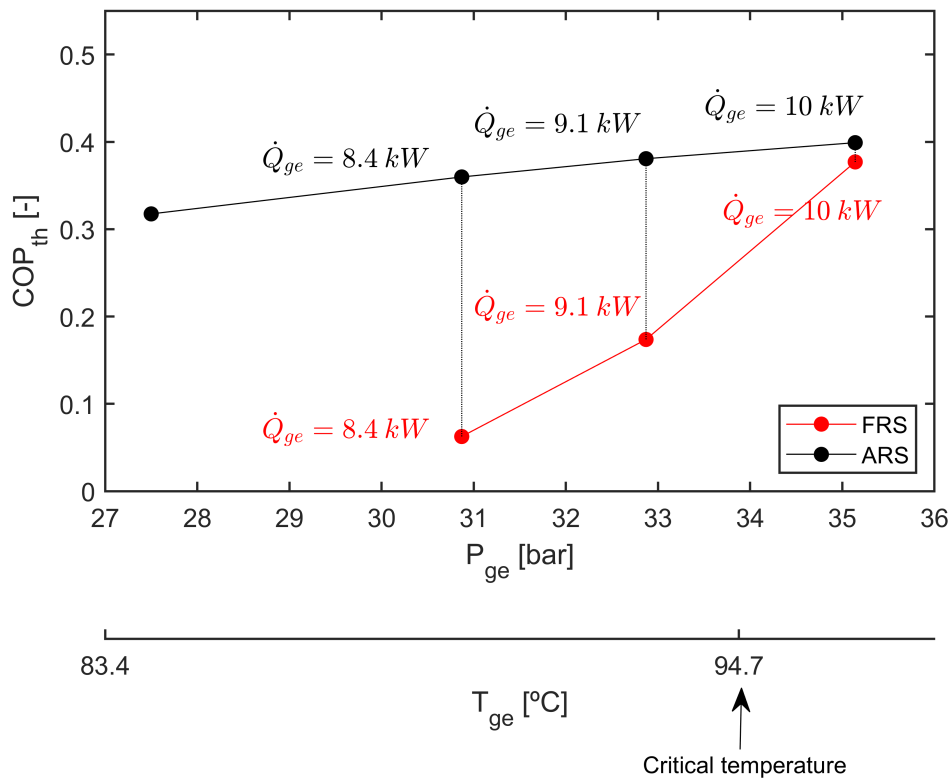
Figure 6.8: *FRS and ARS response under a reduction of the driving source temperature or, equivalently, a diminution on the generating pressure. Throughout the comparison, the condensing temperature has been assumed to be constant $T_{co} = 40°C$*

Oppositely, if the primary flow does not receive enough thermal power from the heat transfer fluid, the system might incur in malfunctioning operation since the primary flow stream might not receive enough thermal energy to evaporate completely and/or superheat the refrigerant. In such a case, two-phase flow might appear at the heat exchanger outlet and/or during the primary nozzle expansion. Figure 6.9 shows the effect of producing excessive (i), adequate (ii), and insufficient (iii) superheating in the primary flow stream leaving the generator with a fixed jet-ejector geometry.

To utilize a spindle to compensate for wrong sizing of the jet-ejector is useless since it cannot alter the mass flows passing through it without affecting its capacity to entrain the secondary flow. The ambient temperature is what dictates the spindle movement. The best alternative to effectively use the variation of mass flow rate as a thermal management mechanism would be to implement a multiejector system in which several jet-ejectors are placed in parallel and are activated/deactivated according to the real-time situation and the refrigeration needs.
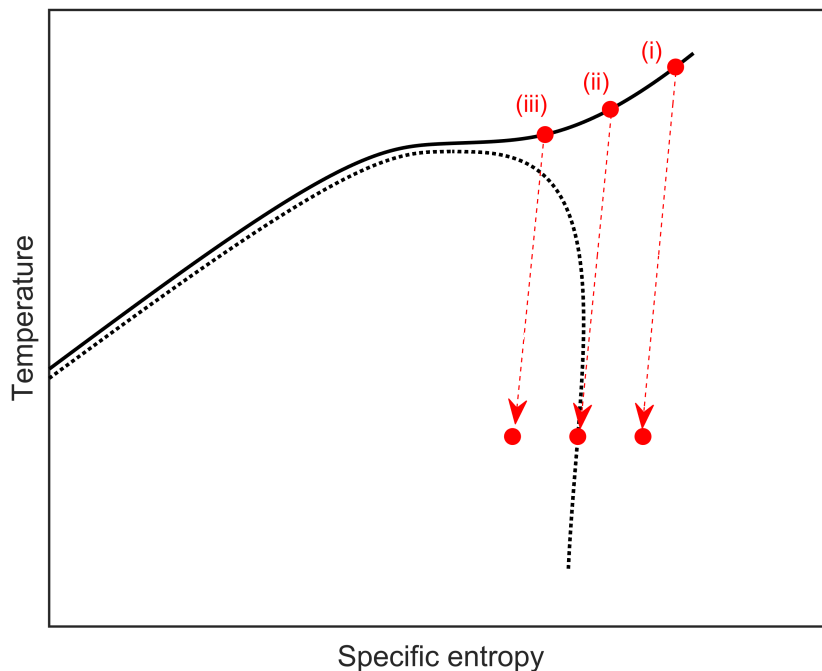
Figure 6.9: (*i*) : *Excess of thermal energy transference from the thermal oil side of the generator,* (*ii*) : *Sufficient thermal energy transference from the thermal oil side of the generator,* (*iii*) : *Deficiency of thermal energy transference from the thermal oil side of the generator.*

6.7   Summary

The convenience of using new generation benign refrigerants has been evaluated from the overall system perspective. The refrigerant R1234yf has proven to be the most

appropriate option, closely followed by R600a and R1234ze. On a practical level, other criteria should prevail in the refrigerant selection like the operating pressure, safety issues, or the installation cost, rather than the efficiency. The reason can be found in the similarities in peak system efficiency for each working fluid, which are achieved thanks to a thorough jet-ejector optimization.

The results of the present chapter evidence the superiority of the ARS architecture in off-design scenarios affecting the condensing pressure/temperature and the hot driving source temperature. After this simplified evaluation, the necessity of characterizing the system assuming a dynamic and more realistic evolution of the boundary conditions is deduced. The present analysis is helpful to understand the magnitude of the off-design performance degradation but, in a real scenario, the environmental conditions are constantly changing and the static conditions are virtually non-existent.

Chapter 7

Steady-state performance characterization of the FRS for an automotive application

7.1   Introduction

This chapter aims to analyze the refrigeration capacity that can be attained in the intake line of an automotive 1.6 l Internal Combustion Engine (ICE) using a Fixed-geometry Refrigeration System (FRS) as a mechanism to harnessing waste heat from the ICE exhaust line. The assessment is centered on the refrigeration system response in design and off-design scenarios as well as the direct and most evident impact on the engine performance. The intention is to verify that the thermal power available in the engine exhaust is sufficient to achieve a significant temperature reduction in the exhaust line. The temperature reduction achieved in the ICE intake line has been considered the main performance indicator of the FRS effect. The lower limit of admissible temperature reduction has been set in $0°C$ to avoid ice formation.

For different steady-state and representative engine operating points, the ICE intake temperature reduction has been quantified considering (i) an idealized scenario in which the jet-ejector scale could be selected for each operating point and (ii) an off-design scenario in which the jet-ejector size is fixed and the system performance is tested in engine operating points different from the operating point used to size the refrigeration system. As will be discussed, the penalty of inserting only one jet-ejector prototype is evident and causes a performance degradation away from the design point.

A more comprehensive analysis to determine the real improvement potential over the engine would have been required an engine test bench and specific refrigeration equipment. These experimental means have not been available throughout the development of the computational activities.

7.2 Definition of the study

7.2.1 Definition of boundary conditions

The model described in detail in Chapter 3, based on energy and mass balance in all the elements of the cycle has been used being fed with the ICE boundary conditions. The arrangement of the compound system has been illustrated in Figure 3.2. The jet-ejector is the same designed for the solar refrigeration application operating with R1234yf because its design conditions (condensing, evaporating temperature, and thermodynamic state in the generator) fit well also with the automotive application.

The ICE is coupled in the model using exclusively four boundary conditions: the mass flow rate and temperature in the intake line downstream the intercooler and mass flow rate and temperature downstream the turbine in the exhaust line. The influence of each ICE operating point over the boundary conditions is illustrated in Figures 7.1 and 7.2. As can be observed in Figures 7.1 and 7.2:

- The intake and exhaust mass flow rates are essentially the same, being the only difference the injected fuel during combustion.

- The mass flow rates passing through the engine tend to increase as the engine speed does. For example, the mass flow rate drawn by the ICE in the operating point defined by 1500 rpm, 25% load is almost six times lower than in the point 3000 rpm, 75% load.

- The temperature in the ICE exhaust line is relatively high, tending to increase with the engine load. This gives an idea about the favorable conditions in the ICE exhaust line.

The previous boundary conditions together with the cycle response and the operational constraints (pinch points in the heat exchangers, vapor quality restrictions...) define the refrigeration capacity and the thermal power extracted from the exhaust line.

7.2.2 Design analysis

In the design analysis, the thermal power available in the exhaust line is assumed to be a heat rejection starting from the exhaust temperature in each operating point to a temperature of 150 $°C$. The lower limit is thought to avoid the condensation of combustion products. In the design conditions, the exploitation of all the available exhaust thermal power is considered to be the optimum strategy and the refrigeration system should be scaled according to the thermal power harnessed.

The manipulable variables in this analysis are the jet-ejector scale (λ) and the evaporating pressure of the refrigeration system, or analogously, the evaporating temperature (P_{ev}, T_{ev}) since the minimum temperature achievable in the ICE intake line is, a priori, unknown.

The optimum combination of inputs is selected by a genetic algorithm under ther-
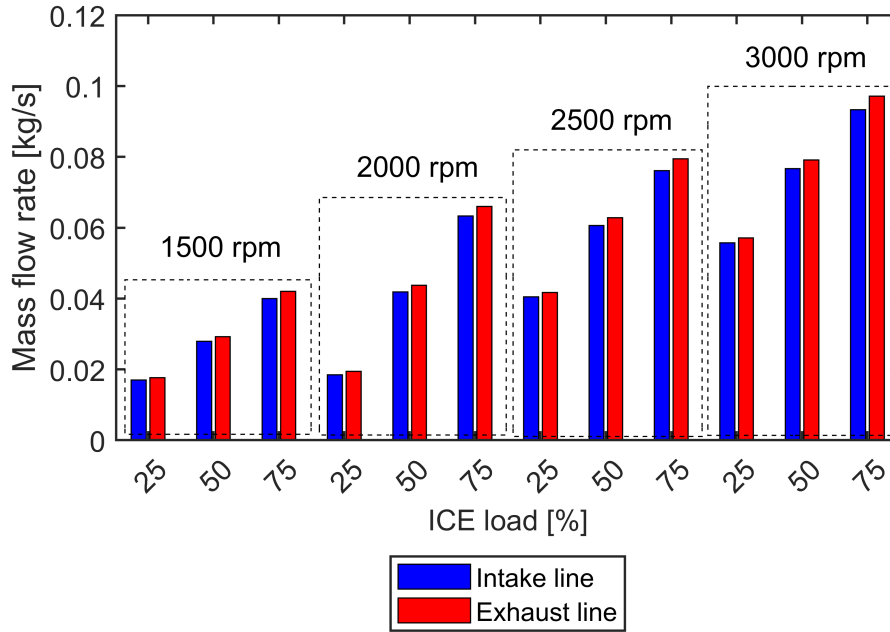
Figure 7.1: *Intake and exhaust mass flow rates passing through the ICE in different operating points.*

modynamic constraints expressed mathematically, intending to minimize the intake temperature after the refrigeration effect.

7.2.3 Off-design analysis

In the off-design analysis the jet-ejector scaling factor (λ) is fixed and corresponds to the one that maximized the refrigeration capacity for the engine point of 2000 rpm and 50% load. This is assumed to be an operating point of intensive use in passenger vehicle cruise conditions and, therefore, representative of a standard behavior. The off-design approach is more realistic because only one jet-ejector exists; the design scenario, however, represents an ideal case in which different jet-ejector prototypes could be switched in real-time as a function of the operating point.

The evaporating pressure (P_{ev}) or, analogously, the evaporating temperature (T_{ev}) is the first design or manipulable variable. The fraction of the total thermal power available ($\tau \in [0,1]$) is the second design variable (see Equation 7.1). The parameter τ would be equivalent to a bleeding or a bypass valve implemented in real equipment. Since the jet-ejector might be smaller than the one required there might be an excess of thermal power. In this analysis, the minimum admissible threshold of 150°C in the outlet temperature of the exhaust gasses is still applicable.

$$\dot{Q}_{ge} = \dot{Q}_{ge,max} \cdot \tau \tag{7.1}$$
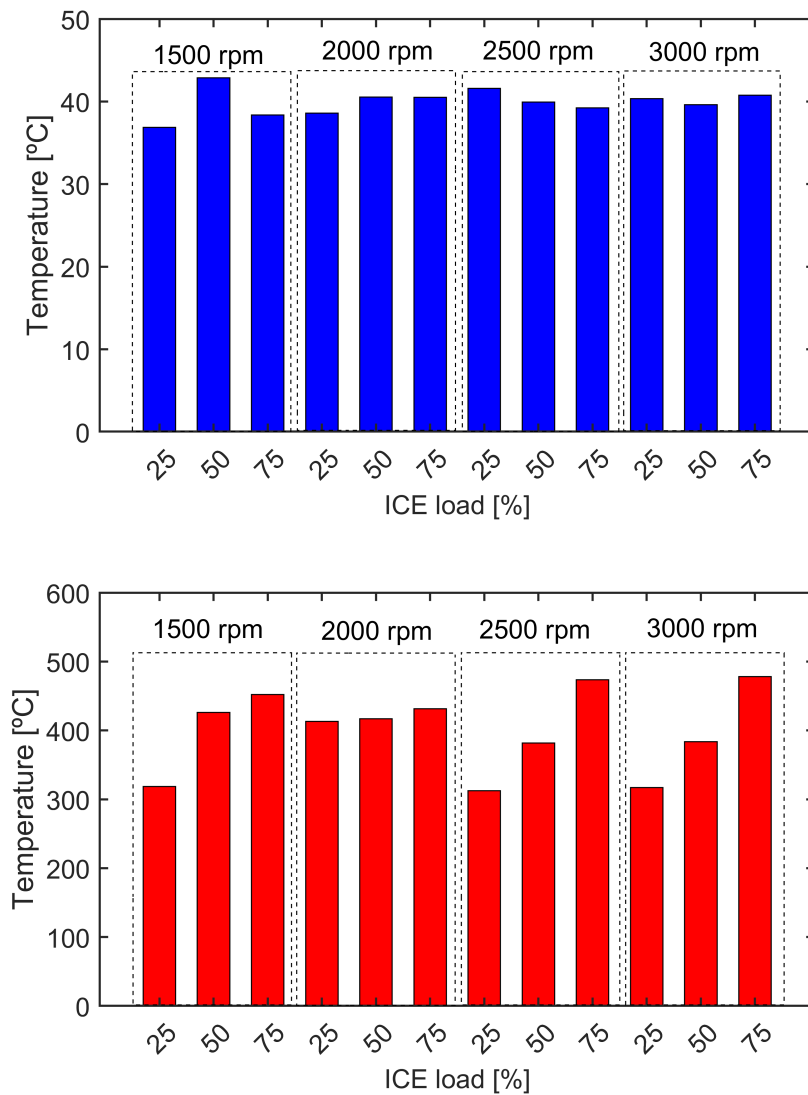
Figure 7.2: *Temperatures of the ICE intake and exhaust flows in different operating points.*

7.3   Results

7.3.1   Design analysis

In the design analysis, the jet-ejector scale can be adjusted optimally for each ICE operating point. Figure 7.3 shows the optimum scaling factors of the jet-ejector, which should be applied to the values of Table 4.1 to know the real dimensions. As can be observed, there is a remarkable difference between the optimum jet-ejector scales for the two extreme engine operating points (3000 rpm - 75% load and 1500 rpm - 25% load), which evidences the problem of designing a robust refrigeration system in the whole engine map.
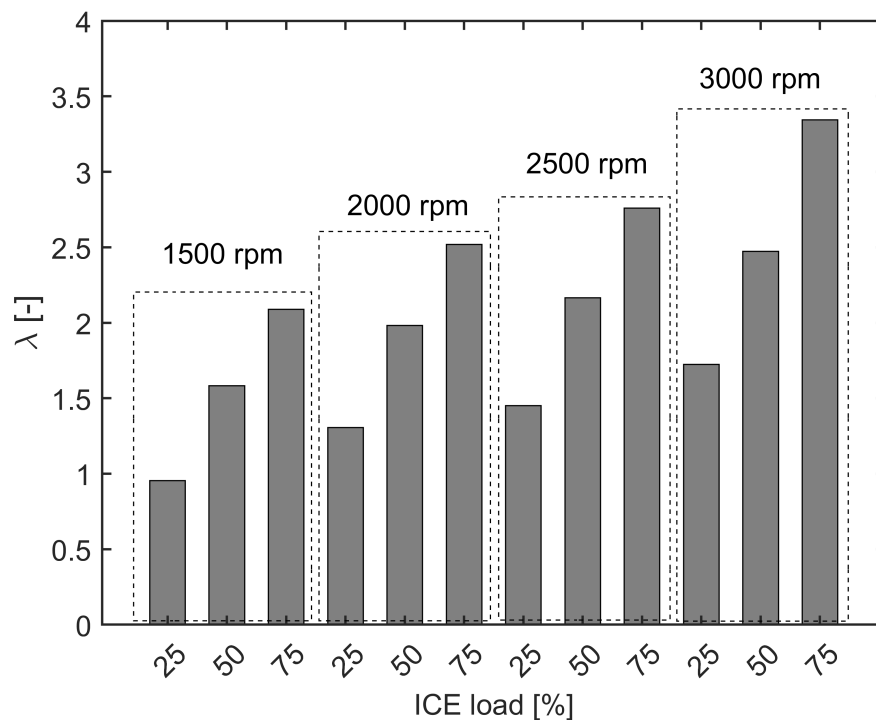
Figure 7.3: *Optimum jet-ejector scaling factor for each ICE operating point*

Temperatures close to zero degrees can be achieved according to Figure 7.4 because the optimization algorithm reaches a lower evaporating temperature at the expense of degrading the refrigeration system efficiency and jet-ejector entrainment ratio. Temperatures in the intake line ranging from $3.5°C$ to $5.9°C$ could be achieved using the present refrigeration solution. The greatest temperature reduction in the intake line ($38.1°C$) is found for the operating point 1500 rpm, 50% load. The COP_{th} ranges between 0.043 and 0.102 but this is not a critical issue because the available ICE exhaust energy is abundant and, in contrast to the solar application, here the efficiency is not a critical parameter because the reception of thermal energy has no associated cost.

The design analysis evidences that the implementation of a multiejector rack with different jet-ejector scales would be effective to maintain the system performance.

153

7.3.2 Off-design analysis

In the off-design analysis the scale of the jet-ejector operating in the point 2000 rpm, 50% load has been selected ($\lambda = 1.98$). Figure 7.4 shows the temperature reduction that can be achieved with the off-design approach. As can be expected, the refrigeration system operation suffers performance degradation.

In the ICE operating points marked in light blue color, the FRS can achieve a substantial temperature reduction but not as high as the design approach. These points are characterized by higher availability of exhaust line power but also higher refrigeration needs in the ICE intake line. To counteract the off-design conditions, the algorithm increases the evaporating temperature to improve the jet-ejector entrainment ratio. This improves the refrigeration capacity and the COP_{th} but affects the minimum temperature achievable in the ICE intake line. The temperature reduction, notwithstanding is comparable to the one achieved by the design approach as illustrated in Figure 7.5, and the maximum differences are found in the point 3000 rpm and 75 % load ($+3.2°C$). Figure 7.5 also shows the fraction of the total available power in the ICE exhaust line that can be harvested. As the ICE conditions deviate from the reference ICE point (2000 rpm and 50 % load), the fraction of thermal power used is lower.

As can be observed, in those ICE operating points characterized by lower load and, therefore, lower drawn mass flow and lower exhaust thermal power, the FRS model is unable to make predictions (bars marked in grey color). This is a malfunctioning situation in which the system response is uncertain. The jet-ejector CFD maps do not tolerate the two-phase flow condition and any prediction would not be reliable.

7.3.3 Impact over engine efficiency and discussion of architectures

Assuming an ideal gas law, the reduction in the ICE intake line temperature can be directly related to an increment in the ICE intake line air density. Assuming that the ICE performance parameters remain the same, the temperature reduction brings increments in trapped mass flow rates and ICE power of about 10 % as depicted in Figure 7.6.

To quantify with precision the indirect benefits caused by the intake air refrigeration, like pollutant emissions, a dedicated experimental facility would be required.

To sum up, there would three implementation options:

- **Turbocharger exclusively:** This is the current implementation and the benefits are well known. This would probably be the cheapest option.

- **Jet-ejector refrigeration system exclusively:** The refrigeration system would produce the ICE intake air refrigeration but the positive effect over engine performance caused by turbocharger air compression would be lost. The jet-ejector coupling without a turbocharger would not be competitive due to, (i) poor off-design performance of the jet-ejector refrigeration system, (ii) response delay to produce the refrigeration effect due to thermal inertia of the refrigeration system.
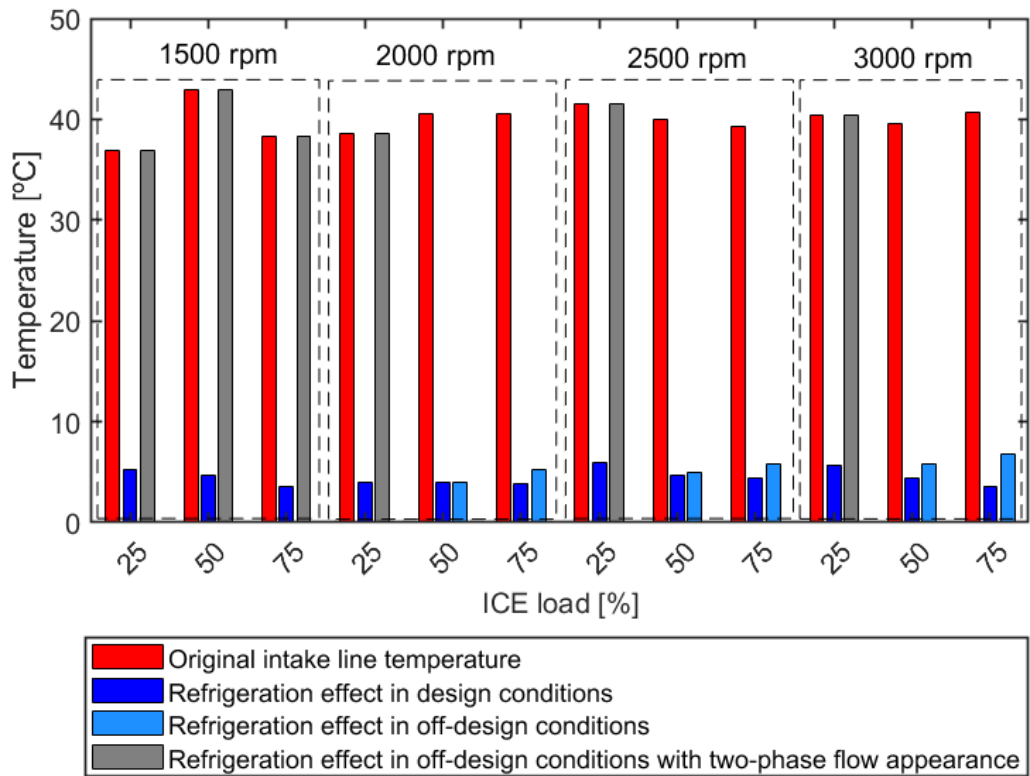
Figure 7.4: *Refrigeration effect in design and off-design conditions produced by the jet-ejector refrigeration system.*
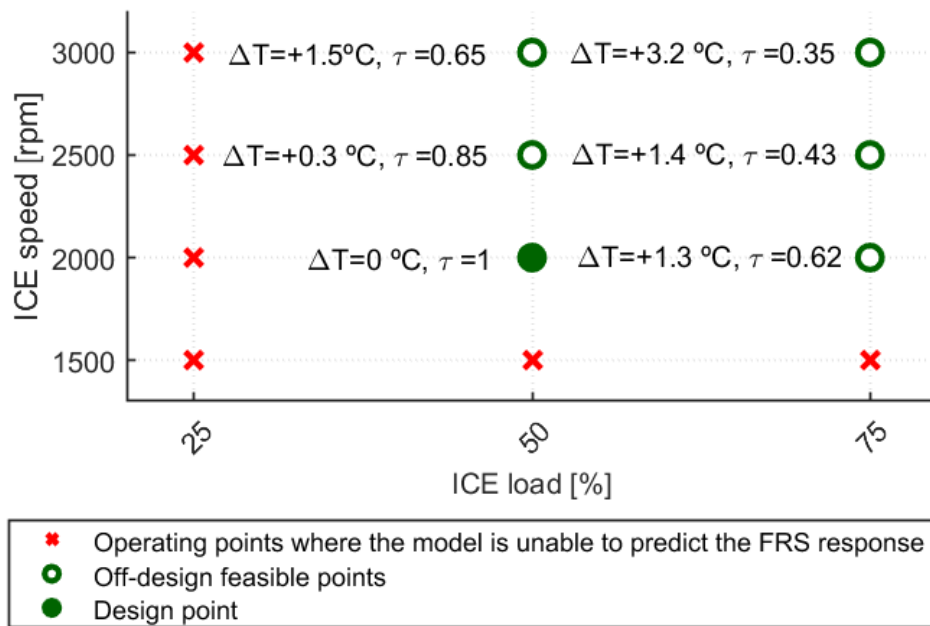
Figure 7.5: *Difference in temperature reduction between the design and off-design
approaches together with the fraction of the exhaust energy harnessed.*

This contrasts with the relatively fast response of the turbocharger.

- **Combination of systems:** This would be the best option from the operational
  point of view, however, some of the expected potential outcomes, like the reduc-
  tion in pollutant emissions have not been characterized in the present research
  work due to the unavailability of experimental facilities. Hence, some the rele-
  vant information to discern if the system would have economic and operational
  profitability is missing. Without a doubt, this arrangement would be the costlier
  option and the final decision would not be straightforward. Financial sustain-
  ability criteria, together with pollutant regulations would be the most relevant
  factors to take a decision. The final decision would depend mainly on the follow-
  ing aspects:

  1. Design and off-design response of the system with recalibrated engine set-
     tings under real driving behaviours.

  2. Real pollutant emissions abatement.

  3. Equipment cost (assuming large scale manufacturing).

  4. Gravimetric and volumetric power densities of the refrigeration system.
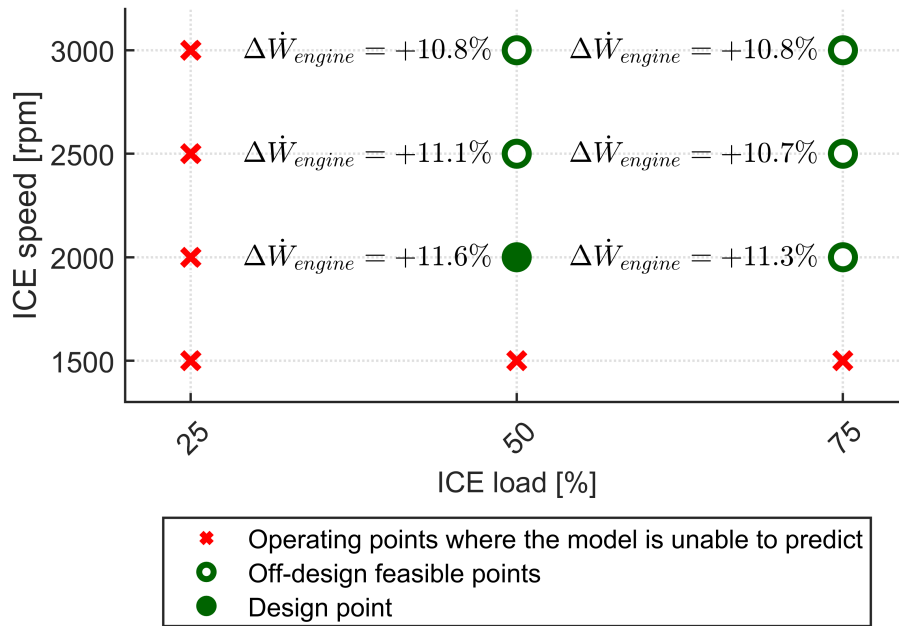
Figure 7.6: *Improvement of the ICE power associated to the intake air refrigeration*

7.4 Summary

In the present chapter, the feasibility of inserting a FRS to recover waste heat from an automotive 1.6 l Diesel engine to produce a refrigeration capacity on the engine intake is analyzed. This represents an application with peculiar boundary conditions: (i) the thermal source has a lot of energy available and (ii) the mass flow rate of the hot driving flow and the flow with refrigeration needs are essentially the same.

The main conclusion is that the exhaust thermal power is sufficient to produce a remarkable refrigeration effect. In design conditions temperatures below $5°C$ can be attainable. Such a low temperature can be achieved at the expense of reducing the system efficiency, that is, assuming a higher thermal power consumption per unit of refrigeration capacity, however, this is admissible because of the high availability of thermal power in the exhaust line at no additional cost.

Another relevant finding is that a refrigeration system operating with a unique jet-ejector has a limited operative range. The ICE conditions (mass flow rates and temperatures in the intake and exhaust lines) are highly changeable during a standard driving behavior. The FRS behaves robustly only in a region close to ICE operating point used to optimize and size the refrigeration system. Away from that region, the thermal power is insufficient to drive the system in some points or it is excessive in others, so only a fraction of the thermal power can be exploited. The underexploitation of the exhaust power produces a refrigeration effect less pronounced.

The direct effect of the refrigeration capacity over some engine performance indicators has been highlighted. The highest potential of the concept described might be visible in the so-called indirect effects, like the pollutant emissions abatement, as outlined in the literature. Reliable estimations should be made in an engine test bench modifying default ICE settings.

Part II

Dynamic response of the refrigeration system

Chapter 8

Dynamic response of the FRS and the ARS architectures in a solar refrigeration application

8.1   Introduction

The present chapter is dedicated to present the dynamic study of the Jet-Ejector Refrigeration System (JERS) using two cycle architectures. The aim is to evaluate the superior performance of the Adjustable Refrigeration System (ARS) anticipated in the steady-state analysis when compared to the Fixed-geometry Refrigeration System (FRS). That is, the benefits of using an advanced adaptive strategy (ARS) during continuous operation are compared with the capabilities of the standard and simpler strategy (FRS) widely postulated in research works dealing with jet-ejector refrigeration systems. To carry out a fair comparative, two complementary approaches have been considered: The first analysis attempts to explain the differences between both cycle architectures considering a short period. The analysis at this level offers useful insights because it allows assessing in detail the system's response against some frequent adverse events. However, these specific events and their random nature have a strong influence on the system's performance and impede to elucidate general findings.

The system response against a succession of these random climatic events, though, makes the evaluation independent of punctual climatic phenomena and allows to obtain generalized and global conclusions. The second analysis is focused on global averaged figures, which are helpful and adequate to estimate the expected performance over a month, for example. However, some information is lost since a high amount of data is summarized in few averaged figures.

A combination of the aforementioned approaches has delivered a detailed and in-depth evaluation, bringing to light which are the strengths and weaknesses of each system architecture.

8.2 Definition of the study

8.2.1 Hypothesis and constraints

The response of both the FRS and ARS has been evaluated feeding the transient models with the instantaneous evolution of solar irradiance and ambient temperature over a minimum of few days and a maximum of whole months. The TMY datasets have been selected to feed the dynamic model because it represents a consistent sample of the long-term averages for the geographic location in question. The geographical area selected to carry out the analysis is a region with abundant sunny hours during summer periods. The available hourly data has been interpolated linearly to increase the resolution of the temporal grid.

On the first day of the month, the system is turned on at 00:00 hours, being the initial temperature of all the elements the ambient temperature. The first hours after the sunrise are dedicated to heating the TSS if the solar irradiance conditions are favorable. The aim is to achieve a certain temperature in the tank to start the JERS operation. With scarce or no-existent solar irradiance the system start-up is inevitably delayed. After reaching the thermal level threshold, the JERS can be started and produces a refrigeration capacity. From this moment on, the system remains operative if there exist refrigeration needs, i.e., when $T_{amb} > 25°C$ and within the hours 08:00-19:00.

The following hypothesis and simplifications have been considered:

- Pressure losses are neglected in the heat exchangers and the conduction lines.

- The JERS heat exchangers have been assumed to have negligible thermal inertia when compared to the TSS or the PTC line. Hence, the TSS and the PTC line govern the system's transient response.

- The JERS rate of energy consumption corresponds to 15 kW at the reference condensing temperature $T_{co} = 40°C$, which corresponds approximately to a refrigeration capacity of 5.4 kW at the targeted evaporating temperature $T_{ev} = 13°C$. Since the jet-ejector scale is fixed the spindle is only displaced to counteract changes in ambient conditions. Hence, the spindle movement is not a degree of freedom to change the thermal power consumed by the ARS. The refrigeration system control law moves the spindle trying to maximize COP_{th} or, equivalently, in this case, the refrigeration capacity.

- The TSS volume selected in this chapter $(2.04 \, m^3)$ is not subject to analysis but it has been fixed. According to preliminary trial-and-error simulations, this TSS volume fits well with the PTC line span (7.08 m) and the rated thermal power consumption (15 kW). Such system dimensioning of the elements allows a continuous operation when the solar irradiance is temporarily unavailable. The influence of the TSS size on overall system performance has been assessed in the following chapter since an optimum must exist.

- The jet-ejector spindle in the ARS is displaced instantaneously to its optimum

position, which is determined as a function of the current ambient temperature.

8.2.2 Resolution strategy and post-processing

The system is resolved following the scheme depicted in Figure 3.23. The set of discretized equations are solved for each time step over a month. The instantaneous performance indicators are recorded during the calculation and then, in the postprocessing stage, the time interval subject to analysis is easily extracted from the dataset. The instantaneous data practically does not require postprocessing activities and its representation is very visual.

The averaged indicators translate the instantaneous behavior to general and more readable figures. The first step is to compute the time lapses in which there are refrigeration needs along the whole period under examination. The second step is to determine the system response over the time periods with refrigeration needs. The averaged performance indicators over a selected period have been obtained by averaging each variable using auxiliary data sets registered during the calculation like the system state (activation/deactivation flags) in each time step. This operation is performed at the local scale, inspecting the instantaneous data with automated functions.

8.3 Results comparing the FRS and ARS architectures

8.3.1 Instantaneous evolution of the performance indicators

Figure 8.1 represents the temporal evolution of the refrigeration system's main performance indicators and the evolution of some relevant climatic data over a whole month (July of the TMY). The intention is to compare the FRS and the ARS in terms of flexibility and capacity to withstand adverse operating conditions.

It is observed in Figure 8.1 that when the climatic conditions are favorable, that is, in clear-sky scenarios, the TSS size, the nominal power extracted from the TSS, and the PTC line span are adequately selected to maintain a continuous operation. Hence, under favorable climatic conditions, the system operates correctly and the delivered refrigeration capacity could meet other design requirements by simply scaling the installation.
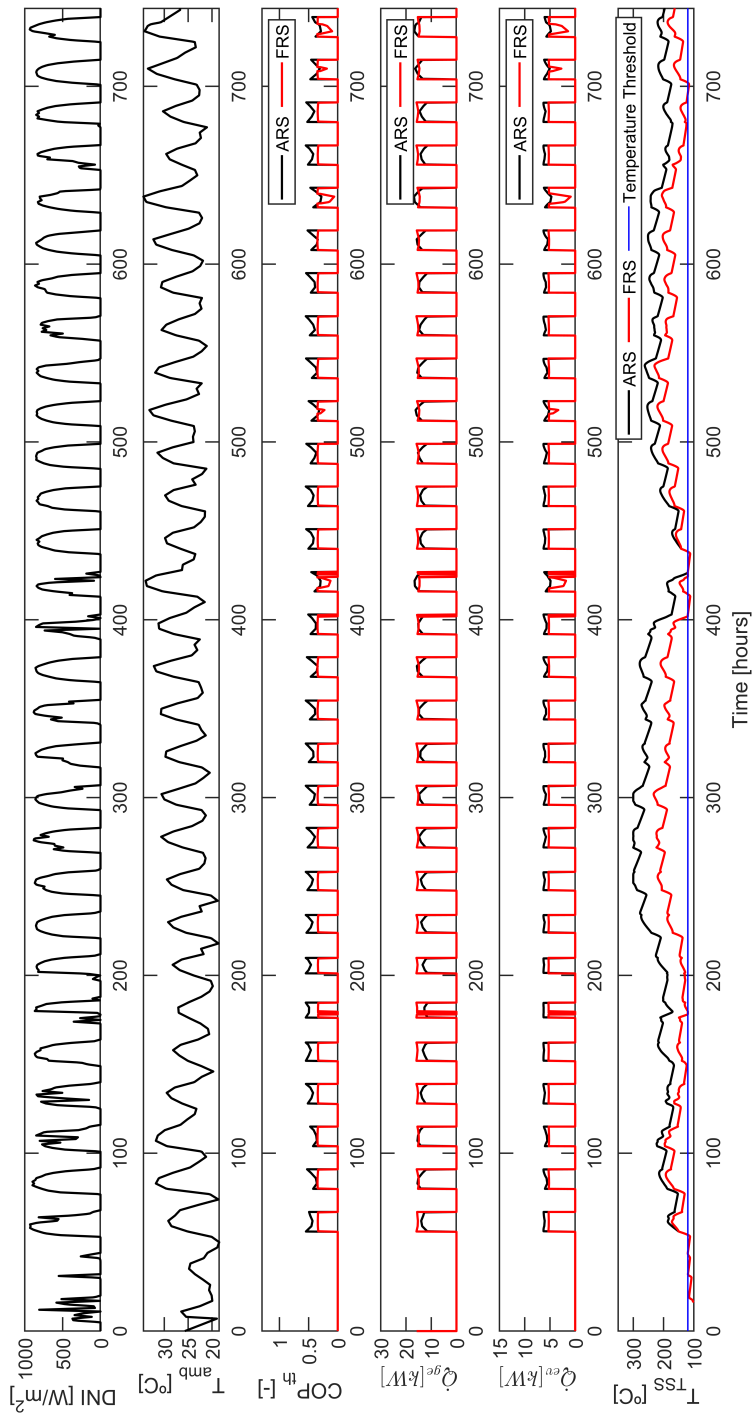
Figure 8.1: *Instantaneous evolution of the main performance parameters of the refrigeration system along the whole month of July of the TMY*

Some differences in behavior are observed between both configurations, indicating that the jet-ejector architecture has a decisive impact on its performance. To discern the cause of such discrepancies Figure 8.2 focuses on the system start-up during the early hours of the month (1st of July). The precise start-up moment is marked in a green rectangle with transparency. In the initial instant, the temperature of all the equipment corresponds to the ambient temperature. At sunrise, the TSS starts to increase its temperature as the sunbeams reach the PTC and the thermal oil recirculates to the tank. Being the ambient temperature far lower from the FRS design temperature ($31\ ^\circ C$), the ARS spindle is adapted conveniently to this off-design scenario increasing the system efficiency. As a result, the ARS consumes less thermal energy to produce a refrigeration capacity very similar to the one produced by the FRS. The lower consumption maintains a higher temperature inside the tank as can be observed in the green boxes. The key aspect is that the more efficient solution (ARS) makes more efficient management of the heat reservoir avoiding greater consumption. This trend observed in the first hours after the startup is going to have a decisive influence over the rest of the month.

Two particular situations occurring in the reference month (July) have been analyzed in more detail to compare the dynamic behavior of the FRS and the ARS under specific circumstances. These specific events, despite their random nature, are likely to occur in continuous operation during the warmer months of the year.

The first one has a duration of three days and envisages the appearance of a partially cloudy day and the consequent lack of thermal level in the thermal storage system as depicted in Figure 8.3. The dashed vertical lines delimit the hourly interval of interest (08:00-19:00) when computing the performance parameters. It is worth emphasizing that the ambient temperature in this interval is always below $31\ ^\circ C$, which is the reference ambient temperature for the FRS. Under these circumstances, the ARS has great potential to improve the efficiency of the refrigeration system.

When either the FRS or the ARS are activated, the rate of energy supply in the TSS is slightly greater than the rate of energy extracted towards the refrigeration system if the climatic conditions are favorable. Given this narrow margin, both refrigeration systems behave differently depending on their configuration. The ARS required less thermal power coming from the TSS in the preceding hours and days to operate the refrigeration system. This fact is visible when the parameter T_{HTF} of both configurations are compared at the beginning of the first day (7th of July). Owing to this better management of the TSS thermal level, the heat reservoir is enough to face the temporary lack of solar irradiance occurring on the second day depicted in Figure 8.3. The instantaneous temperature in the TSS is all the time above the temperature defined as the threshold ($120\ ^\circ C$).

At the beginning of the third day, the thermal level of the TSS is still sufficient to drive the ARS despite the thermal losses to the ambient occurring during the night. Along these sample days, the ARS is running 100% of the time showing an average $COP_{th} = 0.5$. By contrast, the FRS extracted more heat power from the heat reservoir in the preceding days so that it has a lower capacity to cope with the absence of solar
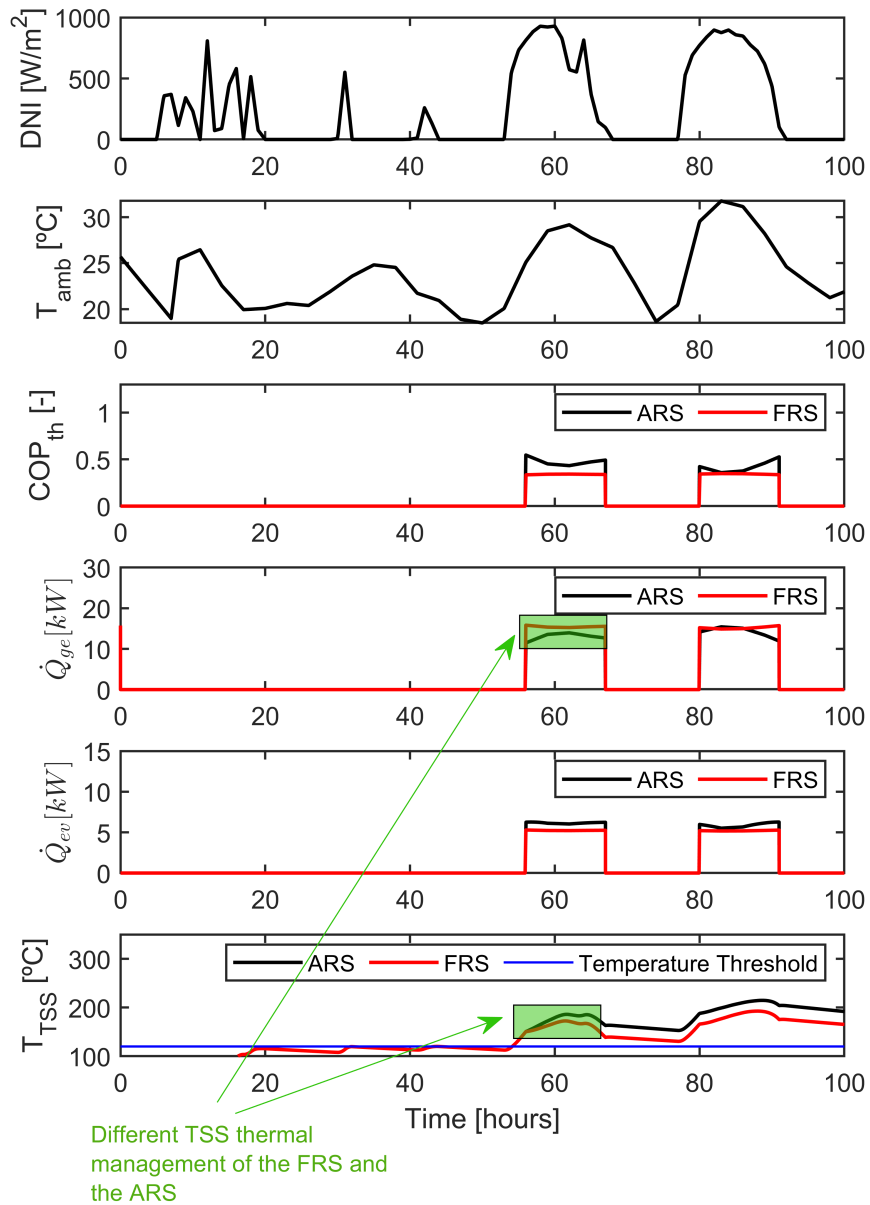
Figure 8.2: *Different behaviour observed in the FRS and the ARS after the system start-up*

irradiance in the early hours of the second day. When the low-temperature threshold is reached, the control law deactivates the refrigeration system. This aims to restore rapidly the thermal level in the TSS with the hot flow coming from the PTC.

The lack of available thermal power causes an irregular functioning of the refrigeration system leading to successive on and off sequences that are marked in Figure 8.3 with shaded profiles. The interruption harms the average COP_{th} and cooling capacity as can be seen in Figure 8.3. The average COP_{th} equals 0.32 and the activation percentage reaches 95.3 %.

The second scenario (see Figure 8.4) is characterized by an almost continuous solar irradiance supply, which translates into a continuous operation along the five sample days. Indeed, both refrigeration systems remain active 100% of the required period. The ambient temperature along these days, notwithstanding, exceeds the FRS reference ambient temperature of 31 °C at certain moments. This means that in the FRS the jet-ejector might operate in the single-choking mode or even in its backflow mode in certain time slots with the consequent performance drop. Indeed, it occurs and it is visible in Figure 8.4 when the refrigeration capacity and COP_{th} decrease sharply. The unusually high temperatures occur in the 1st, 4th and 5th days and coincide with the performance degradation. The average COP_{th} shown by the FRS corresponds in this sample five days to 0.30. Conversely, the adaptation capability shown by the ARS in this off-design scenario has a positive impact on the average efficiency, reaching a $COP_{th} = 0.40$.

As a general trend, it has been observed that the ARS is an effective method to extend the operative range of the refrigeration system in the absence of solar irradiance as well as increasing its performance. Its superior performance lies in the more efficient management of the thermal energy available in the storage system when the operating conditions differ from the reference/design conditions. Indeed, when the analysis is extended to the overall month, the ARS exhibits a superior average COP_{th} (0.42 versus 0.31) and activation percentage (96.5% versus 95.2%) when compared to the FRS.

8.3.2 Time-averaged performance indicators

The analysis of the monthly figures provides a more comprehensive overview of the real improvement potential derived from the ARS utilization. To do so, the instantaneous evolution of the main performance indicators along the TMY months with frequent utilization of air-conditioning units has been collected to present daily and monthly average figures. This exploration allows examining general trends more precisely.

The histogram plot of Figure 8.5 illustrates that the ARS improves the FRS efficiency irrespective of the month under consideration. To homogenize the representation of both configurations, ten levels of COP_{th} have been considered for each jet-ejector architecture to create the histogram, except for May, in which three levels are considered. This decision is sustained in the low dispersion of the results found in May.

The FRS has been designed to operate satisfactorily with an ambient temperature up to 31 $°C$, however, the appearance of more favorable outdoor conditions does not
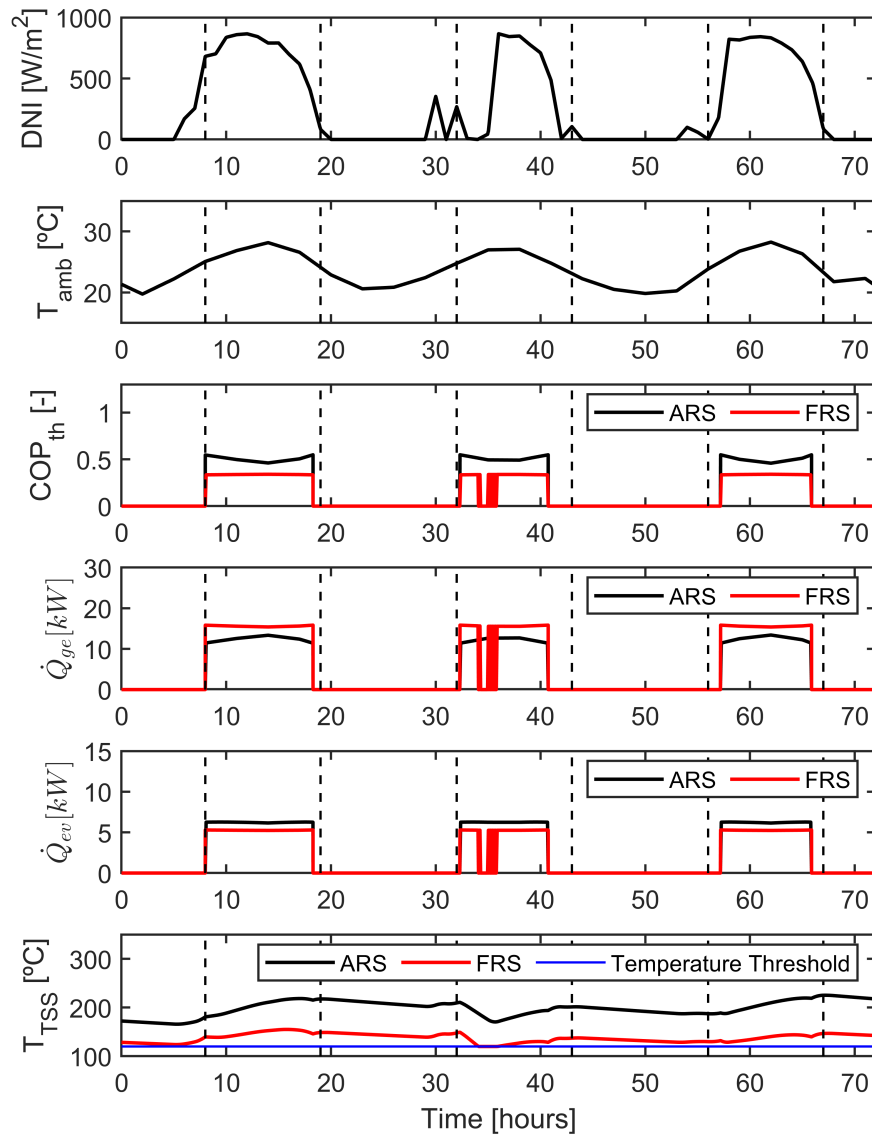
Figure 8.3: *Instantaneous evolution of the main performance parameters of the re-frigeration system: case of study 1: $7^{th} - 9^{th}$ of July*
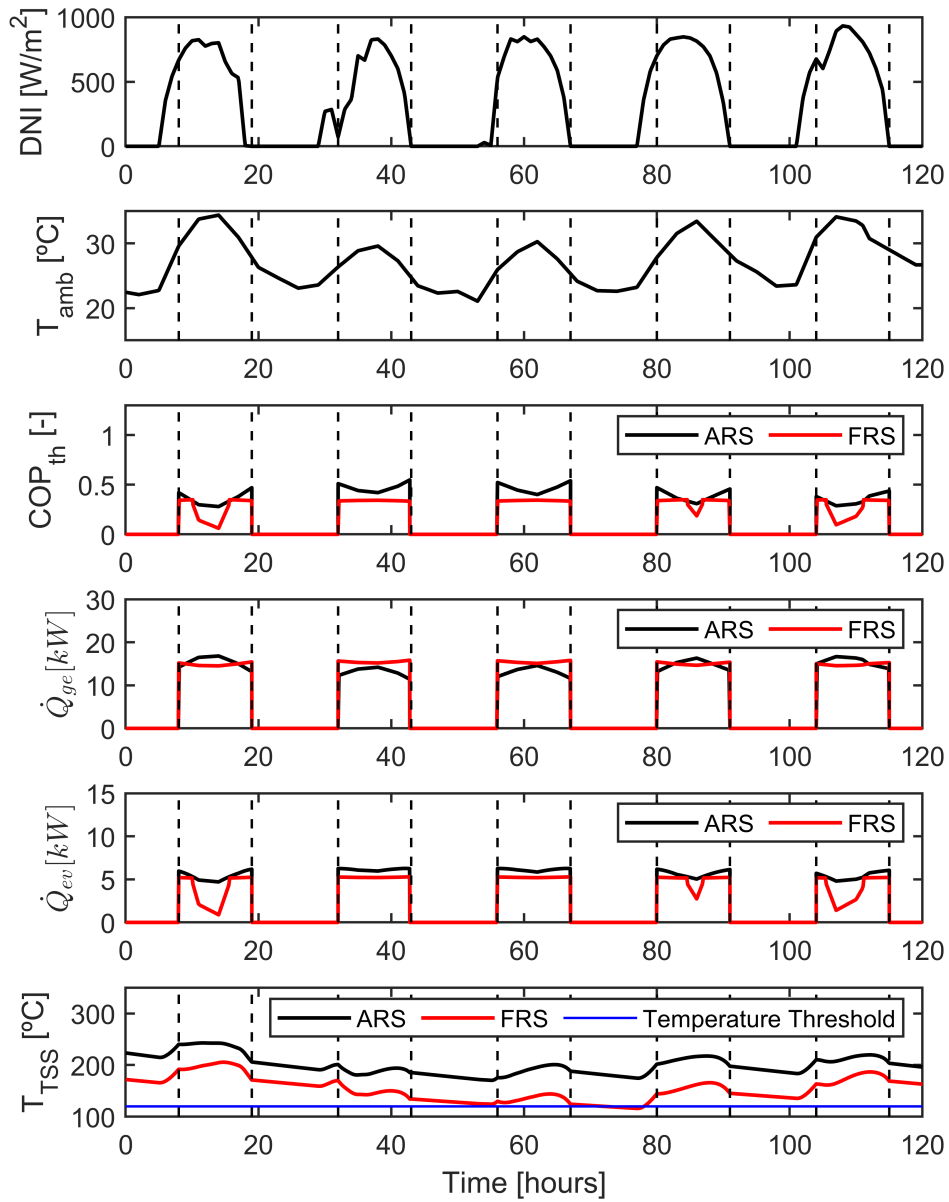
Figure 8.4: *Instantaneous evolution of the main performance parameters of the refrigeration system: case of study 2: $27^{th} - 31^{st}$ of July*

bring any benefit owing to the invariable response of the FJE when it works in the so-called double-choking operating mode. This establishes an upper limit in the maximum achievable COP_{th} for the FRS. Taking the month of July as a representative sample it is observed that 25 days show a COP_{th} ranging between 0.31 and 0.35. Contrarily, the ARS allows gradual adaptation to outdoor conditions and has a great potential for improving the jet-ejector entrainment ratio. It guarantees smooth operation and prevents the jet-ejector from functioning in single-choking mode, where its performance is severely degraded. Indeed, in 5 days along this month, the ARS operates with a COP_{th} ranging between 0.47 and 0.52.

It must be outlined that the penalty caused by FRS is more evident in those months with lower average ambient temperature, that is, May and September (Figure 8.6). In these months, the average ambient temperature differs more from the FRS design ambient temperature (31 $°C$) and the improvement potential offered by the ARS is greater. The average ARS COP_{th} in May and September corresponds to 0.48 and 0.44, respectively, while the FRS reaches COP_{th} values of 0.34 and 0.31.

As highlighted before, the ARS can harness the thermal energy of the storage system more efficiently, especially in those periods with lower average ambient temperature, which in turn contributes to preserving the thermal storage system temperature above the threshold. Ultimately, it allows the ARS system to remain in operation more time than the FRS. This effect is visible in Figure 8.7. The ARS achieves greater activation percentages in all the months under evaluation. It must be noted that this performance indicator strongly depends on the climatic conditions and the appearance of recurrent events with intermittent solar irradiance. For instance, the lower activation percentage observed in August can be attributed to incapacity to activate the refrigeration system because of successive partially-cloudy days occurring throughout the month. Under these circumstances, an efficient management of the TSS thermal level facilitates reaching the TSS temperature threshold and putting the refrigeration system into operation. Indeed, the difference in the activation percentage between both architectures is more pronounced in this month (84.5% attained by the ARS versus 81.1% attained by FRS).

8.4 Summary

In this chapter, the dynamic response of a solar-driven jet-ejector refrigeration system equipped with a hot thermal storage system and two different jet-ejector architectures has been evaluated numerically. The first one consists of utilizing a jet-ejector with fixed geometry, which is optimized to operate satisfactorily against a relatively high condensing temperature (40 $°C$). The second one lies in a jet-ejector with an adjustable spindle that is actively controlled depending on the instantaneous condensing temperature.

The adjustable jet-ejector refrigeration system showed a significant improvement in all the months evaluated when compared to the fixed-geometry refrigeration system. The average COP_{th} along the month with the highest outdoor temperature (July) cor-
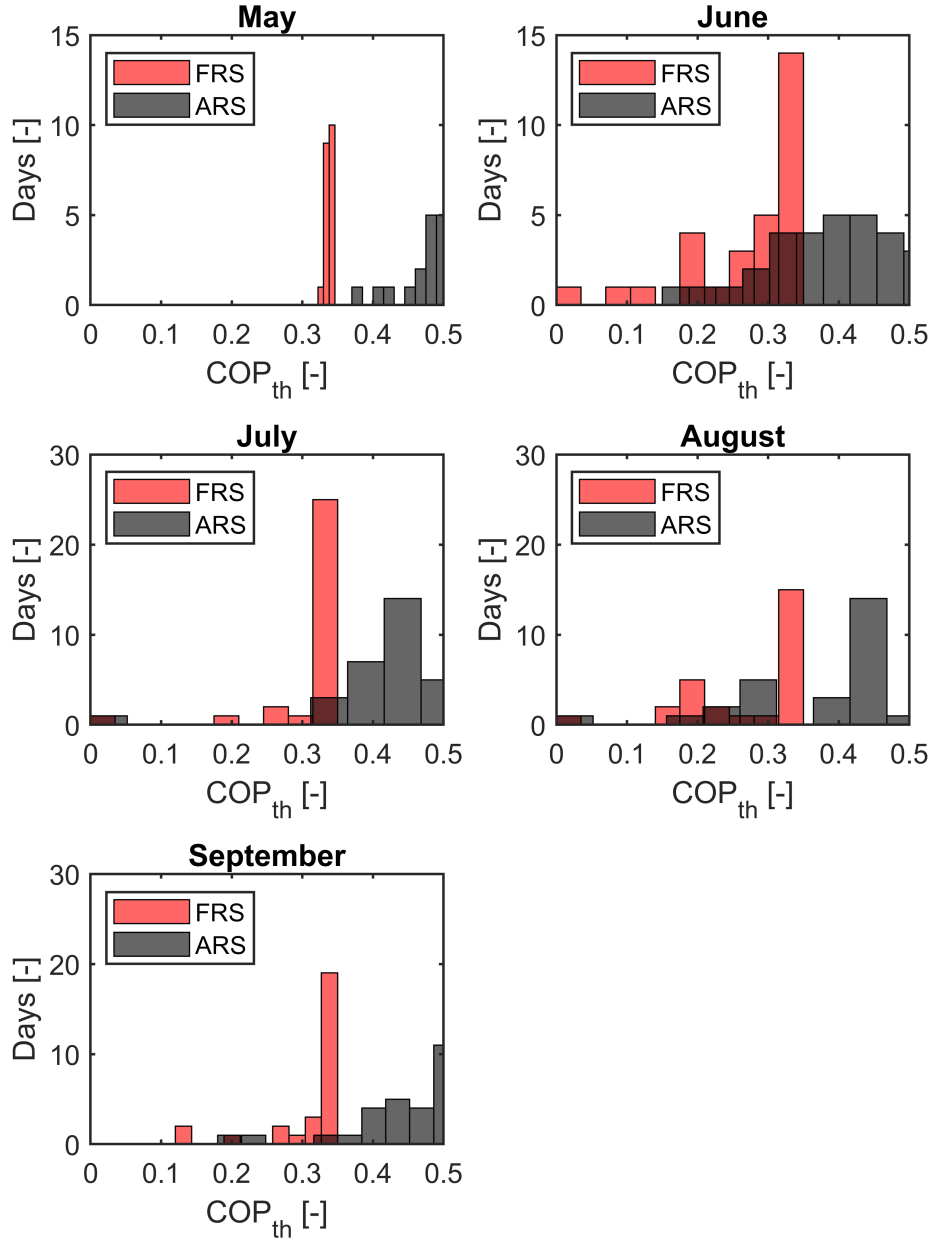
Figure 8.5: *Distribution of the daily average COP_{th} achieved by the FRS and the ARS along the warm months of the TMY. *Only the days with refrigeration needs have been represented: May (20 days), June (30 days), July (30 days), August (27 days), September (28 days).*
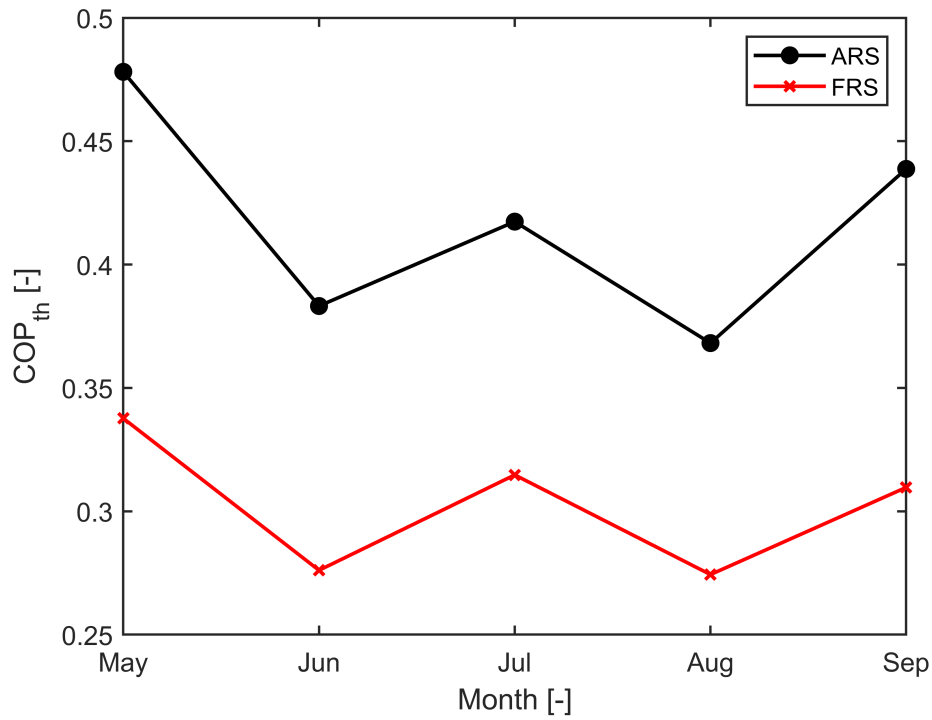
Figure 8.6: *Monthly average COP_{th} in the warm months of the TMY.*
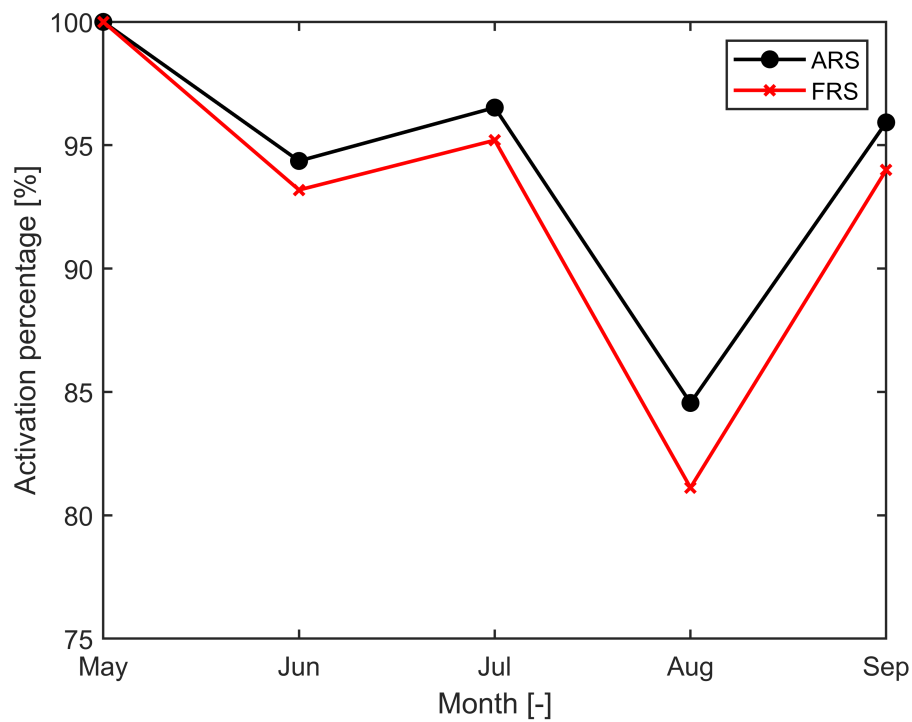
Figure 8.7: *Monthly average activation percentage in the warm months of the TMY.*

responds to 0.31 when the fixed-geometry configuration is used, whereas the adjustable layout reaches $COP_{th} = 0.42$. The potential improvement is even greater in May and September, when the average condensing temperature is normally far lower from the fixed jet-ejector design condensing temperature. Indeed, in May the greatest performance difference is found. In this month, the fixed-geometry architecture exhibits an average $COP_{th} = 0.34$ while the adjustable layout reaches a $COP_{th} = 0.48$. The adjustable jet-ejector has demonstrated to be a useful mechanism to both extend the operational range of the refrigeration system as well as improving its performance due to its:

- Greater flexibility allowing for a smooth operation when the fixed jet-ejector critical condensing temperature is exceeded.

- More efficient management of the thermal level available in the storage tank thanks to the lower thermal power consumption when the instantaneous condensing temperature is below its critical value. This explains its superior ability to remain in operation when the solar irradiance is insufficient.

Given the superior performance of the ARS, this configuration has been selected for the following analysis. The intention is to evaluate the refrigeration system with the layout that offers the greatest potential.

Chapter 9

Influence of the thermal storage system sizing on the ARS in a solar refrigeration application

9.1 Introduction

As evidenced by the transient analysis of the conventional and advanced architectures of the refrigeration system, its ability to deliver continuous operation depends to a large extent on the thermal energy storage system. Its size is directly related to its thermal inertia and its effectiveness to prolong the system operation with a scarcity of thermal power supply. Furthermore, as indicated by the mathematical models found in the literature, its sizing has implications in its investment cost. A coherent system sizing has the potential to improve notoriously the system efficiency and autonomy as well as its competitiveness against well-established traditional refrigeration solutions.

The definition of a robust methodology to make an informed selection is something that has not been addressed in the open literature. There is not a clear consensus or design rules that establish a direct relationship between the optimum solar collector size, the rated refrigeration capacity, or, analogously, the thermal power consumption and the storage tank volume. This chapter intends to bridge this gap.

9.1.1 Hypothesis, constraints, definition of performance indicators and design variables

The hypotheses of the model are the same described in Chapter 8. The model used for the TSS sensitivity analysis is essentially the same already presented in Chapter 8, however, here is focused exclusively on the ARS since it has proven to be the most efficient and promising solution.

Two constructive and operational variables have been manipulated in the sensitivity study in search for the TSS optimum design:

- **TSS volume factor (f):** This parameter informs about the size of the TSS referenced to the solar collector size. Its mathematical definition is presented in Equation 9.1. Higher f values represent higher storage capacities in relation to the thermal energy collecting system.

$$f = \frac{V_{TSS}}{A_{col}} \tag{9.1}$$

- **TSS thermal power consumption $\left(\dot{Q}_{ge}\right)$:** The thermal power consumed from the TSS to drive the refrigeration system has an impact on the TSS thermal level management and the potential of the refrigeration system to improve its refrigeration capacity. A higher thermal energy consumption rate would signify higher refrigeration capacity production and depletion of stored energy. Furthermore, the thermal energy consumed from the TSS is directly related to the ARS sizing. The proposed study could be helpful to define a methodology for the optimum determination of $\left(\dot{Q}_{ge}\right)$, which at the same time is helpful to scale the rest of the refrigeration system (jet-ejector, heat exchangers, pump...).

The effect and influence of different TSS sizes over the system response has been quantified by monitoring several operational and thermodynamic metrics:

- **Activation percentage:** The activation percentage informs about the self-reliance of the refrigeration system. Given a total amount of time in which there are refrigeration needs, arbitrarily defined as the time interval between 08:00 and 19:00 in which the ambient temperature is above $25°C$, the activation percentage measures the fraction of that time in which the TSS had sufficient thermal level to activate the refrigeration system. To achieve a competitive refrigeration system, the activation percentage should be maximized.

An activation percentage of 100% would mean that the system is completely autonomous and is capable of operating without interruptions. On the contrary, low activation percentages would indicate that the refrigeration system operates irregularly.

The thermal power extracted from the TSS as well as its size are likely to be influential design factors.

- **Thermodynamic indicators:** The goodness and flexibility of the refrigeration system has been also assessed studying the instantaneous and averaged COP_{th} and $\dot{Q}_{ev}$. It is desirable for the designer that both the efficiency parameter (COP_{th}) and the refrigeration capacity $\left(\dot{Q}_{ev}\right)$ be maximum.

9.1.2 Definition of the study and resolution strategy

The design variables defined as manipulable $\left(f, \dot{Q}_{ge}\right)$ are altered assuming a fixed size of the solar collector. As mentioned in previous chapters, the solar collector has a span

of 7.08 m and a total collecting area of 40.78 m^2. With a fixed solar collector size, the effect of different TSS architectures and different thermal management architectures can be studied more clearly.

Two types of data coming from the simulations have been deemed as relevant:

- Instantaneous response of the system in the short-term (local timescale). This study aims to compare the system response when prescribing different TSS architectures or thermal energy consumption strategies under the same succession of climatic events. In addition to the refrigeration capacity and thermal efficiency, special focus has been put on the instantaneous evolution of the TSS internal temperature. The TSS volume factor has varied in this analysis between $f = 0.02$ m and $f = 0.08$ m while $\dot{Q}_{ge}$ has varied between 10 kW and 20 kW. The effect of each manipulable variable has been assessed separately.

  This study has been helpful to take a closer look of the instantaneous response.

- Averaged performance indicators over a month (global response). The purpose of this analysis is to average the performance indicators to obtain global representative figures of the system response. In this case, the effect of each manipulable variable has been assessed following a complete factorial study. The TSS volume factor has varied in this analysis between $f = 0.02$ m and $f = 0.14$ m while $\dot{Q}_{ge}$ has varied between 5 kW and 30 kW.

  Given the high sensitivity of the system performance to the two manipulable variables, a high number of cases is required to achieve high resolution and describe the response surface. The elevated number of cases necessary to create a dense grid arises some computing cost issues. The computational function that calculates the instantaneous system behavior has been evaluated using the parallelization toolbox available in Matlab. The cases have been solved using high-performance computing nodes, which makes the study affordable.

  This study has been helpful to take a closer look of the global and macroscopic response.

9.2 Results

9.2.1 Sensitivity analysis of the system sizing: Short-term insights

Impact of the TSS thermal power consumption strategy $\left(\dot{Q}_{ge} \right)$

Figures 9.1 and 9.2 show the instantaneous evolution of the main performance indicators along three days of different dates. For each figure three different nominal rates of energy consumed from the TSS $\left(\dot{Q}_{ge} \right)$ for a fixed tank size ($f = 0.05$) are compared. In both analyses it is assumed that the system is initially switched off, hence, the initial temperature of the PTC and the TSS corresponds with the ambient temperature. The

main difference between both scenarios depicted in Figures 9.1 and 9.2 lies in the solar irradiance profile. The first solar irradiance pattern (Figure 9.1) corresponds with an almost clear-sky scenario while the second pattern (Figure 9.2) is affected by occasional cloud coverage.

In the clear-sky situation, extracting a nominal thermal power of 15 kW seems to be the best strategy if priority is given to reaching a continuous operation; a thermal power of $\dot{Q}_{ge} = 15$ kW maximizes the refrigeration capacity without affecting the COP_{th} and the system's ability to be operative as summarized in Table 9.1. The nominal power of 20 kW, nevertheless, causes irregular functioning.

As mentioned in the previous chapter, the shaded profiles marked in the figures represent an irregular functioning of the system due to the low thermal level in the tank. As can be appreciated in the figures, the shaded profiles coincide with those time instants in which the minimum temperature threshold of 120 $°C$ in the TSS is not reached.

Nevertheless, the nominal thermal power of 10 kW seems to be the most adequate selection in the partially cloudy scenario (Figure 9.2), it guarantees a continuous operation although it exhibits a lower nominal refrigeration capacity. With an irregular solar energy supply, the nominal thermal power of 15 kW leads to a TSS discharge in the early hours of the third day. This is reflected in Table 9.1 when the average COP_{th} is examined (decrease from 0.384 when $\dot{Q}_{ge} = 10$ kW to 0.342 when $\dot{Q}_{ge} = 15$ kW).

The instantaneous response of the refrigeration system provides a comprehensive description of the phenomena occurring in a limited period; however, it lacks a global perspective. In other words, the conclusions about the appropriateness of a particular system sizing are biased because they are strongly influenced by the climatic conditions of the sample days under examination. This makes it difficult to decide the most appropriate nominal power extracted from the tank $\left(\dot{Q}_{ge}\right)$ and, consequently, a particular jet-ejector scale that may operate satisfactorily in multiple scenarios. Though, it anticipates that a trade-off exists, and, for a fixed storage tank size, a higher thermal power extracted from the tank would increase the system's nominal refrigeration capacity but, at the same time, it would sacrifice the system's ability to remain in operation.

Impact of the TSS volume factor (f)

An equivalent analysis could be carried out to determine the influence of different TSS volume factors (f) for a fixed nominal thermal power $\left(\dot{Q}_{ge} = 12\,kW\right)$. Two specific scenarios showing different irradiance profiles have been analyzed. The first one (Figure 9.3) covers the first 6 days of June of the TMY and it is characterized by an almost continuous solar irradiance supply except for the appearance of clouds during the 4th day. The cloudless-sky found during the first three days facilitates a progressive heating-up of the TSS for all the volume factors. In the configuration with an intermediate volume ($f = 0.05$), the TSS works effectively as a heat reservoir allowing the system to face the temporary lack of thermal energy supply.

Figure 9.1: *Instantaneous evolution of the climatic conditions and the refrigeration system performance indicators along the days $1^{st} - 3^{rd}$ of June of the TMY. The tank size factor remains fixed ($f = 0.05$). The evaporating temperature is assumed to be constant ($T_{ev} = 13°C, T_{out,rl} = 20°C$).*

Figure 9.2: *Instantaneous evolution of the climatic conditions and the refrigeration system performance indicators along the days $1^{st} - 3^{rd}$ of August of the TMY. The tank size factor remains fixed ($f = 0.05$). The evaporating temperature is assumed to be constant ($T_{ev} = 13°C, T_{out,rl} = 20°C$).*

Case	$COP_{th}[-]$ (average)	$\dot{Q}_{ev}$ [kW] (average)	Activation percentage [%] (average)
Figure 9.1 ($1^{st} - 3^{rd}$ of June), $\dot{Q}_{ge} = 10$ kW	0.371	3.46	88.7
Figure 9.1 ($1^{st} - 3^{rd}$ of June), $\dot{Q}_{ge} = 15$ kW	0.371	5.20	88.7
Figure 9.1 ($1^{st} - 3^{rd}$ of June), $\dot{Q}_{ge} = 20$ kW	0.312	5.88	75.7
Figure 9.2 ($1^{st} - 3^{rd}$ of August), $\dot{Q}_{ge} = 10$ kW	0.384	3.58	90.4
Figure 9.2 ($1^{st} - 3^{rd}$ of August), $\dot{Q}_{ge} = 15$ kW	0.342	4.77	80.3
Figure 9.2 ($1^{st} - 3^{rd}$ of August), $\dot{Q}_{ge} = 20$ kW	0.289	5.42	68.6

Table 9.1: *Performance indicators averaged along three days for a fixed TSS volume factor ($f = 0.05$)*

Some differences in the dynamic response are distinguished from the other TSS volumes under examination. The inability of the smaller TSS ($f = 0.02$) to cope with the interruption in solar irradiance contrasts with its higher capacity to acquire rapidly the threshold thermal level after discharge events as observed, for instance, in the start-up on the 1st day and the recharge at the beginning of the 5th day. Despite this, the smaller TSS shows better average performance as can be seen in Table 9.2. The larger TSS ($f = 0.08$), however, undergoes difficulties to acquire a high thermal level during continuous operation and discharges on the 4th day. Its high thermal inertia also affects the system negatively during the early hours of the 5th day impeding a rapid heating-up.

The second scenario covers the first six days of August of the TMY. The solar irradiance distribution is characterized by an unstable and changing behavior. As observed by monitoring the instantaneous evolution of the performance indicators (Figure 9.4) and the averaged results (Table 9.2), the choice of small tank volumes ($f = 0.02$) clearly brings more benefits. The heating-up processes after start-up or discharge events are faster due to the lower thermal inertia of the TSS (as can be seen in the early hours after system start-up in Figure 9.4). The greater storage capacity of larger tank volumes ($f = 0.05$, $f = 0.08$) does not produce tangible benefits because the TSS does not acquire a high thermal level due to the irregular and discontinuous irradiance reception. Under this scenario, the TSS is not working as an effective thermal reservoir. What is more, the TSS with the highest volume factor ($f = 0.08$) undergoes an irregular functioning during the 3rd day and is unable to work in the late hours of the 5th day and the early hours of the 6th day. The average COP_{th} of the smallest tank (0.395), its activation percentage (97.9%), and its average refrigeration capacity (4.54 kW) suggest that the rapid heating-up is the most convenient strategy. Again, the results are strongly influenced by the sample days under examination, and an extended analysis would

shed light on the most adequate mid-term design strategy. This analysis is conducted in the following part of the study.

Case	$COP_{th}[-]$ (average)	$\dot{Q}_{ev}$ [kW] (average)	Activation percentage [%] (average)
Figure 9.3 ($1^{st} - 6^{th}$ of June), $f = 0.02$ m	0.418	4.60	96.5
Figure 9.3 ($1^{st} - 6^{th}$ of June), $f = 0.05$ m	0.409	4.49	94.4
Figure 9.3 ($1^{st} - 6^{th}$ of June), $f = 0.08$ m	0.386	4.24	89.1
Figure 9.4 ($1^{st} - 6^{th}$ of August), $f = 0.02$ m	0.395	4.54	97.9
Figure 9.4 ($1^{st} - 6^{th}$ of August), $f = 0.05$ m	0.368	4.23	91.6
Figure 9.4 ($1^{st} - 6^{th}$ of August), $f = 0.08$ m	0.336	3.85	83.4

Table 9.2: *Performance indicators averaged along six days for a fixed TSS thermal energy consumption $\left(\dot{Q}_{ge} = 12\,kW\right)$.*

9.2.2 Sensitivity analysis of the system sizing: Mid-term insights

When the instantaneous performance is averaged throughout the whole month, the performance indicators account for multiple random climatic events, hence the conclusions are more representative. Figure 9.5 depicts, for different TSS volumes (f) and operating strategies $\left(\dot{Q}_{ge}\right)$, the main performance indicators (COP_{th}, Q_{ev} and activation percentage) averaged throughout June of the TMY. Small TSS volumes, as well as small rates of thermal energy consumption at the TSS $\left(\dot{Q}_{ge}\right)$, are preferred to maximize the COP_{th} and activation percentage, nevertheless, relatively low refrigeration capacities $\dot{Q}_{ev}$ are found. Oppositely, high thermal power consumption values cause frequent interruptions and COP_{th} degradation due to the TSS discharge. In contrast, the refrigeration capacity increases although the rise is less pronounced.

The suitability and versatility of a particular nominal thermal power for a given tank volume would depend on the designer's criteria, and a trade-off exists:

- The TSS volume factor (f) does not have a decisive influence over the system response for a fixed rate of thermal energy consumption $\left(\dot{Q}_{ge}\right)$ but small TSS volumes are preferred to reduce the thermal inertia during heating-up processes. This suggests that the TSS storage capacity losses relevance because the solar irradiance is nearly synchronized with the refrigeration needs. The benefits of

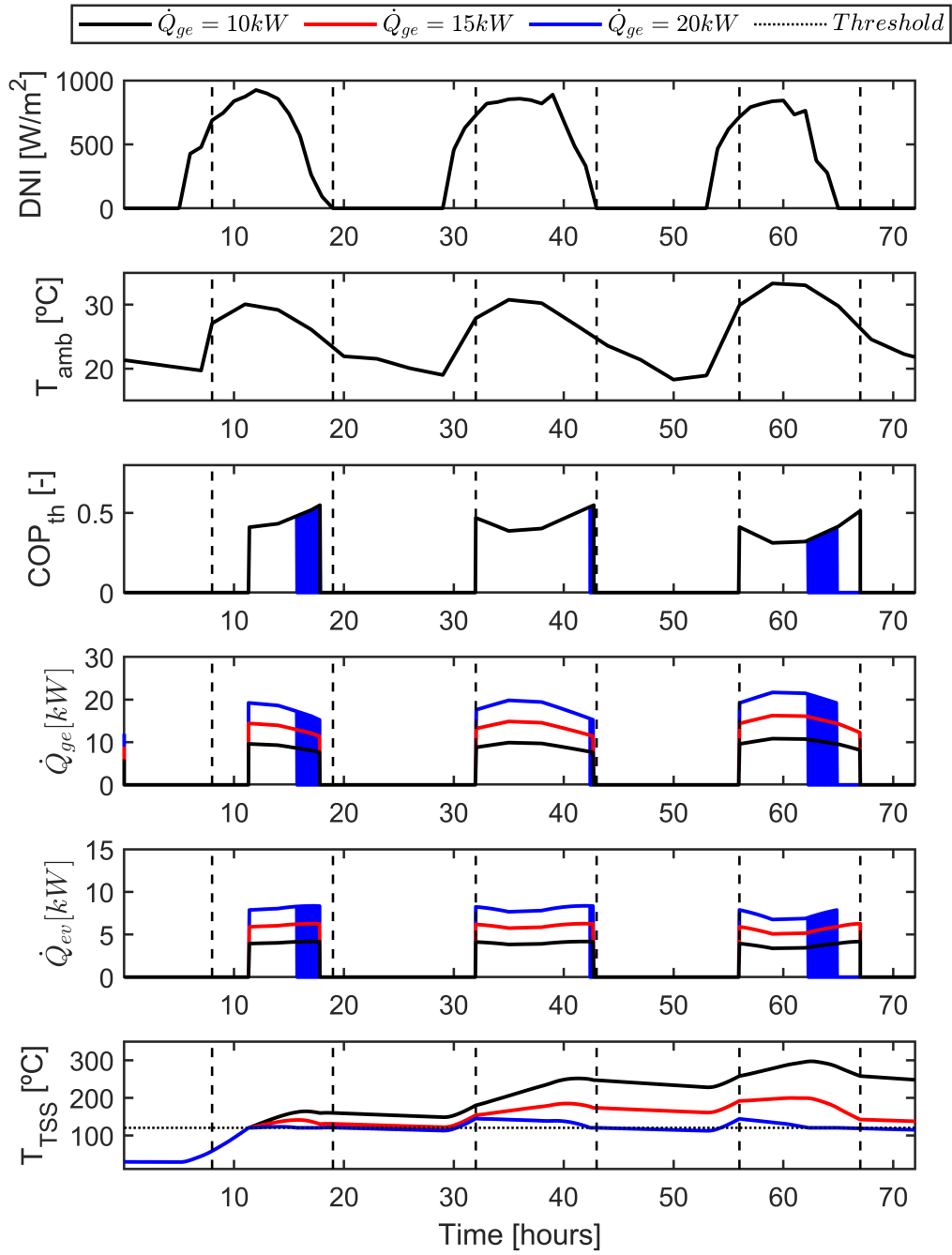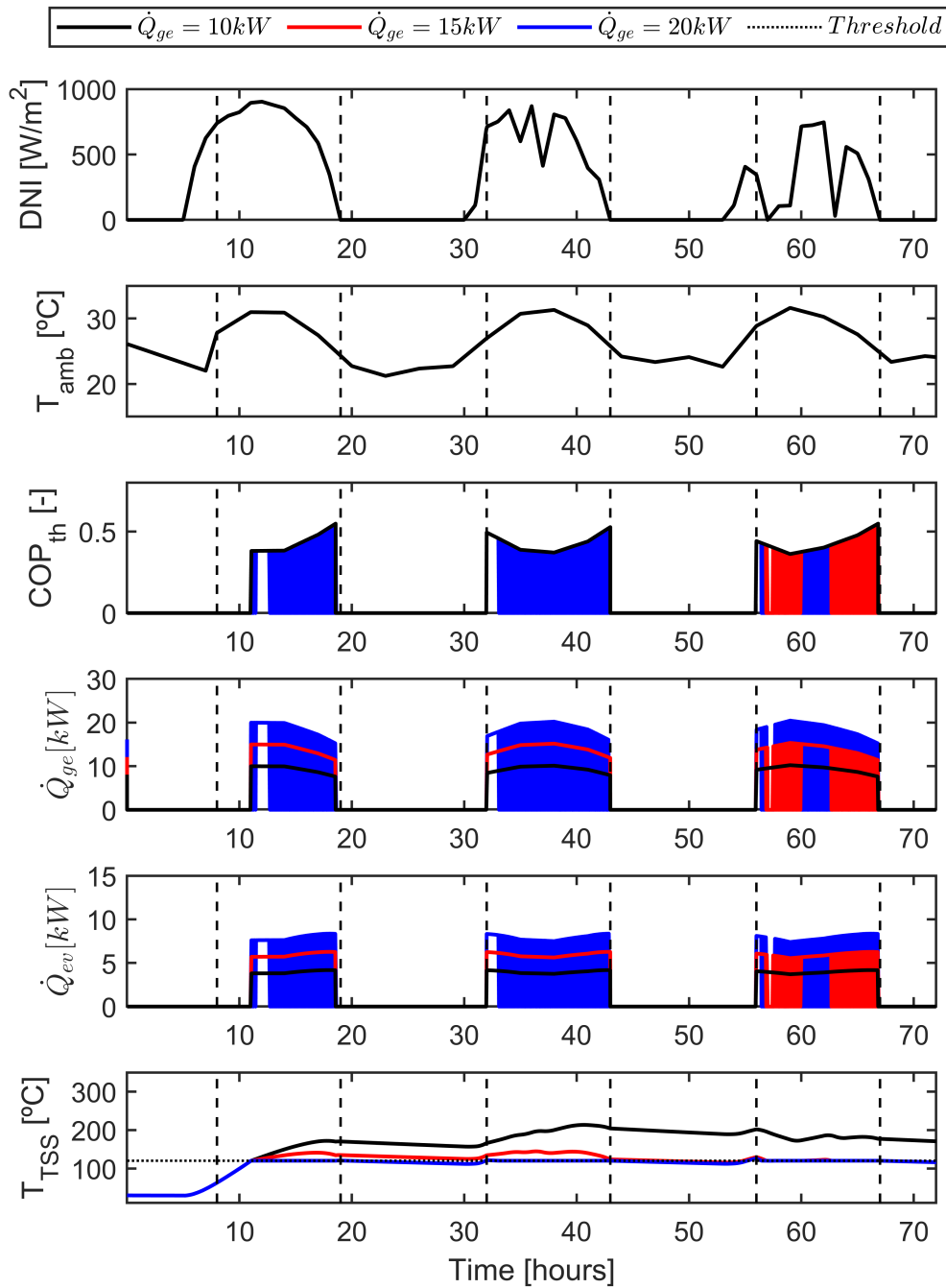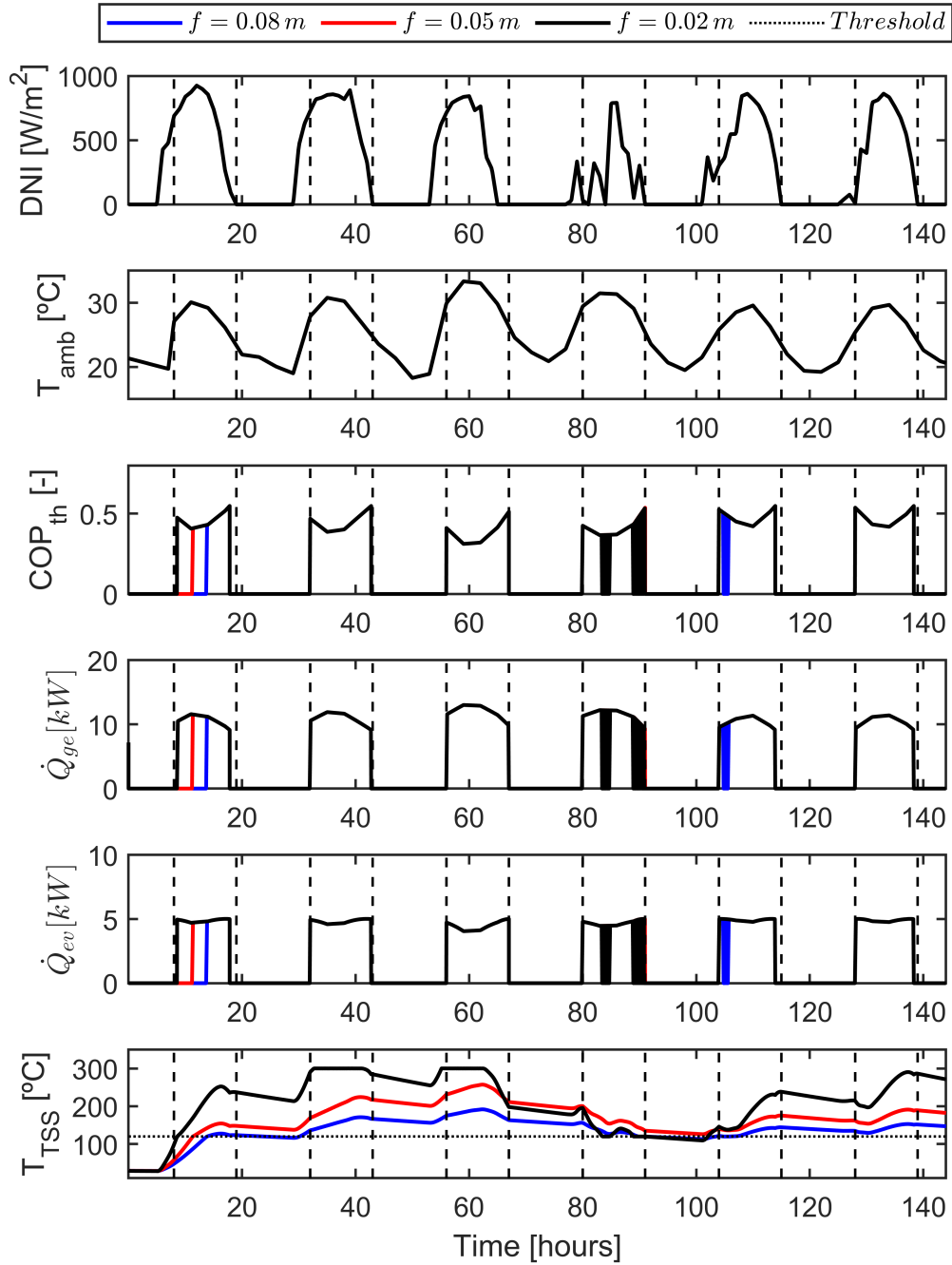**Figure 9.3:** *Instantaneous evolution of the climatic conditions and the refrigeration system performance indicators along the days 1st - 6th of June of the TMY. The nominal thermal power consumed remains fixed $\left(\dot{Q}_{ge} = 12\,kW\right)$. The evaporating temperature is assumed to be constant $(T_{ev} = 13°C, T_{out,rl} = 20°C)$.*
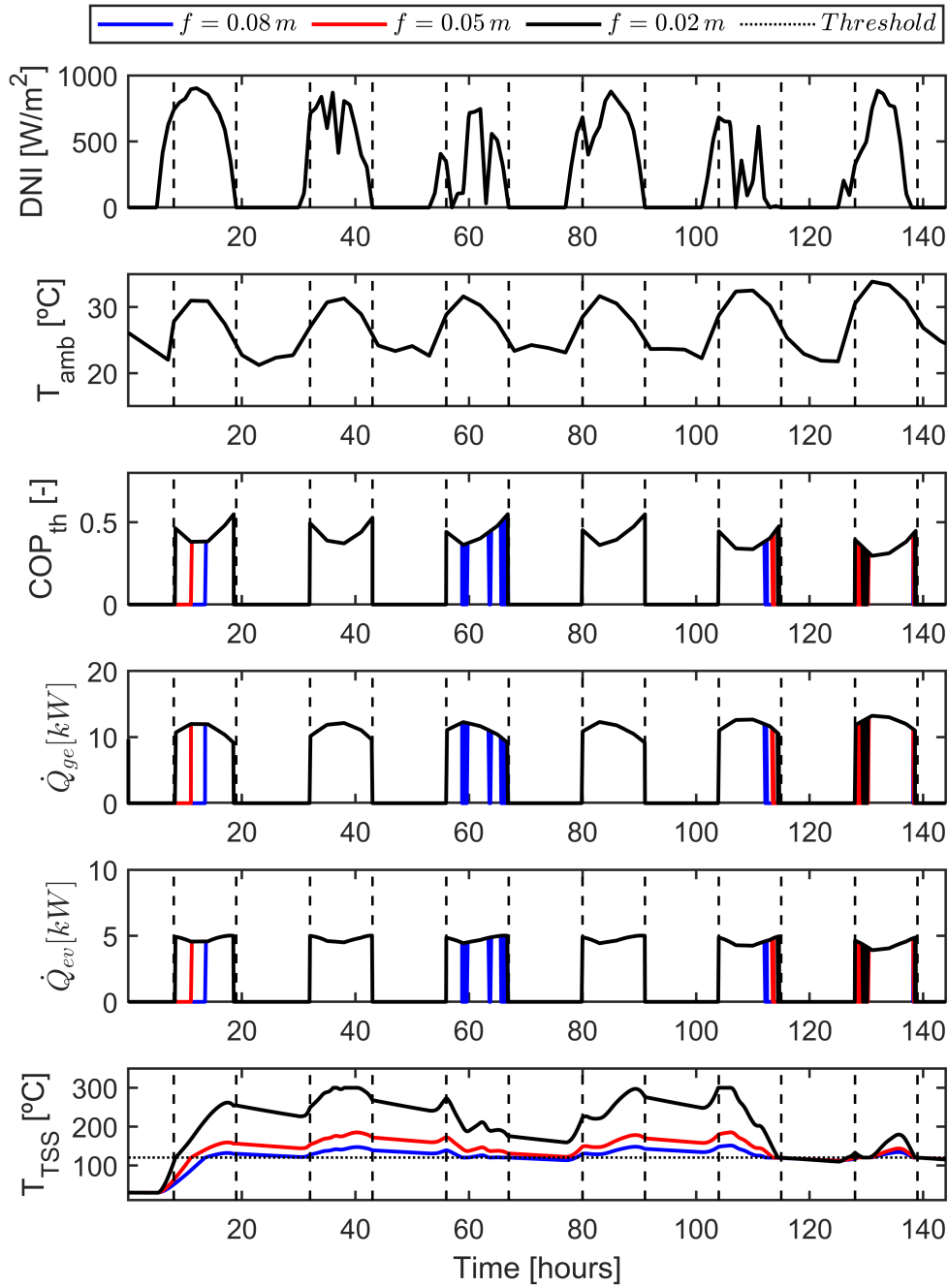
Figure 9.4: *Instantaneous evolution of the climatic conditions and the refrigeration system performance indicators along the days 1st - 6th of August of the TMY. The nominal thermal power consumed remains fixed $\left(\dot{Q}_{ge} = 12\,kW\right)$. The evaporating temperature is assumed to be constant $(T_{ev} = 13°C, T_{out,rl} = 20°C)$.*

larger storage capacities would be visible with other design criteria, i.e, whether the intention is to prolong the system utilization beyond the daily hours with solar irradiance. In such a case, a lower thermal energy consumption rate for the same volume would allow increasing the TSS temperature, and it would act effectively as a heat reservoir. Under the prescribed requirements, there is no need to prolong the refrigeration capacity supply beyond sunny hours. Hence, the TSS ability to act as a large heat reservoir has lower importance.

- The TSS nominal thermal power consumption $\left(\dot{Q}_{ge}\right)$ greatly affects the system's dynamic response and the aforementioned trade-off between $\dot{Q}_{ge}, COP_{th}$, and activation percentage is applicable. Figure 9.6 denotes the existence of an inflection point: the increase in the thermal power consumption increases the attainable refrigeration capacity with no remarkable negative impact on COP_{th} and activation percentage until a certain critical value. This critical value is suggested as the preferred design point. For the present system layout (PTC span of 7.08 m) and the selected $\dot{Q}_{ge}$ discretization scheme this value seems to be around 13.3 kW.

9.3 Summary

In the present chapter, the decisive influence of an adequate TSS selection has been demonstrated. The TSS size and the prescribed thermal energy consumption strategy affect the availability of thermal power inside the tank.

The ARS has been examined at the local scale focusing the analysis on the system response against random climatic events of short duration. This analysis is helpful to understand how the TSS charge and discharge occur and to identify behavior trends or patterns, but lacks a global perspective. The cause is that the number of climatic samples is reduced and is not representative of a whole warm season. The analysis of the ARS averaged response provides complementary insights and has been very helpful to assess the macroscopic response summarized in global specific figures. The averaged indicators have proven to be more rigorous to make design decisions.

A nominal thermal power consumption from the TSS of 13.3 kW has been optimum for a PTC span of 7.08 m. Such dimensioning achieves the highest refrigeration capacity that can be generated preserving the system efficiency and maintaining the blackout periods at their minimum. General trends and guidelines are presented so the system response can be predicted if priority is given to other criteria such as maximum refrigeration capacity generation, rather than efficiency conservation.
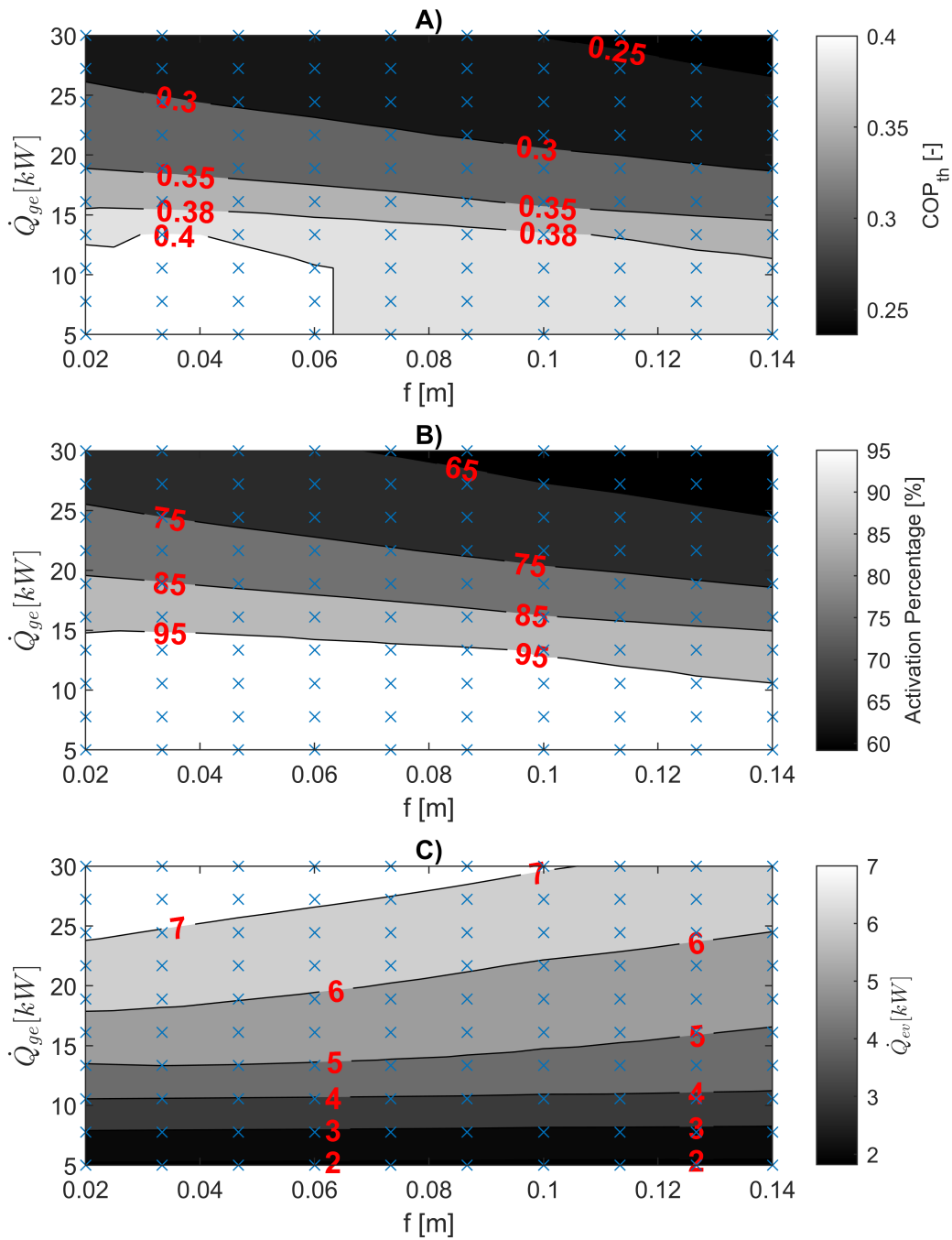
Figure 9.5: *Averaged COP_{th} (subfigure A), activation percentage (subfigure B), and refrigeration capacity $\dot{Q}_{ev}$ (subfigure C) averaged along the month of June of the TMY for different TSS volume factors (f) and nominal thermal power extracted from the TSS $\left(\dot{Q}_{ge}\right)$.*
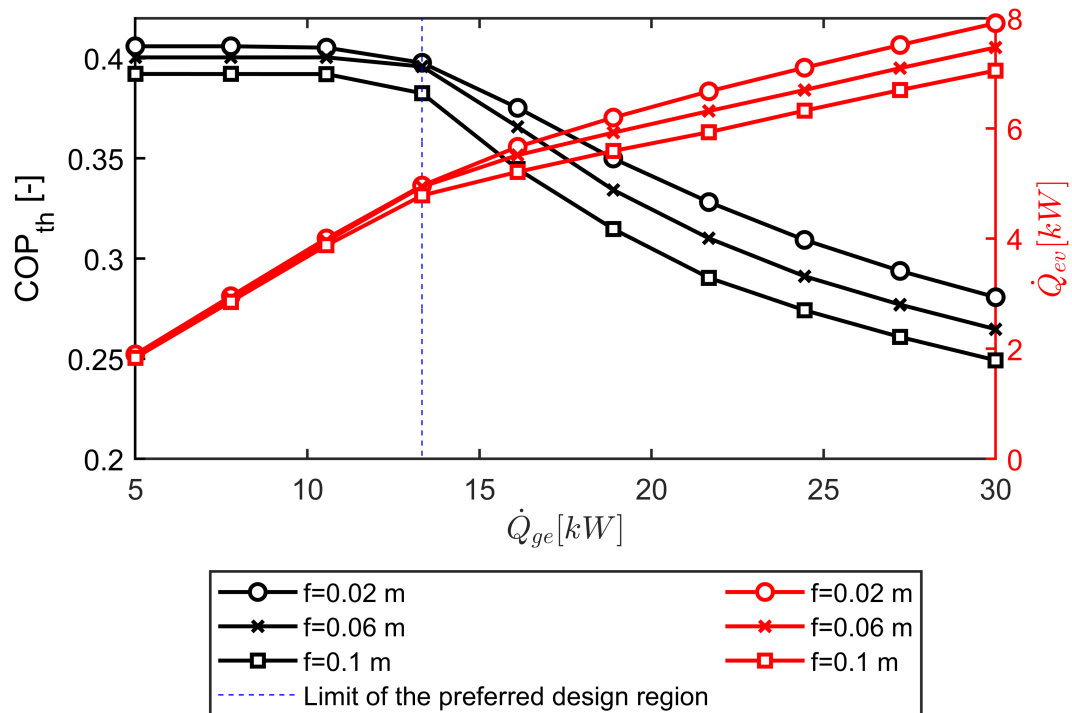
Figure 9.6: *Averaged COP_{th} (left axis) and refrigeration capacity (right axis) for different TSS volumes (f) and nominal thermal power consumption $\left(\dot{Q}_{ge}\right)$.*

Chapter 10

Thermoeconomic analysis

10.1 Introduction

This chapter aims to quantify the operating expenses (OPEX) and the capital expenditures (CAPEX) of the Adjustable Refrigeration System (ARS) and compare them with technical solutions predominantly adopted in the market, that is, a Vapor Compression Refrigeration System (VCRS). It must be outlined that only the ARS has been considered since it has been demonstrated to be the most convenient solution in terms of efficiency. Since the ARS is very sensitive to the ambient conditions, a comparison of the ARS and the VCRS separately would not be fair because on some occasions the ARS is inevitably turned off due to the lack of thermal level in the Thermal Storage Sysem (TSS). Furthermore, the ARS efficiency is coupled with the ambient temperature and the preservation of a constant rated refrigeration capacity is not possible. Hence, for the present analysis both refrigeration solutions coexist. The rationale is that the ARS should be the main contributor to the refrigeration capacity target and the VCRS should assist to deliver the remaining part.

Firstly, the dynamic response of the combined system is evaluated along two warm months of the Typical Meteorological Year (TMY). This has been very helpful to envisage the unstable behavior of the ARS under variable ambient conditions and the necessity of using the VCRS as a backup.

Then, the CAPEX of the ARS and the VCRS is estimated based on reference operating conditions and the correlations given in Chapter 3. Subsequently, the energy consumed by each system is determined along one warm month of the TMY based on dynamic simulations. With the current electricity costs, it is possible to appraise the monetary savings when the combined system (ARS+VCRS) is compared with a VCRS operating solely under the same ambient conditions and refrigeration needs. To conclude, a rough approximation of the amortization cost is provided.

10.2   Definition of the study: Comparison between a VCRS+ARS and a single VCRS

The benefits of using a solar-driven machine in comparison with traditional refrigeration technologies have been quantified by comparing two refrigeration system architectures combined to reach a refrigeration capacity target of 10 kW. In an ideal situation, the ARS would provide a high fraction of the demanded refrigeration capacity and the VCRS would add the remaining part to achieve the target. Hence there are two architectures subject to analysis:

- **System 1: ARS combined with an auxiliary VCRS:** The refrigeration needs are distributed between the ARS and the VCRS as shown in Figure 10.2. The ARS and the PTC are sized to provide a rated refrigeration capacity of 5.4 kW at a reference ambient temperature of 31 $°C$, extracting 15 kW from the TSS to do so. The ARS capability to produce the refrigeration effect varies according to the thermal level in the TSS and also according to the instantaneous variation of the ambient temperature. The VCRS system is dedicated to delivering the supplementary refrigeration capacity to meet the target, as illustrated in Figure 10.1. When compared to a single VCRS configuration, the OPEX of this system, associated with its electricity consumption, are expected to be lower at the expense of a higher CAPEX (more expensive components).
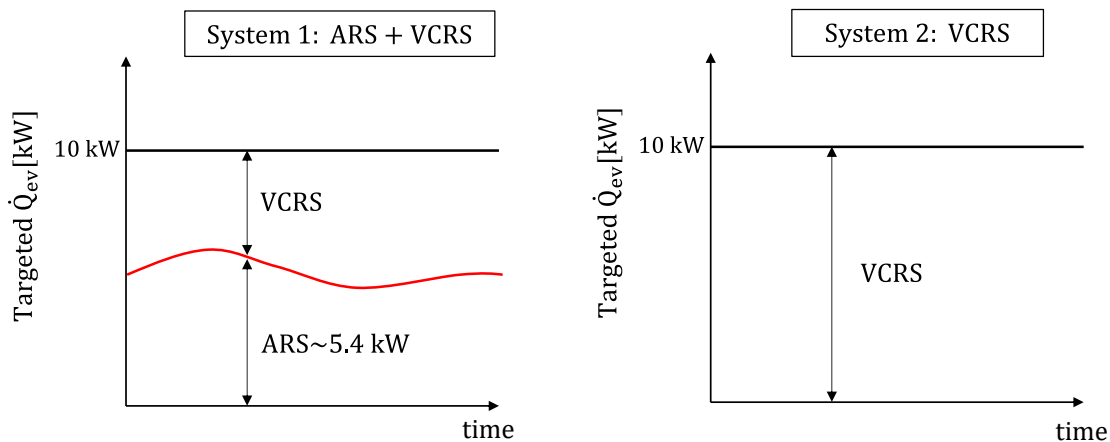
Figure 10.1: *Distribution of the targeted refrigeration capacity* $(10\,kW)$ *in both approaches (ARS+VCRS and single VCRS)*

- **System 2: Single VCRS:** The refrigeration needs are delivered exclusively by the VCRS as illustrated in Figure 10.3. This configuration is reproduced in the vast majority of the commercial equipment.

As a global scope, the study is dedicated to discerning if the reduction in OPEX of the hybridized system is sufficient to compensate for the elevated CAPEX associated with equipment investment costs.
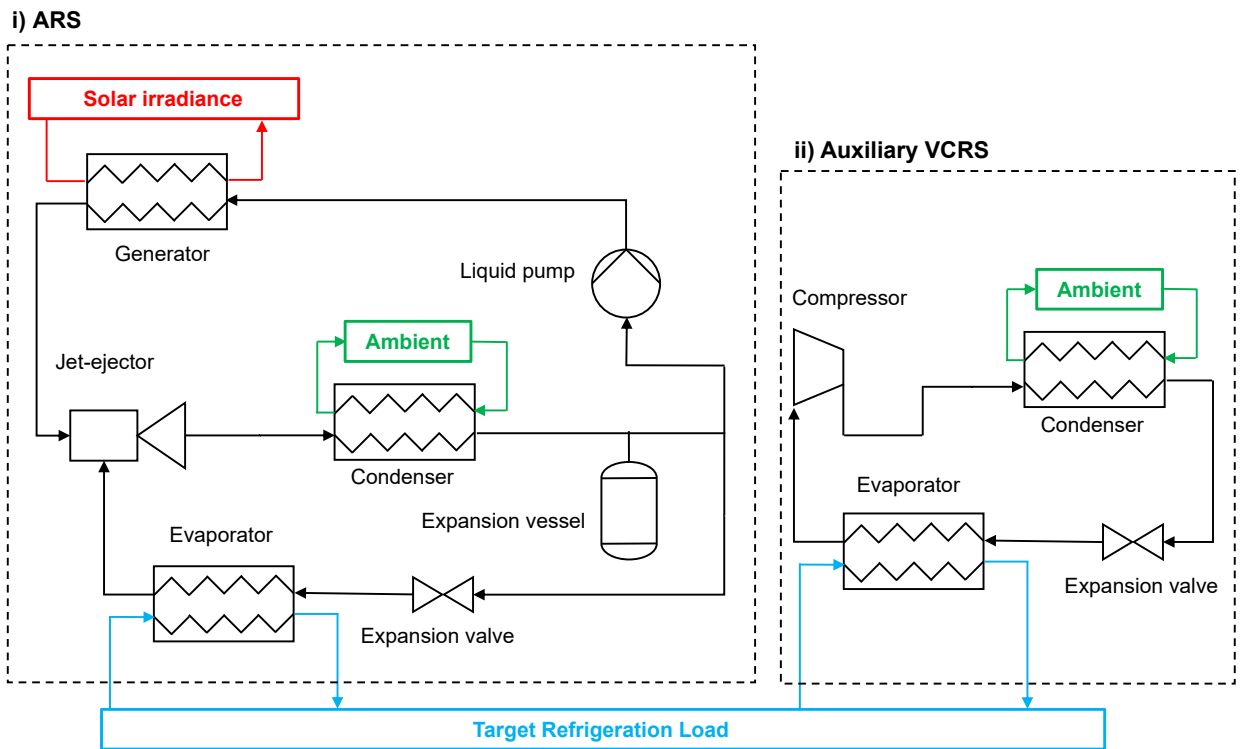
Figure 10.2: *Combination of the ARS and an auxiliary VCRS to achieve the targeted refrigeration load*
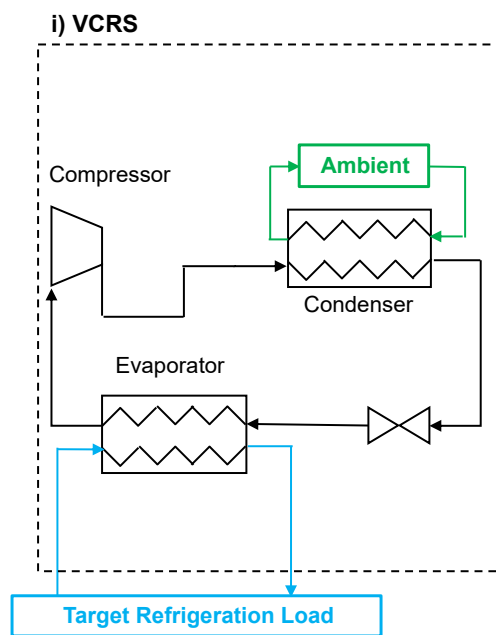
Figure 10.3: *VCRS working solely to achieve the targeted refrigeration load*

10.2.1 Hypothesis and constraints

The temporal evolution of the main performance indicators has been computed using the transient model described in Chapter 3. The following hypothesis have been assumed to simplify the analysis:

- The components are sized for reference operating conditions shown in Table 10.1. In the end, the target refrigeration capacity must be the same and the evaporating and the condensing conditions remain the same regardless of whether the ARS+VCRS or the VCRS are used. The secondary fluids are the same in the common elements of both systems (water for the condenser and air for the evaporator) while the secondary fluid of the generator is thermal oil.

- The parasitic power consumption of auxiliary systems, that is, cooling fans, recirculating pumps, electronics, control systems..., have been neglected. The real COP_{hyd} is expected to be lower in a real system accounting for these contributions to total power consumption. However, this underestimation affects both configurations, which makes the comparison consistent.

- The VCRS dynamic response is only affected by the instantaneous changes in the ambient temperature.

- The dynamic effects govern the functioning of the PTC and the TSS but the thermal inertia of the rest of the components has been neglected.

- The maintenance costs in OPEX computation have been neglected due to the difficulties to fairly compare both systems. There is still a lack of practical experience when operating the ARS, apart from prototypes and pilot plants. A priori, the maintenance needs would be simpler and cheaper in the ARS thanks to its reduced number of moving parts.

- The depreciation of the elements over time has been neglected since the results are intended to provide preliminary insights rather than making an in-depth analysis.

- The transformation efficiency from electric to mechanical power has been considered 100 % in all the refrigeration machines.

10.3 Results

10.3.1 Dynamic response of the combined system (ARS+VCRS)

Figure 10.4 shows the instantaneous evolution of the main performance indicators of the combined system VCRS+ARS over July of the TMY. It must be stressed that the ARS operates with a nominal $\dot{Q}_{ge} = 15\ kW$. In the ambient temperature subplot, the low-temperature threshold ($25°C$) and the reference ambient temperature ($31°C$) are marked with dashed lines along the time slot. As mentioned in the preceding chapters, the low-temperature bound together with the time slot 08:00-19:00 delimits the time slots that are susceptible to need the targeted refrigeration load. As can be observed the ARS can provide a significant fraction of the required refrigeration

Reference operating conditions							
ARS (R1234yf)				VCRS (R1234yf)			
Component	Parameter	Units	Value	Component	Parameter	Units	Value
Generator	P_{ge}	bar	35.14	Condenser	P_{co}	bar	10.18
	$T_{in,ge}$	°C	40.3		$T_{in,co}$	°C	50.6
	$T_{out,ge}$	°C	99.1		$T_{out,co}$	°C	38
	P_{TSS}	bar	1		P_w	bar	1
	$T_{in,TSS}$	°C	115		$T_{in,w}$	°C	31
	$T_{out,TSS}$	°C	120		$T_{out,w}$	°C	33
	$\dot{Q}_{ge}$	kW	15	Evaporator	P_{ev}	bar	4.8
Condenser	P_{co}	bar	10.18		$T_{in,ev}$	°C	13
	$T_{in,co}$	°C	46.1		$T_{out,ev}$	°C	24
	$T_{out,co}$	°C	38		P_{rl}	bar	1
	P_w	bar	1		$T_{in,rl}$	°C	31
	$T_{in,w}$	°C	31		$T_{out,rl}$	°C	20
	$T_{out,w}$	°C	33	Compressor	$\dot{m}$	kg/s	0.0434
Evaporator	P_{ev}	bar	4.8				
	$T_{in,ev}$	°C	13				
	$T_{out,ev}$	°C	24				
	P_{rl}	bar	1				
	$T_{in,rl}$	°C	31				
	$T_{out,rl}$	°C	20				
Jet-ejector	$\dot{m}_{pf}$	kg/s	0.104				
	$\dot{m}_{sf}$	kg/s	0.0434				
	$\dot{m}_{mf}$	kg/s	0.1474				
	ω	-	0.417				

Table 10.1: *Reference operating conditions used to conduct the OPEX and CAPEX estimation. Again, the reference ambient temperature corresponds to* 31°C

capacity and under favorable climatic conditions can bring an almost uninterrupted operation. Only during the system start-up and in one specific event concatenating two days with partially with cloudy skies and high ambient temperature, the VCRS must cover all the refrigeration load. Analogously, Figure 10.5 shows the evolution of performance indicators during August. This period of the TMY, characterized by frequent cloudy days and more instability in the evolution of the ambient temperature, shows a bit different behavior. The VCRS acts effectively as a backup in this case delivering the targeted refrigeration capacity entirely. Again, the activation of the ARS seems to alleviate the overall system power consumption.

In all the scenarios discussed in Figures 10.4 and 10.5 the COP_{hyd} of the ARS is greater since the pump has a reduced power consumption. The benefit of the ARS is evident if the series of this plot are contrasted (see COP_{hyd} subplot).
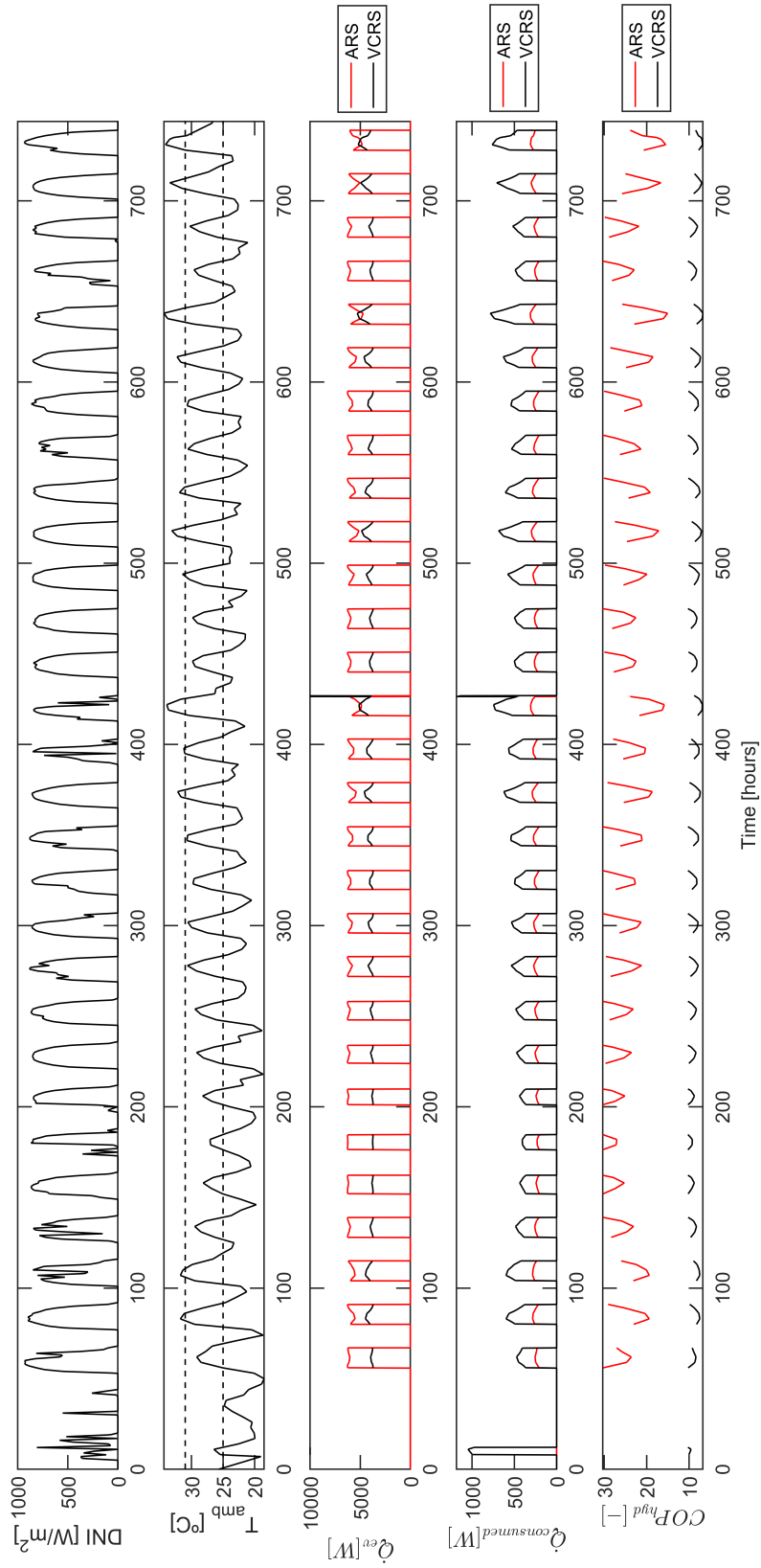
Figure 10.4: *Instantaneous evolution of the main performance indicators of the ARS and the VCRS along the month of July of the TMY. In this analysis, both systems are intended to operate combinedly to meet the target refrigeration capacity (10 kW).*
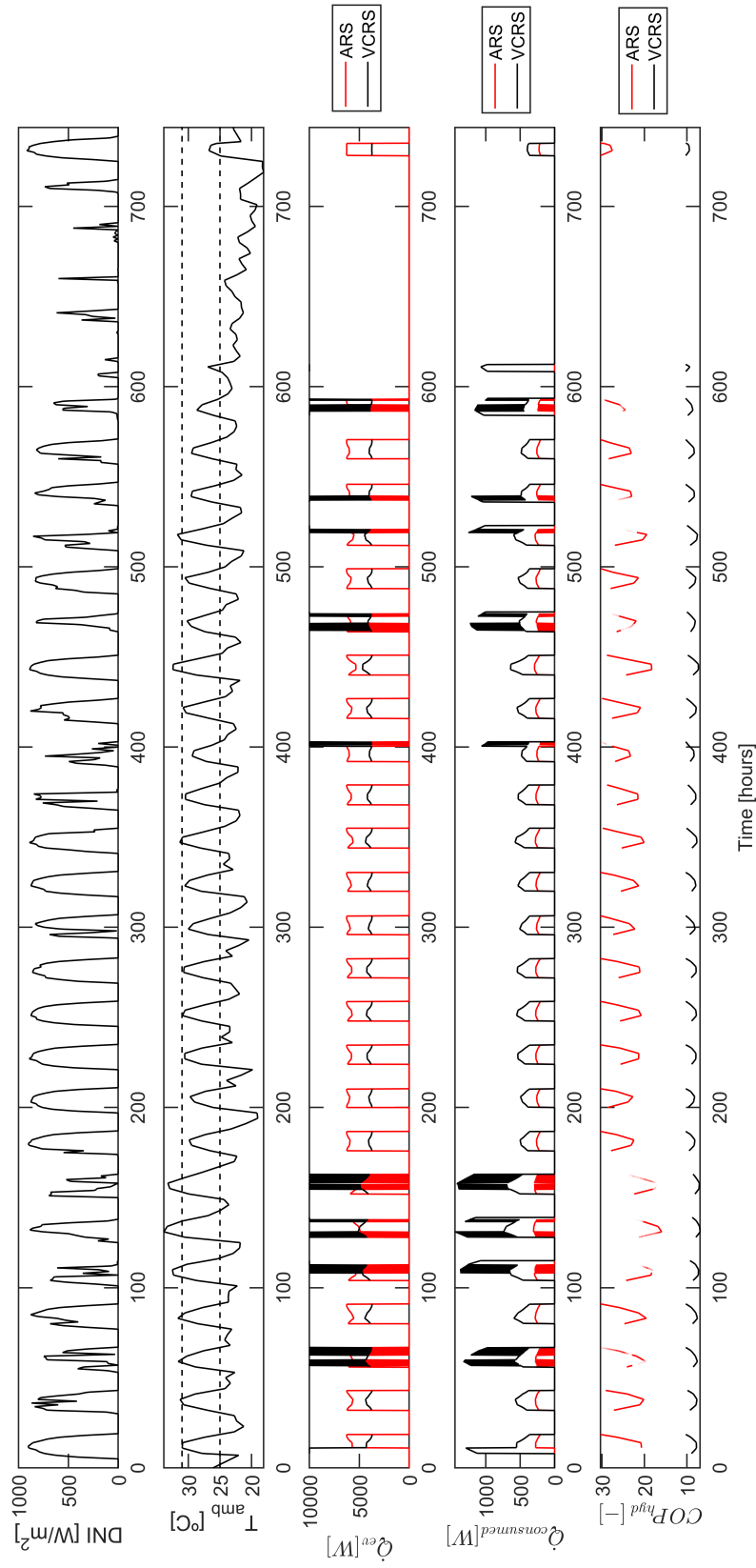
Figure 10.5: *Instantaneous evolution of the main performance indicators of the ARS and the VCRS along the month of August of the TMY. In this analysis, both systems are intended to operate combinedly to meet the target refrigeration capacity (10 kW).*

10.3.2   OPEX and CAPEX quantification

Figure 10.6 shows the ARS CAPEX for different nominal thermal power consumption strategies from the TSS $\left(\dot{Q}_{ge}\right)$. Here, the $\dot{Q}_{ge}$ can be interpreted as a metric of the ARS scale. The most remarkable conclusion is that the monetary cost is around 15,000 € and a reduced room for improvement exists even when the TSS thermal management strategy is modified. In the end, this change in strategy only affects the size of the generator, the condenser, and the evaporator, without modifying the PTC and TSS expenditures. The PTC and the TSS represent around 77% of the system total cost according to Figure 10.7. This trend is in line with conclusions drawn in research works dealing with solar air-conditioning systems [150, 21].

Figure 10.8 splits the CAPEX cost of the VCRS. The total cost amounts to 1337 €, being the compressor the most expensive component. Comparing the ARS CAPEX with the VCRS CAPEX it is found that the VCRS is notoriously cheaper, specifically, one order of magnitude cheaper. Hence, the ARS is far from being competitive in terms of CAPEX.
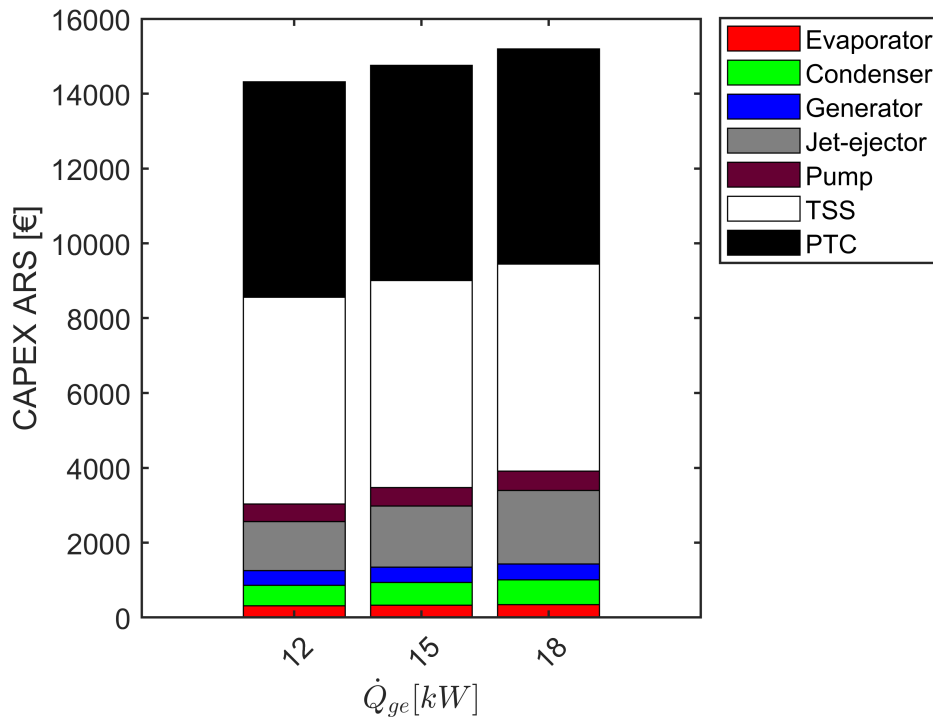
Figure 10.6: *CAPEX of the configurations subject to analysis. The values correspond to the operation along the month of July of the TMY with different power consumption strategies from the TSS*

Figure 10.9 compares the OPEX of the traditional VCRS system with the pair VCRS+ARS. If the single VCRS delivers all the required refrigeration capacity a cost of 41.18 € can be expected for this sample month. The cost associated with the operation of the pair ARS+VCRS depends on the TSS energy consumption rate. Despite the combined system operating with $\dot{Q}_{ge} = 18\,kW$ shows more savings than the case with

$\dot{Q}_{ge} = 12\ kW$

$\dot{Q}_{ge} = 15\ kW$

$\dot{Q}_{ge} = 18\ kW$
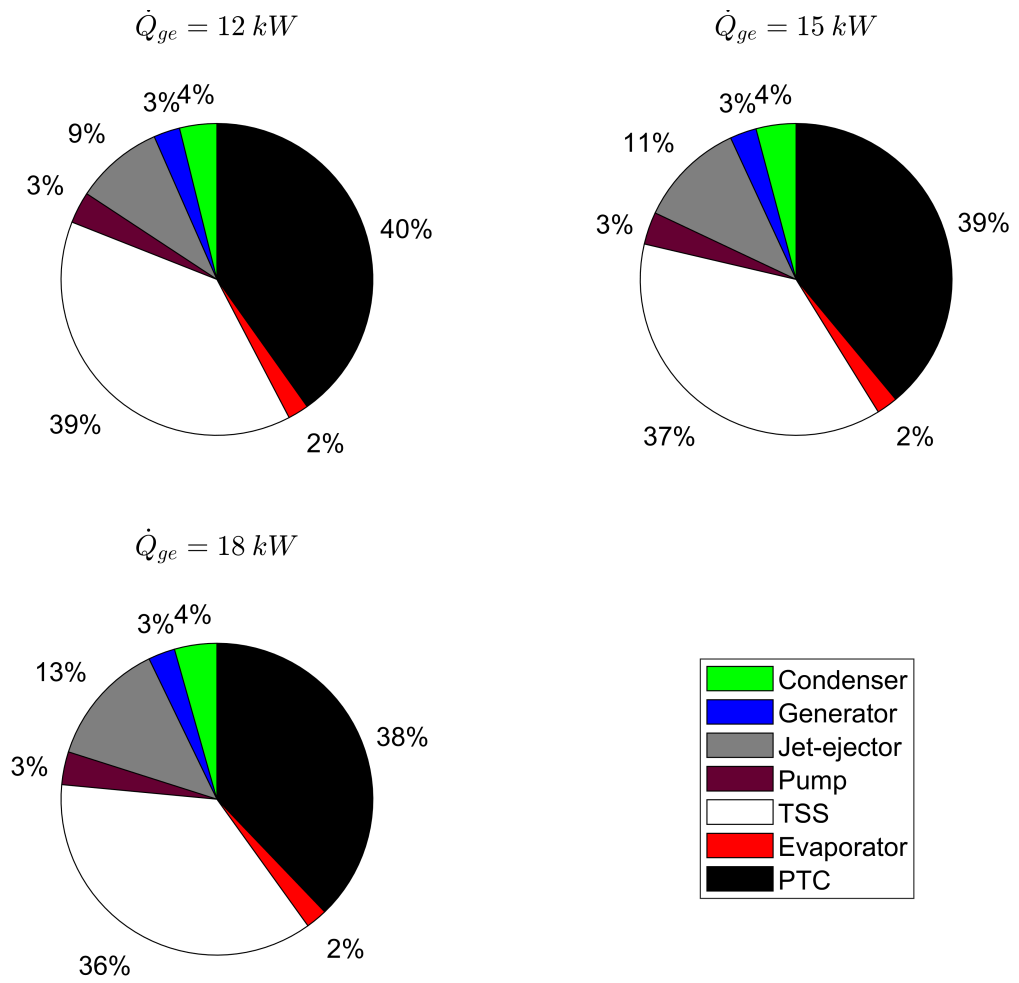
Figure 10.7: *Splitting of ARS CAPEX by the percentage cost of each element*
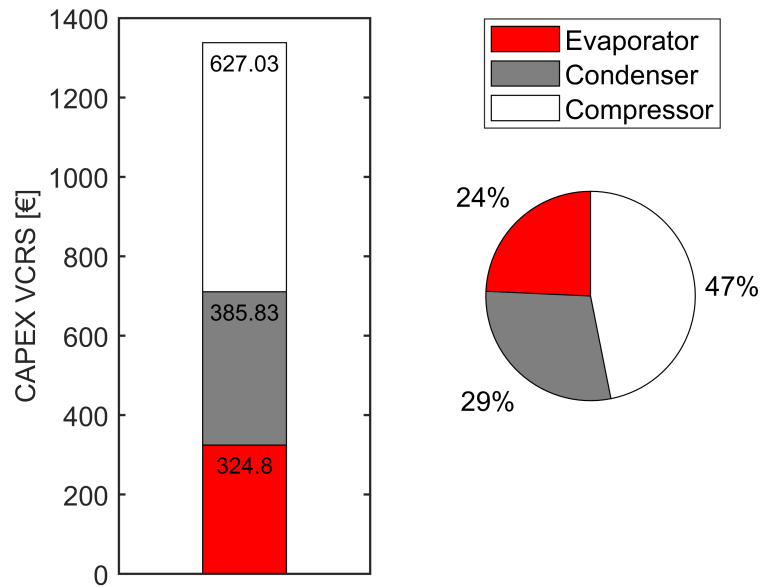
Figure 10.8: *Splitting of VCRS CAPEX by the magnitude and percentage cost of each element*

$\dot{Q}_{ge} = 15\,kW$ it exhibits irregular functioning due to inappropriate TSS thermal level management. The ARS works more intensively saving energy but it is turned off several times due to TSS discharge and this is, indeed, counterproductive.

The higher COP_{hyd} observed in Figures 10.4 and 10.5 translates in a lower electricity consumption even though the refrigeration capacity delivered by the ARS is higher than those delivered by the VCRS. In turn, the expenses associated with the ARS operation are lower. A constant electricity price of 0.11 €/kWh to convert the energy consumed by the compressor in the VCRS and the pump in the ARS to monetary price has been considered.

To carry out the succeeding comparative analysis, the monetary cost saved by the pair operating with $\dot{Q}_{ge} = 15kW$, that is, 15.32 € has been taken. Figure 10.10 depicts the OPEX savings with a time horizon of 10, 20, and 30 years together with the CAPEX cost. It has been assumed that the OPEX saving of one month (15.32 €) is achieved during five months of the year. Given the low OPEX savings, an extensive utilization during several years is still far to overcome the high CAPEX.

Table 10.2 summarizes the monetary cost of both systems (VCRS and VCRS+ARS) in terms of total CAPEX and yearly OPEX. As can be observed, the novel system VCRS+ARS has a lower OPEX than the traditional system (VCRS) but it could not compensate the high CAPEX in a reasonable time horizon.
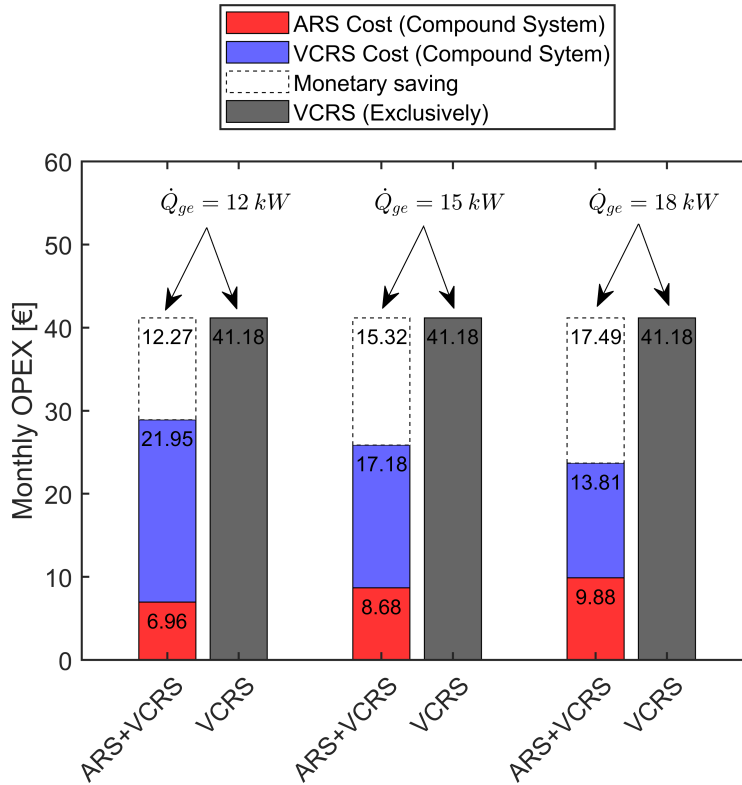
Figure 10.9: *OPEX of the configurations subject to analysis. The values correspond to the operation along the month of July of the TMY*

	Total CAPEX	Total CAPEX	Yearly OPEX	Yearly OPEX
	[€]	[€/$kW_{cooling}$]	[€]	[€/$kW_{cooling}$]
VCRS	1337,66	133,77	205,90	20,59
VCRS+ARS	16095,00	1609,50	129,30	12,93

Table 10.2: *Total CAPEX and OPEX of the refrigeration system architectures subject to study*
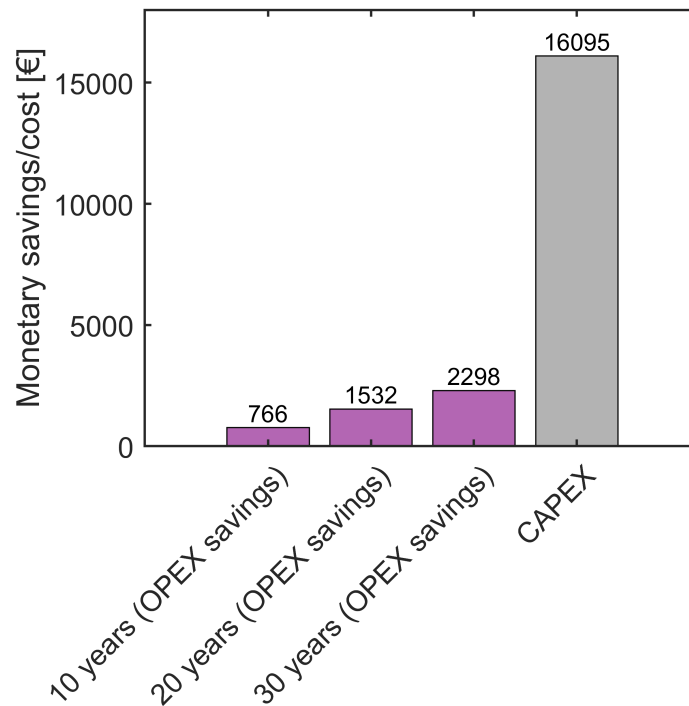
Figure 10.10: *Accumulated OPEX savings in different time horizons for the dual system CAPEX (ARS+VCRS)*

10.4 Measures to achieve a financially sustainable refrigeration system

The analysis presented in this chapter evidences that the combined system ARS+VCRS is far from being feasible in economical terms. The main drawback is its high initial investment cost in equipment and the relatively low income generated by the savings during system operation. The main part of the cost is concentrated in the solar field, specifically, in the PTC and the TSS. In future research works priority should be given to hybridized solutions designed to integrate the thermally driven refrigeration system with existing solar collectors dedicated to indoor heating. If the solar collectors are reused from an existing installations and are excluded from the CAPEX computation of the refrigeration system,the concept becomes more attractive.

Furthermore, it might be interesting to prescind from the TSS due to its high investment cost at the expense of sacrificing continuous operation or to do a detailed integration with the TSS of the indoor heating system. The suppression or size reduction of the TSS in the refrigeration mode would not be a critical issue since the refrigeration demands are almost synchronized with the daily hours with solar irradiance supply.

One of the main conclusions of the thermoeconomic analysis is that the combined system should do an efficient and smart integration to avoid duplicity of equipment

and, consequently, additional CAPEX. In an interesting hybridization alternative, the VCRS could be the main system and it would be assisted by the triplet pump-generator-jet-ejector when the thermal level in the hot source is sufficient. This way, the CAPEX would be reduced and the impact in OPEX might permit a refrigeration system financially sustainable. A solution complying with the above-mentioned demands would be that depicted in Figure 10.11. In the interest of flexibility, the system layout should be commuted as shown in Figure 10.11 depending on the current climatic situation. The if there exists a lack of solar irradiance and the generator is unable to evaporate the refrigerant at the required high pressure, the jet-ejector is bridged and the system operates like a traditional vapor-compression refrigeration system.
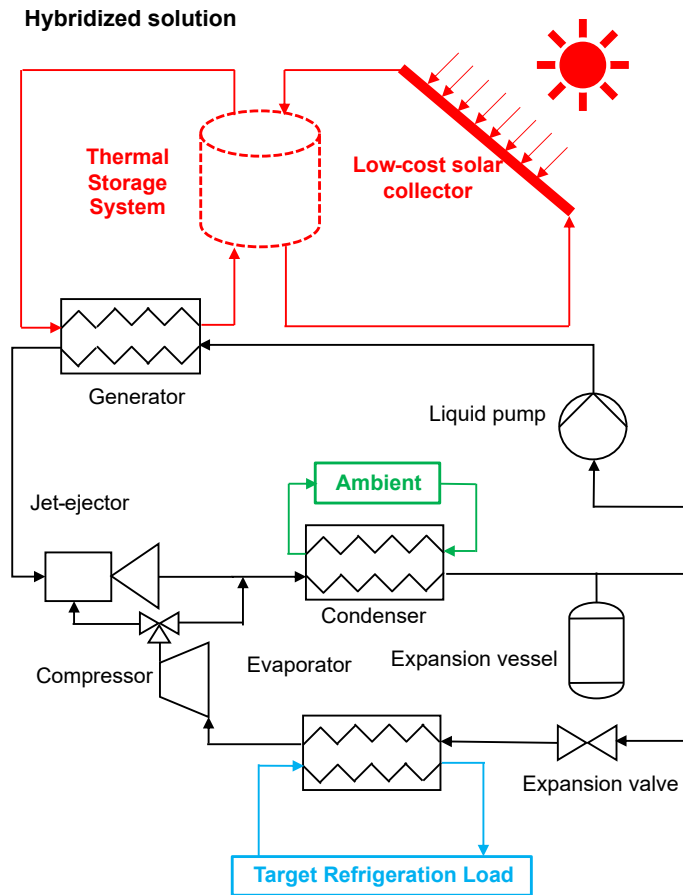
Figure 10.11: *Hybridized solution aimed to maximizing OPEX savings and reducing CAPEX.*

10.5   Summary

The present chapter shows a financial evaluation of the adjustable refrigeration system, which has proven to be the most efficient configuration. The fixed cost (CAPEX) and the variable cost (OPEX) have been assessed for reference and representative operating conditions. To establish a fair comparison between the proposed system with existing solutions which are not activated by thermal power, two configurations have been

evaluated: (i) The baseline configuration of a VCRS targeted for a refrigeration capacity of 10 kW, (ii) An ARS complemented with a VCRS to reach the targeted capacity 10 kW continuously.

The main conclusion obtained in the financial analysis is that the refrigeration system is still far from being economically feasible due to the elevated CAPEX cost, which is mainly attributed to the PTC and the TSS, and the modest OPEX savings. The PTC cost could be reduced by improving the refrigeration system efficiency to diminish the required collector area. The TSS, however, could be suppressed or downsized sacrificing some efficiency and autonomy.

A hybridized configuration based on a smart integration with a traditional vapor-compression refrigeration system and a solar-based heating system intended for winter periods has been proposed to minimize the system CAPEX.

Chapter 11

Conclusions and future works

11.1   Introduction

During the present research work, a scientific contribution has been done to understand the operation of jet-ejector refrigeration systems applied in different contexts. The methodology employed throughout the research work is grounded in numerical models:

- Jet-ejector numerical models.

- Overall system numerical models.

- Thermoeconomic numerical models.

Firstly, the key milestones are highlighted when modeling the jet-ejector response using computational fluid dynamics techniques. Secondly, the key findings of the overall system response are presented following a steady-state and a transient approach. Both approaches provide complementary information and are a fundamental part of the refrigeration system design and evaluation process. Lastly, the financial feasibility of the system is assessed in representative and realistic operating conditions.

11.2   Main contributions

11.2.1   Jet-ejector modeling and characterization

The jet-ejector is the key element of the refrigeration system and a reliable characterization of its behavior is essential to obtain a predictive model. A robust methodology has been developed in the commercial CFD code to predict the jet-ejector entrainment ratio accounting for real gas effects and the thermodynamic properties of a wide variety of refrigerants, different geometrical configurations, or boundary conditions. Hence, the modeling approach is very useful to find optimum jet-ejector geometries as well as characterizing the jet-ejector response under off-design operating conditions.

For an evaporating temperature of $13\,^{\circ}C$ and a condensing temperature of $40\,^{\circ}C$ the optimum jet-ejector working with R1234yf, R600a, and R1234ze reached a maximum

entrainment ratio of 0.417, 0.464, and 0.405, respectively.

Validation process

The process has been validated using data coming from experimental campaigns and discrepancies do not exceed 9.5% in the double-choking operating mode. The model is also a good predictor of the entrainment ratio in the single-choking operating mode, and the slight deviations could be explained by introducing artificially a reasonable surface roughness ($10\,\mu m$).

The same process has been reproduced and validated successfully using the open-source CFD code OpenFoam.

Automation of the process

The process of generating new geometries, meshing the internal domain, setting up the simulation parameters, and solving the simulation changing gradually the boundary conditions has been automated making it possible to perform easily laborious jet-ejector design and characterization campaigns. This is considered a key milestone due to the difficulties of initializing, calculating, and converging the simulation when NIST real gas models are used.

11.2.2 Overall system modeling

Steady-state characterization approach, influence of working fluids and operating conditions

The steady-state analysis is helpful to design a highly-optimized reference system for standard or representative operating conditions, in the present research, the reference conditions to design the system are an evaporating temperature of 13 $^\circ C$ and a condensing temperature of 40 $^\circ C$.

For the solar application, it has been proven that the influence of the working fluid used in the cycle is not a critical issue if the jet-ejector internal geometry is optimized thoroughly for each refrigerant, reaching COP_{th} of 0.377, 0.355, and 0.352 for R1234yf, R600a, and R1234ze, respectively. In addition, it has been demonstrated that the conditions at the generator have low influence in the maximum achievable COP_{th} if the jet-ejector internal geometry is carefully designed, given that the pinch point in the heat exchanger is satisfied. The overall system efficiency, that is, the efficiency transformation from solar irradiance to refrigeration capacity is $\eta_{ov} = 0.201$ for R1234yf, closely followed by R1234ze ($\eta_{ov} = 0.187$) and R600a ($\eta_{ov} = 0.184$).

In the automotive application, it has been proven that the thermal energy available in the exhaust line is abundant and the engine intake can be refrigerated below 5 $^\circ C$ even with poor efficiency transformation. However, the operating conditions in an automotive engine are highly changeable and the jet-ejector baseline setup is unable to adapt to those changes maintaining efficiency. The need for a multiejector rack becomes

evident as a mechanism to operate robustly, maximizing the refrigeration production at different engine loads and speeds.

The main conclusion is that, other technical difficulties, like the extra weight, the packaging problems, or the necessity of modifying the default engine calibration settings are the most remarkable limiting factors in this application, rather than the system efficiency.

Dynamic approach

The response of the fixed-geometry (FRS) and adjustable jet-ejector architectures (ARS) have been compared when the refrigeration system operates during a typical meteorological year. The ARS configuration shows its greatest potential in May and September, where the average COP_{th} reaches 0.48 and 0.44, respectively. The FRS configuration has a lower adaptation potential and the COP_{th} in the same months is 0.34, and 0.31. These trends are maintained in the rest of the months (June, July, and August) but the differences are less pronounced.

Besides, the adjustable architecture shows in all the scenarios higher or equal activation percentages and shows a smoother temporal evolution of the refrigeration capacity $\left(\dot{Q}_{ev}\right)$ because this configuration avoids the performance decay beyond the critical condensing temperature, which is unavoidable in the FRS architecture. Below the critical condensing temperature, the ARS also operates with higher efficiency, guaranteeing better thermal management of the thermal storage tank.

To sum up, the adjustable jet-ejector refrigeration system offers a superior performance in all the facets analyzed, at the expanse of higher mechanical complexity and the requirement of more elaborated control laws.

The other advanced strategy studied in depth is the thermal storage tank. It has proven to be very helpful to prolong the system operation when the supply of solar irradiance is temporarily interrupted. The research efforts have been focused on studying the coupled influence between the thermal storage tank sizing, the solar collector size, and the thermal power consumption of the refrigeration system, closely related to the achievable refrigeration capacity. For a parabolic trough collector span of 7.1 m, a thermal power consumption of 13.3 kW and a thermal storage tank volume of 0.82 m^3 maximize the refrigeration system efficiency without increasing refrigeration power outage. For that thermal storage system and collector size, if more thermal power is consumed, more refrigeration capacity is produced but the system efficiency is deteriorated and the activation percentage decreases. Oppositely, if less thermal power is consumed, less refrigeration capacity is produced with no remarkable positive impact on the system efficiency, being the system under-exploited.

As a general trend, it has been found that higher thermal storage tanks act better as a thermal reservoir but hinder rapid heating after discharge events due to their high thermal inertia. In the present investigation, the refrigeration needs are concentrated in a time slot with solar irradiance supply (08:00-19:00), so a large thermal storage system capable of feeding the system beyond the sunny hours does not produce tangible

benefits.

11.2.3 Thermoeconomic analysis

The thermoeconomic analysis sheds light on the financial feasibility of the refrigeration system and it has been focused in the solar-driven air-conditioning application because here the efficiency is crucial and the investment cost is the main barrier.

To meet a targeted refrigeration capacity of 10 kW, the jet-ejector refrigeration system must be installed together with an auxiliary vapor-compression refrigeration system (VCRS). The total capital expenditures (CAPEX) of the primary and auxiliary machines (ARS+VCRS) are estimated at approximately 16,100 €, being the solar collector and the thermal storage system the most expensive elements (77% of the overall cost). If the operating expenditures (OPEX) are compared with a conventional VCRS, the savings during a whole warm season are quantified in approximately 77 €. Given the low annual OPEX savings, even with an extensive utilization of the system during several years, the CAPEX would not be monetized.

The thermoeconomic analysis highlights the importance of avoiding redundancy or duplicity in equipment to minimize CAPEX, thus making hybridizations a promising alternative.

11.3 Future works

The electricity bill could end in 2021 with record figures in Europe. In this sense, low-consumption thermally driven refrigeration systems could play a major role in energy savings since a significant fraction of the energy bill in households, commercial areas, or industries is attributed to refrigeration. Further research and pilot plants are needed to explore the technical feasibility of these concepts. A great effort will be needed in research and development among designers, builders, research centers, or public institutions to promote and disseminate the benefits and the abilities of this technology. The present research has been useful to identify strengths, weaknesses, opportunities, and promising lines of action.

11.3.1 Theoretical future works

- Feasibility evaluation of several hybrid concepts intended to have the autonomy of a conventional vapor-compression refrigeration system and the low consumption of a jet-ejector refrigeration system.

- Theoretical evaluation of the potential gains obtained when a multiejector system in a parallel arrangement is used.

- Development of thermal storage system management laws, and jet-ejector control laws based on short-term weather forecast using machine learning techniques.

- Efficiency comparison between a low-cost reversible jet-ejector machine providing

heating a refrigeration demands with a reversible vapor-compression refrigeration system powered by photovoltaic panels.

11.3.2 Experimental future works

- Development of dedicated pilot plants to test the system operation and control laws under real conditions and corroborate the main findings of the present computational study.

- Smart integration of the refrigeration concepts explored in the present research with existing heating facilities powered by solar thermal energy.

Bibliography

[1] J. Galindo, A. Gil, V. Dolz, A. Ponce-Mora, Numerical optimization of an ejector for waste heat recovery used to cool down the intake air in an IC engine, Journal of Thermal Science and Engineering Applications (2020) 1–32doi:10.1115/1.4046906.
URL https://doi.org/10.1115/1.4046906

[2] J. Galindo, V. Dolz, A. Tiseira, A. Ponce-Mora, Thermodynamic Analysis and Optimization of a Jet Ejector Refrigeration Cycle Used To Cool Down the Intake Air in an Ic Engine, International Journal of Refrigeration 103 (2019) 253–263. doi:10.1016/j.ijrefrig.2019.04.019.
URL https://doi.org/10.1016/j.ijrefrig.2019.04.019

[3] J. Galindo, V. Dolz, L. M. García-Cuevas, A. Ponce-Mora, Numerical evaluation of a solar-assisted jet-ejector refrigeration system: Screening of environmentally friendly refrigerants, Energy Conversion and Management 210 (December 2019) (2020) 112681. doi:10.1016/j.enconman.2020.112681.
URL https://doi.org/10.1016/j.enconman.2020.112681

[4] J. Galindo, V. Dolz, A. Tiseira, A. Ponce-Mora, Numerical assessment of the dynamic behavior of a solar-driven jet-ejector refrigeration system equipped with an adjustable jet-ejector, International Journal of Refrigeration 121 (2021) 168–182. doi:10.1016/j.ijrefrig.2020.10.019.
URL https://doi.org/10.1016/j.ijrefrig.2020.10.019

[5] J. M. Luján, J. Galindo, V. Dolz, A. Ponce-Mora, Optimization of the thermal storage system in a solar-driven refrigeration system equipped with an adjustable jet-ejector, Journal of Energy Storage 45 (2021). doi:10.1016/j.est.2021.103495.

[6] J. Galindo, V. Dolz, B. Pla, A. Ponce-Mora, Advanced exergy analysis of a jet ejector refrigeration cycle used to cool down the intake air in an internal combustion engine, International Journal of Exergy (2020). doi:10.1504/IJEX.2020.108948.

[7] F. J. Cabrera, A. Fernández-García, R. M. Silva, M. Pérez-García, Use of parabolic trough solar collectors for solar refrigeration and air-conditioning applications, Renewable and Sustainable Energy Reviews 20 (2013) 103–118. doi:10.1016/j.rser.2012.11.081.

[8] M. T. Zegenhagen, F. Ziegler, Experimental investigation of the characteristics of a jet-ejector and a jet-ejector cooling system operating with R134a as a refrigerant, International Journal of Refrigeration 56 (2015) 173–185. `doi:10.1016/j.ijrefrig.2015.01.001`.
URL `http://dx.doi.org/10.1016/j.ijrefrig.2015.01.001`

[9] European Commission, Stepping up Europe's 2030 climate ambition Investing in a climate-neutral future for the benefit of our people, Journal of Chemical Information and Modeling 53 (9) (2020) 1689–1699. `arXiv:arXiv:1011.1669v3`.

[10] Eurostat (European Commission), Renewable energy statistics (2020).
URL `https://ec.europa.eu/eurostat/statistics-explained/index.php?title=Renewable_energy_statistics`

[11] S. Pezzutto, M. De Felice, R. Fazeli, L. Kranzl, S. Zambotti, Status quo of the air-conditioning market in europe: Assessment of the building stock, Energies 10 (9) (2017) 1–18. `doi:10.3390/en10091253`.

[12] M. T. Zegenhagen, F. Ziegler, Feasibility analysis of an exhaust gas waste heat driven jet-ejector cooling system for charge air cooling of turbocharged gasoline engines, Applied Energy 160 (2015) 221–230. `doi:10.1016/j.apenergy.2015.09.057`.
URL `http://dx.doi.org/10.1016/j.apenergy.2015.09.057`

[13] The Use of Ejector Refrigeration Systems for Turbine Inlet Air Cooling: A Thermodynamic and CFD Study, Vol. ASME 2007 of Energy Sustainability. `doi:10.1115/ES2007-36044`.
URL `https://doi.org/10.1115/ES2007-36044`

[14] B. M. Diaconu, S. Varga, A. C. Oliveira, Numerical simulation of a solar-assisted ejector air conditioning system with cold storage, Energy 36 (2) (2011) 1280–1291. `doi:10.1016/j.energy.2010.11.015`.
URL `http://dx.doi.org/10.1016/j.energy.2010.11.015`

[15] C. Pollerberg, A. H. H. Ali, C. Dötsch, Solar driven steam jet ejector chiller, Applied Thermal Engineering 29 (5-6) (2009) 1245–1252. `doi:10.1016/j.applthermaleng.2008.06.017`.
URL `http://dx.doi.org/10.1016/j.applthermaleng.2008.06.017`

[16] S. A. Tassou, J. S. Lewis, Y. T. Ge, A. Hadawey, I. Chaer, A review of emerging technologies for food refrigeration applications, Applied Thermal Engineering 30 (4) (2010) 263–276. `doi:10.1016/j.applthermaleng.2009.09.001`.
URL `http://dx.doi.org/10.1016/j.applthermaleng.2009.09.001`

[17] J. I. Hernández, R. J. Dorantes, R. Best, C. A. Estrada, The behaviour of a hybrid compressor and ejector refrigeration system with refrigerants 134a and 142b, Applied Thermal Engineering 24 (13) (2004) 1765–1783. `doi:10.1016/j.applthermaleng.2003.12.016`.

[18] H. Vidal, S. Colle, Simulation and economic optimization of a solar assisted com-

bined ejector-vapor compression cycle for cooling applications, Applied Thermal Engineering 30 (5) (2010) 478–486. `doi:10.1016/j.applthermaleng.2009.10.008`.
URL `http://dx.doi.org/10.1016/j.applthermaleng.2009.10.008`

[19] D. W. Sun, I. W. Eames, Performance characteristics of HCFC-123 ejector refrigeration cycles, International Journal of Energy Research 20 (10) (1996) 871–885. `doi:10.1002/(SICI)1099-114X(199610)20:10<871::AID-ER201>3.0.CO;2-4`.

[20] S. Shen, X. Qu, B. Zhang, S. Riffat, M. Gillott, Study of a gas-liquid ejector and its application to a solar-powered bi-ejector refrigeration system, Applied Thermal Engineering 25 (17-18) (2005) 2891–2902. `doi:10.1016/j.applthermaleng.2005.02.012`.

[21] D. S. Kim, C. A. Infante Ferreira, Solar refrigeration options - a state-of-the-art review, International Journal of Refrigeration 31 (1) (2008) 3–15. `doi:10.1016/j.ijrefrig.2007.07.011`.

[22] X. B. Bu, H. S. Li, L. B. Wang, Performance analysis and working fluids selection of solar powered organic Rankine-vapor compression ice maker, Solar Energy 95 (2013) 271–278. `doi:10.1016/j.solener.2013.06.024`.

[23] S. Aphornratana, T. Sriveerakul, Analysis of a combined Rankine-vapour-compression refrigeration cycle, Energy Conversion and Management 51 (12) (2010) 2557–2564. `doi:10.1016/j.enconman.2010.04.016`.

[24] M. Zeyghami, D. Y. Goswami, E. Stefanakos, A review of solar thermo-mechanical refrigeration and cooling methods, Renewable and Sustainable Energy Reviews 51 (2015) 1428–1445. `doi:10.1016/j.rser.2015.07.011`.
URL `http://dx.doi.org/10.1016/j.rser.2013.03.024`

[25] J. Bao, L. Zhang, C. Song, N. Zhang, X. Zhang, G. He, Comparative study of combined organic Rankine cycle and vapor compression cycle for refrigeration: Single fluid or dual fluid?, Sustainable Energy Technologies and Assessments 37 (November 2019) (2020) 100595. `doi:10.1016/j.seta.2019.100595`.
URL `https://doi.org/10.1016/j.seta.2019.100595`

[26] X. Bu, L. Wang, H. Li, Performance analysis and working fluid selection for geothermal energy-powered organic Rankine-vapor compression air conditioning, Geothermal Energy 1 (1) (2013) 1–14. `doi:10.1186/2195-9706-1-2`.

[27] M. Aneke, B. Agnew, C. Underwood, M. Menkiti, Thermodynamic analysis of alternative refrigeration cycles driven from waste heat in a food processing application, International Journal of Refrigeration 35 (5) (2012) 1349–1358. `doi:10.1016/j.ijrefrig.2012.04.008`.
URL `http://dx.doi.org/10.1016/j.ijrefrig.2012.04.008`

[28] S. Langdon-Arms, M. Gschwendtner, M. Neumaier, Development of a solar-powered liquid piston Stirling refrigerator, Energy Procedia 142 (2017) 570–575.

doi:10.1016/j.egypro.2017.12.095.
URL https://doi.org/10.1016/j.egypro.2017.12.095

[29] H. Sun, Z. Xu, H. Wang, R. Wang, A Solar/gas Fired Absorption System for Cooling and Heating in a Commercial Building, Energy Procedia 70 (2015) 518–528. doi:10.1016/j.egypro.2015.02.156.
URL http://dx.doi.org/10.1016/j.egypro.2015.02.156

[30] H. Z. Hassan, A. A. Mohamad, A review on solar cold production through absorption technology, Renewable and Sustainable Energy Reviews 16 (7) (2012) 5331–5348. doi:10.1016/j.rser.2012.04.049.
URL http://dx.doi.org/10.1016/j.rser.2012.04.049

[31] X. Q. Zhai, M. Qu, Y. Li, R. Z. Wang, A review for research and new design options of solar absorption cooling systems, Renewable and Sustainable Energy Reviews 15 (9) (2011) 4416–4423. doi:10.1016/j.rser.2011.06.016.

[32] R. Nikbakhti, X. Wang, A. K. Hussein, A. Iranmanesh, Absorption cooling systems – Review of various techniques for energy performance enhancement, Alexandria Engineering Journal 59 (2) (2020) 707–738. doi:10.1016/j.aej.2020.01.036.
URL https://doi.org/10.1016/j.aej.2020.01.036

[33] Y. Agrouaz, T. Bouhal, A. Allouhi, T. Kousksou, A. Jamil, Y. Zeraouli, Energy and parametric analysis of solar absorption cooling systems in various Moroccan climates, Case Studies in Thermal Engineering 9 (June 2016) (2017) 28–39. doi:10.1016/j.csite.2016.11.002.
URL http://dx.doi.org/10.1016/j.csite.2016.11.002

[34] M. C. Hidalgo, P. R. Aumente, M. I. Millán, A. L. Neumann, R. S. Mangual, Energy and carbon emission savings in Spanish housing air-conditioning using solar driven absorption system, Applied Thermal Engineering 28 (14-15) (2008) 1734–1744. doi:10.1016/j.applthermaleng.2007.11.013.

[35] A. Syed, M. Izquierdo, P. Rodríguez, G. Maidment, J. Missenden, A. Lecuona, R. Tozer, A novel experimental investigation of a solar cooling system in Madrid, International Journal of Refrigeration 28 (6) (2005) 859–871. doi:10.1016/j.ijrefrig.2005.01.007.

[36] R. Novella, V. Dolz, J. Martín, L. Royo-Pascual, Thermodynamic analysis of an absorption refrigeration system used to cool down the intake air in an Internal Combustion Engine, Applied Thermal Engineering 111 (2017) 257–270. doi:10.1016/j.applthermaleng.2016.09.084.
URL http://dx.doi.org/10.1016/j.applthermaleng.2016.09.084

[37] J. Koehler, W. J. Tegethoff, D. Westphalen, M. Sonnekalb, Absorption refrigeration system for mobile applications utilizing exhaust qases, Heat and Mass Transfer/Waerme- und Stoffuebertragung 32 (5) (1997) 333–340. doi:10.1007/s002310050130.

[38] A. Ouadha, Y. El-gotni, Integration of an ammonia-water absorption refrigeration system with a marine Diesel engine : A thermodynamic study, Procedia - Procedia Computer Science 19 (Seit) (2013) 754–761. `doi:10.1016/j.procs.2013.06.099`.
URL `http://dx.doi.org/10.1016/j.procs.2013.06.099`

[39] D. S. Ayou, A. Coronas, New developments and progress in absorption chillers for solar cooling applications, Vol. 10, 2020. `doi:10.3390/app10124073`.

[40] M. S. Fernandes, G. J. Brites, J. J. Costa, A. R. Gaspar, V. A. Costa, Review and future trends of solar adsorption refrigeration systems, Renewable and Sustainable Energy Reviews 39 (2014) 102–123. `doi:10.1016/j.rser.2014.07.081`.
URL `http://dx.doi.org/10.1016/j.rser.2014.07.081`

[41] Y. L. Liu, R. Z. Wang, Z. Z. Xia, Experimental study on a continuous adsorption water chiller with novel design, International Journal of Refrigeration 28 (2) (2005) 218–230. `doi:10.1016/j.ijrefrig.2004.09.004`.

[42] C. Hildbrand, P. Dind, M. Pons, F. Buchter, A new solar powered adsorption refrigerator with high performance, Solar Energy 77 (3) (2004) 311–318. `doi:10.1016/j.solener.2004.05.007`.

[43] S. Jiangzhou, R. Z. Wang, Y. Z. Lu, Y. X. Xu, J. Y. Wu, Z. H. Li, Locomotive driver cabin adsorption air-conditioner, Renewable Energy 28 (11) (2003) 1659–1670. `doi:10.1016/S0960-1481(03)00007-7`.

[44] L. W. Wang, R. Z. Wang, J. Y. Wu, K. Wang, S. G. Wang, Adsorption ice makers for fishing boats driven by the exhaust heat from diesel engine: Choice of adsorption pair, Energy Conversion and Management 45 (13-14) (2004) 2043–2057. `doi:10.1016/j.enconman.2003.10.021`.

[45] A. Milazzo, F. Mazzelli, Future perspectives in ejector refrigeration, Applied Thermal Engineering 121 (2017) 344–350. `doi:10.1016/j.applthermaleng.2017.04.088`.

[46] N. Ruangtrakoon, T. Thongtip, S. Aphornratana, T. Sriveerakul, CFD simulation on the effect of primary nozzle geometries for a steam ejector in refrigeration cycle, International Journal of Thermal Sciences 63 (2013) 133–145. `doi:10.1016/j.ijthermalsci.2012.07.009`.
URL `http://dx.doi.org/10.1016/j.ijthermalsci.2012.07.009`

[47] Y. Zhu, W. Cai, C. Wen, Y. Li, Numerical investigation of geometry parameters for design of high performance ejectors, Applied Thermal Engineering 29 (5-6) (2009) 898–905. `doi:10.1016/J.APPLTHERMALENG.2008.04.025`.
URL `https://www.sciencedirect.com/science/article/pii/S1359431108002135?via%3Dihub`

[48] Z. Aidoun, K. Ameur, M. Falsafioon, M. Badache, Current Advances in Ejector Modeling, Experimentation and Applications for Refrigeration and Heat Pumps. Part 1: Single-Phase Ejectors, Inventions 4 (1) (2019). `doi:10.3390/`

inventions4010015.
URL https://www.mdpi.com/2411-5134/4/1/15

[49] G. Besagni, Ejectors on the cutting edge: The past, the present and the perspective, Energy 170 (2019) 998–1003. doi:10.1016/j.energy.2018.12.214.
URL https://doi.org/10.1016/j.energy.2018.12.214

[50] P. R. Pereira, S. Varga, A. C. Oliveira, J. Soares, Development and Performance of an Advanced Ejector Cooling System for a Sustainable Built Environment, Frontiers in Mechanical Engineering 1 (June) (2015) 1–12. doi:10.3389/fmech.2015.00007.

[51] K. Pianthong, W. Seehanam, M. Behnia, T. Sriveerakul, S. Aphornratana, Investigation and improvement of ejector refrigeration system using computational fluid dynamics technique, Energy Conversion and Management 48 (9) (2007) 2556–2564. doi:10.1016/j.enconman.2007.03.021.

[52] J. Mahmoudian, A. Rocchetti, F. Mazzelli, A. Milazzo, A heat-powered ejector chiller working with low-GWP fluid R1233zd(E) (Part 1: Experimental results), International Journal of Refrigeration 121 (2021) 1–9. doi:10.1016/j.ijrefrig.2020.10.015.
URL https://doi.org/10.1016/j.ijrefrig.2020.10.015

[53] J. Chen, S. Jarall, H. Havtun, B. Palm, A review on versatile ejector applications in refrigeration systems, Renewable and Sustainable Energy Reviews 49 (2015) 67–90. doi:10.1016/j.rser.2015.04.073.
URL http://dx.doi.org/10.1016/j.rser.2015.04.073

[54] J. Chen, H. Havtun, B. Palm, Screening of working fluids for the ejector refrigeration system, International Journal of Refrigeration 47 (0) (2014) 1–14. doi:10.1016/j.ijrefrig.2014.07.016.

[55] K. Smierciew, M. Kędzierski, D. Butrymowicz, J. Gagan, Assesment of refrigerant selection for ejection system driven by low-grade heat, Refrigeration Science and Technology 2017-Septe (2017) 22–29. doi:10.18462/iir.compr.2017.0245.

[56] J. Kasperski, B. Gil, Performance estimation of ejector cycles using heavier hydrocarbon refrigerants, Applied Thermal Engineering 71 (1) (2014) 197–203. doi:10.1016/j.applthermaleng.2014.06.057.
URL http://dx.doi.org/10.1016/j.applthermaleng.2014.06.057

[57] B. Huang, J. Chang, C. Wang, V. Petrenko, A 1-D analysis of ejector performance, International Journal of Refrigeration 22 (5) (1999) 354–364. doi:10.1016/S0140-7007(99)00004-3.
URL https://www.sciencedirect.com/science/article/pii/S0140700799000043

[58] B. Gil, J. Kasperski, Efficiency analysis of alternative refrigerants for ejector cooling cycles, Energy Conversion and Management 94 (2015) 12–18. doi:10.1016/j.enconman.2015.01.056.

URL `http://dx.doi.org/10.1016/j.enconman.2015.01.056`

[59] Y. Allouche, S. Varga, C. Bouden, A. C. Oliveira, Dynamic simulation of an integrated solar-driven ejector based air conditioning system with PCM cold storage, Applied Energy 190 (2017) 600–611. `doi:10.1016/j.apenergy.2017.01.001`.
URL `http://dx.doi.org/10.1016/j.apenergy.2017.01.001`

[60] B. Tashtoush, A. Alshare, S. Al-Rifai, Hourly dynamic simulation of solar ejector cooling system using TRNSYS for Jordanian climate, Energy Conversion and Management 100 (2015) 288–299. `doi:10.1016/j.enconman.2015.05.010`.
URL `http://dx.doi.org/10.1016/j.enconman.2015.05.010`

[61] W. Chen, M. Liu, D. Chong, J. Yan, A. B. Little, Y. Bartosiewicz, A 1D model to predict ejector performance at critical and sub-critical operational regimes, International Journal of Refrigeration 36 (6) (2013) 1750–1761. `doi:10.1016/J.IJREFRIG.2013.04.009`.
URL `https://www.sciencedirect.com/science/article/pii/S0140700713000984`

[62] J. García Del Valle, J. M. Sáiz Jabardo, F. Castro Ruiz, J. San José Alonso, A one dimensional model for the determination of an ejector entrainment ratio, International Journal of Refrigeration 35 (4) (2012) 772–784. `doi:10.1016/j.ijrefrig.2011.11.020`.

[63] Y. Zhu, P. Jiang, Experimental and numerical investigation of the effect of shock wave characteristics on the ejector performance, International Journal of Refrigeration 40 (2014) 31–42. `doi:10.1016/j.ijrefrig.2013.11.008`.
URL `http://dx.doi.org/10.1016/j.ijrefrig.2013.11.008`

[64] J. Yan, G. Chen, C. Liu, L. Tang, Q. Chen, Experimental investigations on a R134a ejector applied in a refrigeration system, Applied Thermal Engineering 110 (2017) 1061–1065. `doi:10.1016/j.applthermaleng.2016.09.046`.
URL `http://dx.doi.org/10.1016/j.applthermaleng.2016.09.046`

[65] J. García Del Valle, J. M. Saíz Jabardo, F. Castro Ruiz, J. F. San José Alonso, An experimental investigation of a R-134a ejector refrigeration system, International Journal of Refrigeration 46 (2014) 105–113. `doi:10.1016/j.ijrefrig.2014.05.028`.

[66] D. Scott, Z. Aidoun, M. Ouzzane, An experimental investigation of an ejector for validating numerical simulations, International Journal of Refrigeration 34 (7) (2011) 1717–1723. `doi:10.1016/j.ijrefrig.2011.06.001`.
URL `http://dx.doi.org/10.1016/j.ijrefrig.2011.06.001`

[67] A. Omidvar, M. Ghazikhani, S. M. R. Modarres Razavi, Entropy analysis of a solar-driven variable geometry ejector using computational fluid dynamics, Energy Conversion and Management 119 (2016) 435–443. `doi:10.1016/j.enconman.2016.03.090`.
URL `http://dx.doi.org/10.1016/j.enconman.2016.03.090`

[68] Z. Chen, X. Jin, C. Dang, E. Hihara, Ejector performance analysis under overall operating conditions considering adjustable nozzle structure, International Journal of Refrigeration 84 (2017) 274–286. `doi:10.1016/j.ijrefrig.2017.08.005`.
URL `https://doi.org/10.1016/j.ijrefrig.2017.08.005`

[69] Z. Chen, X. Jin, A. Shimizu, E. Hihara, C. Dang, Effects of the nozzle configuration on solar-powered variable geometry ejectors, Solar Energy 150 (2017) 275–286. `doi:10.1016/j.solener.2017.04.017`.
URL `http://dx.doi.org/10.1016/j.solener.2017.04.017`

[70] X. Ma, W. Zhang, S. A. Omer, S. B. Riffat, Experimental investigation of a novel steam ejector refrigerator suitable for solar energy applications, Applied Thermal Engineering 30 (11-12) (2010) 1320–1325. `doi:10.1016/j.applthermaleng.2010.02.011`.
URL `http://dx.doi.org/10.1016/j.applthermaleng.2010.02.011`

[71] P. R. Pereira, S. Varga, J. Soares, A. C. Oliveira, A. M. Lopes, F. G. De Almeida, J. F. Carneiro, Experimental results with a variable geometry ejector using R600a as working fluid, International Journal of Refrigeration 46 (2014) 77–85. `doi:10.1016/j.ijrefrig.2014.06.016`.

[72] R. H. Yen, B. J. Huang, C. Y. Chen, T. Y. Shiu, C. W. Cheng, S. S. Chen, K. Shestopalov, Performance optimization for a variable throat ejector in a solar refrigeration system, International Journal of Refrigeration 36 (5) (2013) 1512–1520. `doi:10.1016/j.ijrefrig.2013.04.005`.
URL `http://dx.doi.org/10.1016/j.ijrefrig.2013.04.005`

[73] S. Varga, P. M. Lebre, A. C. Oliveira, CFD study of a variable area ratio ejector using R600a and R152a refrigerants, International Journal of Refrigeration 36 (1) (2013) 157–165. `doi:10.1016/j.ijrefrig.2012.10.016`.
URL `http://dx.doi.org/10.1016/j.ijrefrig.2012.10.016`

[74] S. Varga, A. C. Oliveira, A. Palmero-Marrero, J. Vrba, Preliminary experimental results with a solar driven ejector air conditioner in Portugal, Renewable Energy 109 (2017) 83–92. `doi:10.1016/j.renene.2017.03.016`.
URL `http://dx.doi.org/10.1016/j.renene.2017.03.016`

[75] B. W. Sparber, A. Napolitano, G. Eckert, A. Preisler, Task 38, Solar Air-Conditioning and Refrigeration: State of the art of existing solar heating and cooling systems, Tech. rep., International Energy Agency, Solar Heating Cooling Program (2009).

[76] M. Dennis, K. Garzoli, Use of variable geometry ejector with cold store to achieve high solar fraction for solar cooling, International Journal of Refrigeration 34 (7) (2011) 1626–1632. `doi:10.1016/j.ijrefrig.2010.08.006`.
URL `http://dx.doi.org/10.1016/j.ijrefrig.2010.08.006`

[77] X. Chen, M. Worall, S. Omer, Y. Su, S. Riffat, Experimental investigation on PCM cold storage integrated with ejector cooling system, Applied Thermal Engineering 63 (1) (2014) 419–427. `doi:10.1016/j.applthermaleng.2013.11.029`.

URL `http://dx.doi.org/10.1016/j.applthermaleng.2013.11.029`

[78] V. Van Nguyen, S. Varga, J. Soares, V. Dvorak, A. C. Oliveira, Applying a variable geometry ejector in a solar ejector refrigeration system, International Journal of Refrigeration 113 (2020) 187–195. `doi:10.1016/j.ijrefrig.2020.01.018`.
URL `https://doi.org/10.1016/j.ijrefrig.2020.01.018`

[79] Y. Cheng, M. Wang, J. Yu, Thermodynamic analysis of a novel solar-driven booster-assisted ejector refrigeration cycle, Solar Energy 218 (February) (2021) 85–94. `doi:10.1016/j.solener.2021.02.031`.
URL `https://doi.org/10.1016/j.solener.2021.02.031`

[80] R. Dorantes, C. A. Estrada, I. Pilatowsky, Mathematical simulation of a solar ejector-compression refrigeration system, Applied Thermal Engineering 16 (8-9) (1996) 669–675.

[81] J. Bodys, M. Palacz, M. Haida, J. Smolka, A. J. Nowak, K. Banasiak, A. Hafner, Full-scale multi-ejector module for a carbon dioxide supermarket refrigeration system: Numerical study of performance evaluation, Energy Conversion and Management 138 (2017) 312–326. `doi:10.1016/j.enconman.2017.02.007`.
URL `http://dx.doi.org/10.1016/j.enconman.2017.02.007`

[82] S. Singh, P. M. Maiya, A. Hafner, K. Banasiak, P. Neksa, Energy efficient multiejector CO2 cooling system for high ambient temperature, Thermal Science and Engineering Progress 19 (June) (2020) 100590. `doi:10.1016/j.tsep.2020.100590`.
URL `https://doi.org/10.1016/j.tsep.2020.100590`

[83] X. Chen, S. Omer, M. Worall, S. Riffat, Recent developments in ejector refrigeration technologies, Renewable and Sustainable Energy Reviews 19 (2013) 629–651. `doi:10.1016/j.rser.2012.11.028`.
URL `http://dx.doi.org/10.1016/j.rser.2012.11.028`

[84] F. Aligolzadeh, A. Hakkaki-Fard, A novel methodology for designing a multi-ejector refrigeration system, Applied Thermal Engineering 151 (November 2018) (2019) 26–37. `doi:10.1016/j.applthermaleng.2019.01.112`.
URL `https://doi.org/10.1016/j.applthermaleng.2019.01.112`

[85] M. Sokolov, D. Hershgal, Enhanced ejector refrigeration cycles powered by low grade heat. Part 2. Design procedures, International Journal of Refrigeration 13 (6) (1990) 357–363. `doi:10.1016/0140-7007(90)90024-Q`.

[86] C. A. Balaras, G. Grossman, H. M. Henning, C. A. Infante Ferreira, E. Podesser, L. Wang, E. Wiemken, Solar air conditioning in Europe-an overview, Renewable and Sustainable Energy Reviews 11 (2) (2007) 299–314. `doi:10.1016/j.rser.2005.02.003`.

[87] EU, Increasing the market implementation of Solar-air-conditioning systems for small and medium applications in residential and commercial buildings

(SOLAIR), Tech. rep. (2014).
URL https://ec.europa.eu/energy/intelligent/projects/sites/iee-projects/files/projects/documents/solair_key_results.pdf

[88] A. Shirazi, R. A. Taylor, S. D. White, G. L. Morrison, A systematic parametric study and feasibility assessment of solar-assisted single-effect, double-effect, and triple-effect absorption chillers for heating and cooling applications, Energy Conversion and Management 114 (2016) 258–277. doi:10.1016/j.enconman.2016.01.070.
URL http://dx.doi.org/10.1016/j.enconman.2016.01.070

[89] A. J. Abdulhamed, N. M. Adam, M. Z. A. Ab-Kadir, A. A. Hairuddin, Review of solar parabolic-trough collector geometrical and thermal analyses, performance, and applications, Renewable and Sustainable Energy Reviews 91 (March) (2018) 822–831. doi:10.1016/j.rser.2018.04.085.
URL https://doi.org/10.1016/j.rser.2018.04.085

[90] S. A. Kalogirou, Solar thermal collectors and applications, Vol. 30, 2004. doi:10.1016/j.pecs.2004.02.001.

[91] H. Fathabadi, Novel low-cost parabolic trough solar collector with TPCT heat pipe and solar tracker: Performance and comparing with commercial flat-plate and evacuated tube solar collectors, Solar Energy 195 (February 2019) (2020) 210–222. doi:10.1016/j.solener.2019.11.057.
URL https://doi.org/10.1016/j.solener.2019.11.057

[92] K. M. Pandey, R. Chaurasiya, A review on analysis and development of solar flat plate collector, Renewable and Sustainable Energy Reviews 67 (2017) 641–650. doi:10.1016/j.rser.2016.09.078.
URL http://dx.doi.org/10.1016/j.rser.2016.09.078

[93] V. Belessiotis, S. Kalogirou, E. Delyannis, V. Belessiotis, S. Kalogirou, E. Delyannis, Indirect Solar Desalination (MSF, MED, MVC, TVC), Thermal Solar Desalination (2016) 283–326doi:10.1016/B978-0-12-809656-7.00006-4.
URL https://www.sciencedirect.com/science/article/pii/B9780128096567000064

[94] M. Tian, Y. Su, H. Zheng, G. Pei, G. Li, S. Riffat, A review on the recent research progress in the compound parabolic concentrator (CPC) for solar energy applications, Renewable and Sustainable Energy Reviews 82 (October 2017) (2018) 1272–1296. doi:10.1016/j.rser.2017.09.050.

[95] A. Kumar, Z. Said, E. Bellos, An up-to-date review on evacuated tube solar collectors, Journal of Thermal Analysis and Calorimetry (January) (2020). doi:10.1007/s10973-020-09953-9.
URL https://doi.org/10.1007/s10973-020-09953-9

[96] G. Pei, G. Li, X. Zhou, J. Ji, Y. Su, Comparative experimental analysis of the thermal performance of evacuated tube solar water heater systems with and without a mini-compound parabolic concentrating (CPC) reflector(C ¡ 1), Energies

5 (4) (2012) 911–924. `doi:10.3390/en5040911`.

[97] I. Sarbu, C. Sebarchievici, A comprehensive review of thermal energy storage, Sustainability (Switzerland) 10 (1) (2018). `doi:10.3390/su10010191`.

[98] A. A. Al-Abidi, S. Bin Mat, K. Sopian, M. Y. Sulaiman, C. H. Lim, A. Th, Review of thermal energy storage for air conditioning systems, Renewable and Sustainable Energy Reviews 16 (8) (2012) 5802–5819. `doi:10.1016/j.rser.2012.05.030`.
URL `http://dx.doi.org/10.1016/j.rser.2012.05.030`

[99] S. Pintaldi, C. Perfumo, S. Sethuvenkatraman, S. White, G. Rosengarten, A review of thermal energy storage technologies and control approaches for solar cooling, Renewable and Sustainable Energy Reviews 41 (1) (2015) 975–995. `doi:10.1016/j.rser.2014.08.062`.
URL `http://dx.doi.org/10.1016/j.rser.2014.08.062`

[100] A. A. Manzela, S. M. Hanriot, L. Cabezas-Gómez, J. R. Sodré, Using engine exhaust gas as energy source for an absorption refrigeration system, Applied Energy 87 (4) (2010) 1141–1148. `doi:10.1016/j.apenergy.2009.07.018`.
URL `http://dx.doi.org/10.1016/j.apenergy.2009.07.018`

[101] S. Du, R. Z. Wang, X. Chen, Development and experimental study of an ammonia water absorption refrigeration prototype driven by diesel engine exhaust heat, Energy 130 (2017) 420–432. `doi:10.1016/j.energy.2017.05.006`.

[102] R. Cipollone, D. Di Battista, D. Vittorini, Experimental assessment of engine charge air cooling by a refrigeration unit, Energy Procedia 126 (2017) 1067–1074. `doi:10.1016/j.egypro.2017.08.226`.
URL `https://doi.org/10.1016/j.egypro.2017.08.226`

[103] F. Payri, J. Desantes, Motores de Combustión Interna Alternativos, Reverte, 2011.

[104] E. Bellos, C. Tzivanidis, Optimum design of a solar ejector refrigeration system for various operating scenarios, Energy Conversion and Management 154 (August) (2017) 11–24. `doi:10.1016/j.enconman.2017.10.057`.
URL `https://doi.org/10.1016/j.enconman.2017.10.057`

[105] T. Fasquelle, Q. Falcoz, P. Neveu, F. Lecat, G. Flamant, A thermal model to predict the dynamic performances of parabolic trough lines, Energy 141 (2017) 1187–1203. `doi:10.1016/j.energy.2017.09.063`.
URL `https://doi.org/10.1016/j.energy.2017.09.063`

[106] A. Desideri, R. Dickes, J. Bonilla, L. Valenzuela, S. Quoilin, V. Lemort, Steady-state and dynamic validation of a parabolic trough collector model using the ThermoCycle Modelica library, Solar Energy 174 (August) (2018) 866–877. `doi:10.1016/j.solener.2018.08.026`.
URL `https://doi.org/10.1016/j.solener.2018.08.026`

[107] L. A. Chidambaram, A. S. Ramana, G. Kamaraj, R. Velraj, Review of solar cooling methods and thermal storage options, Renewable and Sustainable Energy Reviews 15 (6) (2011) 3220–3228. `doi:10.1016/j.rser.2011.04.018`.
URL `http://dx.doi.org/10.1016/j.rser.2011.04.018`

[108] M. C. Rodríguez-Hidalgo, P. A. Rodríguez-Aumente, A. Lecuona, M. Legrand, R. Ventas, Domestic hot water consumption vs. solar thermal energy storage: The optimum size of the storage tank, Applied Energy 97 (2012) 897–906. `doi:10.1016/j.apenergy.2011.12.088`.

[109] Ministerio de Fomento (Gobierno de España), Documento Básico HE. Ahorro de energía (Código Técnico de la Edificación) (2017) 1–77.
URL `http://www.arquitectura-tecnica.com/hit/Hit2016-2/DBHE.pdf`

[110] F. Zaversky, J. García-Barberena, M. Sánchez, D. Astrain, Transient molten salt two-tank thermal storage modeling for CSP performance simulations, Solar Energy 93 (2013) 294–311. `doi:10.1016/j.solener.2013.02.034`.

[111] T. Zhang, S. Mohamed, Conceptual Design and Analysis of Hydrocarbon-Based Solar Thermal Power and Ejector Cooling Systems in Hot Climates, Journal of Solar Energy Engineering 137 (2) (sep 2014). `doi:10.1115/1.4028365`.
URL `https://doi.org/10.1115/1.4028365`

[112] Y. Lee, D. Jung, A brief performance comparison of R1234yf and R134a in a bench tester for automobile applications, Applied Thermal Engineering 35 (1) (2012) 240–242. `doi:10.1016/j.applthermaleng.2011.09.004`.
URL `http://dx.doi.org/10.1016/j.applthermaleng.2011.09.004`

[113] M. Fallah, S. M. S. Mahmoudi, M. Yari, R. Akbarpour Ghiasi, Advanced exergy analysis of the Kalina cycle applied for low temperature enhanced geothermal system, Energy Conversion and Management 108 (2016) 190–201. `doi:10.1016/j.enconman.2015.11.017`.
URL `http://dx.doi.org/10.1016/j.enconman.2015.11.017`

[114] P. Chen, G. He, Y. Gao, X. Zhao, D. Cai, Conventional and advanced exergy analysis of an air-cooled type of absorption-ejection refrigeration cycle with R290-mineral oil as the working pair, Energy Conversion and Management 210 (March) (2020) 112703. `doi:10.1016/j.enconman.2020.112703`.
URL `https://doi.org/10.1016/j.enconman.2020.112703`

[115] S. Varga, A. C. Oliveira, B. Diaconu, Influence of geometrical factors on steam ejector performance - A numerical assessment, International Journal of Refrigeration 32 (7) (2009) 1694–1701. `doi:10.1016/j.ijrefrig.2009.05.009`.
URL `http://dx.doi.org/10.1016/j.ijrefrig.2009.05.009`

[116] N. Ruangtrakoon, S. Aphornratana, T. Sriveerakul, Experimental studies of a steam jet refrigeration cycle: Effect of the primary nozzle geometries to system performance, Experimental Thermal and Fluid Science 35 (4) (2011) 676–683. `doi:10.1016/j.expthermflusci.2011.01.001`.
URL `http://dx.doi.org/10.1016/j.expthermflusci.2011.01.001`

[117] M. T. Zegenhagen, F. Ziegler, A one-dimensional model of a jet-ejector in critical double choking operation with R134a as a refrigerant including real gas effects, International Journal of Refrigeration 55 (2006) (2015) 72–84. doi:10.1016/j.ijrefrig.2015.03.013.
URL http://dx.doi.org/10.1016/j.ijrefrig.2015.03.013

[118] M. Richter, M. O. McLinden, E. W. Lemmon, Thermodynamic properties of 2,3,3,3-tetrafluoroprop-1-ene (R1234yf): Vapor pressure and p - ϕ - T Measurements and an Equation of State, Journal of Chemical and Engineering Data 56 (7) (2011) 3254–3264. doi:10.1021/je200369m.

[119] M. J. O. Mclinden, M. Thol, E. W. Lemmon, Thermodynamic Properties of Measurements of Density and Vapor Pressure and a Comprehensive Equation of State, International Refrigeration and Air Conditioning Conference (2010).

[120] D. Bücker, W. Wagner, Reference equations of state for the thermodynamic properties of fluid phase n-butane and isobutane, Journal of Physical and Chemical Reference Data 35 (2) (2006) 929–1019. doi:10.1063/1.1901687.

[121] S. Croquer, S. Poncet, Z. Aidoun, Turbulence modeling of a single-phase R134a supersonic ejector. Part 1: Numerical benchmark, International Journal of Refrigeration 61 (2016) 140–152. doi:10.1016/j.ijrefrig.2015.07.030.
URL http://dx.doi.org/10.1016/j.ijrefrig.2015.07.030

[122] J. Kolář, V. Dvořák, Verification of K-ω SST Turbulence Model for Supersonic Internal Flows, Waset.Org 5 (2) (2011) 262–266.
URL https://waset.org/journals/waset/v57/v57-50.pdf

[123] F. Mazzelli, A. Milazzo, Performance analysis of a supersonic ejector cycle working with R245fa, International Journal of Refrigeration 49 (0) (2015) 79–92. doi:10.1016/j.ijrefrig.2014.09.020.
URL http://dx.doi.org/10.1016/j.ijrefrig.2014.09.020

[124] G. Besagni, R. Mereu, P. Chiesa, F. Inzoli, An Integrated Lumped Parameter-CFD approach for off-design ejector performance evaluation, Energy Conversion and Management 105 (2015) 697–715. doi:10.1016/j.enconman.2015.08.029.
URL http://dx.doi.org/10.1016/j.enconman.2015.08.029

[125] A. Hakkaki-Fard, M. Poirier, Z. Aidoun, M. Ouzzane, D. Giguère, An experimental study of ejectors supported by CFD, Refrigeration Science and Technology (September) (2015) 2030–2037. doi:10.18462/iir.icr.2015.0609.

[126] J. Gagan, K. Smierciew, D. Butrymowicz, J. Karwacki, Comparative study of turbulence models in application to gas ejectors, International Journal of Thermal Sciences 78 (2014) 9–15. doi:10.1016/j.ijthermalsci.2013.11.009.
URL http://dx.doi.org/10.1016/j.ijthermalsci.2013.11.009

[127] A. Hakkaki-Fard, Z. Aidoun, M. Ouzzane, A computational methodology for ejector design and performance maximisation, Energy Conversion and Management 105 (2015) 1291–1302. doi:10.1016/j.enconman.2015.08.070.

URL `http://dx.doi.org/10.1016/j.enconman.2015.08.070`

[128] S. Mohamed, Y. Shatilla, T. J. Zhang, CFD-based design and simulation of hydrocarbon ejector for cooling, Energy 167 (2019) 346–358. `doi:10.1016/j.energy.2018.10.057`.
URL `https://doi.org/10.1016/j.energy.2018.10.057`

[129] K. O. Shestopalov, B. J. Huang, V. O. Petrenko, O. S. Volovyk, Investigation of an experimental ejector refrigeration machine operating with refrigerant R245fa at design and off-design working conditions. Part 2. Theoretical and experimental results, International Journal of Refrigeration 55 (2015) 212–223. `doi:10.1016/j.ijrefrig.2015.02.004`.
URL `http://dx.doi.org/10.1016/j.ijrefrig.2015.02.004`

[130] J. R. García-Cascales, F. Vera-García, J. M. Corberán-Salvador, J. Gonzálvez-Maciá, Assessment of boiling and condensation heat transfer correlations in the modelling of plate heat exchangers, International Journal of Refrigeration 30 (6) (2007) 1029–1041. `doi:10.1016/j.ijrefrig.2007.01.004`.

[131] Y. Y. Yan, H. C. Lio, T. F. Lin, Condensation heat transfer and pressure drop of refrigerant R-134a in a plate heat exchanger, International Journal of Heat and Mass Transfer 42 (6) (1999) 993–1006. `doi:10.1016/S0017-9310(98)00217-8`.

[132] R. Eldeeb, V. Aute, R. Radermacher, A survey of correlations for heat transfer and pressure drop for evaporation and condensation in plate heat exchangers, International Journal of Refrigeration 65 (2016) 12–26. `doi:10.1016/j.ijrefrig.2015.11.013`.
URL `http://dx.doi.org/10.1016/j.ijrefrig.2015.11.013`

[133] I.-K. Kim, J.-H. Park, Y.-H. Kwon, Y.-S. Kim, Experimental Study on R-410a Evaporation Heat Transfer Characteristics in Oblong Shell and Plate Heat Exchanger, Heat Transfer Engineering 28 (7) (2007) 633–639. `doi:10.1080/01457630701266454`.
URL `https://doi.org/10.1080/01457630701266454`

[134] P. Forooghi, K. Hooman, Experimental analysis of heat transfer of supercritical fluids in plate heat exchangers, International Journal of Heat and Mass Transfer 74 (2014) 448–459. `doi:10.1016/j.ijheatmasstransfer.2014.03.052`.
URL `http://dx.doi.org/10.1016/j.ijheatmasstransfer.2014.03.052`

[135] S. Quoilin, S. Declaye, B. F. Tchanche, V. Lemort, Thermo-economic optimization of waste heat recovery Organic Rankine Cycles, Applied Thermal Engineering 31 (14-15) (2011) 2885–2893. `doi:10.1016/j.applthermaleng.2011.05.014`.
URL `http://dx.doi.org/10.1016/j.applthermaleng.2011.05.014`

[136] J. Galindo, H. Climent, V. Dolz, L. Royo-Pascual, Multi-objective optimization of a bottoming Organic Rankine Cycle (ORC) of gasoline engine using swashplate expander, Energy Conversion and Management 126 (2016) 1054–1065. `doi:10.1016/j.enconman.2016.08.053`.

URL `http://dx.doi.org/10.1016/j.enconman.2016.08.053`

[137] S. Lecompte, H. Huisseune, M. van den Broek, S. De Schampheleire, M. De Paepe, Part load based thermo-economic optimization of the Organic Rankine Cycle (ORC) applied to a combined heat and power (CHP) system, Applied Energy 111 (2013) 871–881. `doi:10.1016/j.apenergy.2013.06.043`. URL `http://dx.doi.org/10.1016/j.apenergy.2013.06.043`

[138] L. Cao, J. Wang, L. Chen, J. Lou, J. Wang, Y. Dai, Thermoeconomic Analysis and Multi-Objective Optimization of a Combined Cooling and Power System Using Ammonia-Water Mixture: Case Study, Journal of Energy Engineering 144 (3) (2018) 1–17. `doi:10.1061/(ASCE)EY.1943-7897.0000538`.

[139] S. Sanaye, M. Emadi, A. Refahi, Thermal and economic modeling and optimization of a novel combined ejector refrigeration cycle, International Journal of Refrigeration 98 (2019) 480–493. `doi:10.1016/j.ijrefrig.2018.11.007`. URL `https://doi.org/10.1016/j.ijrefrig.2018.11.007`

[140] B. Peris Pérez, J. A. Expósito Carrillo, F. J. Sánchez de La Flor, J. M. Salmerón Lissén, A. Morillo Navarro, Thermoeconomic analysis of CO2 Ejector-Expansion Refrigeration Cycle (EERC) for low-temperature refrigeration in warm climates, Applied Thermal Engineering 188 (2021) 116613. `doi:https://doi.org/10.1016/j.applthermaleng.2021.116613`. URL `https://www.sciencedirect.com/science/article/pii/S1359431121000697`

[141] A. A. Mabrouk, A. S. Nafey, H. E. Fath, Thermoeconomic analysis of some existing desalination processes, Desalination 205 (1-3) (2007) 354–373. `doi:10.1016/j.desal.2006.02.059`.

[142] P. Kurup, C. S. Turchi, Parabolic Trough Collector Cost Update for the System Advisor Model (SAM), Technical Report NREL/TP-6A20-65228 National Renewable Energy Laboratory (November) (2015) 1–40. URL `http://www.nrel.gov/docs/fy16osti/65228.pdf`

[143] H. Sayyaadi, M. Nejatolahi, Multi-objective optimization of a cooling tower assisted vapor compression refrigeration system, International Journal of Refrigeration 34 (1) (2011) 243–256. `doi:10.1016/j.ijrefrig.2010.07.026`. URL `http://dx.doi.org/10.1016/j.ijrefrig.2010.07.026`

[144] S. Elbel, P. Hrnjak, Experimental validation of a prototype ejector designed to reduce throttling losses encountered in transcritical R744 system operation, International Journal of Refrigeration 31 (3) (2008) 411–422. `doi:10.1016/j.ijrefrig.2007.07.013`.

[145] L. Wang, J. Liu, T. Zou, J. Du, F. Jia, Auto-tuning ejector for refrigeration system, Energy 161 (2018) 536–543. `doi:10.1016/j.energy.2018.07.110`. URL `https://doi.org/10.1016/j.energy.2018.07.110`

[146] S. Chen, G. Chen, L. Fang, An experimental study and 1-D analysis of an ejector

with a movable primary nozzle that operates with R236fa, International Journal of Refrigeration 60 (2015) 19–25. doi:10.1016/j.ijrefrig.2015.08.011.
URL http://dx.doi.org/10.1016/j.ijrefrig.2015.08.011

[147] EUMETSAT CM SAF web user interface.
URL https://wui.cmsaf.eu/safira/action/viewProduktSearch

[148] European Commission Joint Research Centre (JRC), PVGIS.
URL http://re.jrc.ec.europa.eu/pvgis.html

[149] E. Nehdi, L. Kairouani, M. Elakhdar, A solar ejector air-conditioning system using environment-friendly working fluids, International Journal of Energy Research 32 (13) (2008) 1194–1201. doi:10.1002/er.1413.
URL https://onlinelibrary.wiley.com/doi/abs/10.1002/er.1413

[150] R. Gabbrielli, P. Castrataro, F. Del Medico, Performance and Economic Comparison of Solar Cooling Configurations, Energy Procedia 91 (2016) 759–766. doi:10.1016/j.egypro.2016.06.241.
URL http://dx.doi.org/10.1016/j.egypro.2016.06.241